IMPACT OF DISTRIBUTED GENERATION ON POWER NETWORK OPERATION

A Thesis
Presented to
The Academic Faculty

by

Aleksandar Pregelj

In Partial Fulfillment
of the Requirements for the Degree
Doctor of Philosophy

School of Electrical and Computer Engineering
Georgia Institute of Technology
December 2003

IMPACT OF DISTRIBUTED GENERATION ON POWER NETWORK OPERATION

Approved by:

Ron Harley, Committee Chair

Miroslav Begovic, Advisor

Ajeet Rohatgi, Co-Advisor

A. P. Sakis Meliopoulos

Date Approved

ACKNOWLEDGEMENTS

I am indebted to many people who have contributed ideas and thoughts during my research at Georgia Tech. First, I would like to thank my supervisors, Dr. Miroslav Begović and Dr. Ajeet Rohatgi for providing the infrastructure and motivation for this research, and for their thoughtful mentorship on all matters of science and life. I would also like to thank Dr. Ron Harley, Dr. Sakis Meliopoulos, Dr. David Taylor and Dr. Branislav Vidaković for serving as members of my thesis committee.

I would like to express gratitude to my co-workers, the students and engineers of UCEP for providing a stimulating and fun environment in which to learn and grow. I would like to thank especially the following: Vijay Yelundur, Mike Ropp, Alan Ristow, Ben Damiani, Mohamed Hilali, Dean C. Sutter and Ajay Upadhyaya. Special acknowledgements are expressed to Ms. Denise Taylor for her friendly and skillful administrative assistance.

Outside the group, I would especially like to thank my dear friends, Borka Milošević, Mile Milisavljević and Branislav Radibratović for many hours of inspiring conversation and for putting up with me during the more difficult times.

Lastly and most importantly, I owe the greatest debt of gratitude to my parents, Jelena and Jovan Pregelj, for the unconditional love and support that they have given me as I pursue my dreams. For all this and much more, I dedicate this thesis to them.

TABLE OF CONTENTS

LIST OF TABLES

LIST OF FIGURES

SUMMARY

The objective of this research is to address some of the challenges associated with the increased penetration of distributed generation (DG) systems into the existing distribution network. Tools and algorithms are proposed that are useful for planning, designing, and operating such a network. Throughout the text, renewable photovoltaic (PV) systems are used as an example of distributed generators. The inherent additional complexity associated with the probabilistic nature of their output makes them a good example for application of the proposed algorithms.

In Task 1, the case is developed for a comprehensive utility-grade PV system simulation tool. The shortcomings of the existing programs are demonstrated, and the outline of the developed general PV simulation program is presented. Using the software model of the PV system, the reliability analysis is incorporated in the model of PV systems, and a novel reliability-based performance derating coefficient is introduced. Furthermore, a novel inverter control algorithm is presented for systems with multiple inverters. The algorithm is designed to increase overall DC/AC conversion efficiency by selectively shutting down some of the inverters during periods of low insolation, thus forcing the remaining inverters to operate at higher efficiency.

In Task 2, the computational difficulties associated with accurate prediction of the effects of renewable DG on distribution feeders are presented. The impact on various feeder operating variables is complicated by both the probabilistic nature of the system's input (solar flux, wind, etc.) and the fact that their actual sizes, positions on the feeder, and operating states may not be known a priori by the utility. Then, a feature-extraction method for reducing the number of computational steps necessary for efficient modeling of the

DG-enhanced feeder operation is presented. The method is based on a clustering algorithm that reduces the input set by grouping the similar data points into groups (clusters), while extracting the important information contained in the underlying data. Because of the inherent averaging properties of the clustering algorithm, the method is augmented by a companion procedure that samples from the original data set only those points that yield estimates of extreme feeder conditions. A Monte Carlo analysis is then performed on a reduced set, allowing the investigation of effects caused by various PC penetrations, control strategies, spatial distributions, etc.

In Task 3, the radial distribution feeder protection strategy is first presented without consideration of DG. Then, the addition of DG across the feeder (constrained in terms of power and/or energy capacity) is introduced in the model. If islanded operation of these DG sources is allowed on a feeder subjected to disturbance, DG may reduce the number of interruptions and/or durations for customers residing within their protection zones, thus increasing the reliability of service. To that end, a procedure for finding optimal positions for DG and protection devices is presented for a feeder equipped with capacity-constrained distributed generators, using a custom-tailored genetic algorithm. The parameters of the genetic algorithm are tuned using three typical distribution feeders. Finally, an adaptive genetic algorithm that eliminates the need for parameter tuning is implemented.

CHAPTER 1

INTRODUCTION AND BACKGROUND

Historically, electricity generation in the regulated environment was driven by the economies of scale - using generating plants as large as possible to drive down the cost per unit of output. In the past 20 years, several driving forces have contributed to the reversal of this trend and sparked interest in decentralized power generation. Technological advances, such as the stationary gas turbine, have made possible production of electricity on a much smaller scale at marginal generation costs lower than those of the traditional large power plants. Utility industry restructuring has brought increased competition. Costs and reliability concerns associated with large power plants have made them even less appealing. Furthermore, increased customer awareness and new societal trends toward "green" generating technologies, have promoted an interest in cleaner, sustainable generators that may be safely installed in the distribution system. The trend toward smaller power plants is evident in Figure 1 [1], and their logical locations are in low-voltage (distribution) networks.

The distributed resources are defined as small, modular electric energy generation or storage systems located relatively close to the customer. Distributed generators (DG) span a variety of operating technologies and sizes, ranging from several kW to hundreds of MW. They may be interconnected with a grid, or operate in "stand alone" mode, without grid support. Conventional DG technologies, dependent on the fuel supply, include industrial gas turbines, gas-fired reciprocating turbines (also called internal combustion engines), microturbines, and fuel cells.

Renewable DG technologies include photovoltaic (PV) generators, wind generators, biomass, and small hydro turbines. The operating principles for all these technologies have

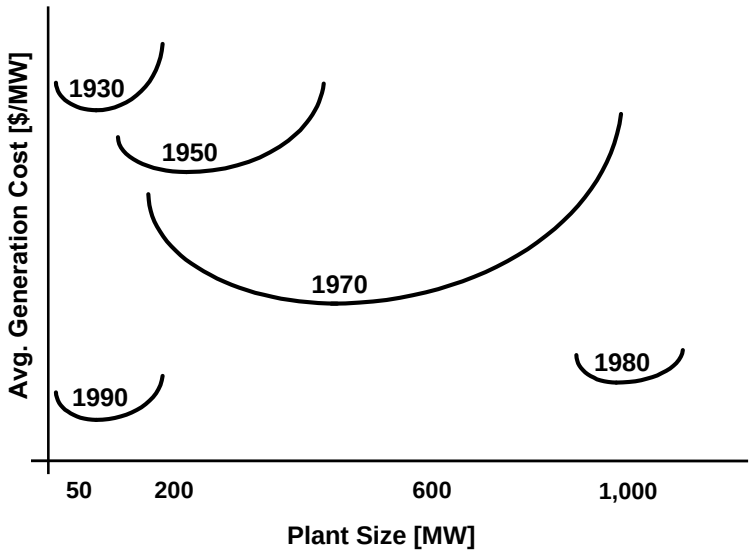

Figure 1: Optimal size of a power plant as a function of its cost (1930-1990) [1].

been known for quite some time, but only recent technology breakthroughs have made them interesting as conventional energy generators. Distributed storage systems, such as batteries, flywheels, superconducting magnetic energy storage systems, or supercapacitors may also be present on the feeder. They may allow renewable generators to be used more effectively, while also reducing the spinning reserve requirements or effectively creating avoided capacity in the bulk power market, which may be useful when the prices are high. The costs and benefits associated with some of the most promising DG technologies are summarized in Table 1.

The internal combustion engine is the workhorse of the electric power industry and smaller installations may be used for DG. They are readily available in a wide range of sizes, with a proven reliability record and competitive price to performance ratio. However, as they are fueled by natural gas or diesel, they face increased environmental concerns when placed in the distribution system.

Wind power has been the fastest growing energy source in the last decade with the worldwide generating capacity surpassing 31 GW in 2002 [4]. Although a small fraction

Table 1: The summary of existing DG technologies as of 2003 [2, 3].

	Internal combustion engine	Wind turbine	Microturbine	Fuel Cell	Solar cell
Size range [kW]	50 kW - 5 MW	50 kW - 5 MW	25 kW - 500 kW	5 kW - 10 MW	<1 kW -100 kW
Installed cost [$/kWh]	200 - 800	1000 - 1500	1000 - 1500	3000 - 4000	1500 - 6500
Electricity cost [¢/kWh]	5.5 - 10	5.5 - 10	7.5 - 10	10 - 15	15 - 20
Fuel	Natural gas, diesel	Wind	Natural gas, hydrogen, propane, diesel	Natural gas, hydrogen, propane, diesel…	Sunlight
Environmental issues	Emmission control required	No emissions	Low	Low	No emissions
Commercial availability	Yes	Yes	Commercial prototypes available	Commercial prototypes available	Yes

of the world's total energy production capacity, wind power provides more than 1% of the energy in many European nations. For example, Denmark already produces almost 20% of its electricity from wind. Germany has the largest installed wind power capacity (12 GW),

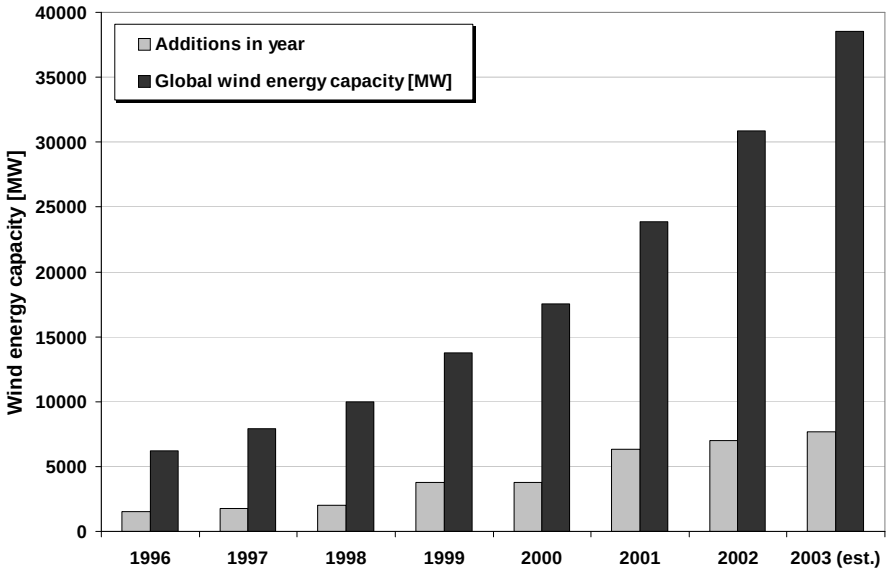

Figure 2: Global wind energy capacity and annual additions per year [4].

enough to meet approximately 4.7% of its electricity needs [4]. The global wind energy capacity and annual worldwide capacity additions are shown in Figure 2 [4].

The installed power of wind systems ranges from several kW for small wind turbines up to the hundreds of MW for large wind farms. The cost of the energy produced from wind is presently in the 0.05-0.10 $/kWh range, making it competitive with traditional fossil-fuel plants. The output of the wind generator is strongly dependent on the available wind energy, which is a probabilistic quantity. For low wind speeds the blades may not turn at all; the generation starts at the cut-in wind speed and rises until the rated generator power is reached. For higher wind speeds, the generation is kept at rated power until the wind speed reaches critical values, when the blades are stopped.

Fuel cells may be the technology that has the most potential to reshape the energy horizon. Fuel cells provide electricity via an electrochemical reaction that can best be described as the reverse electrolysis. They consist of two electrodes in contact with an electrolyte. The anode and cathode are supplied with fuel and air respectively, and the electrochemical reaction generates the voltage between them. They will generate power as long as the fuel is supplied and their response time is extremely small. This makes fuel cells a natural complement to PV and wind generation systems to eliminate the sudden production drops experienced with passing clouds or loss of wind energy.

The cost of PV produced energy has dropped by 80% in the last two decades, but still needs to decrease by an additional 50-75% to be competitive with conventional sources. Several promising PV technologies are in the market today, but none have been able to meet the cost-efficiency requirements for mass-market commercialization. The majority of solar cells produced today are made using monocrystalline or multicrystalline silicon. Monocrystalline cells provide the best efficiency, but are expensive due to high material cost. Multicrystalline material is less expensive, but defects and impurities that are present decrease cell efficiency. Thin-film technologies, which are gaining momentum but still suffer from low efficiency, reliability and scalability problems, have a potential to be the

first solar cell technology to reach the cost-efficiency margin.

Worldwide shipments of PV modules have been increasing at an annual growth rate of 25-35% in the recent years. World production of PV increased by a record 43.8% to 561 MW during the year 2002, with most sales going into the grid-connected sectors in Japan, Germany and California [5]. The total annual production for the period 1994-2002 is shown in Table 2.

Table 2: World photovoltaic module production, consumer and commercial, 1994-2002 [6].

Region	PV production by year (MW)								
	1994	1995	1996	1997	1998	1999	2000	2001	2002
Japan	16.50	16.40	21.20	35.00	49.00	80.00	128.60	171.22	251.07
Europe	21.70	20.10	18.80	30.40	33.50	40.00	60.66	86.38	135.05
US	25.64	34.75	8.85	51.00	53.70	60.80	74.97	100.32	120.60
Rest of world	5.60	6.35	9.75	9.40	18.70	20.50	23.42	32.62	55.05
TOTAL	69.44	77.60	88.60	125.80	154.90	201.30	287.65	390.54	561.77

However, despite steady growth rates and cost reductions, DG systems are still not fully competitive with conventional power plants based on the energy cost alone, although the additional benefits may make them competitive for some applications. Additional benefits may include increased reliability and power quality, loss reduction, peak shaving capability, voltage and reactive support, environmental benefits, grid investment deferment, etc.

The key issues for the sustained growth of distributed energy sources are:

- Continued decline in the cost of DG technologies
- Cooperation from utilities and local governments to ensure the appropriate interconnection requirements for accepting DG into the existing electricity network

- Obtaining full value for DG-produced electricity by accurately modeling and quantifying *all* DG benefits

The objective of this research is to address some of the issues along this path, focusing primarily on the last item - accurate modeling and quantification of DG effects.

1.1 Thesis Overview

In Chapter 2, a photovoltaic system simulation program is developed. The accurate modeling of a PV system performance is essential for a variety of reasons: it allows optimized system designs, avoids overdesigning the system to meet design goals, avoids unrealistically optimistic performance predictions, etc. As PV systems become more widespread, more complicated designs are likely to be introduced that cannot be handled easily with the existing programs, which have essentially been developed for planar PV arrays. Performance of the developed program is compared with the existing commercial PV software tools. The program enables accurate modeling of multi-planar and multi-inverter systems for the first time. Finally, a case study of a multistoried building with PV modules mounted on all four sides is presented.

Chapter 3 describes the availability analysis incorporated into the PV simulation program. PV systems are typically considered very reliable, mainly because of the high reliability of PV modules. Other system components, such as inverters, are not nearly as reliable, and may significantly decrease system performance. These components are typically unaccounted for when system life cycle costs are calculated. Suitability of several inverter configurations is investigated based on their total lifetime energy output and life cycle costs, and a novel control strategy for systems with multiple inverters connected in parallel is introduced.

In Chapter 4, a method for reducing the number of computational steps necessary (number of power flow simulations) when modeling the operation of a DG-enhanced feeder is

developed. The method is based on a clustering algorithm that reduces the input set by grouping similar data points into groups (clusters), while still retaining the necessary information contained in the underlying data. Because of the inherent averaging properties of the clustering algorithm, the method is augmented by a companion procedure that uses only those points from the original data set that yield approximate extreme feeder conditions. Both procedures are demonstrated by investigating the effects of random DG placement on a radial distribution feeder model.

Chapter 5 presents the reliability model of a conventional radial feeder. Methods to improve reliability by adding protection devices, such as reclosers and fuses, are described. The economic analysis, based on determining the sensitivities of standard reliability indices with respect to the increased costs (incurred by adding more protection devices on the feeder) is presented. A Monte Carlo procedure for treatment of uncertainties associated with variable costs of protection devices is also presented.

In Chapter 6, the effects of DG islanded operation on overall feeder reliability are investigated. A reliability model of an unbalanced distribution feeder is developed and validated using the Cooper Power's Distrely Lite program. The model is then extended to allow modeling of a non-radial feeder with capacity-constrained DGs, and quantifying their effect on overall feeder reliability. Finally, a genetic algorithm for optimal placement of protection devices on such feeders is developed. The algorithm is also used to determine optimal DG locations, given the recloser locations, and to optimize both DG and recloser placement to obtain lowest values of reliability indices. Both the standard genetic algorithm (GA), with parameters tuned using three typical feeder designs, and an adaptive GA that eliminates the need for parameter tuning are presented.

Finally, accomplishments and contributions are summarized in Chapter 7.

CHAPTER 2

MODELING OF RENEWABLE DISTRIBUTED GENERATION

2.1 Introduction

Distributed generators (DGs) exist in many forms and, for the purpose of analysis, should be treated differently than conventional large capacity synchronous generators. Conventional non-renewable DGs have the advantage of being fully dispatchable, subject to fuel availability. In addition, they typically have lower installation costs and higher energy density. Renewable DGs, such as photovoltaic and wind systems without storage, are intermittent generators. This is due to the probabilistic nature of their energy input (solar flux, wind), making their effect on the feeder somewhat uncertain in the absence of energy storage. Although PV systems may also be installed as a central station power plant, they can be even more efficiently deployed as a large number of extremely small systems (in the kW range) installed in convenient locations, such as on the roofs of individual customer houses. In that sense, they are an excellent example of the distributed generator uncertainty paradigm for planning and performance forecasting purposes.

PV system output depends on a variety of meteorological parameters (available insolation, temperature, wind speed, etc.) and design parameters (orientation, tilt, shading, dust, electrical losses, module design, system configuration, etc.). Accurate modeling of all parameters is necessary to avoid either unreasonably optimistic performance and life cycle cost predictions or over-designing the system to meet its design goals, as well as to determine the cumulative effects of many such systems on the existing power distribution

network.

Several PV system simulation programs have been developed, offering various degrees of accuracy, speed, and modeling complexity [7, 8, 9]. However, they are often designed as straightforward input-to-output tools, calculating the power output after all system parameters have been provided by the user. Any attempt at system optimization requires a tedious manual trial-and-error process based on repetitive use of the model for a variety of conditions spanning the search space of the tunable parameters. As commercial programs, they are using proprietary models, offering little insight into the details of the simulation process. Furthermore, they are not suitable for modeling more complex PV systems, such as the systems with variable tilts and orientations, commonly found in building-integrated PV systems.

In Task 1, the general procedure for calculating power output of a PV system is presented. Then, a review of existing PV simulation programs is given, indicating possible areas for improvement. A complete PV simulation program, based on the most rigorous theoretical models, is developed, and its performance is tested against commercial programs for the case of single-planar arrays. The ability to model multi-planar and multi-inverter systems has been implemented for the first time in a PV simulation program. The developed program is then used to quantify the effect of random inverter failures on PV system performance and to develop a procedure for choosing optimal inverter configuration and control algorithm.

2.2 Development of a flexible PV system simulation tool

The simplified diagram of a PV system is presented in Figure 3. An illuminated PV module transforms the energy obtained by the sun into DC power, which is inverted into AC power using a power conditioning system. The power conditioning system also operates the PV array at or near its optimal operating point and synchronizes its operation with the

utility grid. The AC power is used to feed the local load, and the remainder is passed on to the utility. Similar to this process, a PV system simulation program has several main procedures that are performed sequentially:

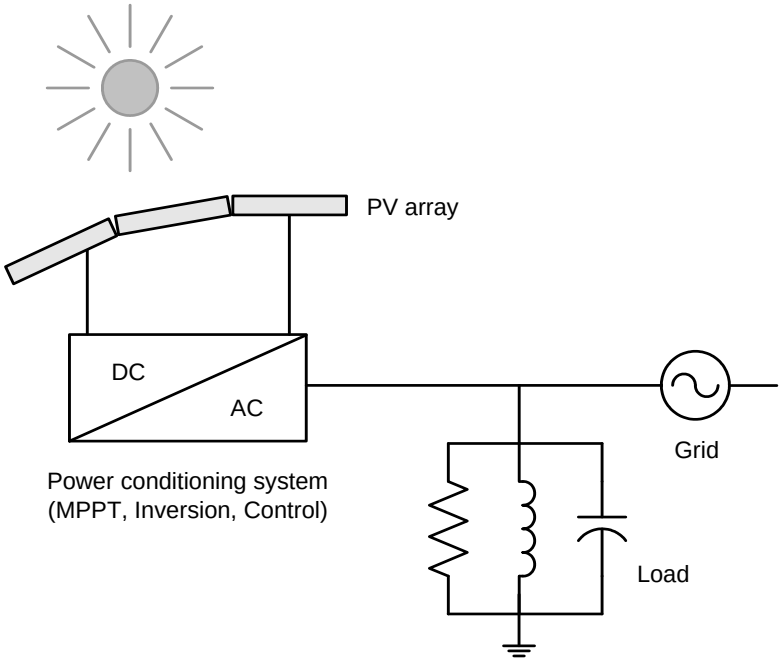

Figure 3: Diagram of a photovoltaic (PV) system

- **Insolation model** translates the available standardized weather data into the plane of array insolation, which is received by a solar module.
- **Thermal model** uses calculated plane of array insolation with measurements of ambient temperature and wind speed to obtain the operating temperature of the module.
- **DC model** calculates the DC power output of the entire PV system, using the previously calculated plane of array insolation(s) and temperature(s).
- **AC model** calculates the AC power output of the system, based on the available DC power and chosen inverter configuration and control strategy.

2.2.1 Insolation model

The amount of solar radiation (insolation) received by the solar module depends on a variety of parameters such as its tilt, orientation, height, albedo of surrounding ground, shading by nearby objects, etc. Weather databases, used as sources of insolation data, typically provide insolation measurements suitable for a fixed horizontal system or a system equipped with a tracking mechanism. The insolation model therefore uses those standard measurements to calculate insolation incident on an arbitrarily tilted and oriented PV module. To that end, the total (measured) insolation is divided into components that are calculated separately. There are three components of the solar radiation:

- **Beam (direct) radiation**, *B*, is the radiation received from the sun without having been scattered by the atmosphere. It is measured as a radiation that falls within a 5.7° field of view centered on the Sun.
- **Diffuse radiation**, *D*, is the radiation received from the sun after its direction has been changed by scattering by the atmosphere.
- **Reflected radiation**, *R*, is the radiation received from the sun after it has been reflected from nearby surfaces.

The total (global) radiation, *G*, incident upon any given surface is the sum of these three components. Depending on the orientation of the surface, the following special cases of global insolation are usually used:

- **Horizontal insolation** (denoted with subscript *hor*) is the insolation falling on a horizontal surface. The horizontal insolation has only direct and diffuse components, since there is no ground-reflected component.
- **The insolation normal to the rays** (denoted with subscript $\perp$) is the insolation received by a surface perpendicular to the sun rays, i.e. the insolation that would be captured by a system equipped with the sun tracking mechanism.

- **The plane of array insolation** (denoted with subscript *POA*) is the insolation received by the surface (array) tilted at an angle β and oriented with an azimuth angle γ.

The usual source for weather data, for US locations, is the Typical Meteorological Year (TMY2) database [10], which consists of sets of hourly values of various meteorological parameters for a one-year period. It consists of months selected from individual years from a 30-year observed period, and concatenated to form a complete year. The data thus represents conditions judged to be typical over a long period of time. The TMY2 database provides two insolation measurements: total horizontal insolation, G_{hor}, (total insolation received on a horizontal surface) and beam (or direct) component of the normal insolation, $B_{\perp}$, (direct insolation received within the 5.7° field of view centered on the sun). The insolation model uses these two standardized measurements to obtain the total insolation received by the arbitrarily tilted and oriented surface (module). The procedure is split into the following steps:

Step 1. The exact position of sun is determined by calculating the following sun angles:

- *Solar elevation (altitude) angle*, α_s, describes how high the sun appears in the sky. It is measured between the horizontal and the line to the sun. Its complement is the zenith angle, θ_z, the angle between the vertical and the line to the sun.
- *Solar azimuth angle*, γ_s, is the angular displacement (from south) of the projection of the line to the sun on the horizontal plane.
- *Declination of the Sun*, δ, is the angle between the earth's equatorial plane and the line joining the centers of the sun and the earth.

These three angles completely determine the position of the sun. By knowing these angles, the PV array azimuth angle (γ), and the array tilt angle (β), the angle of incidence (θ) can be calculated. The angle of incidence is the angle between the line

to the sun and a line perpendicular to the array surface. It determines the mutual position between the sun and the PV module, and allows the calculation of the plane of array insolation from the standardized horizontal measurements. The detailed procedure for determining all solar angles is given in Appendix A.

Step 2. Total horizontal insolation, G_{hor}, is separated into beam, B_{hor}, and diffuse component, D_{hor}, using the geometric relationship between the beam horizontal, B_{hor}, and beam normal insolation, $B_{\perp}$, (available from the TMY2 database).

$$B_{hor} = B_{\perp} \sin \alpha_s \tag{1}$$

$$D_{hor} = G_{hor} - B_{hor} \tag{2}$$

where α_s is the solar elevation angle.

Step 3. The beam component of the plane of array insolation, B_{POA}, is calculated from the available beam normal insolation, $B_{\perp}$, again on the basis of geometry.

$$B_{POA} = \begin{cases} B_{\perp} \cos\theta & \text{if } |\gamma_s - \gamma| < 90^\circ \\ 0 & \text{if } |\gamma_s - \gamma| \geq 90^\circ \end{cases} \tag{3}$$

The condition $|\gamma_s - \gamma| \geq 90^\circ$ indicates that the sun is behind the module, and thus direct insolation is zero.

Step 4. The diffuse component of the plane of array insolation (D_{POA}) is the insolation received by the module after it has been scattered by the atmosphere out of the direct beam. It is very difficult to calculate because of its nondirectional nature and is considered the largest potential source of computational error [11]. The diffuse insolation models can be divided into two categories: isotropic and anisotropic. Isotropic models assume that the diffuse component of the plane of array insolation is received from a uniformly bright sky dome, which leads to simple, but relatively inaccurate calculation methods [12]. The anisotropic models take into account the fact that the circumsolar region and a narrow horizon band are brighter than the rest of the

sky. This leads to more accurate (but also more complex) models, such as the Perez model [13], generally considered to be the most accurate diffuse insolation model. The Perez model divides the sky into two regions of different brightness (circumsolar region and an infinitely small horizon band) and the isotropic dome or background. All three regions are shown in Figure 4 [14].

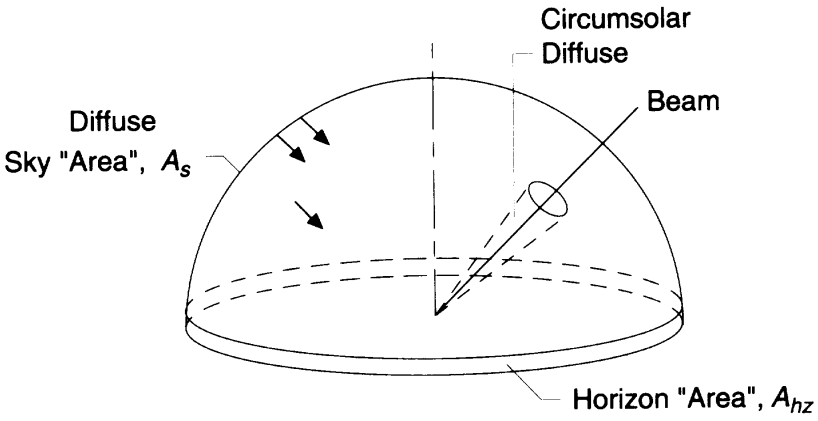

Figure 4: Three regions of the sky dome used for the calculation of the diffuse portion of insolation in Perez model [14].

The contribution of each band is calculated separately using the following formula:

$$D_{POA} = D_{hor}[\frac{1+\cos\beta}{2}(1-F_1) + \frac{a}{b}F_1 + F_2\sin\beta] \tag{4}$$

where the terms in parentheses represent the contributions from the isotropic background, circumsolar, and horizon band, respectively. The geometric factors a and b account for the angles of incidence of the cone of the circumsolar radiation on the tilted and horizontal surface, and the brightness coefficients F_1 and F_2 are functions of three parameters that describe the sky conditions: the clearness parameter ε, sky brightness parameter Δ, and the sun zenith angle θ_z. The detailed procedure for obtaining these parameters is given in [13].

Step 5. The reflected component R_{POA}, received by the module after it has been reflected

from the surroundings, can be estimated from the total horizontal insolation G_{hor} and the albedo (reflectance) ϱ of the surrounding ground.

$$R_{POA} = \varrho \frac{1 - \cos\beta}{2} G_{hor} \tag{5}$$

Step 6. The total insolation received by the tilted plane G_{POA} is obtained by summing the contributions from the beam (B_{POA}), diffuse (D_{POA}), and reflected (R_{POA}) components.

The contribution of all components is shown in Figure 5 [14].

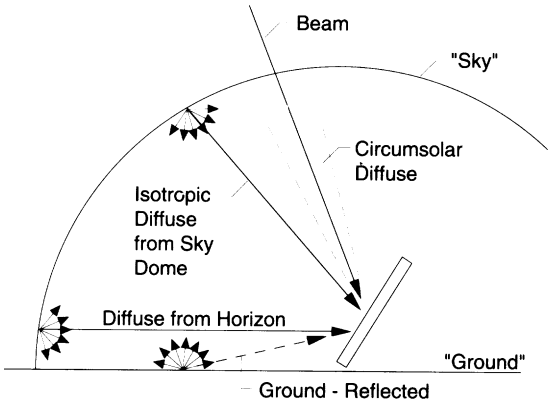

Figure 5: Components of the solar radiation reaching a tilted surface: beam, diffuse (from the sky dome, circumsolar region and the horizon band) and ground-reflected radiation. [14].

2.2.2 Thermal model

The cell's operating temperature heavily influences its power output. The silicon solar cell's efficiency drops by approximately 0.35% – 0.5% per 1°C increase in temperature above the standard reference temperature of 25°C. Multiple cells are connected in a series–parallel configuration to form a solar module. Clearly, a relatively small error in temperature calculation may introduce significant error in the calculation of a PV module's energy output.

There are three commonly used models for obtaining the cell's temperature. The Sandia model and Fuentes model [15, 16], calculate the cell temperature sequentially, using the ambient temperature and wind speed data, available from the TMY2 database, and previously calculated plane of array insolation. The third method iterates the calculation of the cell's temperature and efficiency until a feasible solution is reached [14]. The Sandia method is an experimental method, dependent on various module-specific empirical coefficients, some of which are typically not supplied by module manufacturers. The Fuentes method is generally considered as the most rigorous temperature model. It is based on a differential energy balance equation for a PV module:

$$\alpha G_{POA} = h_c(T_c - T_a) + \varepsilon\sigma(T_c^4 - T_s^4) + \varepsilon\sigma(T_c^4 - T_g^4) + mc\frac{dT_c}{dt} \tag{6}$$

The incoming energy from the sun, on the left hand side of (6), is equal to the sum of the energy dissipated by convection, radiation to the sky, radiation to the ground, and the energy stored in the module, respectively. The terms in (6) are the module's absorptivity α, convective heat transfer coefficient h_c, cell temperature T_c, ambient temperature T_a, "sky" temperature T_s, ground temperature T_g, module emissivity ε, Steffan-Boltzmann constant σ, module mass m, and the module's heat capacity c. Equation (6) is integrated numerically, until the solution for T_c is obtained. The Fuentes model also acknowledges that the module mounting configuration influences the operating cell temperature, and allows modeling of such cases by introducing a parameter called the installed nominal operating cell temperature (INOCT).

2.2.3 DC power model

The general way to obtain the DC power output of the solar cell (module) is to use the diode model of a solar cell (7), with data supplied by the module manufacturer, to determine its operating point at any given meteorological conditions. The DC power output of the solar

module is given by

$$I = I_l - I_o(e^{\frac{V+R_sI}{a}} - 1) \tag{7}$$

$$P = VI \tag{8}$$

where V and I are the module operating voltage and current, I_l is the so-called light current, I_o is the diode reverse saturation current, R_s is the series resistance, and a represents a diode ideality parameter. The parameters I_l, I_o, and a, and consequently the actual operating voltage and current of a solar module, are strongly dependent on cell temperature T_c and/or plane of insolation G_{POA}. The following relationships are good approximations for many PV modules [17].

$$a = a_{ref}\frac{T_c}{T_{c,ref}} \tag{9}$$

$$I_l = \frac{G_{POA}}{G_{POA,ref}}[I_{l,ref} + \mu_{I_{sc}} \cdot (T_c - T_{c,ref}] \tag{10}$$

$$I_o = I_{o,ref}(\frac{T_c}{T_{c,ref}})^3 \exp[\frac{\varepsilon N_s}{a_{ref}}(1 - \frac{T_{c,ref}}{T_c})] \tag{11}$$

The subscript *ref* in (9–11) indicates the quantity at standard reference conditions (STC), defined as the insolation of $G_{POA,ref} = 1000\frac{W}{m^2}$ and ambient temperature of $T_{amb,ref} = 298K$. The remaining terms in (9–11) are the temperature coefficient for short-circuit current $\mu_{I_{sc}}$, the cell material bandgap energy ε, and the number of cells in series per module N_s. The fourth parameter, R_s is assumed independent of the cell temperature. The resulting I-V curves for various combinations of insolation and temperature are shown in Figure 6 [14].

Figure 7 shows the resulting power output characteristics (P-V curves) of a PV module for several combinations of cell temperature and plane of array insolation. Unfortunately, analytical solution of (7) is not possible. For a given voltage value V, an iterative fixed-point or Newton algorithm may be used to obtain the current value I. The I-V curve is then traced by repeating this procedure for voltage values from zero to the open-circuit voltage V_{oc}, thus finding the maximum power (as per (8)) in the process.

The same procedure can be applied to the entire array if all modules that form the array

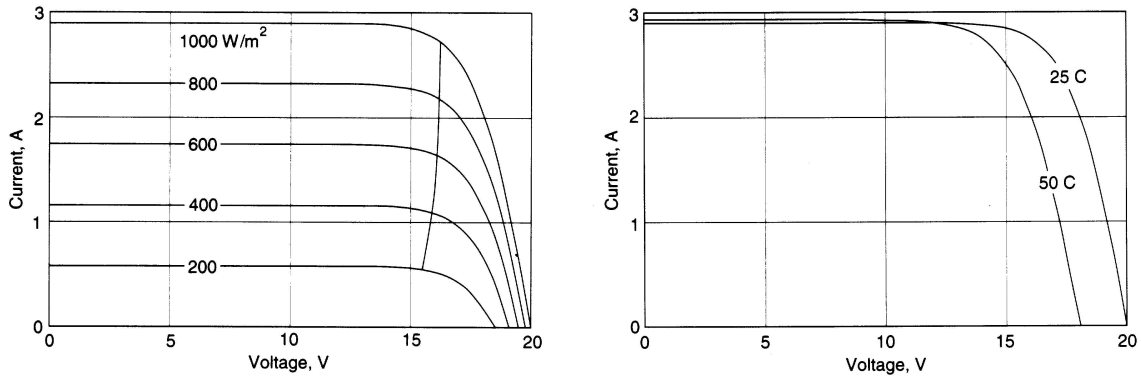

Figure 6: The influence of insolation (left) and temperature (right) on the I-V curve of a solar cell [14].

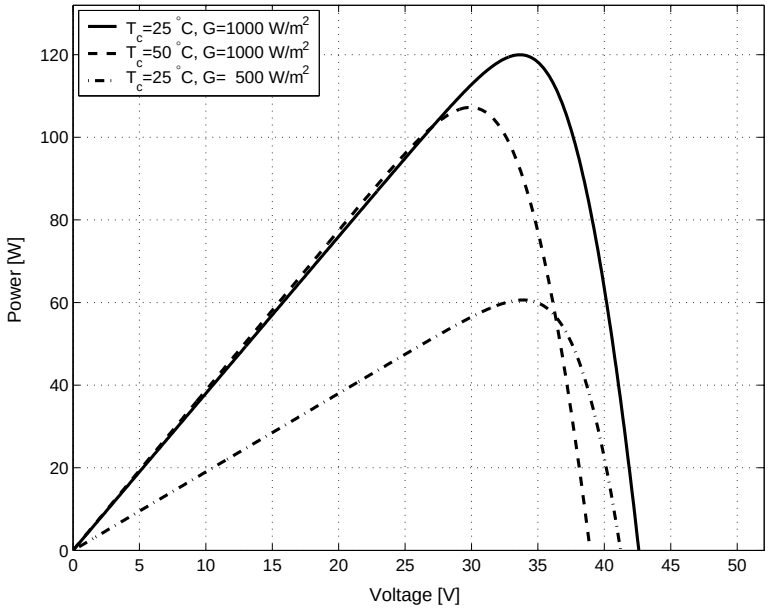

Figure 7: The influence of cell temperature and insolation on PV module power production and the position of the maximum power point.

lie in the same plane. However, in the case of the multi-planar arrays (when modules are oriented and/or tilted differently), modules receive different amounts of insolation, operate at different temperatures, and consequently have different output I-V characteristics. All modules with the same orientation and tilt form a section (subarray) that has a unique P-V curve. By connecting these sections (subarrays) in parallel, the array operating point shifts away from the optimal points for each of the individual sections. To determine the operating

point of the array, P-V curves for all sections need to be determined and summed, obtaining the equivalent P-V curve for the entire array. The actual power output of the whole system is thus determined as the maximum of that equivalent P-V curve. The whole procedure should then be repeated for each time point. Typically, at least 8760 time points are needed, as the operation of a PV system is simulated for one year in ten minute intervals.

Fortunately, the dependence of operating voltage on insolation is only logarithmic, as seen in Figure 6, meaning that the change of insolation does not move the operating point significantly. The influence of temperature is more pronounced, but temperature variations between different array sections are typically much smaller than variations in insolation. The performance loss due to array coupling is therefore usually neglected, as virtually all available commercial programs avoid I-V curve calculations. They do so typically by linearly adjusting the nominal cell's efficiency (obtained at Standard Test Conditions) for a given operating temperature, thus obtaining the estimate of the peak of the P-V curve. The Sandia method relies on empirical parameters obtained using standardized field measurements, which are available for only a limited number of modules.

Neglecting the subarray coupling may be justified for systems with few subarrays when the difference in tilts and azimuths between the arrays is relatively small and when all modules in the system are of the same type (i.e. have the same nominal voltage and temperature characteristics). Modeling of such systems using a so-called curvature derating factor has been presented in [18]. However, as PV systems become more widespread, they will become more and more complex and their interaction may no longer be neglected. This is especially the case for the so-called building integrated PV, in which solar modules are integrated into a building itself, becoming part of the building's roof or wall structure. PV cells can also be laminated into the window glass used in the building. Such complex systems can not be modeled using tools essentially developed for planar arrays.

In this research, the procedure for determining the operating voltage and power output is split into five steps:

Step 1. For each subarray, the parameters I_l, I_o, R_s, and a are calculated at Standard Test Conditions (STC) using the standardized data supplied by the manufacturer.

Step 2. The parameters are recalculated according to the previously determined plane of array insolation(s) G_{POA} and module temperature(s) T_c, using relationships from [17].

Step 3. The P-V curves are traced by solving (7) for voltages ranging from zero up to the open-circuit voltage. The iterative numerical procedure is replaced by an approximate analytical procedure by manipulating (7), as explained in Section 2.2.3.1.

Step 4. All individual P-V curves are concatenated to obtain the equivalent P-V curve of the entire array.

Step 5. The system's operating point is determined as the peak of the resulting P-V curve.

2.2.3.1 Analytical procedure for solving diode equation

Solving the I-V curve equation is the most computationally intensive component of the PV modeling procedure, and it must be repeated a large number of times throughout the simulation. To be able to maintain relatively fast execution times (comparable with existing commercial programs), an approximate analytical solution of (7), based on [19], is presented and used in the developed program, called the GT simulator. The procedure greatly improves the calculation speed by performing a Taylor series expansion of (7), and may be made arbitrarily close to the exact solution by using the appropriate number of terms in Taylor expansion.

First, a change of variables is introduced, allowing (7) to be presented in a more compact form. Defining the normalized variables as

$$i = \frac{R_s(I_l + I_o - I)}{a} \tag{12}$$

$$u = \frac{V + R_s(I_l + I_o)}{a} + \ln\frac{R_s I_l}{a} \tag{13}$$

equation (7) becomes

$$i = \exp(u - i) \tag{14}$$

A trial function, i_t, is introduced, which approximates the correct solution of (14) for all values of u.

$$i_t = \ln(1 + \exp(u)) \tag{15}$$

More complex trial functions may be constructed, as long as they and their derivatives are continuous [19]. For a given value of u, the trial function has the value i_t. Consequently, the exact value of u_t corresponding to $i = i_t$ is found by solving (14).

$$u_t = i_t + \ln(i_t) \tag{16}$$

Finally, a precise solution for $i(u)$ may be obtained by performing a Taylor series expansion of (14) around $u = u_t$.

$$i(u) = i_t + \left.\frac{di}{du}\right|_{u_t} (u - u_t) + \frac{1}{2} \left.\frac{d^2 i}{du^2}\right|_{u_t} (u - u_t)^2 + \ldots \tag{17}$$

The process is illustrated in Figure 8.

While (14) is an implicit function, its derivatives depend only on voltage. They are calculated exactly as follows:

$$\frac{di}{du} = \frac{i}{1 + i} \tag{18}$$

$$\frac{d^2 i}{du^2} = \frac{i}{(1 + i)^3} \tag{19}$$

$$\frac{d^3 i}{du^3} = \frac{i(1 - 2i)}{(1 + i)^5} \tag{20}$$

The second-order Taylor series expansion around $u = u_t$ is then simply:

$$i(u) \approx i_t(u)\{1 + \frac{u - u_t(u)}{1 + i_t(u)} + \frac{1}{2}\frac{[u - u_t(u)]^2}{[1 + i_t(u)]^3}\} \tag{21}$$

Finally, to obtain the correct module current, the scaled current i is transformed back to the original variable I.

$$I = I_l + I_o - \frac{ai}{R_s} \tag{22}$$

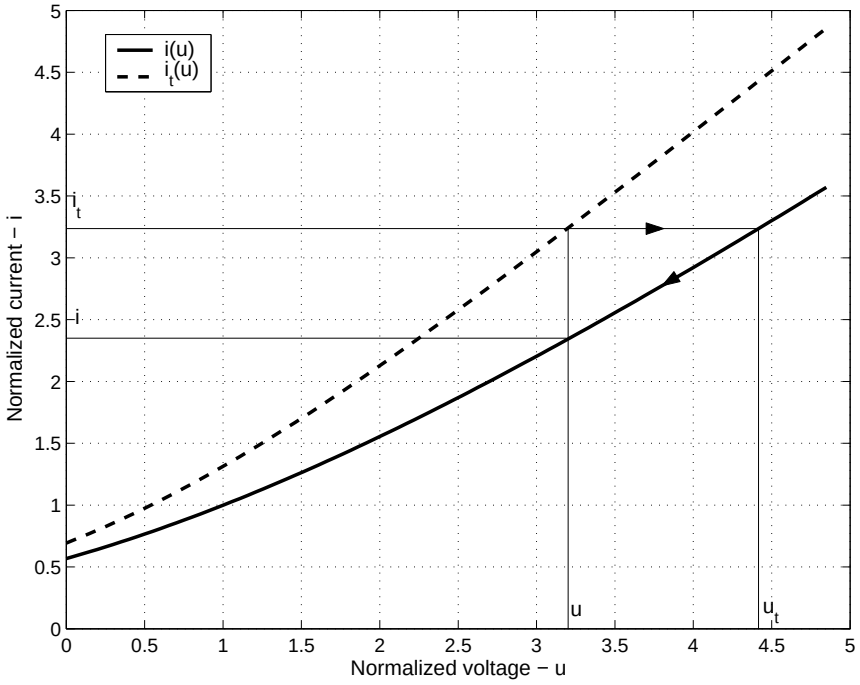

Figure 8: Principle of deriving the approximate solution of the solar cell's I-V equation.

The second order Taylor expansion yields satisfactory results, especially near the maximum power point, as shown in Figure 9. The solution may be made arbitrarily precise by including more Taylor terms in (21). The actual P-V curve and the associated error obtained using the second order Taylor series is shown in Figure 9.

Note that the error is almost negligible for voltage values lower than 40 V, and remains under 2% for almost the entire voltage range. The relative error increases as the power sharply decreases with voltage at the end of the P-V curve, mainly because the absolute power values are rather small. This behavior may be further reduced or eliminated by using a higher order Taylor series, or by choosing a more complex trial function.

2.2.4 AC model of a PV system

The AC model of a PV system calculates the AC power output of the system, based on the previously calculated DC power and chosen inverter configuration and control strategy. The DC/AC conversion stage of a PV system is typically modeled as a single inverter

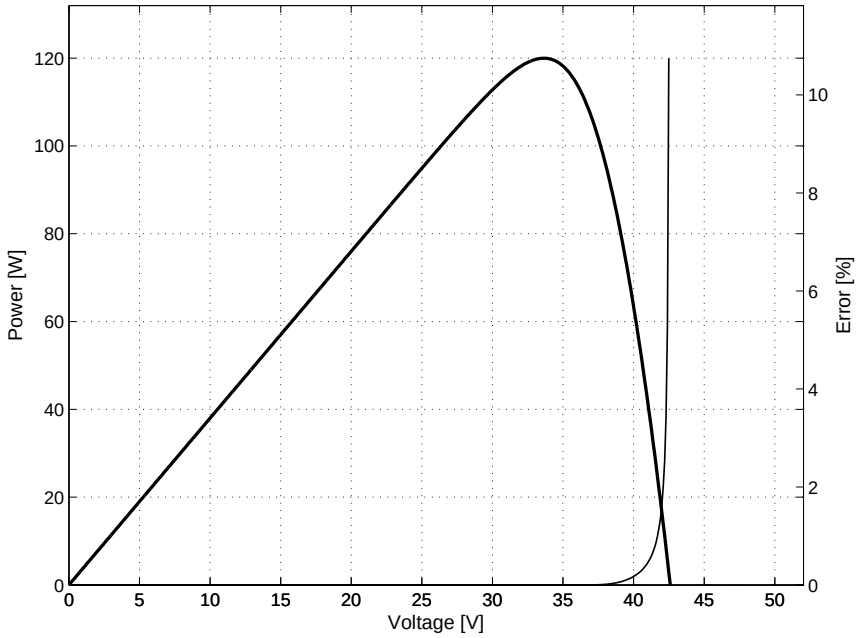

Figure 9: Relative error in the calculation of the P-V curve using second order Taylor expansion.

represented using its conversion efficiency curve, which is a function of the actual DC power being processed. Commercial software programs often approximate the efficiency curve using measured or estimated efficiency at various discrete loading levels. Although a single inverter case is the most commonly used configuration in PV systems, a multiple-inverter configuration may provide some additional benefits, either due to increased reliability or increased overall conversion efficiency. These benefits are qualitatively described and quantified using a procedure introduced in Chapter 3.

2.3 Summary of commercial PV simulation programs

A summary of the existing PV simulation programs is presented below and in Table 3.

- **PVFORM** is a program written by Sandia National Laboratories [7], utilizing rigorous Perez and Fuentes models for calculating the insolation and temperature of solar modules. However, it uses an obsolete TMY1 weather database, linear efficiency

scaling for DC power calculation, and a fifth order polynomial with fixed coefficients for inverter conversion efficiency.

- **PVGRID** is a program developed by Pacific Energy Group [8], which uses proprietary models, but has been tested extensively using field results. It uses modified Perez and Fuentes models, allows limited I-V curve modeling of modules (assuming that the user specifies the R_s and a parameters, which are *not* given by manufacturers), and assumes that all modules lie in the same plane.
- **PV DESIGN PRO** is the most recent PV simulation program [9], with a superior graphical user interface. It relies on the new Sandia experimental model, and can also perform parametric analyses to identify the interdependencies between various system parameters. However, the thermal model assumes that the modules are mounted in the open rack structure, which may lead to significant modeling errors for other mounting configurations. For example, roof-integrated modules may operate at temperatures up to 20°C above those in open racks [15].

None of the existing commercial programs are capable of simulating variable-tilt and/or variable-azimuth arrays, typical for building-integrated PV (BIPV) systems fitted to curved roofs, or other non-planar structures. Multi-inverter systems cannot be easily modeled either.

In this research, a complete PV simulation program, called the GT simulator, utilizing the most rigorous models for each of the four basic PV models is developed in MATLAB and compared extensively with the existing programs. The insolation model implemented is the full Perez model. The calculation of insolation early in the morning and late in the evening is made more accurate by calculating the exact times of sunrise and sunset and incorporating them into the Perez model, as explained in Appendix A. The thermal model implemented is the full Fuentes model. The DC output of a module is obtained by determining the full I-V curve of the array, which allows modeling of multi-planar arrays, as explained in Section 2.2.3. The DC to AC power conversion model allows modeling of

Table 3: Comparative analysis of models implemented in commercial PV simulation programs and in the GT simulator.

	PVFORM 3.3	PVGRID 7.1	PV Design Pro 5.0	GT simulator
Weather database	TMY1	TMY2	TMY2	TMY2
Insolation model	Perez	Proprietary (based on Perez)	Perez	Perez
Thermal model	Fuentes	Proprietary	Sandia's experimental model	Fuentes
Arrray DC model	Linear temperature efficiency scaling	Simplified diode model (proprietary)	Sandia's experimental model	Full diode model
PCU model	Fixed coefficients	10-point curve	3-point curve	7-th order polyfit, various control strategies
Multi-planar arrays	No	No	No	Yes (using I-V curves)
Multi-inverter systems	No	No	No	Yes
Reliability analysis	No	No	No	Yes

multi-inverter systems, which led to the introduction of a novel inverter control strategy, as explained in Chapter 3. Modeling of voltage source inverters that inject both active and reactive power is supported, as per Section 4.7. Table 3 also shows models implemented in the MATLAB-based PV simulation tool.

The main screen of the GT simulator is shown in Figure 10. In the following sections, the capabilities of the GT simulator will be demonstrated on several examples. First, its performance will be compared to the existing commercial programs for the case of a planar PV system. Than, a multi-planar PV system will be modeled, showing the increased modeling accuracy, compared to the existing programs.

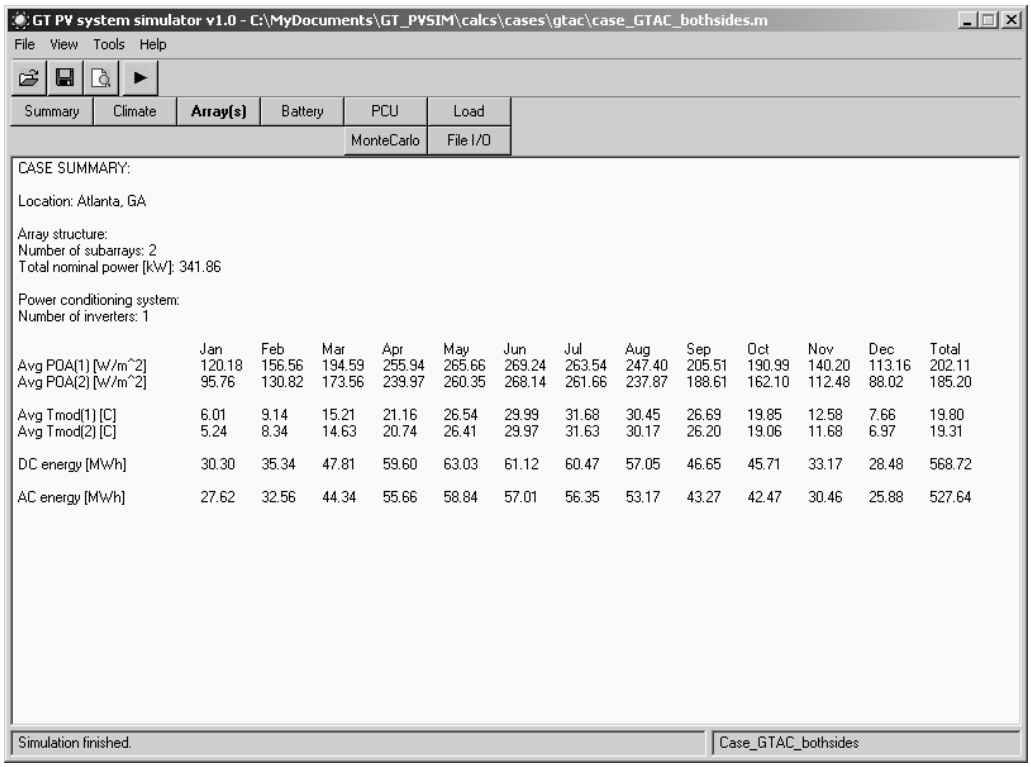

Figure 10: The main screen of the GT simulator.

2.4 Case study: Georgia Tech Aquatic Center PV system

The PV array on top of the Georgia Tech Aquatic Center (GTAC) was the world's largest roof-mounted PV system at the time of its construction in 1996. The system consists of 2856 multicrystalline Si modules, each rated at 120 Wp, wired in 238 series strings of 12 modules each, giving the total rated system installed power of 342 kW. The system is shown in Figure 11. The black panels along the roof edges are the collectors of a solar thermal system which maintains the desired pool water temperature. The remainder of the roof is covered by 2856 PV modules.

As it can be seen in Figure 11, the roof of the GTAC is not flat. One side of the roof is facing north (12 degrees east of north) with curvature varying from 0 to 10 degrees. The opposite side of the roof is facing south (12 degrees west of south), with curvature varying

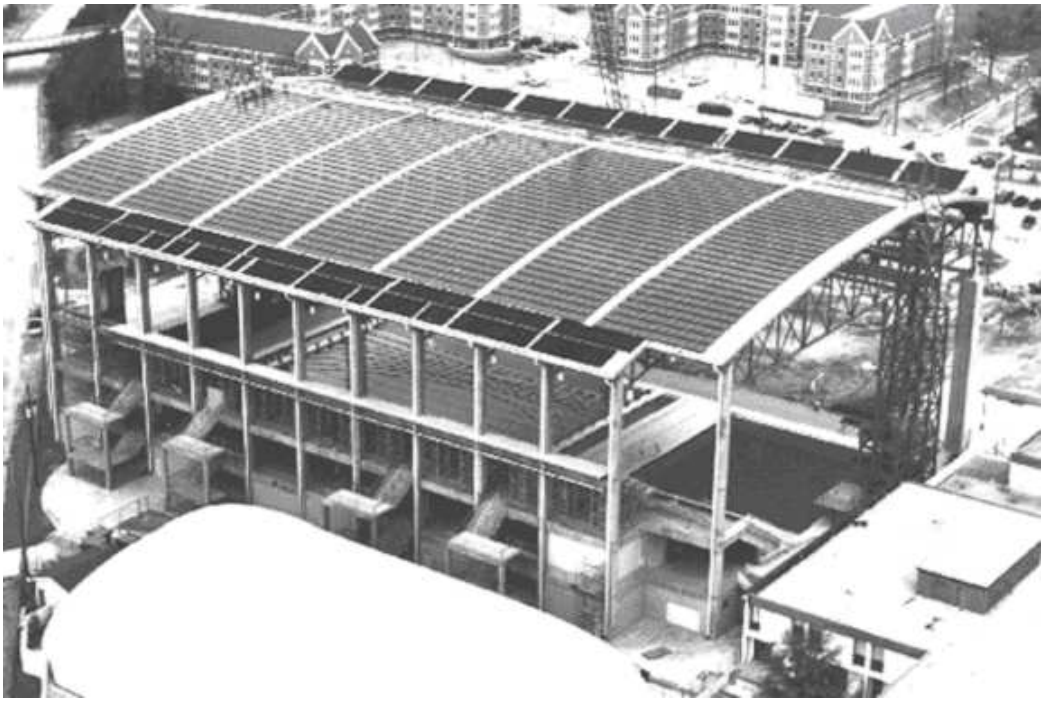

Figure 11: An aerial view of the Georgia Tech Aquatic Center.

from 0 to 13 degrees. The modules are installed directly on the roof and therefore follow its curvature.

There is a total of 34 rows - six on the north side and 28 on the south side. Each row has a different tilt angle, however modules in the same row have the same tilt and azimuth, and therefore receive equal amount of insolation. The wiring diagram of the system is shown in Figure 12, and tilts and azimuths of individual rows are shown in Table 4.

The array is mounted to the roof using clamps that attach directly to the aluminium standing seams. The total standoff height is approximately 3.5 inches – 1.5 inches for the height of the clamps and 2 inches for the height of the standing seams. The array mounting scheme is shown in Figure 13.

The power from the roof is fed to the electrical room, located underneath the diving pool, via seven circuits through the single 315 kW (DC) power conditioning unit (PCU), which performs the inversion. The power is then injected into the grid through a $\Delta - Y$ isolation transformer. The system is described in detail in [20, 21, 22, 23].

Table 4: Measured tilts of modules in the GTAC PV system (per row). Row designation is as depicted in Figure 12.

Row designation	Tilt angle [deg]
6N	9.75
5N	8.00
4N	6.50
3N	5.00
2N	3.75
1N	2.25
1S	0.00
2S	0.00
3S	1.00
4S	1.00
5S	2.00
6S	2.50
7S	2.50
8S	3.00
9S	3.00
10S	4.50
11S	5.00
12S	5.50
13S	6.00
14S	6.00
15S	6.50
16S	7.00
17S	7.25
18S	9.00
19S	9.25
20S	9.25
21S	10.00
22S	10.00
23S	11.00
24S	11.00
25S	11.00
26S	11.50
27S	12.50
28S	13.00

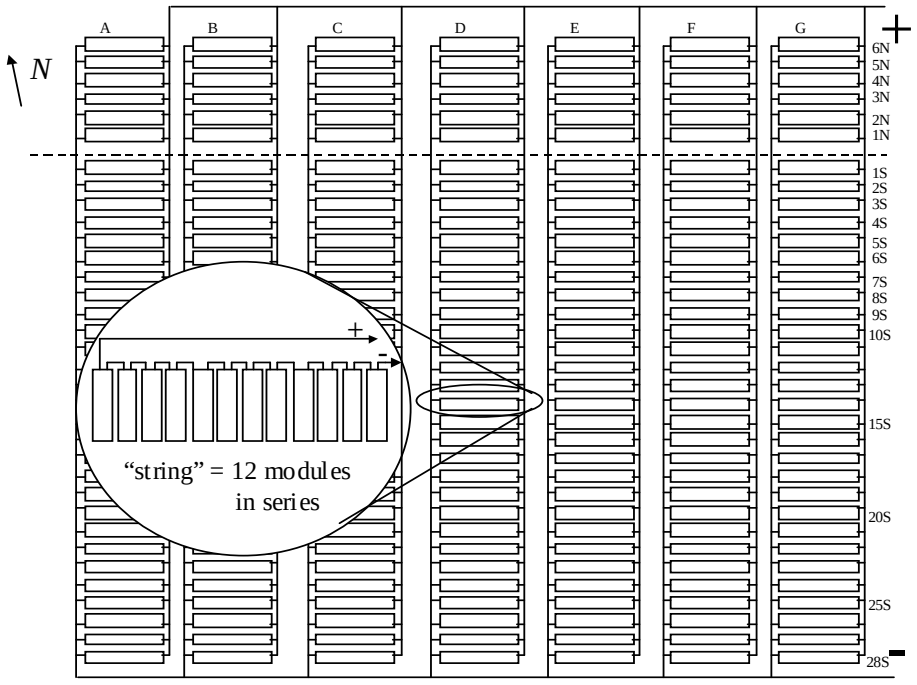

Figure 12: Wiring diagram of the Georgia Tech Aquatic Center PV system.

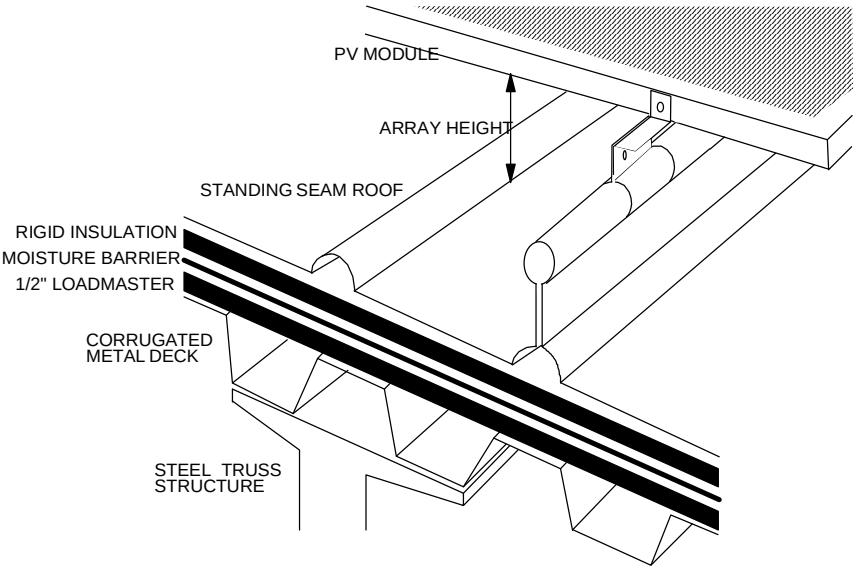

Figure 13: Schematic representation of the array mounting scheme.

2.4.1 Validation of the GT simulator for planar surfaces

To validate the GT simulator, a south subarray of the Georgia Tech Aquatic Center PV system has been modeled using PVGRID, PV Design Pro and the GT simulator. The south subarray has been chosen because PVGRID and PV Design Pro cannot model multiplanar arrays. Note that in this analysis, all loss mechanisms are neglected, as the goal is to show only the difference attributable to the use of different insolation, thermal and DC models.

Figures 14-16 represent the plane of array (POA) insolation, module temperature and DC power output of a south subarray for a *typical* day, calculated using PVGRID, PV Design Pro, and GT simulator.

The curves for POA insolation obtained with PV Design Pro and GT simulator are almost identical (Figure 14), as both programs use the full Perez diffuse insolation model. PVGRID estimates higher POA insolation, because of the simplification of the Perez model.

The module temperature obtained with PV Design Pro is significantly lower than the other two curves in Figure 15, as PV Design Pro always assumes an open-rack module mounting configuration. Both PVGRID and the GT simulator account for different mounting configurations by modifying the nominal operating cell temperature (NOCT) parameter, supplied by the module manufacturer. The modules in the GTAC PV system are mounted on the roof, with approximate standoff height of 3 inches, which reduces ventilation and increases their operating temperature. Differences between the two curves are due to the higher estimated POA insolation by PVGRID and a proprietary modification of the Fuentes model used by PVGRID.

Finally, Figure 16 shows the actual power output for all three cases, showing relatively good agreement between all three curves. The error in the thermal model of the PV Design Pro software overestimates of the energy output, while the difference between PVGRID and GT simulator is very small. The total annual energy output is also presented in Figure 17. Note that all loss mechanisms (due to PV module mismatch, DC cabling and maximum

power point tracking mechanism) are neglected in this example, to be able to isolate differences resulting from the use of different insolation, temperature and DC models.

Similar trends are experienced throughout the year. Figures 18-19 show the *annual* plane of array insolation calculated using all three programs, and plotted one against each other. Figure 18 shows the correlation between POA insolation values calculated using the GT simulator and PV Design Pro. As both programs use the Perez diffuse insolation model, the agreement is excellent, except for several points with extremely low insolation values. The agreement between the GT simulator and PVGRID is also good (Figure 19). A slight overestimation of POA insolation by PVGRID is again attributed to the simplification of the Perez diffuse model used by PVGRID.

Figures 20-21 show the *annual* system DC power output, calculated using all three programs, and again plotted one against each other. PV Design Pro consistently overestimates DC power output, as a result of the underestimation of module temperature. The difference in power output between the GT simulator and PVGRID is attributed to the slight overestimation of POA insolation by PVGRID and to the different thermal modules used by two programs.

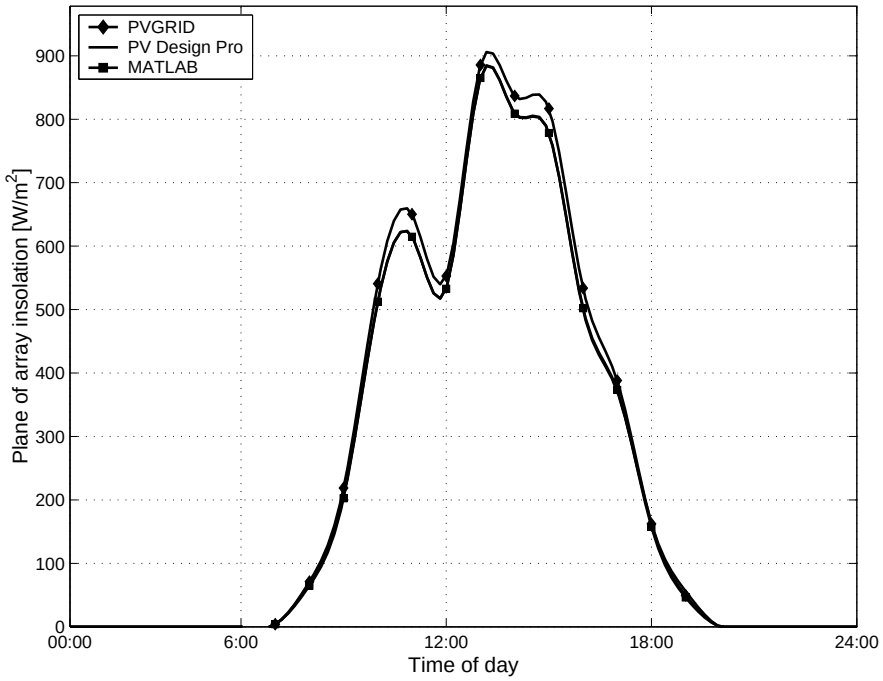

Figure 14: The plane of array insolation calculated with PVGRID, PV Design Pro and the GT simulator.

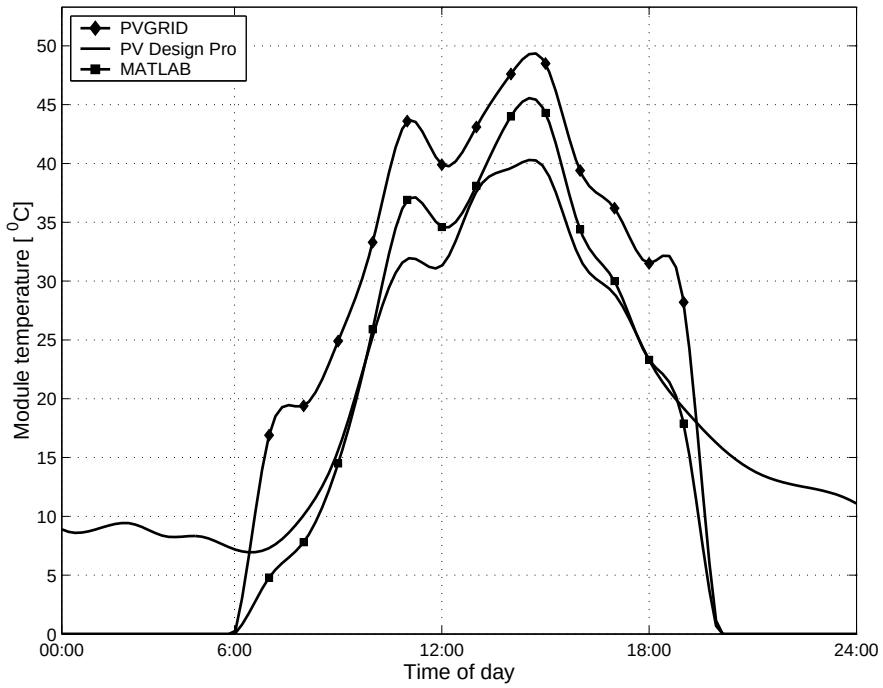

Figure 15: The module temperature calculated with PVGRID, PV Design Pro and the GT simulator.

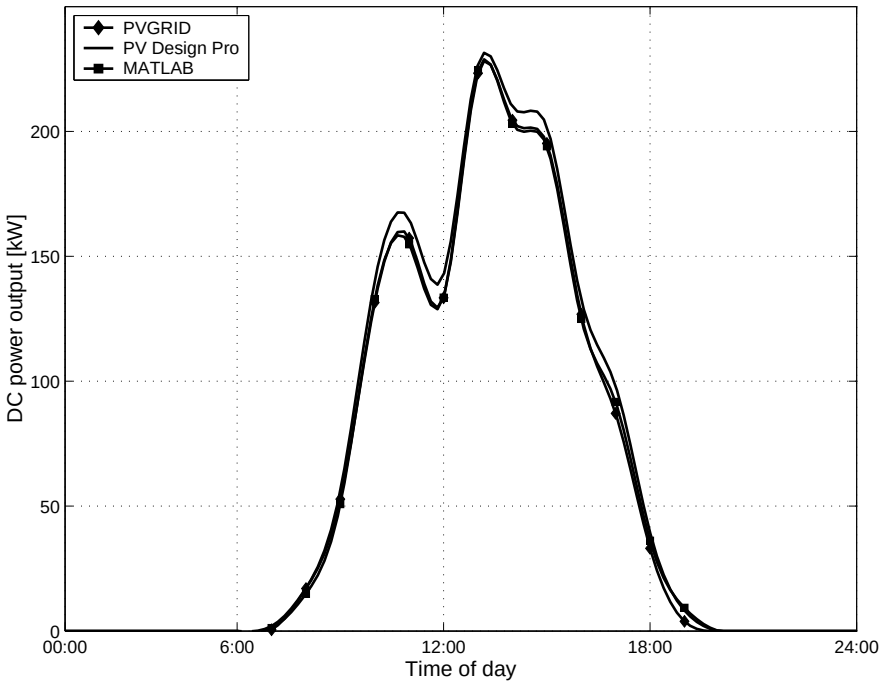

Figure 16: The DC power output calculated with PVGRID, PV Design Pro and the GT simulator.

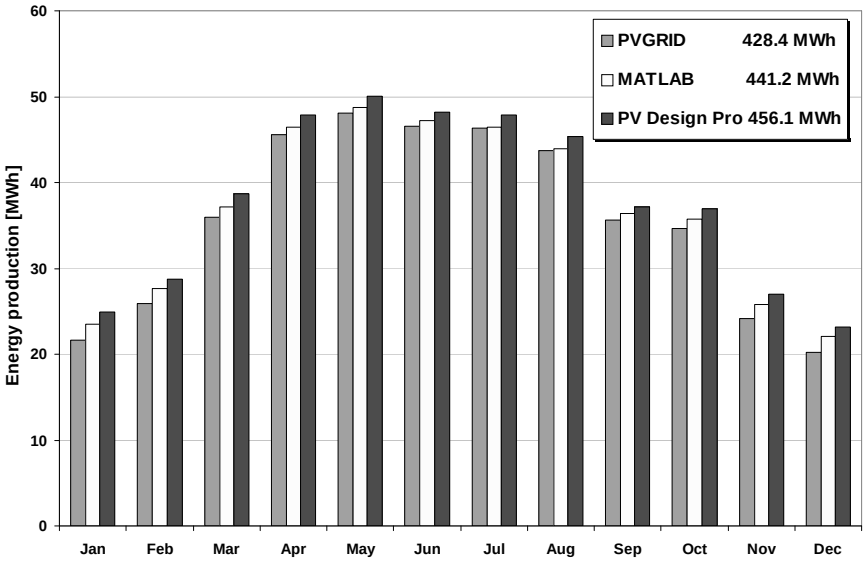

Figure 17: The total annual estimated DC energy output of the system, calculated with PVGRID, PV Design Pro and the GT simulator. All loss mechanisms are neglected.

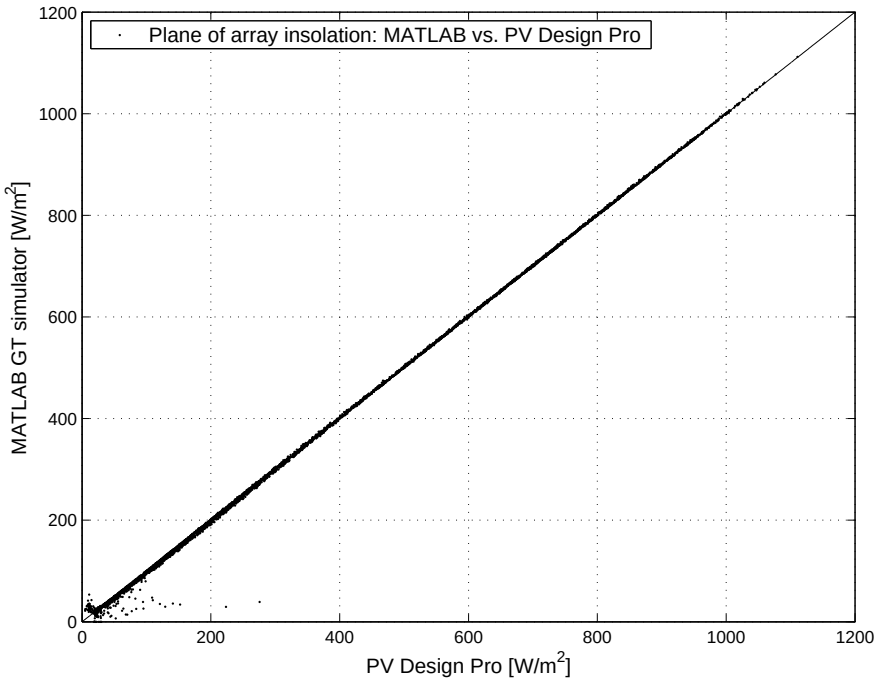

Figure 18: Plane of array insolation throughout one year, calculated using the GT simulator and PV Design Pro.

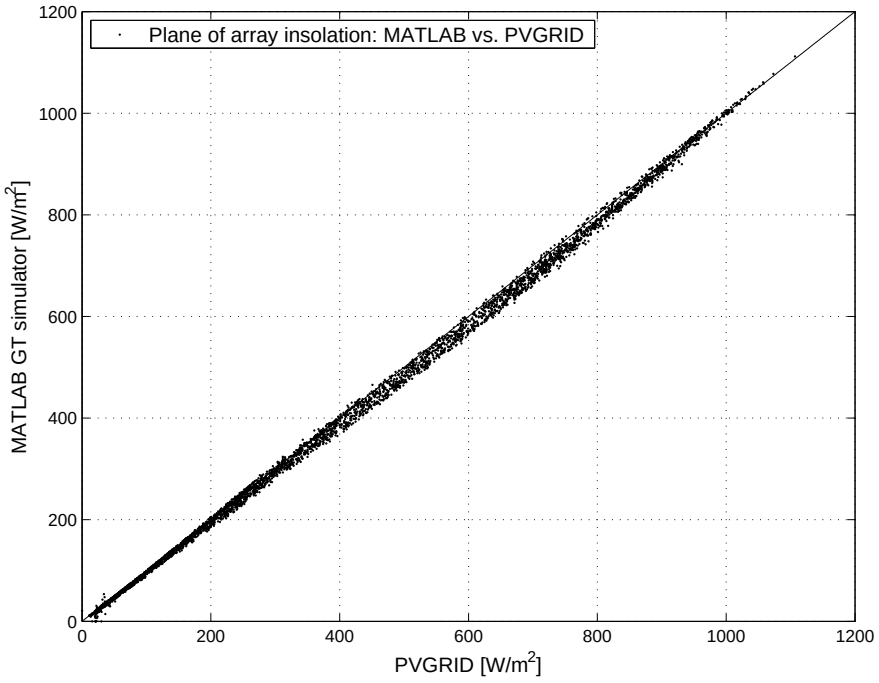

Figure 19: Plane of array insolation throughout one year, calculated using the GT simulator and PVGRID.

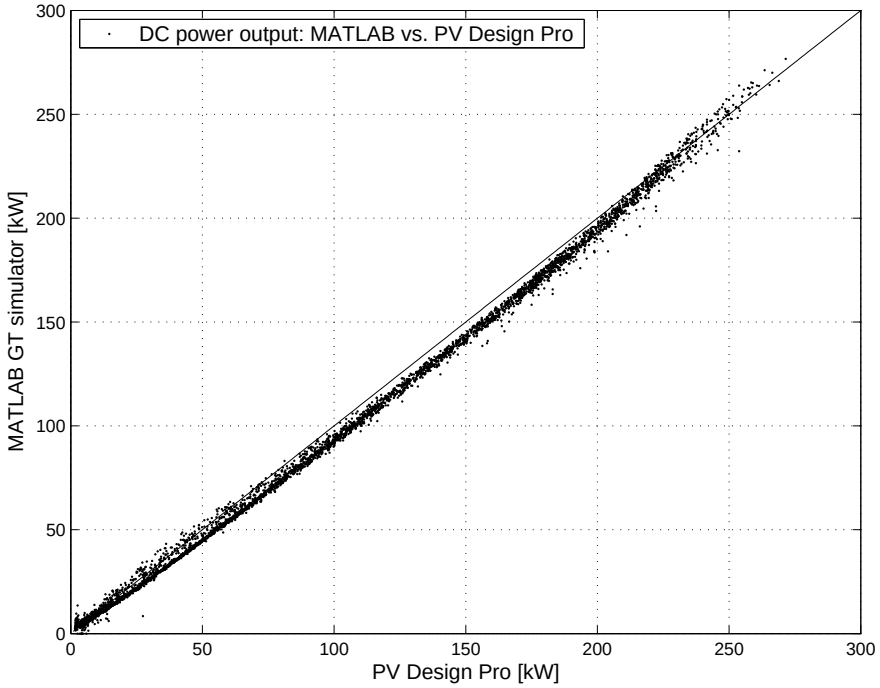

Figure 20: DC power output throughout one year, calculated using the GT simulator and PV Design Pro.

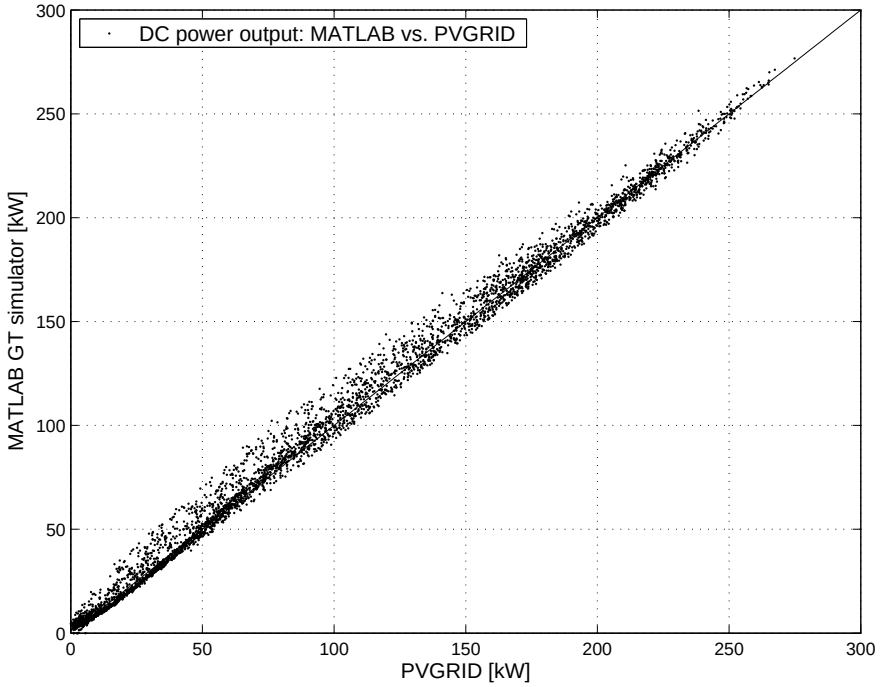

Figure 21: DC power output throughout one year, calculated using the GT simulator and PVGRID.

2.4.2 Modeling GTAC PV system as a multi-planar array

Having validated the GT simulator on a single-planar system, in this section, the detailed modeling of the complete GTAC PV system is presented. To determine the effect of the roof curvature, the following cases are considered:

Case 1. The system is first modeled as a single-planar array, with azimuth equal to the azimuth of the south subarray, and tilt equal to the average tilt of the south subarray. This type of analysis is typically performed using commercial simulation programs designed for planar arrays.

Case 2. All south-facing modules (belonging to rows numbered 1S–28S in Table 4) are modeled as a planar system, with tilt equal to their average tilt. north-facing modules (rows numbered 1N–6N) are modeled accordingly, with tilt equal to the average tilt of all north-facing modules. This approach better approximates the incident insolation and therefore better estimates the system's power output (obtained by summing the power outputs of both equivalent planar arrays). However, this approach cannot model the electrical coupling between the subarrays as it inherently assumes that both arrays operate at their respective maximum power point.

Case 3. Finally, each of the 34 rows are modeled as a separate subarray, as all modules in one row have equal tilt and azimuth. Thus, 28 rows are oriented due south and 6 are oriented due north, with tilts obtained from Table 4. All 34 rows are connected in parallel, and simulated using the GT simulator, obtaining the correct maximum power point of the entire system.

Note that the modeling of Case 2 in PV Design Pro or PVGRID requires repetitive use of the program for each subarray and further postprocessing of output data in order to obtain the total power output of the entire array. In addition, Case 3 cannot be modeled using neither PV Design Pro nor PVGRID, as they have no provisions for modeling multi-planar arrays.

The differences between results obtained in Case 1 and Case 2, and the accurate result obtained in Case 3 are shown in Figures 22-23. As expected, modeling the GTAC PV system as a planar array introduces significant error. On the annual basis, the error in total energy production is 1.59%, while it may be higher than 4% for some months. On the other hand, the effect of electrical coupling is almost nonexistent, as the modeling error introduced by modeling the system as a sum of two independent subarrays is 0.18% on annual basis, and is less than 0.2% for each month. This result is expected because the tilts of individual subarrays are relatively small, and thus variations in insolation (and temperature) are not very pronounced. However, this might not be the case for all systems, as shown in the next example.

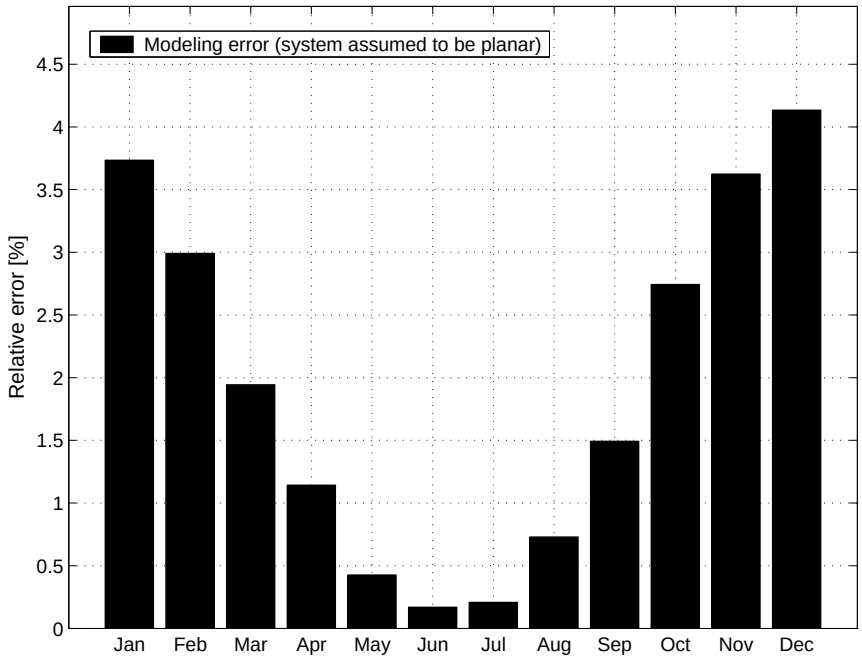

Figure 22: The relative error (per month) introduced by modeling GTAC PV system as a planar array, with tilt and azimuth equal to tilt and azimuth of a south-facing subarray.

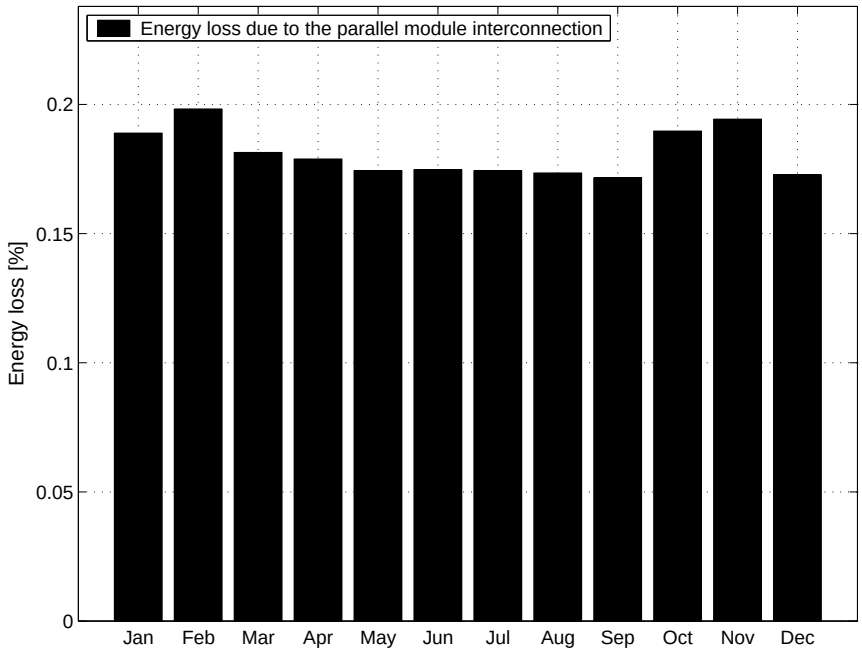

Figure 23: Modeling error (per month) introduced by neglecting the electrical interaction between the individual system subarrays.

2.5 Case study: Photovoltaic Power Tower

As mentioned earlier, a very promising idea for PV is to integrate it into the initial design of the building, which can be done in several ways. For example, the system may be integrated into the walls or roof of a building, becoming a part of the building's structure as well as generating electricity. PV cells can also be laminated into the window glass used in the building. The price of embedding solar photovoltaic modules into buildings is roughly equivalent to that of expensive facade materials. As a proportion of the total building costs, installing solar photovoltaics adds only 2-5%. This cost is partly offset by savings in the purchase of electricity.

However, these kinds of mounting configurations may introduce some additional problems. Consider the case of a highrise building with PV modules mounted on all four sides of the building. Clearly, modules on each side receive different amounts of insolation. Furthermore, as the tilt angle of all modules is 90 degrees, the reflected insolation component may become important, if the albedo (reflectance) of the surroundings is high enough. PV modules installed on different sides of the building may not be of the same type. A model of such a structure is shown in Figure 24. Currently, this kind of a configuration cannot be accurately modeled using existing commercial programs, that are essentially designed for planar arrays. However, it may be successfully modeled using the GT simulator.

As an example, assume that twelve 100 W modules are mounted on each side of the building similar to the one shown in Figure 24. ASE-100-MTF modules are mounted on the south and north sides, while the Astropower AP-100 modules are mounted on the east and west sides of the building. The characteristics of these modules are given in Table 5, while the other configuration details are given in Table 6. Different reflection coefficients are assumed for all four sides of the system. Although both ASE and Astropower modules are rated at 100 W, different insolation and temperature characteristics, coupled with different amounts of insolation received by modules installed at all four sides of the building, lead to differences in DC outputs of all four subarrays.

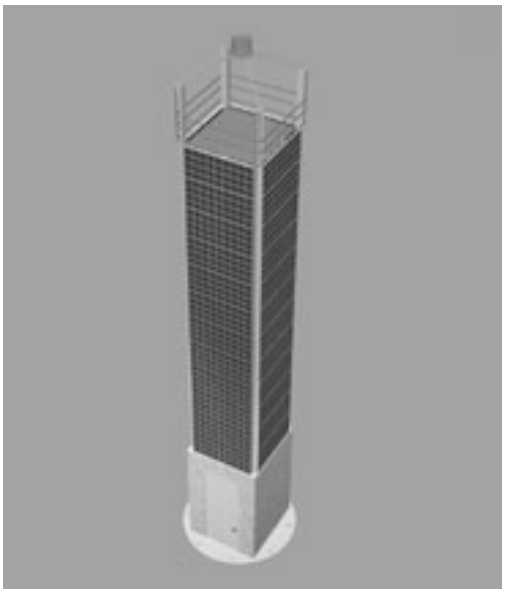

Figure 24: A rectangular PV tower, with photovoltaic modules mounted on all four sides [24].

Table 5: Electrical properties of modules used for the power tower PV system.

Model	ASE-100-ATF/17	AstroPower AP-100
Isc	6.4	7.2
Voc	21.1	20.1
Imp	5.8	6.2
Vmp	17.2	16.1
μIsc	0.00078	0.00033
μVoc	-0.076	-0.084

Table 6: Orientation of four subarrays used in the Power Tower PV system and the associated module temperature coefficients.

	South	East	North	West
Albedo	0.1	0.2	0.4	0.3
INOCT	55	50	55	50

The total energy output of the system is calculated using the GT simulator, assuming that all four subarrays are connected in parallel and connected to the utility through a single power conditioning unit. The maximum power point tracking algorithm in the inverter will

then operate all four subarrays at the voltage that yields the maximal total power of all four subarrays, which is typically away from the optimal point for each individual subarray. As a result, the total system's power output will be lower than it would be if each subarray operated independently.

To quantify that loss, the same PV system is modeled assuming that each individual subarray is connected through a dedicated inverter to make four total inverters in the system. In this configuration, each of the subarrays operates at its optimal point, and the total output of the system can be obtained by adding the outputs of each individual inverter.

The total energy loss due to electrical interaction between subarrays in a single-inverter system has been determined as 2.74% over a period of one year. Energy loss on a monthly basis is shown in Figure 25.

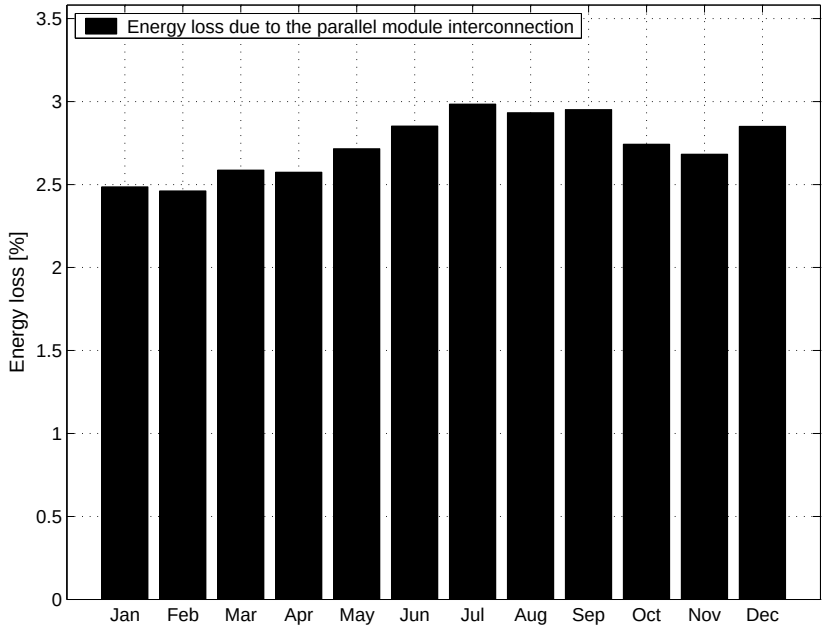

Figure 25: Energy loss (per month) due to the parallel connection of four subarrays.

Note that the relative energy loss is even higher at some time points. Figure 26 shows the P-V curves of all four individual subarrays for a particular time of day. Note how the

maximum power points differ for each of the subarrays. The equivalent P-V curve for the entire array is also shown, as well as the corresponding array operating point. The loss at this time instant was 3.16%; the corresponding operating voltages, maximum power outputs and the actual power outputs of each subarray (and the entire array) are shown in Table 7. The energy loss variations, both daily and seasonal, may need to be taken into account in the data monitoring systems, where the system's output is constantly compared to the calculated output obtained from temperature and insolation measurements.

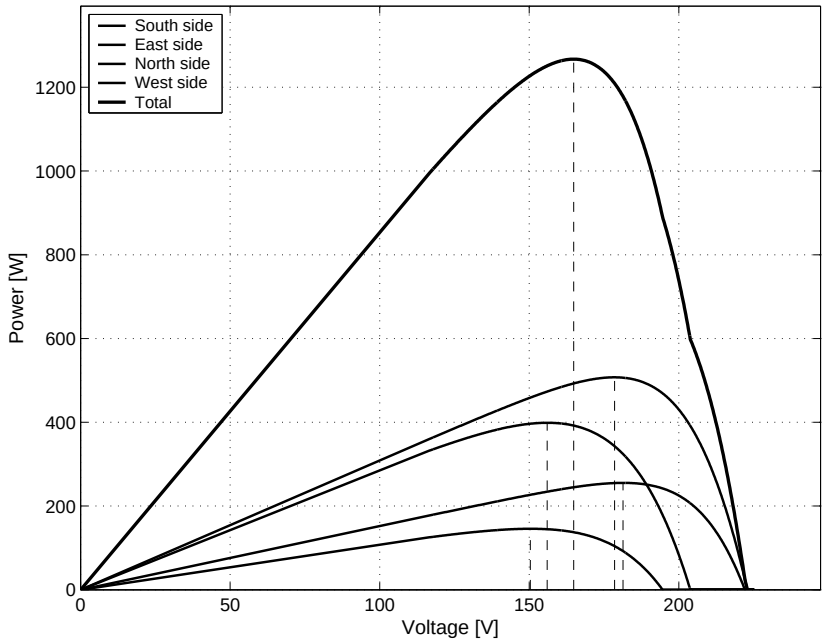

Figure 26: P-V curves of all four subarrays and the equivalent P-V curve for the entire array in a single-inverter configuration.

If the entire structure housing the four subarrays was oriented differently, power output of each subarray would be different as well as the amount of electrical interconnection between subarrays. To demonstrate this effect, the simulations are repeated with the whole power tower structure rotated by 45 degrees due east. This way, the four sides of the building will face southeast, northeast, northwest and southwest, respectively. The total energy loss in this configuration (as a function of month), is shown in Figure 27. The loss

Table 7: The operating voltages and power outputs of four subarrays making the Power Tower PV system. The maximum power outputs of each subarray hadn't they been interconnected (multiple inverter configuration) are also shown.

	U_{max}	P_{max}	P_{actual}
South side	178.499	507.460	492.775
East side	150.330	145.683	137.432
North side	181.316	255.309	244.860
West side	155.964	398.862	392.137
Total	164.848	1307.314	1267.205

is, as expected, higher than when the modules were oriented due south, east, north and west, respectively.

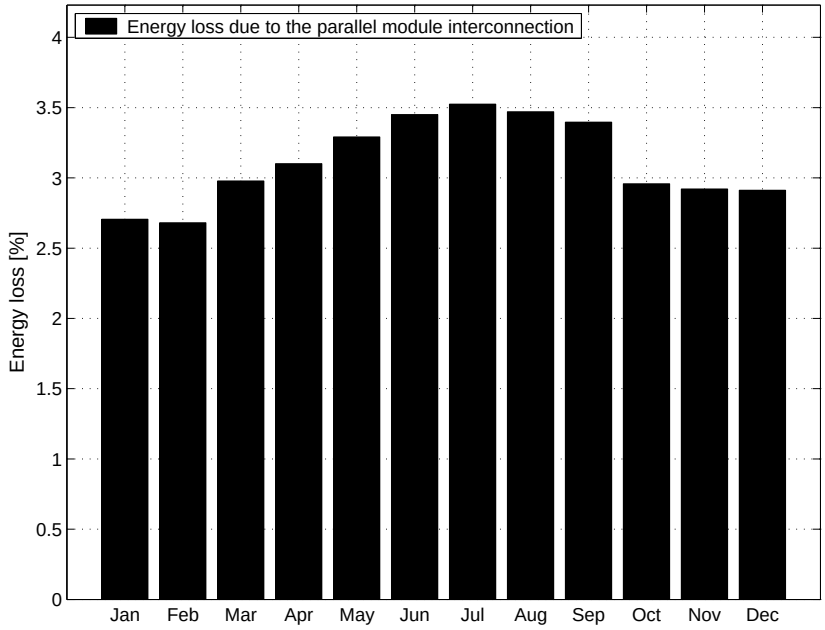

Figure 27: Energy loss (per month) due to the parallel interconnection of four subarrays. Individual subarrays oriented due southeast, northeast, northwest and southwest, respectively.

Over the entire year, the total energy loss due to electrical interaction between subarrays in this configuration is 3.14%. At the same time point that was shown in Figure 26, the P-V curves of the individual subarrays (and the resulting curve of the entire array) are shown

in Figure 28. The actual loss at this time instant is 3.44%, while the operating voltages and power outputs are shown in Table 8.

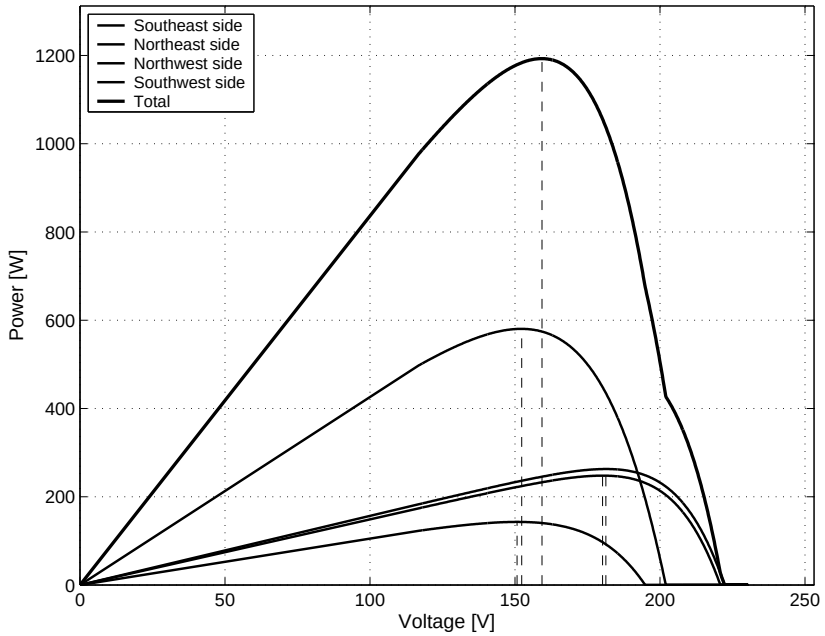

Figure 28: P-V curves of all four subarrays and the equivalent P-V curve for the entire array. Individual subarrays are oriented due southeast, northeast, northwest and southwest, respectively.

Table 8: The maximum and actual operating points of four subarrays. Individual subarrays oriented due southeast, northeast, northwest and southwest, respectively.

	U_{max}	P_{max}	P_{actual}
Southeast side	180.200	247.815	232.823
Northeast side	150.719	142.878	140.333
Northwest side	181.334	262.812	245.492
Southwest side	152.306	580.373	574.221
Total	159.336	1233.877	1192.868

The analysis presented in this section may be used to quantify the energy loss incurred in the single inverter system, and to determine if the loss is significant enough to warrant the use of multiple inverters. The multiple inverter system may also have additional reliability benefits, as addressed later in Chapter 3.

2.6 Conclusions

The emphasis of the work presented in this chapter is on modeling and performance forecasting of photovoltaic systems. The main building blocks of a typical PV system simulation program are presented as a foundation for developing analysis tools. The existing commercial programs (PVFORM, PVGRID and PV Design-Pro) are analyzed and the advantages and disadvantages of each program are discussed. Based on these findings, a PV system simulation program is developed that incorporates the most rigorous models available today. Development of such a flexible model with open source code (MATLAB^{TM}) represents one of the contributions of this thesis. The program is validated by calculating the DC energy production of the south–facing subarray of the 342 kW PV system on top of the Georgia Tech Aquatic Center (GTAC). The total calculated energy output is within 3% of the values calculated with the best commercially available simulation programs.

In the software, the existing state of the art is improved by incorporating the ability to accurately model PV systems with multiple subarrays, oriented and/or tilted differently, but still connected to the shared DC bus, and connected to the utility and/or local load through a single inverter. The DC power output of such a system is typically lower than that of the identical system with individual subarrays equipped with dedicated inverters. As an illustration of the capabilities of the developed program, two case studies are presented.

In the first case study, the complete GTAC PV system consisting of 34 subarrays (each with a different tilt angle) is simulated. As the differences in tilt angles between individual subarrays are relatively small, the modeling loss due to electrical coupling between subarrays is very small – less than 0.2% on an annual basis.

A second case study presents a model of a multistoried rectangular building with PV modules mounted on all four sides. In this example, the energy loss due to the operation at the suboptimal power point is more than 3% on an annual basis. This additional energy may be harvested if the PV system is equipped with four inverters, one per each side of the building.

The presented analysis may be used to determine the most cost-effective interconnection configuration for a PV system with multiple array exposures and capacities. Such analyses will become increasingly more important as building–integrated PV (BIPV) strategies are co–developed with architects and other interested parties, under the circumstances when electrical design is constrained by other considerations.

CHAPTER 3

AVAILABILITY ANALYSIS AND DESIGN OPTIMIZATION OF PV SYSTEMS

3.1 Introduction

In conventional energy sources, failure-related damages are limited to the costs of repair and energy not served. When the generating unit is idle, no fuel is consumed, and production resumes when the failure is cleared. In PV systems, the fuel is free and every time the system is non-operational, the possibility for energy production and revenues are lost. The loss of potential revenues is important, since the large initial investment for a PV system is usually compensated by the price paid (or avoided to be paid) for commercially available electricity. In evaluating the payback time and energy price per kWh generated, the PV system is usually assumed to work without interruptions. Neglecting the effects of those failures can lead to unreasonably optimistic performance and life cycle cost predictions. Several studies [25, 26] have shown that the majority of PV system failures may be attributed to inverter failures. In this section, a procedure for quantifying the effects of inverter failures on total lifetime PV system energy production is presented, and the suitability of several inverter configurations is investigated, based on their total lifetime energy output and life cycle costs. A configuration with multiple inverters connected in parallel is found to be most reliable. Its total energy output can be further increased by using a novel parallel inverter control strategy, introduced in Section 3.3.

3.2 System Configurations

The following inverter configurations are considered and illustrated in Figure 29:

1. A single inverter system
2. A system with N identical smaller inverters (N times smaller rated power), each connected to a portion of the system (string) corresponding to its capacity.
3. A system with N identical smaller inverters (N times smaller rated power), connected to the entire system and working in parallel.

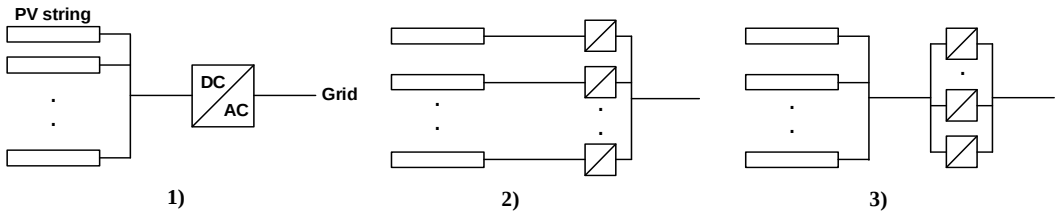

Figure 29: Inverter configurations: (1) single inverter system, (2) system with multiple string inverters, and (3) system with multiple parallel inverters

In the case of a single inverter system (Case 1), a certain number of failures, F, are expected during the lifetime of the system. When the inverter is operational, its output is equal to its input reduced by conversion losses, and when it is non-functional, the total system output is zero. In the case of a multiple string inverter system (Case 2), N times more failures are expected, but each particular failure just reduces the overall conversion ability of the system and does not shut down the entire system. The total expected lifetime energy production is the same as in the single inverter case, since the expected number of failures is $N \cdot F$, but each failure reduces the system's conversion ability by N times smaller amount. However, the multiple-inverter configuration improves the reliability of the system, since each particular failure does not lead to the total system failure. Note that in this analysis, it was assumed that all inverters, regardless of their size, have the same

conversion efficiency, failure characteristics and that the repair time is distributed in the same way. The larger the discrepancies in inverter capacities, the larger is the potential for discrepancies in these characteristics. However, the inclusion of these discrepancies may not present difficulties in the numerical approach presented further in the text.

In a parallel configuration, (Case 3), inverters effectively share the total conversion load. When one inverter fails, remaining inverters may process part or even all of the power that was being converted through the failed inverter, depending on the output of the PV system during the failure of the inverter. Because the output of a PV system (and therefore loading level of the inverter) is a probabilistic quantity, a statistical analysis needs to be performed to determine any potential gains by using this configuration. The PV inverter has to be able to handle maximum (or close to maximum) expected DC power at its input terminals. Due to the nature of the solar energy conversion process for silicon-based solar cells, the maximum solar cell DC power output (and inverter input) is expected under a combination of high insolation and relatively low temperature, which is not likely to occur often. Therefore, a PV inverter operates most of the time at power levels significantly lower than its rated power. Moreover, the inverter's conversion efficiency depends on its fractional loading, defined as a ratio of the input power to its nominal DC rating, as shown in Figure 30. The inverter size is chosen so that its cost and inverter-related losses are minimized, i.e. its nominal power should be as small as possible, to provide high conversion efficiency during normal operation, while not too small in order to minimize revenue losses when its input power has to be limited. There is no need for additional circuitry that will protect the inverter when its input power is higher than its rated power. At those times, the maximum power point tracking algorithm simply moves the inverter away from the maximum power point, maintaining the input power at the rated power. Figure 30 shows a typical histogram of the DC power expected at the inverter input terminals over a period of one year. An inverter efficiency curve is superimposed, showing the misalignment between the actual power being processed and inverter efficiency. Using this data, the expected

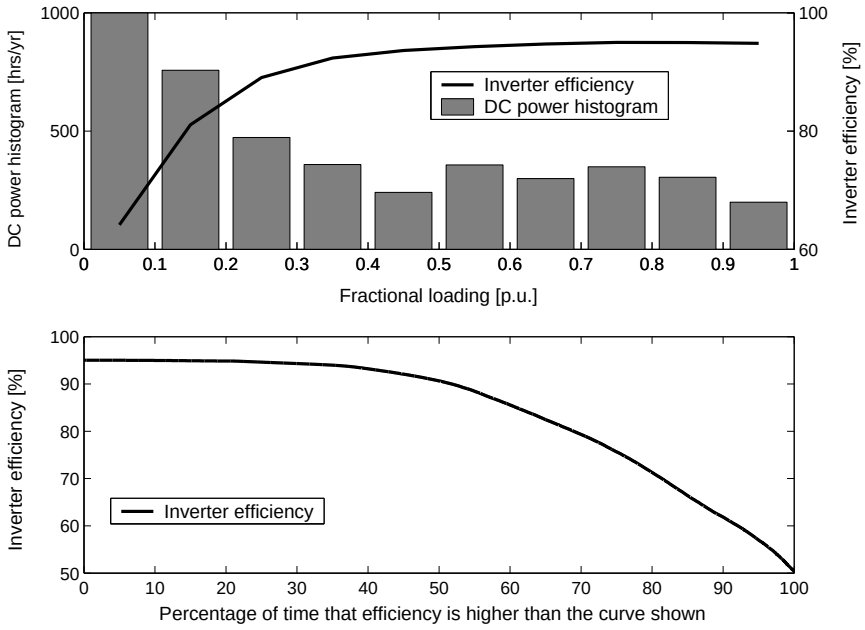

Figure 30: Histogram of the typical PV inverter DC output and its corresponding efficiency (Top), and the efficiency curve (bottom).

inverter efficiency over a period of one year is calculated and shown in the bottom half of Figure 30. Note that, although inverter rated efficiency at full load is 95%, it may drop well below 90% for fractional loading levels lower than 0.5. Figure 30 also reveals that, in this example, inverter efficiency is lower than 80% for more than 25% of the time.

Therefore, the multiple-inverter configuration may be beneficial. In the case of a failure of one inverter, the remaining inverters will continue working and will share the additional load imposed on them. If the input power is higher than the total rated power of remaining $(N-1)$ inverters, they will all operate at their rated power. The expected energy loss due to inverter malfunctions over the lifetime of the system depends on the number of inverters connected in parallel, N, and will be a non-increasing function of N.

3.3 Novel inverter control strategy for multi-inverter systems

Based on these findings, a new control strategy, designed to keep the inverters operating at the optimum efficiency, is proposed. In a multiple-inverter configuration with N inverters connected in parallel, when the total input DC power is lower than the total rated power of $(N - k)$ inverters, k inverters may be purposely turned off, which will force the remaining inverters to operate at higher fractional loadings and therefore improve their conversion efficiency, i.e.:

$$N_{on} = \min(N, ceil(\frac{P_{DC}}{P})) \tag{23}$$

where N_{on} is the number of inverters that should be online, N is the total number of inverters, P_{DC} is the total instantaneous DC input power, P is the nominal power of each inverter, and the function *ceil* rounds to the nearest integer toward infinity. Note that this control strategy may need to be adjusted when the peak conversion efficiency occurs at a power level below the rated power.

3.4 Statistical performance analysis

To quantify the aforementioned effects, a coefficient that adjusts the total lifetime PV system energy output taking into account the inverter-related failures is introduced. The reliability coefficient K_n is defined as the ratio of the expected lifetime AC energy production of the PV system with n inverters ($E(W_n)$) and the lifetime DC energy production of the PV system (W_{DC}). Note that the expected lifetime AC energy production includes the performance loss due to inverter failures.

$$K_n = \frac{E(W_n)}{W_{DC}} \tag{24}$$

The coefficient K_n depends on the geographical location of the system, number of inverters n, their configuration, and the underlying random distribution of both inverter failure and repair processes.

To be able to determine the coefficient K_n, both the time between failures (TBF) and repair time are treated as random variables. Inverter manufacturers typically do not provide failure data, but mean times between failures (MTBF) between 1 and 16 years have been reported based on field data [26]. These data can be used to model the TBF as an exponentially distributed random variable, with parameter $\lambda = 1/MTBF$ [27]. Several initiatives aimed at collecting the performance data for a large number of various PV systems are currently taking place, which would likely provide better insight into the appropriate distributions and distribution parameters to be used for modeling the time between failures.

The repair time varies greatly, between several hours for large continuously monitored systems, to several months for remote installations and large installations that depend on manufacturer's service. Typically, for residential non-monitored systems, it includes a failure identification period of up to one month (using meter data from the utility bill), followed by several weeks for system repair. For large installations (either in size or volume) several monitoring strategies can be utilized, ranging from continuous monitoring of system performance and comparison with predicted output obtained using meteorological data, to a less frequent (weekly, bi-weekly) phone-in of inverter diagnostic data to a central computer. The availability of spare parts or a spare unit—a situation more probable in the case of a system with multiple, standardized inverters may significantly decrease the repair time.

To obtain the statistically valid estimate of the reliability coefficient K_n, in this section, a 20-year lifetime of PV system operation (including failures) is simulated for a given inverter configuration. The system availability data is generated randomly, using the appropriate random distributions for time between failures and repair time, as shown in Figure 31. The total produced energy is calculated, and the procedure is then repeated M times, with a new random set of failure/repair data. The result of such Monte Carlo analysis is the expected AC energy production of the system, including the performance loss resulting from inverter-related downtimes. The value of the reliability coefficient is then obtained by dividing the expected AC energy production by the DC energy produced by the PV array.

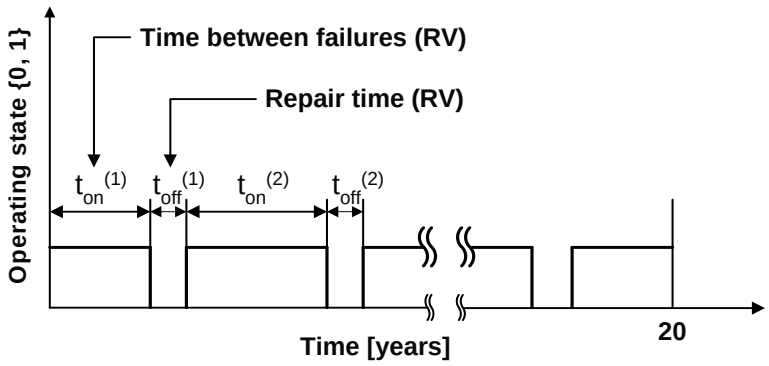

Figure 31: The 20-year data set of PV system operation, including random inverter failures. The times between failures and repair times are obtained by generating random numbers with the appropriate random distribution.

The flowchart of the procedure is presented in Figure 32.

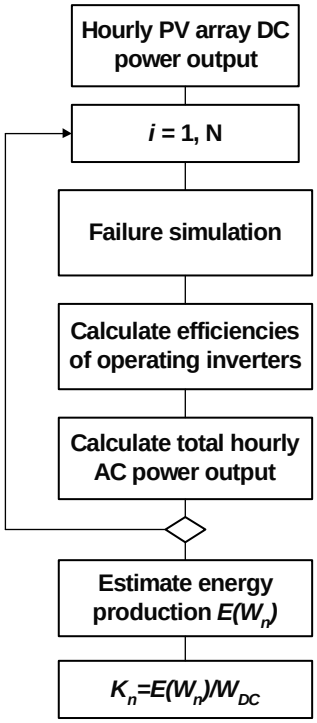

Figure 32: Flowchart of the Monte Carlo procedure for determining the reliability coefficient *K*.

3.5 Optimal Number of Inverters: Cost Vs. Reliability

The presented analysis provides a quantitative demonstration that multiple-inverter configuration improves PV system reliability, and reduces production losses due to inverter failures. However, multiple inverter configurations may have substantially higher up-front and maintenance costs that may offset any possible energy gains. Thus, a relatively straightforward procedure to determine the optimal number of inverters that minimizes the life-cycle costs of such a system is developed.

Lifetime revenues from energy production of the PV system can be estimated using the following formula

$$E(x) = K(x) \cdot E_{DC} \cdot c \cdot r \cdot \frac{1 - r^T}{1 - r} \tag{25}$$

where x is the number of inverters in the system, $K(x)$ is the reliability coefficient that accounts for inverter failure related downtimes, E_{DC} is the total annual DC energy production of the PV array at a given location in kWh, c is the energy cost in \$/kWh, r is the coefficient that accounts for annual variations in energy price and inflation, and T is the expected lifetime of the system (in years).

Multi-inverter systems usually have higher up-front and maintenance costs. The inverter price P is usually quoted in \$/VA, thus the installation and maintenance costs of the multi inverter system can be determined using

$$C(x) = S \cdot P(\frac{S}{x}) \cdot (1 + m) \tag{26}$$

where S is the total installed inverter power, in VA, $P(y)$ is the inverter price as a function of its size, expressed in \$/VA, and m is the coefficient that accounts for the maintenance costs. Based on the data from [25], the following formula for the inverter price (per VA) was used in the numerical example presented in the next section.

$$P(y) = -0.1569 \cdot log(y) + 1.2675 \tag{27}$$

The minimum and maximum prices from [25] and the fitted equation (27) are shown in Figure 33.

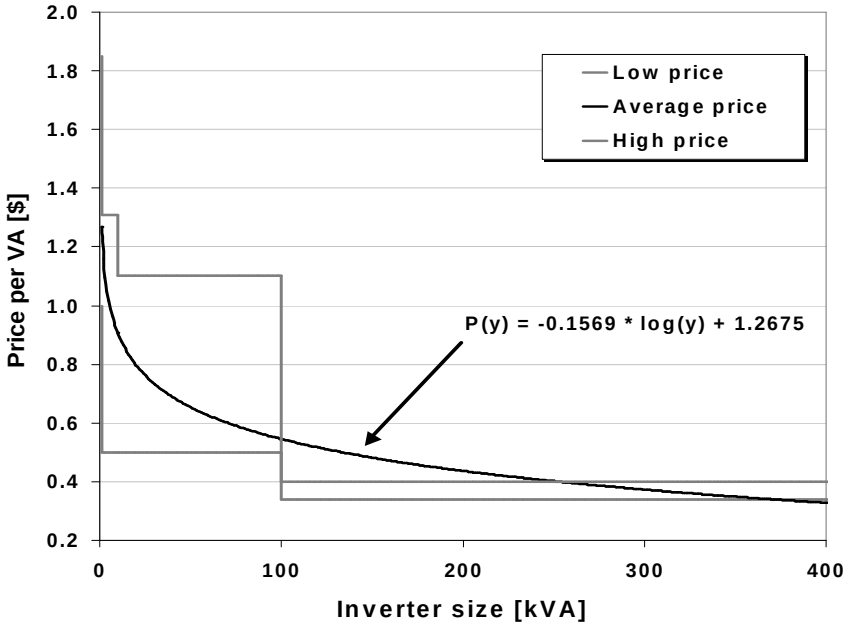

Figure 33: Inverter price (per VA) as a function of its size (data from [25]).

The total lifetime gain from the system, $T(x)$, expressed in dollars, is simply obtained as a difference between revenues $E(x)$ and costs $C(x)$. It is a function of only the number of inverters x, which can be used to obtain the optimal number of inverters that maximizes the benefits over the lifetime of the system. Note that $T(x)$ does not include the costs associated with PV array, which are assumed to be the same in all configurations.

3.6 Case Study: Georgia Tech Aquatic Center PV system

As a numerical example, the inverter failure characteristics determined from five years of field data for the 315 kW single-inverter PV system installed at the Georgia Tech Aquatic Center in Atlanta, Georgia are used [23]. It is assumed that both the time to failure and

repair time are Weibull distributed, with scale (η) and shape (β) parameters estimated from the field data [27]. The corresponding MTBF and mean time to repair (MTTR) are 540 days and 26 days, respectively. The Monte Carlo analysis is performed for the following inverter configurations: string inverters, parallel inverters and parallel inverters with selective inverter shutdown in order to maintain the highest conversion efficiency possible.

The inverter size for the single-inverter case is determined using the condition that the single-inverter system has to be able to process all available DC power for 99.5% of the time, i.e. the inverter power would be limited to its nominal value for only 0.5% of the time. The size of each inverter in the N-inverter system is appropriately N times lower. This approach allows the comparison of results for different geographical locations, as the energy output of the PV array of the same size will be different for different locations, and an inverter of different size may be needed.

The results of the Monte Carlo analysis described in Section 3.4 are summarized in Figure 34. In the case of string inverters, the expected total energy production does not depend on the number of inverters in the system, as shown in the bottom curve of Figure 34. If more inverters are present in the system, the total number of failures increases, but each failure reduces system conversion ability by a smaller fraction.

If inverters are connected in parallel, thus sharing the total load, the expected energy production increases as the number of inverters in the system increases (middle curve in Figure 34). The sharpest increase of the reliability coefficient is for a two-inverter system, where the total expected energy production increases by more than 2.5% compared to a single-inverter system. As the number of inverters increases (to N=10 in this example), the law of diminishing returns kicks in, and the additional improvements eventually become negligible. The curve for the coefficient K_n asymptotically approaches the value for a single-inverter failure free system, as the number of inverters becomes very large.

The same behavior is experienced when only the minimum number of parallel inverters is operational at any given time to maximize the overall conversion efficiency. This strategy

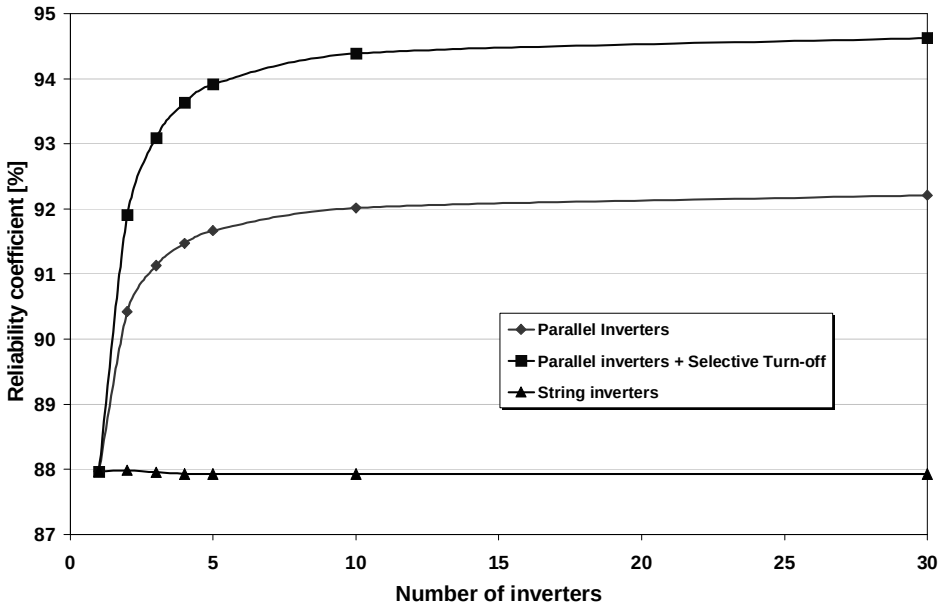

Figure 34: The performance-adjusting reliability coefficient as a function of the number of inverters in the system (using data from the GTAC PV system in Atlanta, GA).

yields a few more percent in energy gain, depending on the number of inverters in the system. It is interesting to note that this strategy may yield more energy over the lifetime of the system than a single-inverter system that has not experienced a single failure throughout its service life. This is evident in Figure 34 – in the case of a selective turn off (top curve), the value of the reliability coefficient for $N > 2$ is higher than the value of the coefficient when $N \rightarrow \infty$ and selective turn off is not employed (middle curve).

The economic analysis, taking into account higher start-up and maintenance costs for multi-inverter systems, shows that, in this example, a three-inverter system with selective inverter shutdown yields the lowest life-cycle costs (Figure 35). Figure 35 shows the values for the total lifetime gain from the system $T(x)$, as a function of the number of inverters in the system, with the highest value of $T(x)$ indicating optimal configuration. The parameters used for this analysis were: MTBF=1 year, MTTR=30 days, $c = 0.12\ \$/kWh$, $r = 1.03$ and $m = 0.15$.

To demonstrate the effect of parameters of the chosen random distribution (Weibull), a

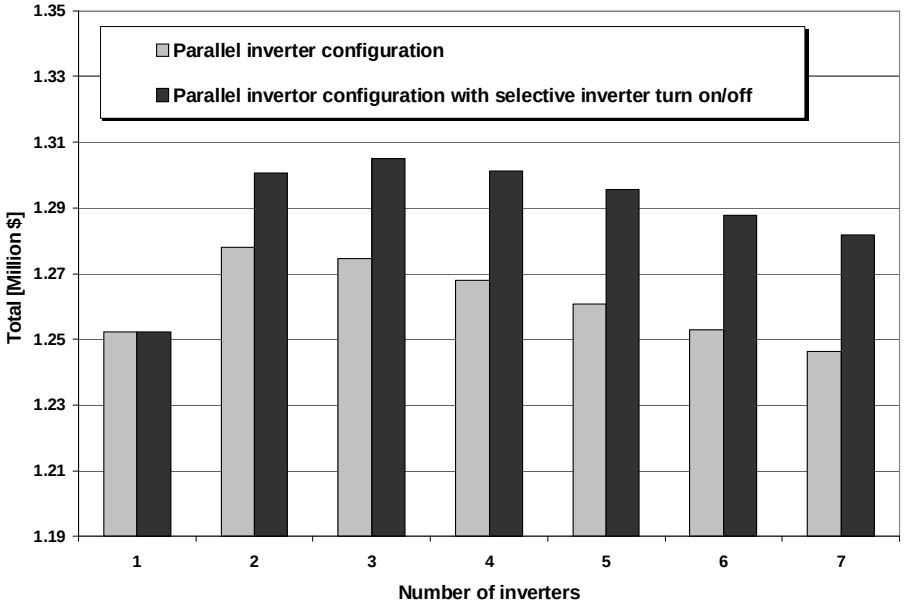

Figure 35: The optimal number of inverters in the system. A two-inverter parallel configuration yields the best overall energy gain. If a selective turn-off inverter strategy is employed, a three-inverter configuration is optimal.

Monte Carlo procedure was repeated for several combinations of distribution parameters for both TBF and repair time, effectively varying MTBF from one to three years and MTTR from 30 to 60 days. In all cases, the changes in MTBF and MTTR are obtained by changing only the appropriate scale (η) parameter, while keeping the shape (β) parameter constant. The results are presented in Figure 36. As expected, increasing MTBF increases reliability coefficient K_n, while increasing MTTR decreases K_n.

It should be noted that all presented results are site specific, as the amount of insolation differs significantly for different geographical locations. However, the general shape of the reliability coefficient curve is similar for all considered locations (Atlanta, GA, Chicago, IL and Scottsbluff, AZ). While the actual coefficient values may differ slightly for different locations, the general trends presented in Figure 34 are observed at all locations. Figure 37 shows the values of the reliability coefficient for three US locations: Atlanta, GA, Chicago, IL and Scottsbluff, NE.

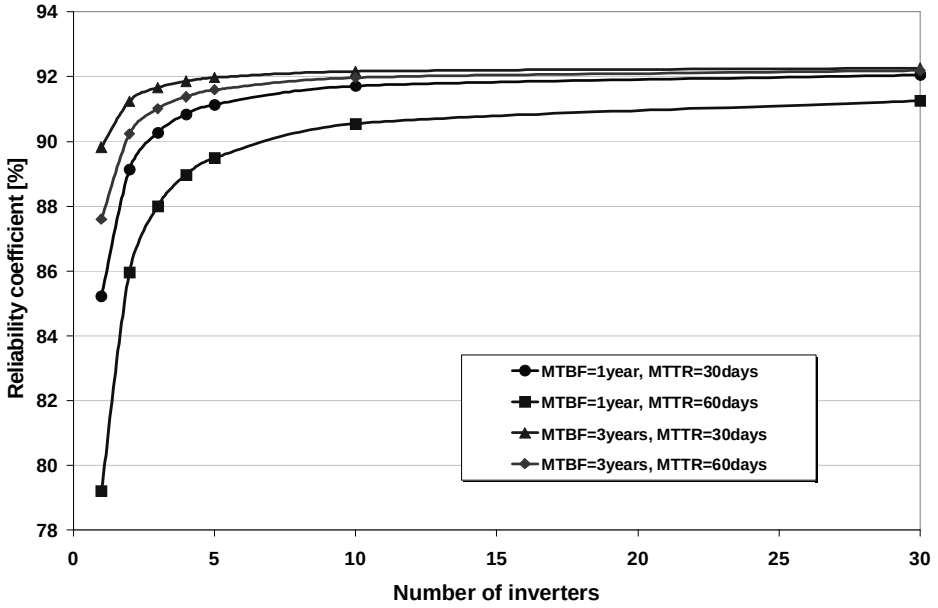

Figure 36: The dependence of the reliability coefficient on the failure characteristics of the inverter and repair time. Results shown are for the parallel inverter configuration without selective turn off, simulated in Atlanta, GA.

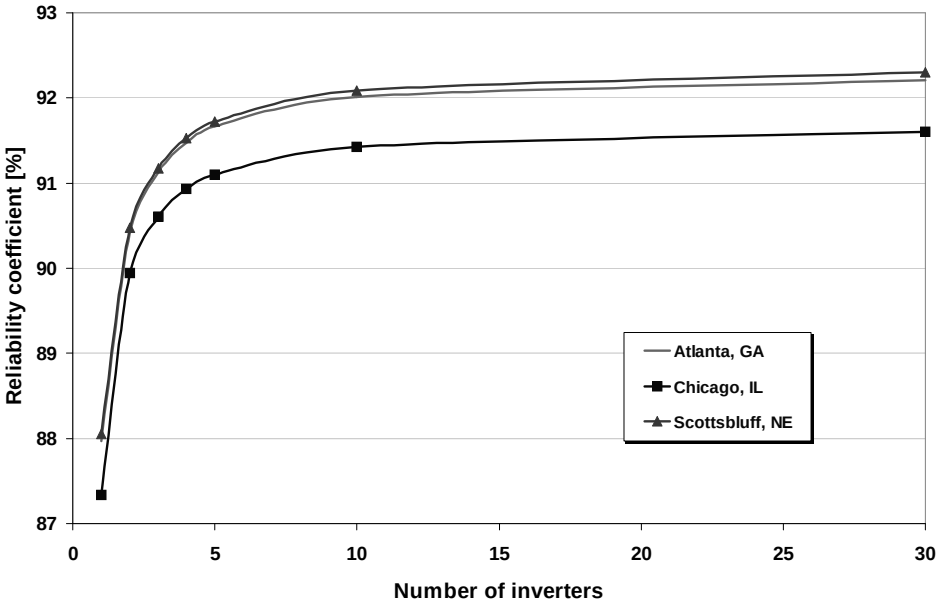

Figure 37: The dependence of the reliability coefficient on the geographical location. Results shown are for the parallel inverter configuration without selective turn off.

3.7 Conclusions

In this chapter, the importance of including random inverter failures in the PV system reliability and life–cycle cost calculations is demonstrated. A new performance-adjusting reliability coefficient, which accounts for system downtime, is proposed, and a Monte Carlo simulation for determining the values of the coefficient for various inverter configurations is presented.

Several commonly used inverter configurations are considered, including a single inverter, string inverters and parallel inverters. The parallel configuration is found to yield maximal energy over the lifetime of the system. In addition, an inverter control strategy in a system with parallel inverters that further improves the total energy yield is proposed. The strategy is designed to selectively shut down one or more inverters during the periods of low insolation, thus enabling the remaining inverters to operate at higher conversion efficiency.

As a multiple inverter configuration may have higher up-front and maintenance costs compared to the single inverter configuration, a procedure for determining the optimal number of inverters (which minimizes the system life-cycle costs) is also developed. The complete procedure is integrated into the previously developed PV simulation program (presented in Chapter 2), and may be used to determine the optimal inverter configuration, based on minimal life–cycle costs.

The developed procedure is demonstrated on the case study of a Georgia Tech Aquatic Center PV system, with inverter failure characteristics obtained from field data. In this example, the parallel inverter configuration yields up to 4% percent more energy over the lifetime of the system, compared to a single–inverter system. The selective inverter shutdown strategy yields additional 2-2.5%, depending on the number of inverters in the system. The energy gain obtained in both parallel configurations depends on the number of inverters in the system, with incremental gains decreasing as the number of inverters increases. The optimal number of inverters in the parallel configuration is two – yielding

$26,000 (approximately 2% of the total system gain) more over the lifetime of the system, compared to a single–inverter system. If the selective shutdown procedure is employed, the optimal configuration is a three-inverter system, with the gain of $53,000, compared to a single–inverter system.

As PV and other renewable energy sources are becoming increasingly interesting as distributed generation resources, modeling and forecasting capabilities that address their performance, as well as treatment of uncertainty of their inputs, are paramount in facilitating their implementation on a larger scale. Some of these issues are investigated in the following chapters.

CHAPTER 4

QUANTITATIVE TECHNIQUES FOR ANALYSIS OF LARGE DATA SETS IN RENEWABLE DISTRIBUTED GENERATION

4.1 Introduction

This chapter investigates the effects of distributed generation (DG) devices on electric power distribution systems. Distributed generators alter the operation of a distribution feeder at which they are installed and may also interfere with its protection and control. The prevailing utility strategy is thus to impose a set of strict rules designed to limit the negative effects that DG systems may have on the distribution feeder. However, DG systems inherently provide some benefits to the utility. They may level the load curve, improve the voltage profile across the feeder, reduce the loading level of branches and substation transformers, and provide environmental benefits by offsetting the emissions of pollutants [28]. Utility economic benefits also include loss reduction, avoided costs of energy production, generation capacity, distribution and transmission capacity investment deferral, reducing risk from uncertain fuel prices, green pricing benefits, etc. The summary of DG benefits is presented below:

- **Energy.** The most obvious benefit of DG installed on a feeder is due to the electrical energy savings. The actual value may differ based on the size and location of DG and based on who owns it. If the DG is owned by the utility and/or it is located in the T&D network, the benefit is based on the avoided cost of energy production.

If DG is placed on the feeder, the actual benefit to the customer is based on a full price of energy. Depending on the agreement between the utility and the customer, it may include premiums based on the time-of-day production of energy. However, net-metering agreements currently in place do not support these premium payments.

- **Electrical loss reduction.** The benefits include electrical loss savings (both active and reactive) on the distribution feeder, in the substation transformer, and in the transmission network. The benefits accrue due to reduced current flows throughout the transmission and distribution network, as a result of generating electricity closer to the consumers.
- **Reactive support.** Typically, DG are connected to the distribution network through an inverter and operate at the unity power factor, supplying only active power. If DG inverters are allowed to operate at power factors other than unity, in addition to the active power (which is determined by meteorological conditions) they may provide additional reactive power, up to the inverter capacity.
- **Voltage support benefits.** DG placement across the feeder also changes local voltage conditions - in general increasing local voltage levels.
- **Reliability.** The overall feeder reliability may increase if islanding is allowed, as DG may continue to serve customers within its island even during outages. If islanding is not allowed, as it is today's practice, DG can still increase the feeder's reliability in some cases. If a connecting branch to the backup feeder with a normally open switch is present, the DG can be allowed to reconnect after the fault is isolated and the switch is closed. Although a backup feeder is used to temporarily restore power, without DG some customers may not receive service due to high impedances at the ends of the backup and primary feeder. DG, if redispatched, may allow more customers to receive service until the main feeder is repaired.

- **Capacity values.** Capacity values include the avoided cost of energy production, which is typically the avoided cost of using a peaking gas turbine.
- **Equipment related.** DG may allow better utilization of existing equipment and prolong its life, allowing substation transformer and line construction deferral. It may also extend maintenance intervals, due to less switching for switched shunts and substation transformer load tap changers.

4.1.1 Renewable distributed generation

In addition to the aforementioned benefits, renewable or green DG may also provide environmental benefits due to the avoided emissions of NO_x, SO_2 and CO_2 that would have been produced by a conventional coal-burning generator. Various state and federal tax credits may be available for renewable DGs, making them even more attractive. But apart from these government-regulated incentives, the driving factor for the additions of renewable DG to the existing electricity networks may be the fact that the general public overwhelmingly supports their continued expansion. For more than 20 years, national polls have shown that the general customer perception of renewable sources is much more favorable than that of the conventional energy sources [29]. Several utility studies in the late 1990s have confirmed these findings [30]. For example, Table 9 shows the response to the question about the favorability toward various energy resources, assuming that the customers had a choice of the source of their electrical energy. Similarly, when asked if they want their utility to use a variety of energy sources, including renewables, the responses were overwhelmingly positive. Of residential customers, 88% were for including renewables into the generation mix, as opposed to 39% for nuclear and 14% for coal.

When asked about the specific renewable energy sources that they would want their utilities to deploy, the majority of respondents again chose wind and PV, as shown in Table 10. In addition to having a favorable opinion on renewable energy sources, a significant percentage of polled customers indicated that they are willing to pay more for electricity

Table 9: Customer preferences among energy resources [30].

Energy resource	Somewhat or strongly favor [%]	Somewhat or strongly oppose [%]	Don't know [%]
Solar	93	5	2
Wind	91	9	0
Natural gas	83	11	6
Geothermal	71	13	16
Landfill gas	64	18	18
Forest waste	59	29	12
Nuclear	31	63	6
Coal	24	69	7

Table 10: Most favorable renewable energy options [30].

Renewable resource	Percent "very favorable"	Percent chosing in top 3 preferred renewable energy sources
PV on public building	69	58
Geothermal	64	63
Wind	61	69
PV on homes	60	64
Biomass	32	26

produced by such sources [31,32]. A 1998 survey in Colorado, for example, found that 76% of homeowners are willing to pay at least $1 more per month for electricity from renewable sources [31]. Figure 38 quantifies some of the extensive results reported in [30]. It indicates that a vast majority of customers (over 90%) are willing to pay a monthly premium price of up to $5 in exchange for receiving a fraction of their electricity from renewable resources.

More and more utilities are beginning to acknowledge the significance of these findings and are starting to change their position on renewables. Instead of treating renewables as a “nuisance”, they are starting to look at them as the opportunity for additional profits, building customer loyalty, enhancing the public perception of the utility and reducing the future possible environmental credits. For example, [33] reports that consumers are more likely to

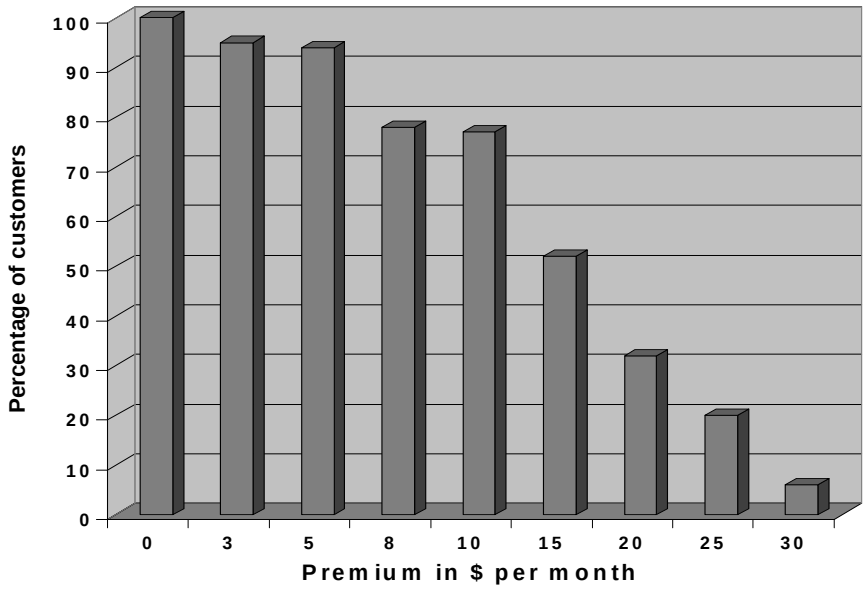

Figure 38: Indications of customers' willingness to pay premium monthly amount for electric power from renewable energy sources obtained from the polls. [30]

identify with utilities that support and promote environmentally sound management practices. Hence, more than 80 utilities have started offering "green" pricing programs. The term "green" energy refers to the energy produced from renewable energy sources. Green pricing programs represent a variety of customer services, usually based on customers' voluntary acceptance of premium rates in order to purchase green power. More than 70 MW of renewable generation has been installed as a result of those programs, and another 120 MW has been planned.

The Sacramento Municipal Utility District (SMUD) is one of a handful of utilities that has, from the very beginning, embraced the renewable technologies. Its PV Pioneers I program started in 1993, offering customers the installation of 2 kW or 4 kW PV systems on their rooftops. The systems are owned by SMUD, and customers pay a flat $4 monthly fee for a period of 10 years, at which point they have an option of purchasing the system or possible rate reduction. More than 450 systems totaling more than 1.5 MW have been installed and the installations continue at a rate of 100 systems per year. As an extension of

this program, in 1998 SMUD introduced a PV PIONER II program, in which customers are offered the opportunity to purchase 2 kW or 4 kW systems, with SMUD contributing more than 50% of the total system's price. The systems are installed at customer's premises, reducing their loads, and the eventual energy surplus is sold back to the utility via a net-metering agreement.

SMUD is also offering a Greenergy program – a green pricing program that offers customers two levels of participation: Greenergy All Renewables and Greenergy Advocate. The Greenergy All Renewables program includes either a $6 flat monthly fee or the additional 1 ¢/kWh charge, while providing 100% of energy from renewable sources. The Greenergy Advocate program includes a 0.5 ¢/kWh surcharge (or a $3 monthly fee), providing 50% of energy from renewables. Forty percent of the premiums go directly toward building new renewable resources. As part of the Greenergy program SMUD is also promoting a Community Solar program that allows customers to fund future solar installations for non-profit organizations in the SMUD's service area by donating 1 ¢/kWh on their monthly bill. More than 600 customers have enrolled in Community Solar program and several installations, such as the 3.7 kW PV system at the Sacramento Zoo have already been completed.

4.2 Problem statement

For reasons described in the previous section, it is reasonable to expect an increased penetration of DG systems into the existing distribution system. Some of those DG systems may be renewable photovoltaic (PV) or wind DG systems. Although the practical capacity of these systems is relatively small, their cumulative effect may significantly alter the behavior of the feeder where they are installed. Accurate modeling of such a DG-enhanced feeder is not trivial for the following reasons:

- The renewable PV and wind DG systems are usually not owned or operated by the utility.

- Their output is a probabilistic quantity, dependent on meteorological conditions.
- The locations of individual systems across the feeder, as well as their sizes and operational status, are not precisely known at the planning stage.

It would be beneficial for utilities to know the effects of a given overall DG feeder penetration (usually expressed as a percentage of the feeder nominal load) on feeder operational characteristics, such as the feeder voltage profile, active and reactive losses, substation power factor, switching times of shunt capacitors, etc. Knowledge of statistically valid estimates of those effects (both the expected and extreme values) is beneficial for feeder planning, and could also be used in designing green power programs.

In this chapter, the operation of a DG-enhanced feeder is described, along with the problems involved with accurately describing such a system. An objective method is developed for reducing the number of computational steps necessary for accurate modeling of the DG-enhanced feeder operation. The method is based on a clustering algorithm that reduces the input set by grouping similar data points into groups or clusters, while still retaining the necessary information contained in the underlying data. Because of the inherent averaging properties of the clustering algorithm, the method is augmented by a companion procedure that uses only those points from the original data set that yield approximate extreme feeder conditions. Both procedures are demonstrated by investigating the effects of random DG placement on a radial distribution feeder.

4.3 Clustering analysis

In radial networks, bus voltages decrease with distance from the distribution transformer. Distributed generators scattered across the feeder effectively decrease the load, change the power flows along the feeder and local voltage conditions. They may also interfere with the operation of switched shunts and protection equipment. The layout of a distribution feeder, based on [34], with one representative allocation of distributed generators, is shown in Figure 39.

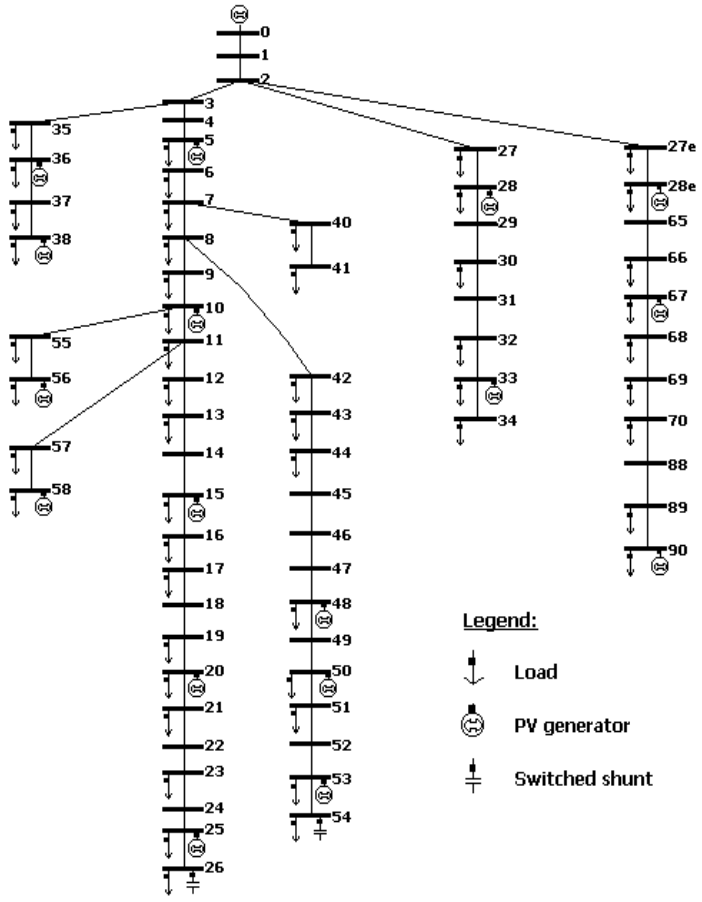

Figure 39: The layout of the distribution feeder (based on [34]) with one possible allocation of renewable distributed generators.

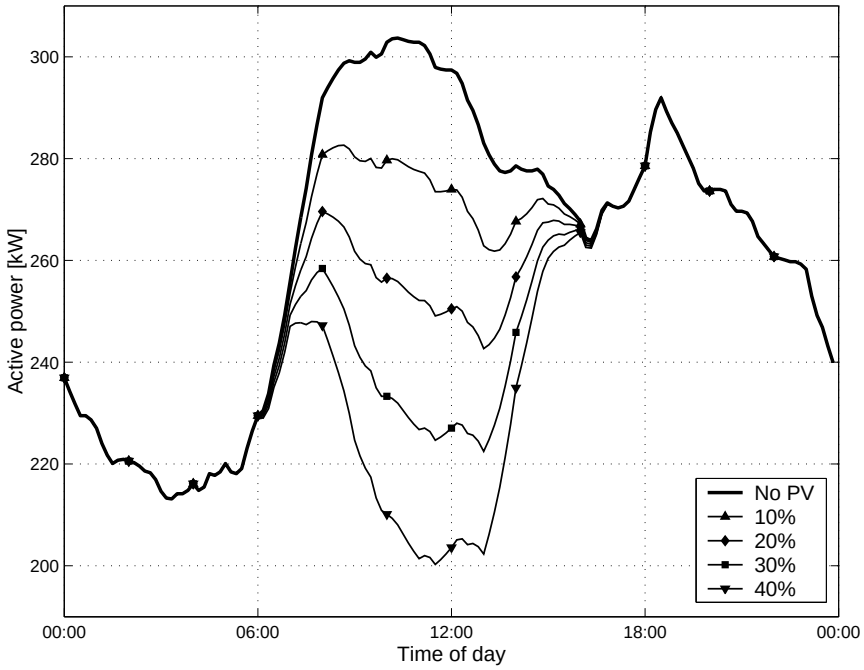

Figure 40: The effect of a PV generator with capacity scaled from 10% to 40% of nominal load on a load profile.

A model of a DG-equipped feeder was developed in MATLAB, based on a MATPOWER simulation package [35]. The package was modified to include the automatic control of shunt capacitors and modeling of renewable distributed generators. It is suitable for simulation and planning purposes by incorporating Monte Carlo analysis capabilities for various modeled uncertainties, which are explained later in this chapter. As an example of the model, Figure 40 shows how the load is decreased in the presence of a PV generator when the peaks of PV generation and load demand are matched, both occurring around 11 am. The capacity of a PV generator in this example was scaled from 0% to 40% of the nominal load.

To accurately determine the effects of daily and seasonal variations of the DG output, a whole system has to be simulated over an extended period of time. Different possible DG system spatial locations across the feeder and their influence must also be considered. One way to obtain this information is via Monte Carlo simulations, where each annual simulation has identical load conditions but different PV generator locations and sizes.

This is a very computer–intensive process. If, for example, the feeder is simulated over a period of one year at 10-minute intervals, a total of 52560 ($6 \cdot 24 \cdot 365$) power flow solutions have to be calculated for *each* of the annual Monte Carlo simulations. Even if the data set is restricted to include only daytime hours, the computational burden is still overwhelming.

An obvious, but somewhat subjective, method for reducing the computational load is to reduce the number of simulation points by picking several "typical" days and then perform the Monte Carlo analysis using only the data for those days. However, in doing so, important annual aggregate values may be lost. Instead of using a complete annual data set or just a couple of typical days, an analytical procedure is proposed for reducing the large input data set. The goal is thus to cluster the large data set X into a smaller set W, and use the reduced data set for power flow calculations. Let X be the data set composed of all daytime vectors x_i of the load active power (P_i) reactive power (Q_i) and PV power (P_{PVi}) throughout the year, i.e.:

$$X = \{x_i | x_i = (P_i, Q_i, P_{PVi}),\ i = 1, \ldots, N\} \tag{28}$$

where P_i and Q_i are scaled by the nominal load active (reactive) power demand, i.e. the actual load demand at the time point i (in kW) at any bus in the system is obtained by multiplying its nominal load by P_i. The same scaling procedure is applied to PV output; at time i it is obtained by multiplying the nominal power of the PV system by P_{PVi}. Note that a three–dimensional set is assumed in (28). The Q_i dimension may be dropped to decrease the simulation time, if a constant load power factor is assumed. On the other hand, if in addition to PV, wind DG systems are present on a feeder, their annual profile would require a more complex data structure. The purpose of this algorithm is to handle multiple uncertainties that arise from intermittent generation and/or load variations and the only impact a different DG or load portfolio may have on the data is a different measurement set and its dimensionality. Such data structures can also be handled by the proposed algorithms.

The m-clustering of a set X (in a conventional sense) is defined as a partition of X into

m sets $C_1, \ldots, C_m$, where the following conditions are met [36]:

$$C_i \neq 0,\ i = 1, \ldots, m \tag{29}$$

$$\bigcup_{i=1}^{m} C_i = X \tag{30}$$

$$C_i \cap C_j = \emptyset,\ i \neq j, j = 1, \ldots, m \tag{31}$$

In other words, there cannot be zero-clusters (29), missed data (30), or overlapping clusters (31). Each point in the original data set is assigned to only one cluster. Fuzzy logic theory extends this idea by allowing a point to be a member of more than one cluster, i.e. each data point x_i belongs to the cluster C_j to some degree specified by its membership grade $u_{ij}, 0 \leq u_{ij} \leq 1$. Fuzzy clustering of a set X into m clusters is defined by a membership matrix U whose elements are membership grades u_{ij} if the following conditions are met [36]:

$$u_{ij} : X \rightarrow [0, 1],\ i = 1, \ldots, N, j = 1, \ldots, m \tag{32}$$

$$\sum_{j=1}^{m} u_{ij} = 1,\ i = 1, \ldots, N \tag{33}$$

$$0 < \sum_{i=1}^{N} u_{ij} < N,\ j = 1, \ldots, m \tag{34}$$

The membership grades close to unity indicate a "high grade" of membership to the corresponding cluster. Conventional "hard" clustering can be considered a special case of fuzzy clustering, with membership grades restricted to take values only from the set $\{0, 1\}$, i.e., each data point has a membership grade of one for one cluster and zeros for all the others. The main advantage of fuzzy clustering is that it may better capture the imprecisions in real-life data, providing more information about the data structure compared to a non-fuzzy scheme, naturally at the expense of increased computational cost.

To separate data into clusters, a proximity measure between data vectors, and between a vector and a cluster, needs to be defined. One such measure is the standard squared Euclidean distance, $d(x_i, x_j)$.

$$d(x_i, x_j) = \|x_i - x_j\|^2 \tag{35}$$

Each cluster can be represented by a simple vector, called the point representative of the cluster and denoted as w_j. Therefore, the distance between the vector and a cluster can be calculated as a distance between the vector and the cluster point representative. The objective of the clustering algorithm is thus to obtain the vector of cluster point representatives, $W = [w_1, w_2, \ldots, w_m]$, and the matrix of membership grades U, by minimizing the cost function of the form

$$J(W, U) = \sum_{i=1}^{N} \sum_{j=1}^{m} u_{ij} d(x_i, w_j) \tag{36}$$

with respect to W and U. Both the conventional and fuzzy algorithms were evaluated, and the conventional *c-means* clustering algorithm [37] was chosen, because of its computational simplicity and obtained accuracy. The objective function (36) is in that case minimized using the following algorithm [37]:

Step 1. Choose an initial vector W of cluster point representatives.

Step 2. For each data point x_i ($i = 1, \ldots, N$), determine the closest cluster point representative w_j.

Step 3. Update cluster point representatives w_j ($j = 1, \ldots, m$) as mean values of the vectors that belong to their respective clusters.

Step 4. Repeat steps 2 and 3 until no change in cluster representatives occurs between two successive iterations.

The performance of the algorithm may be measured by calculating the standard *mean squared error* (MSE):

$$MSE = \frac{1}{N} \sum_{i=1}^{N} ||x_i - \hat{x}_i||^2 \tag{37}$$

where $\hat{x}_i = w_k$ for $x_i \in C_k$. As more data points concentrate around the cluster centers, the cluster structure improves and the MSE decreases. MSE is a monotonically decreasing function of the number of clusters, and can be used to determine the appropriate number of clusters. Note, however, that the MSE validates only the goodness of clustering; it does

not guarantee that the results of analysis using the reduced clustered set will provide an accurate description of the actual feeder behavior. To validate the goodness of clustering, two more validity indices are introduced. They are based on calculated feeder voltage and active losses using the full data set in addition to the same quantities obtained using cluster representatives. The indices, calculated as mean squared errors for the active power loss and feeder voltage, show the discrepancy between the values obtained with the full and reduced set, with lower values indicating better fit.

$$I_{loss} = \frac{1}{N}\sum_{i=1}^{N}(P_t(x_i) - P_c(x_i))^2 \tag{38}$$

$$I_V = \frac{1}{N}\sum_{i=1}^{N}\|V_t(x_i) - V_c(x_i)\|^2 \tag{39}$$

$P_t(x_i)$ is the total active feeder loss for a given data point x_i, $P_c(x_i)$ is the total active feeder loss obtained using the appropriate cluster representative, i.e., $P_c(x_i) = P_t(w_k)$ where $x_i \in C_k$, $V_t(x_i)$ is the feeder voltage vector for x_i, and V_c is the voltage vector obtained using the appropriate cluster representative.

The main drawback of the c-means algorithm is that it requires the number of clusters to be adopted in advance. It may also yield suboptimal, local minima of the objective function (36), depending on the initial conditions used in the Step 1 of the algorithm. The suboptimal clustering problem is usually tackled by repeating the procedure using different initial conditions, and keeping only the cluster representatives that yield the smallest value of the objective function. The most time-consuming part of the c-means algorithm is Step 2, and various algorithms that use approximations for determining the closest w_j may be used as fast alternatives to the c-means algorithm. The algorithm described in [38] converges much faster, but yields suboptimal solution with higher MSE, which may be improved by few additional iterations of the c-means algorithm. Still, the total execution time and resulting MSE are typically lower than that of the randomly initialized c-means algorithm. Thus, it can also be used as a c-means initializer, significantly improving its convergence.

4.4 Detection of boundary points

The c-means clustering algorithm is inherently an averaging algorithm, since it chooses the cluster point representatives as mean vectors of cluster elements. The boundary elements of the original set X, dominant in one of the dimensions, are usually responsible for the extreme function values, but as such will never be picked up as cluster representatives. A procedure is therefore proposed for augmenting the set W of cluster representatives with the boundary points of set X that will be used to estimate extreme feeder conditions.

The convex hull $conv(X)$ of a set of points X is a smallest convex set containing X. The objective is to obtain the set E of extreme points of X, i.e., the minimal subset E of X for which $conv(X) = conv(E)$ holds. The elements of the set E are the vertices of the convex hull of X. In low dimensions ($d \leq 3$), both $conv(X)$ and E may be found optimally in $O(n \log n)$ time [39], n being the number of elements in the set X. The same cannot be extended into higher dimensions because of the exponential growth of the number of facets of the convex hull [40]. Fortunately, the problem of determining set E is generally much simpler than the problem of obtaining the convex hull. The d-dimensional convex hull can be computed optimally in $O(n^{\lceil d/2 \rceil})$ time [40], but set E can be calculated in $O(nk)$, k being the number of extreme points of X, since the problem of finding set E can be deconstructed into solving a set of linear programming problems [39].

In the numerical example that follows, a Quickhull algorithm is employed. The algorithm is implemented in MATLAB using the Qhull package [41]. The Quickhull algorithm recursively divides the set X into subsets, finds their convex hulls, and concatenates them into $conv(X)$. The operation of the algorithm for a two dimensional set is illustrated in Figure 41. Starting from the set X shown in Figure 41(a), the algorithm begins by dividing the plane with a line through two points, which have the smallest and largest abscissa, as shown in Figure 41(b). Then, on each side, a point is selected such that the formed triangle has maximum area (Figure 41(c)). The selected point is on the $conv(X)$, while all points

inside the triangle may be discarded. The procedure is repeated for both sides of the triangle connected to that point until there are no points left (Figure 41(d)-(f)). In Figure 41, points that belong to the convex hull are represented as squares, points that do not belong to the hull are represented as four-point stars and points not yet classified are represented as circles. Qhull can effectively determine both the convex hull and the extreme points of the

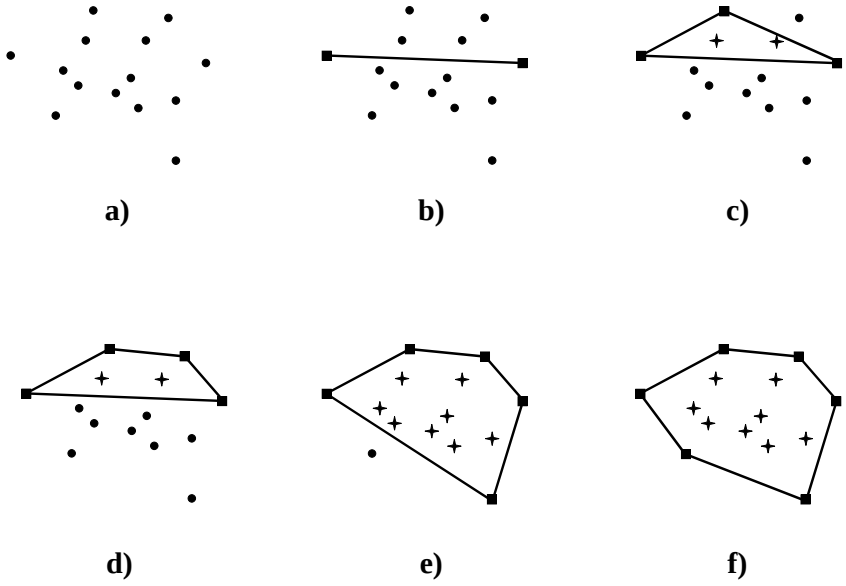

Figure 41: Illustration of the Quickhull algorithm.

set X for up to eight-dimensional sets. For higher dimensional sets, the algorithm described in [39] is recommended.

4.5 Numerical Example

The elements of the set of cluster point representatives W and extreme hull points E form the set that may be used for power flow simulations. Set W is used to obtain histograms (duration curves) of various feeder operational characteristics, while set E is used to determine their extreme values.

The 69-bus, eight-lateral distribution feeder, based on [34], is used as an example. The feeder lateral layout is shown in Figure 39, which also shows the locations of loads and one possible distribution of PV generators. The daily load profile (both active and reactive) is obtained from the actual utility data, provided by Nebraska Public Power District, for the city of Scottsbluff, NE. It is assumed that all the loads at the feeder follow the same load patterns. The measured utility data spans one year in 10-minute intervals, which is also the period considered in this study. Note that the availability of higher resolution data would allow more precise detection of the cluster points, as more information describing the interaction between the PV output and load would be available.

The PV generation is obtained by simulating an ideally oriented and tilted fixed PV system at the actual location (Scottsbluff, NE) using the PV simulation program developed in Task 1. The following derating coefficients are used: shading 4%, dust 4%, mismatch 2%, DC losses 2%, maximum power point tracking losses 4% and inverter efficiency is assumed to be 93%. Non-optimally oriented and tilted systems may be simulated by multiplying the output of the system by the appropriate derating coefficient.

Set X containing only daytime hours (from sunrise to sunset) values for P_i, Q_i, and P_{PVi} has a total of 28137 vectors. The scatter plots of all data vectors with superimposed cluster point representatives for various number of clusters are shown in Figures 42–47. The figures reveal that the clustering algorithm has indeed maintained the intrinsic data structure, but also reiterate the necessity for the companion boundary points detection algorithm.

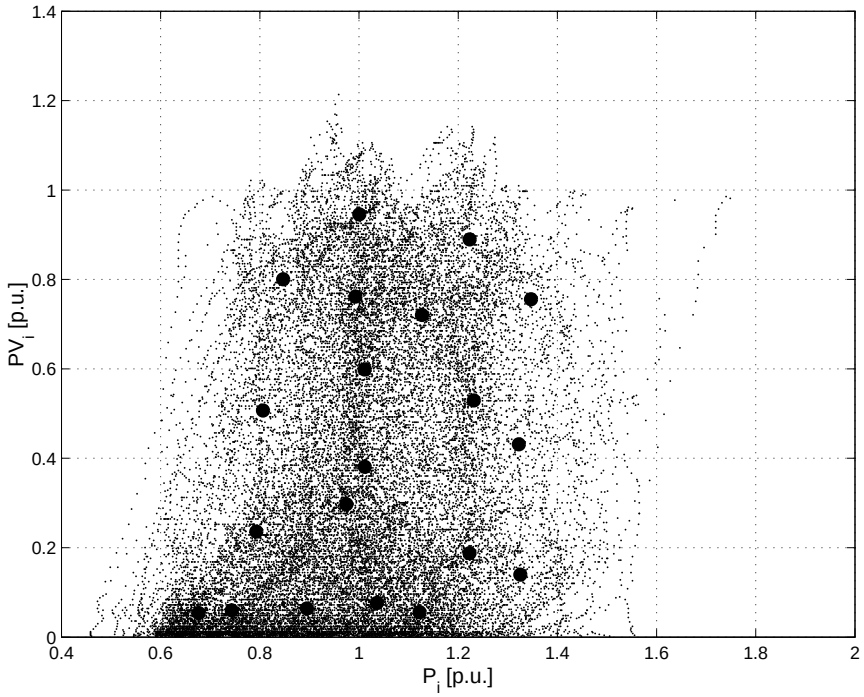

Figure 42: The data and cluster center points (projection onto the PV-P plane). 28137 data points, 20 clusters.

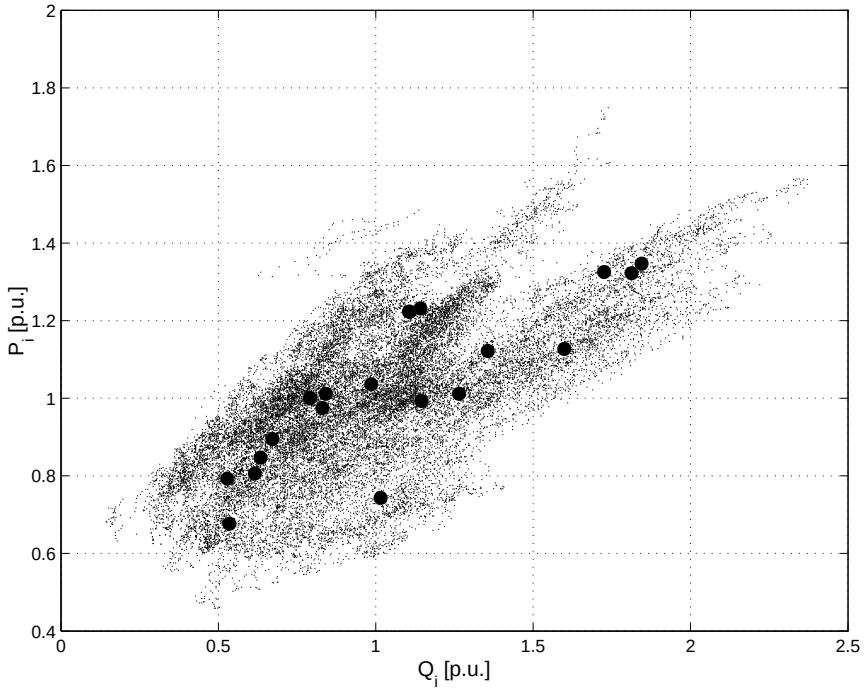

Figure 43: The data and cluster center points (projection onto the P-Q plane). 28137 data points, 20 clusters.

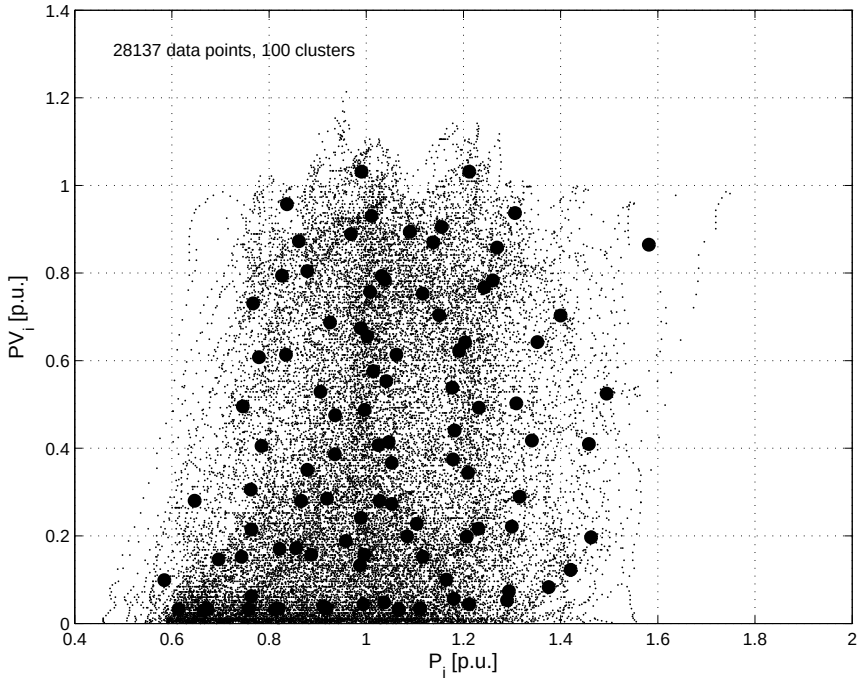

Figure 44: The data and cluster center points (projection onto the PV-P plane). 28137 data points, 100 clusters.

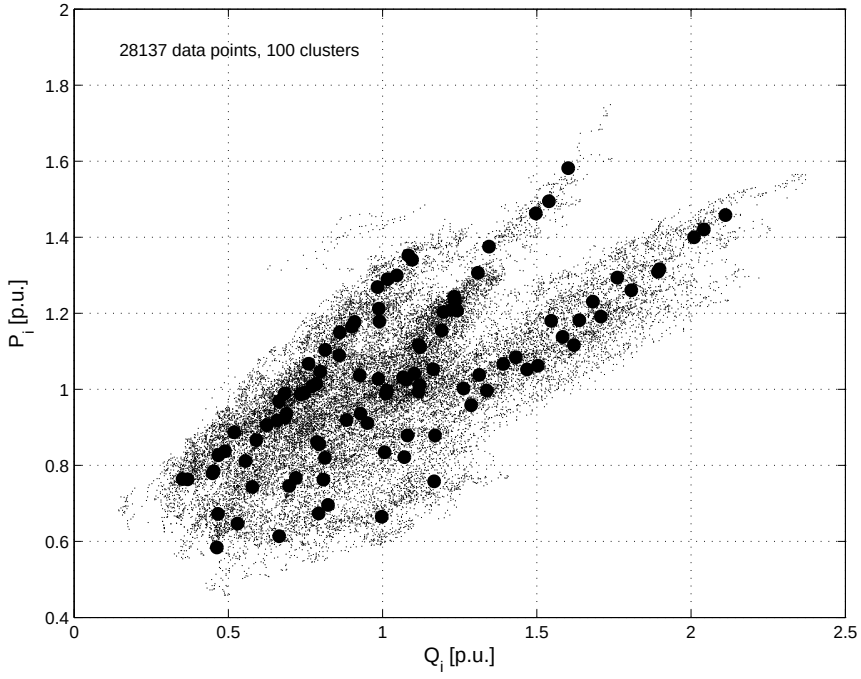

Figure 45: The data and cluster center points (projection onto the P-Q plane). 28137 data points, 100 clusters.

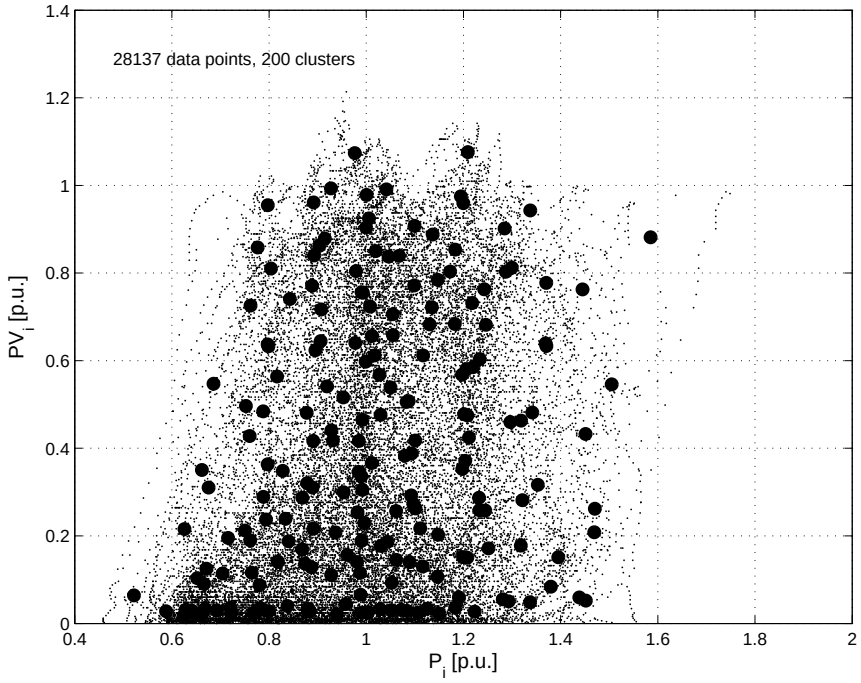

Figure 46: The data and cluster center points (projection onto the PV-P plane). 28137 data points, 200 clusters.

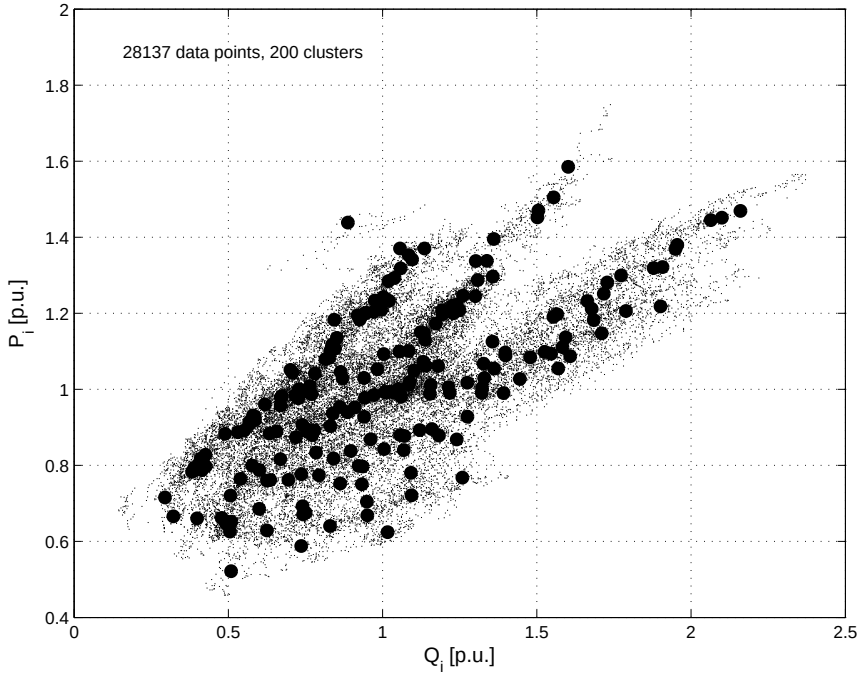

Figure 47: The data and cluster center points (projection onto the P-Q plane). 28137 data points, 200 clusters.

The MSE, power, and voltage indices are shown in Figure 48 for various numbers of clusters. As expected, more clusters will better approximate the original data set. The agreement between the MSE (obtained using only the input data set X, without calculating power flows), and the voltage and power indices (calculated using the results of the power flow analysis on a full set) indicate that the MSE alone may be used to determine the minimal number of clusters which would yield satisfactory results.

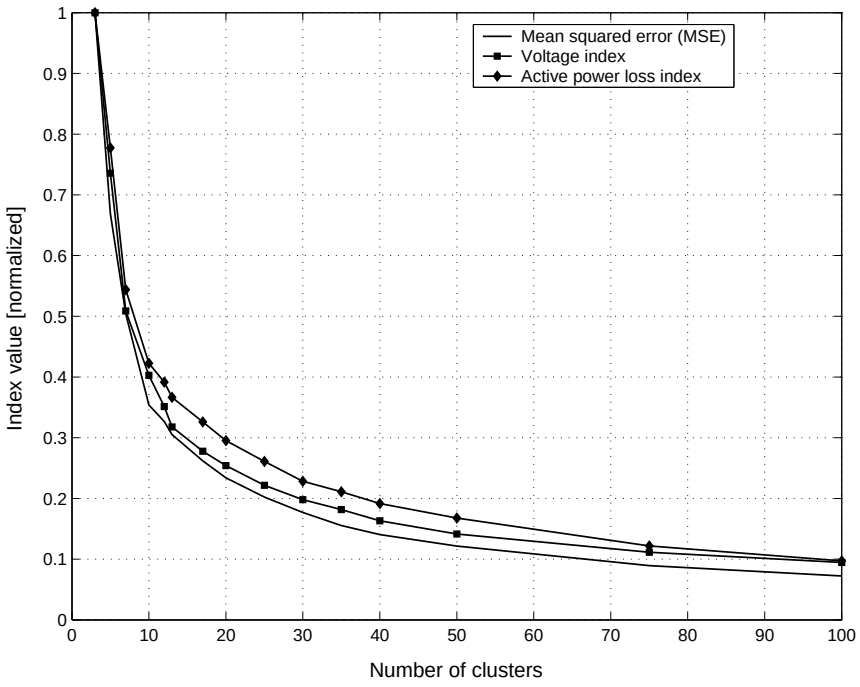

Figure 48: The mean squared error, voltage and active power loss indices.

The convex hull of the set X of 28137 three-dimensional vectors has 184 facets, and 94 extreme points. Figure 49 shows the original set X, and Figure 50 shows the convex hull of X and the set of extreme points E.

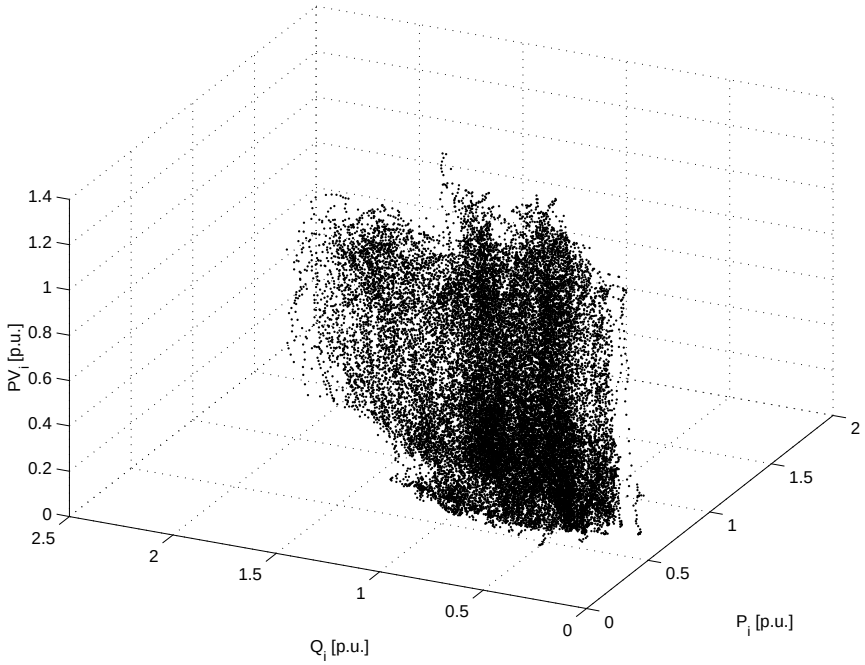

Figure 49: The original data set X (28137 points).

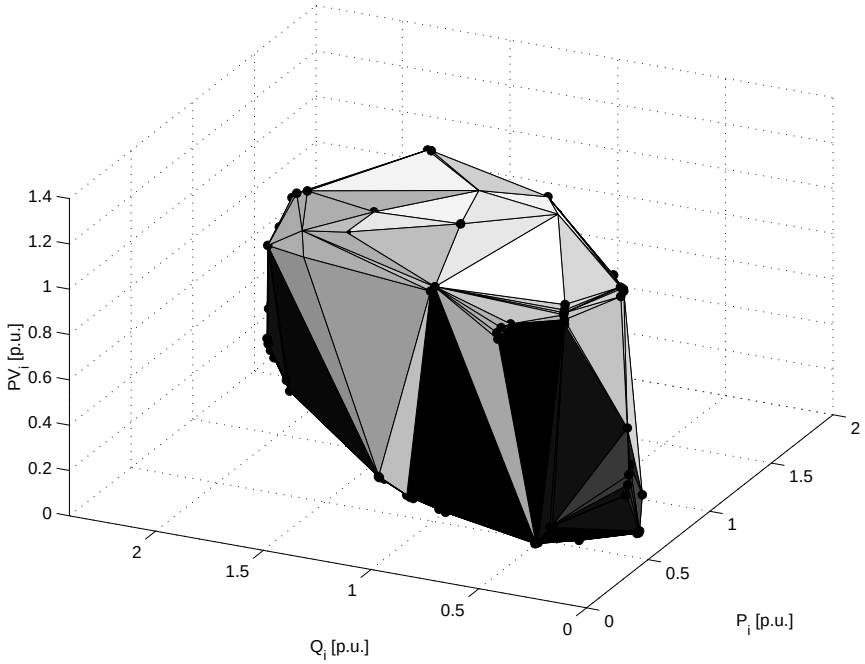

Figure 50: The convex hull of X and the set of extreme points E (94 points).

Table 11 shows the total feeder active P_{loss} and reactive power loss Q_{loss}, and active P_{subst} and reactive power taken from the substation Q_{subst}, calculated using various number of clusters, using only the set of extreme points E, and using the full data set X. Both the extreme values and the total annual energy are calculated for all cases. As expected, the energy can be accurately estimated using an extremely small number of clusters, while even a relatively large number of clusters (100) is still not sufficient for determining the extreme values. However, the extreme values are determined exactly using the set of extreme hull points E.

Table 11: The total annual energy and extreme values for feeder losses and power taken from the substation, obtained using both reduced and full data set.

# of cluster points		P_{loss} [MW/MWh]	Q_{loss} [MVAr/MVArh]	P_{subst} [MW/GWh]	Q_{subst} [MVAr/GVArh]
10	Min	0.029	0.015	2.767	0.863
	Max	0.099	0.052	4.949	2.529
	Total	255.093	131.809	16.761	7.491
100	Min	0.018	0.009	2.165	0.583
	Max	0.131	0.068	5.535	2.657
	Total	256.199	132.507	16.762	7.314
28137	Min	0.012	0.006	1.748	0.245
	Max	0.172	0.088	6.075	3.095
	Total	256.378	132.647	16.762	7.314
Hull points	Min	0.012	0.006	1.748	0.245
	Max	0.172	0.088	6.075	3.095

Figures 51 and 52 represent the duration curves of the annual active feeder losses and substation power factors, calculated using m cluster point representatives, for m equal to 10 and 50, and using all 28137 points. Note a relatively poor match for curves obtained with only 10 clusters, and better match obtained with 50 clusters. However, both fail to match extreme values, which can be determined exactly using the extreme set E, and shown as dot-dashed lines in Figures 51 and 52. Figure 53 represents the voltages across one feeder branch, again obtained using cluster point representatives and with the full data set. The

average voltages are correctly estimated with as little as 10 clusters, as the three lines in the middle of Figure 53 obtained with 10, 50 and 28137 points are practically indistinguishable (line labeled D in Figure 53). The extreme values obtained with 10 (lines C and E) and 50 clusters (lines B and F) differ from the correct values obtained with the full set of 28137 points (lines A and H), again showing that the clustered set cannot be used to estimate extreme values. However, the extreme values obtained using the set E (diamond-marked, lines A and G) are almost identical to the voltages obtained with the full set.

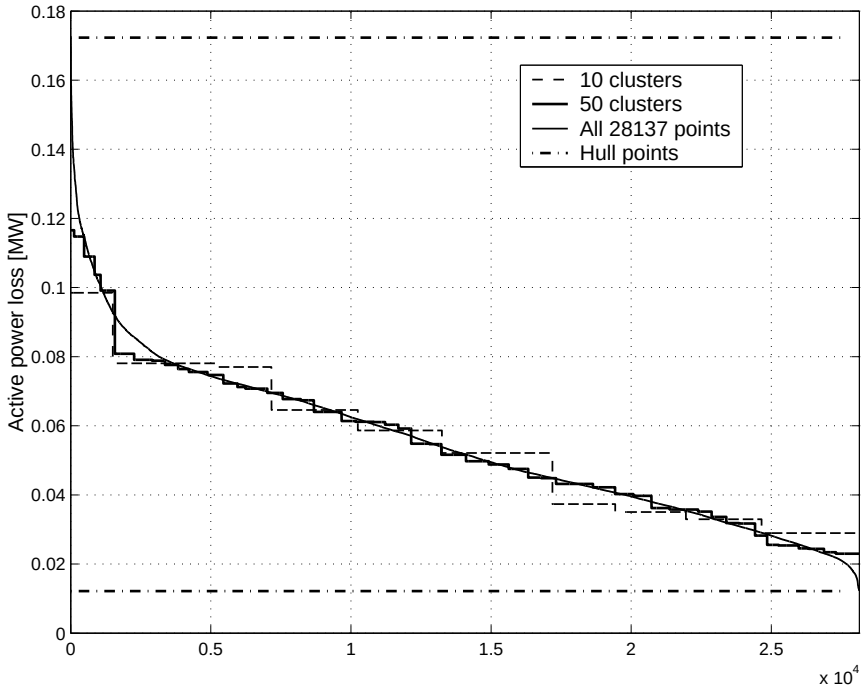

Figure 51: The duration curve for active losses calculated using cluster point representatives ($m = 10, 50$), hull points, and using all 28137 data points.

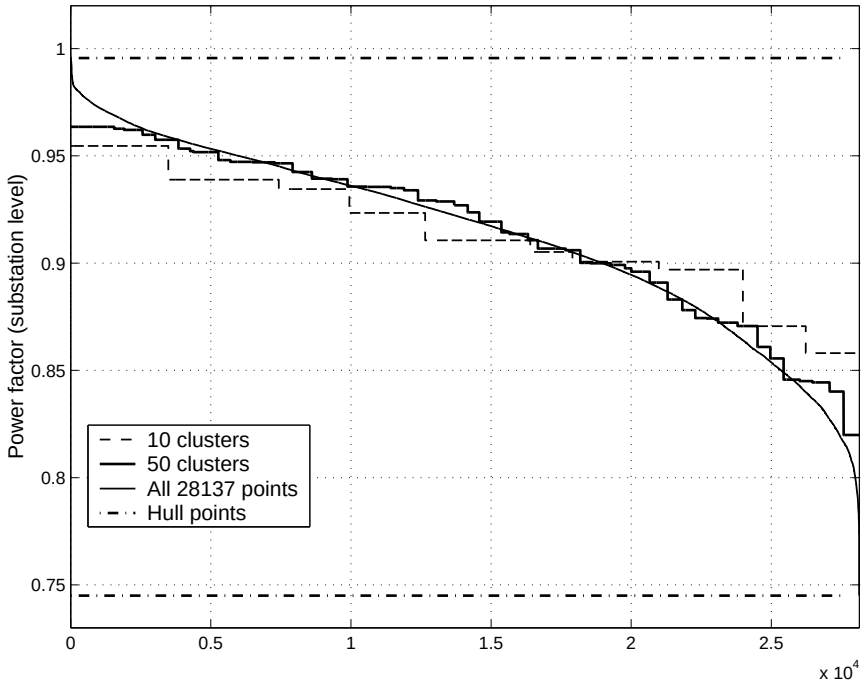

Figure 52: The duration curve for power factors calculated using cluster point representatives ($m = 10, 50$), hull points, and using all 28137 data points.

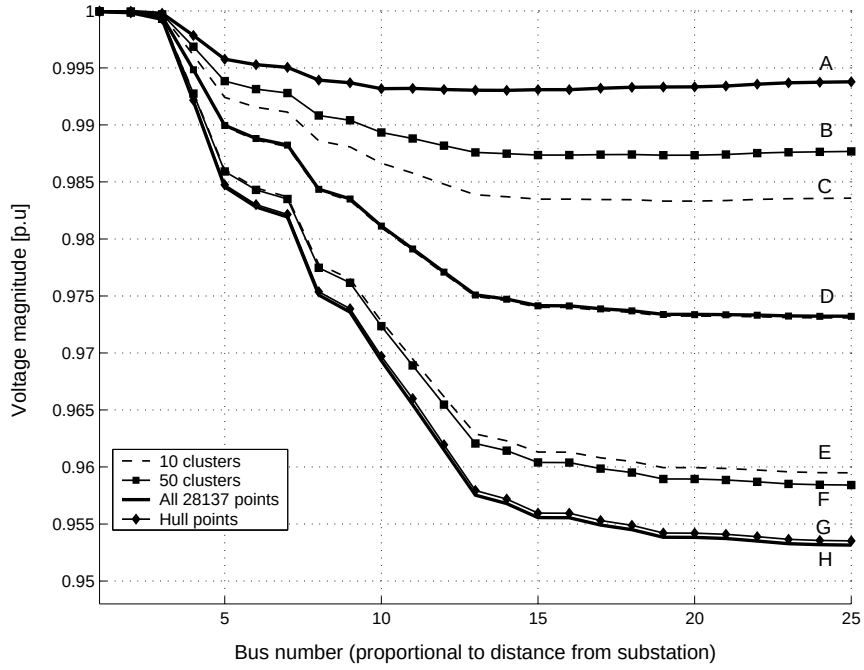

Figure 53: The average annual feeder voltages across one feeder branch, calculated using cluster point representatives ($m = 10, 50$), hull points and using all 28137 data points.

4.6 The effect of random PV system locations

In contrast to a typical scenario in power engineering where a relatively small number of devices (generators, capacitors, etc.) are placed in the existing network, PV systems introduce a situation with a large number of relatively small devices. Additionally, the exact positions and sizes of individual PV systems are not likely to be known at the planning stage. However, total PV penetration may be controlled to some degree, either by limiting the maximum amount of DG allowed on the feeder, or by using green power or similar customer incentives. For example, green power programs typically offer standardized systems to individual customers, such as 2 kW and 4 kW rooftop PV systems offered by Sacramento Municipal Utility District (SMUD) during its PV Pioneers I and II programs [42].

To model this scenario, a random uniform spatial distribution of standardized PV systems ("PV blocks") along the distribution feeder is assumed. Depending on the size of the standardized system (PV block) and total PV penetration on the feeder, the expected amount of DG at each individual bus will differ. Three cases are investigated, with standardized PV systems equal to 2 kW, 20 kW, and 40 kW. Relatively small "block" sizes result in a relatively uniform spread of PV systems along the feeder, as shown in the top part of Figure 54. As the block size of each individual system increases (while keeping the same total PV penetration level), the situation with fewer, larger PV systems is obtained. This situation is shown in the middle and bottom parts of Figure 54.

The reduced data set, obtained in the previous section, is used to determine the expected average and extreme feeder conditions for a given block size and total PV penetration. For a given total PV penetration, a set of Monte Carlo experiments are performed. For each Monte Carlo experiment, PV generators of the appropriate size (2 kW–40 kW) are randomly allocated on the feeder. The power flow simulations are performed using both clustered and extreme sets, and all feeder voltages are recorded. The procedure is repeated 1000 times, allowing the estimation of average and extreme quantities. In Section 4.8, a Monte Carlo experiment is explained in more detail, as well as the obtained results.

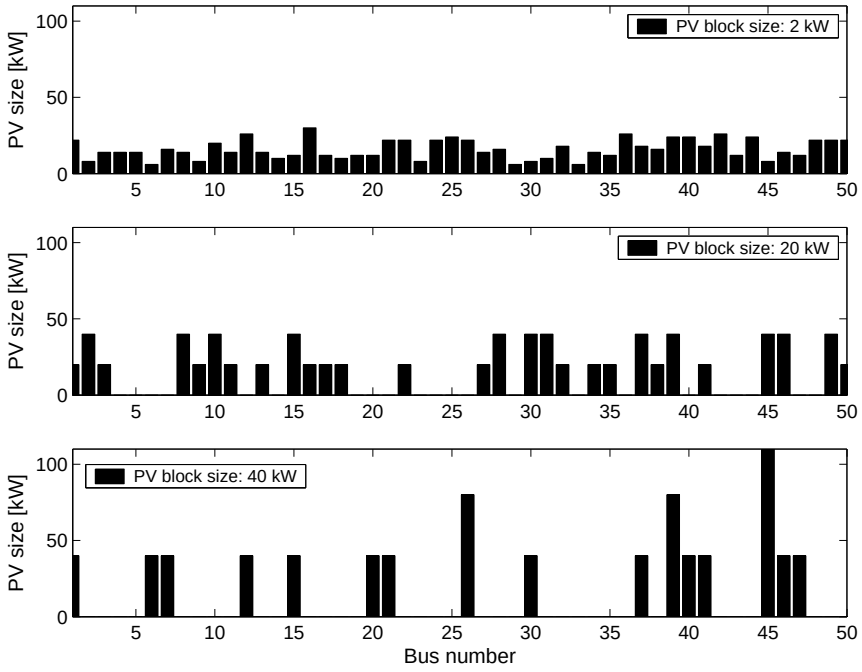

Figure 54: The placement of PV generators along the distribution feeder assuming uniform random distribution, but different PV system block sizes. Total PV power installed at the feeder is 760 kW in all three cases.

4.7 The effect of using voltage source inverters

The majority of contemporary inverters used in DG systems are current source inverters (CSI) that operate at unity power factor and hence decrease the overall substation–level power factor of a distribution feeder. The power factor is decreased because the total active power drawn from the substation is reduced (due to PV active power injection), while the reactive power demand remains the same. Due to the probabilistic nature of the PV system output (as explained in Section 3.2), PV inverters typically operate at relatively low loading levels, and could be used for reactive power support as well. Present regulations dictate that PV inverters should operate at power factors higher than 0.85 when the output is higher than 10% of their rated power [43], although specially designed systems may operate outside this limit with utility approval. The effect of voltage source inverters that can generate reactive power commensurate with the remaining unused capacity at any given

point in time is therefore investigated, by considering the following three scenarios, shown in Figure 55:

1. Inverters supply only active power.
2. Same as 1, but inverters also supply maximum available reactive power up to the limit Q_{max} determined by their rating, or Q_V determined by the maximum allowable voltage at its bus.
3. Same as 2, but under constraint that the power factor is above 0.85, i.e. also limited by Q_{lim}.

To demonstrate the potential for reactive power injection by PV inverters, Figure 56 shows a typical histogram of the annual active power output of a PV system, located in Atlanta, GA, equipped with the inverter with rated power equal to the rated power of the PV system. Figure 56 also shows the corresponding histograms of the maximum reactive annual power output of that inverter for cases when reactive power is limited by Q_{max} and Q_{lim}, i.e. for cases 2 and 3 above.

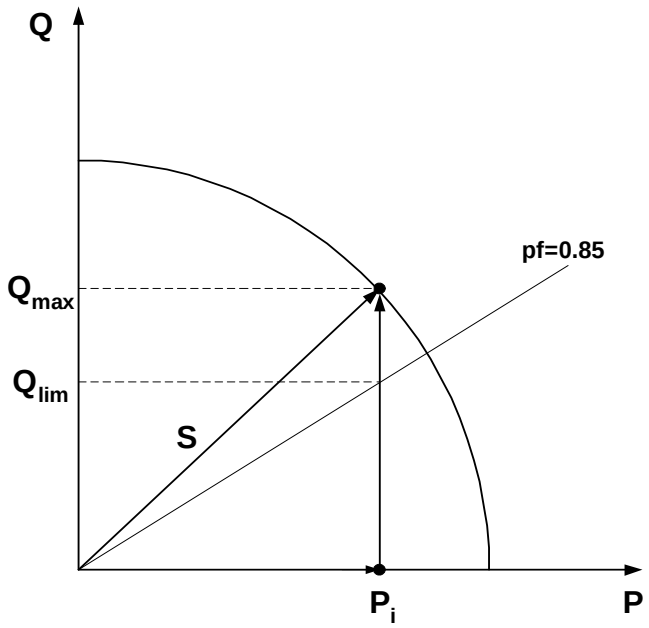

Figure 55: The modes of operation of a voltage source inverter. For a given active power P_i, inverter may produce any amount of reactive power between zero (case 1) and Q_{max} (case 2). If its power factor is limited to be no less than 0.85, its maximum reactive power output is limited by Q_{lim}.

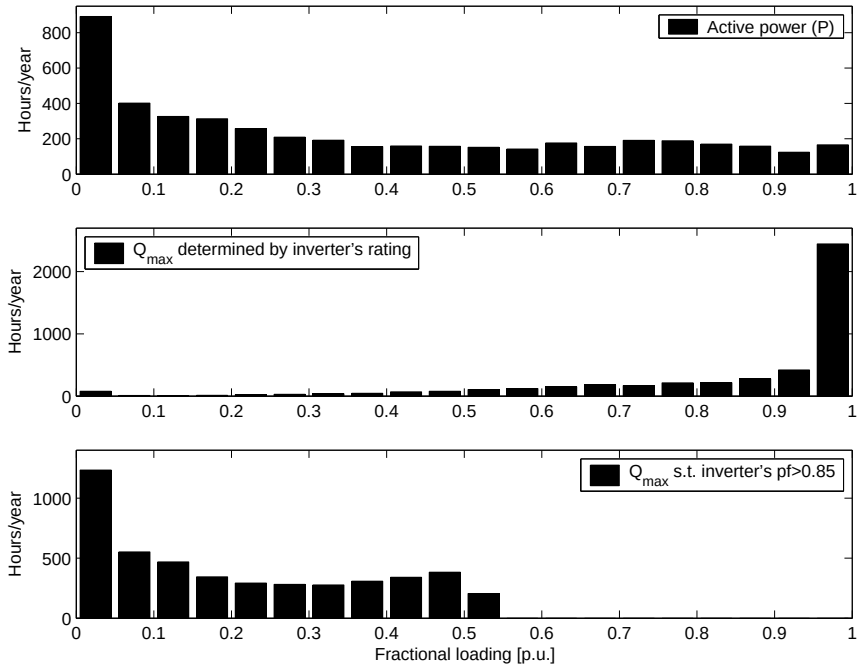

Figure 56: Histograms of annual inverter active energy production and the corresponding reactive production, limited by Q_{max} and Q_{lim}.

4.8 Monte Carlo analysis using the reduced set

With three PV distribution schemes (block sizes of 2 kW, 20 kW, and 40 kW), and three inverter control strategies, a total of nine scenarios are considered. For each scenario, one thousand Monte Carlo simulations are performed using 200 cluster point representatives and 94 hull points. The total nominal installed PV size is fixed at 800 kW, representing the PV penetration level of approximately 20% of the total nominal feeder load.

The average and extreme values of total distribution feeder losses, total energy taken from the transmission network and the substation–level power factor over 1000 Monte Carlo simulations are presented in Table 12. The feeder losses and energy taken from the transmission network are expressed as a percentage of the values calculated for a feeder without PV support. Without PV, the active and reactive losses are 1.66% and 2.19% of the total active and reactive energy taken from the transmission system throughout the year, respectively, and the results in Table 12 represent the improvements over these values. The average power factor for a feeder without PV is 0.9280. Table 12 shows the results for the considered 9 scenarios obtained using three PV distribution schemes (block sizes of 2 kW, 20 kW, and 40 kW) and three inverter control strategies (supplying only active power, both active and reactive power but limiting inverter power factor to be higher than 0.85, and supplying reactive power up to the maximum allowable by the kVA inverter rating). For each scenario, the minimum, average and maximum values obtained over 1000 Monte Carlo simulations are presented. For example, for the case of a 2 kW PV block size and no reactive power injection (first row in Table 12), the minimum total annual active losses are 85.80% of the losses calculated for the case without PV. The average annual power factor is 0.9113, lower than the value of 0.9280 for the case without PV.

In general, both active and reactive feeder losses decrease with the addition of PV generators. The average losses obtained over 1000 Monte Carlo simulations (and thus the expected values) do not depend noticeably on the PV block size, while the possible ranges of their values (min–max ranges) increase as the block size of the individual system

increases. Allowing inverters to supply reactive power further reduces both active and reactive losses.

Similar situation is observed for the total active and reactive power taken from the transmission network. If inverters are supplying reactive power, the amount of reactive power imported from the transmission network is significantly reduced. Consequently, the overall feeder power factor is improved and may reach 0.9642, compared to 0.9280 for a feeder without PV.

Figure 57 shows the duration curves for the voltage at the remote bus 54, for standardized PV system "blocks" of 2 kW and 40 kW. A duration curve is a graph representing the percentage of time during which the value of a given parameter is equaled or exceeded. For example, the bold solid line in Figure 57 shows that for a feeder without PV, the voltage at bus 54 is higher than 0.965 for 20% of the time. Figure 57 shows the maximum, minimum and average duration curves recorded over one thousand Monte Carlo simulations. The improvements over the base case without DG (bold solid line) are clearly noticeable. Although the range of recorded values is, as expected, wider in the case of the 40 kW standard PV system size, the average values (solid lines) are almost identical. The duration curves also offer an estimate of maximum possible voltage improvement at this bus for a given standard PV size. The extreme voltages are determined using the hull points; maximum values of 0.98 for a case without PV, and 0.987 for the case with 40 kW PV system size are recorded. The minimum value was 0.95 in all three cases, due to the presence of regulating shunt capacitors.

Figure 58 shows the duration curves for the power factor at the substation (bus 0), without PV support (bold solid line) and for all three inverter control strategies. If inverters supply only active power, active load demand is reduced while reactive demand remains unchanged, which effectively decreases the overall feeder power factor. However, if inverters are allowed to inject reactive power, the overall power factor may be significantly

Table 12: Total feeder losses, energy consumption and average power factor over 1000 Monte Carlo simulations for different PV distribution schemes and inverter control strategies.

Total PV penetration: 800 kW			Losses		Feeder consumption		Power factor
			P [%]	Q [%]	P [%]	Q [%]	
2 kW block size	No Q	Min	85.80	87.07	91.71	102.63	0.9113
		Avg	87.29	88.31	91.73	103.34	0.9121
		Max	88.95	89.77	91.76	103.93	0.9128
	Max Q, s.t. pf>0.85	Min	83.01	84.52	91.67	91.88	0.9269
		Avg	84.80	86.00	91.70	92.44	0.9276
		Max	86.55	87.55	91.73	93.00	0.9282
	Max Q allowed by kVA rating	Min	77.96	79.75	91.59	60.53	0.9613
		Avg	80.32	81.74	91.63	61.02	0.9618
		Max	82.67	83.89	91.67	61.64	0.9623
20 kW block size	No Q	Min	81.27	83.60	91.63	100.64	0.9100
		Avg	87.44	88.43	91.73	103.21	0.9122
		Max	92.70	93.04	91.82	105.01	0.9153
	Max Q, s.t. pf>0.85	Min	77.53	80.30	91.58	89.55	0.9258
		Avg	84.91	86.10	91.71	92.35	0.9277
		Max	91.22	91.63	91.81	93.96	0.9308
	Max Q allowed by kVA rating	Min	71.98	75.18	91.49	58.43	0.9593
		Avg	80.57	81.96	91.63	61.05	0.9618
		Max	88.82	89.50	91.77	63.84	0.9642
40 kW block size	No Q	Min	81.04	83.41	91.63	100.71	0.9097
		Avg	87.54	88.52	91.73	103.11	0.9123
		Max	94.27	94.14	91.85	105.31	0.9152
	Max Q, s.t. pf>0.85	Min	77.17	79.99	91.58	89.62	0.9256
		Avg	85.05	86.21	91.71	92.25	0.9278
		Max	93.18	93.00	91.84	94.20	0.9307
	Max Q allowed by kVA rating	Min	72.15	75.63	91.49	58.41	0.9592
		Avg	80.90	82.24	91.64	61.02	0.9619
		Max	91.21	90.99	91.81	63.96	0.9642

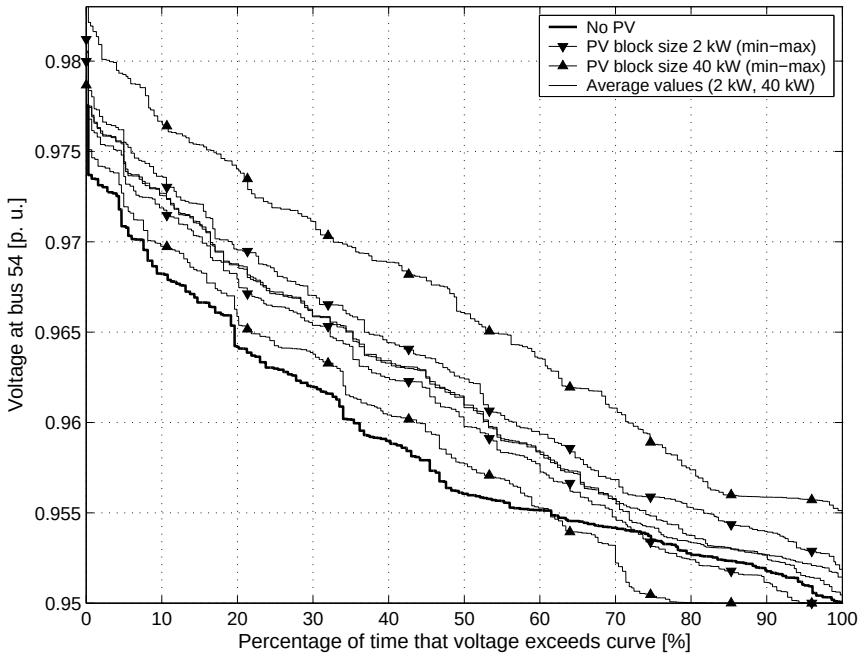

Figure 57: Voltage duration curves at bus 54 for different PV block sizes. Inverters supplying maximum reactive power possible.

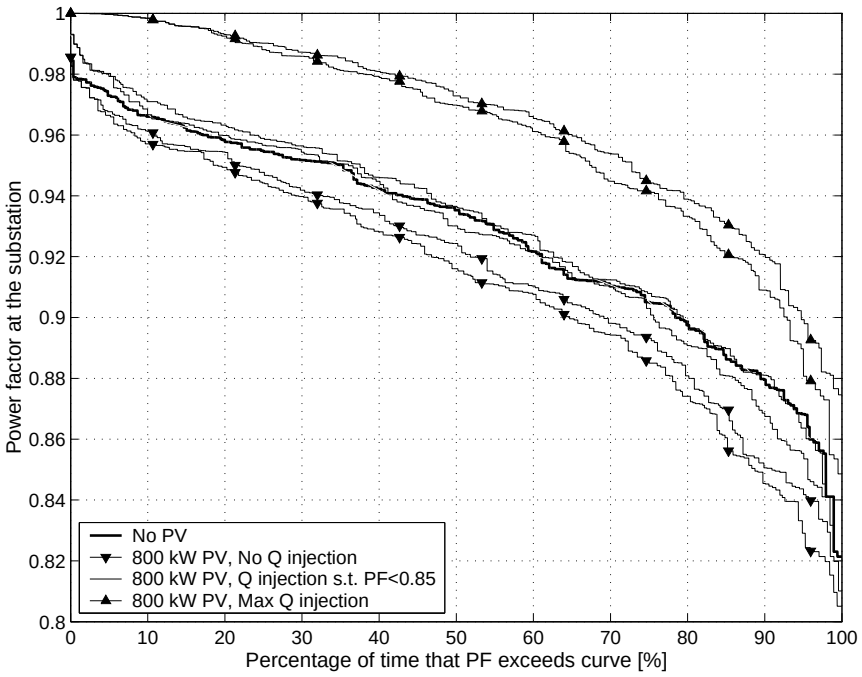

Figure 58: Power factor duration curves for different inverter control strategies. PV system block size is 20 kW.

improved and controlled. This could qualify the use of the feeder for conservative voltage reduction, which some utilities are using for "soft load control" during extreme load peaks. Figure 58 represents a scenario when both PV system and inverter size are 20 kW; additional improvements may be possible if larger capacities of inverters are used. In this example, moderate capacity oversizing (up to 20%) did not provide sufficient benefits to justify additional expenditures. Consideration may be given to selectively boosting capacity at locations where reactive support may provide better system performance, based on traditional methods for determining optimal locations for reactive support.

Figure 59 shows the loading levels of the five most heavily loaded branches, with and without PV support. In this example, the PV system size is 2 kW, and inverters are operating at 0.85 power factor or higher. White bars represent quantile plots for the loading level of a particular branch without PV. The solid lines in the bars represent minimum values, 25^{th}, 50^{th}, 75^{th} percentiles and maximum values respectively, while the dotted lines show the mean values. The lines below and above bars represent extreme loading levels obtained using hull points. Gray bars represent the same quantities obtained over one thousand Monte Carlo simulations, with PV support. The loading levels are normalized, with the loading level of 100% being the extreme loading level of each branch for the case without PV. As expected, the PV generators decrease the branch loading levels. The average loading level of the most heavily loaded branch (branch 2–3 in Figure 39) decreased by approximately 5% due to the addition of PV generators, while the maximum loading level decreased by 9%. As PV generators typically operate below their rated power output, due to the probabilistic nature of their input, the reduction in loading levels is not as significant as it would be for the case with conventional DG. Use of different inverter control strategies, PV "block" sizes or DG spatial allocations may significantly change these values. However, all of these scenarios can be quickly simulated using a reduced data set.

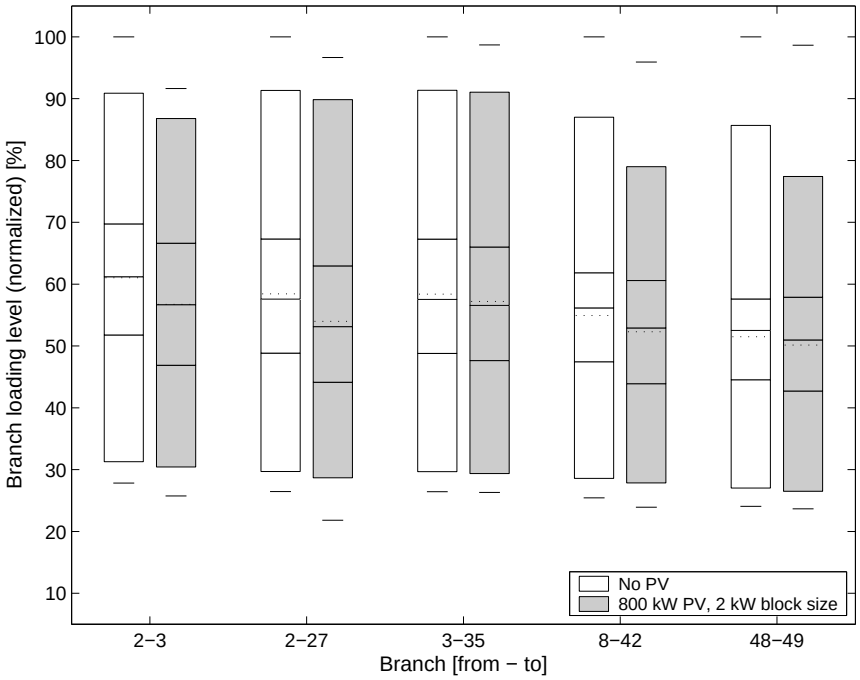

Figure 59: Loading levels for 5 most heavily loaded branches, with and without PV support. PV system block size is 2 kW, inverters operating at 0.85 power factor.

4.9 Algorithm performance and dimensionality

The performance of the Monte Carlo algorithm on the reduced set is shown in Tables 13 and 14. Table 13 shows the reduction in the number of floating point operations (flops) over the base case (without clustering) per 1000 Monte Carlo simulations of a DG-enhanced feeder obtained using the proposed algorithms, if the original data set is three-dimensional, as defined in (28).

One thousand Monte Carlo simulations were performed using various numbers of cluster representatives, ranging from 10 to 200. For each Monte Carlo simulation, a different PV allocation along the feeder was considered. The total nominal installed PV size was kept at 800 kW, representing the PV penetration level of approximately 20% of the total nominal feeder load. The total number of flops per 1000 Monte Carlo simulations is the sum of flops required for: a) obtaining cluster representatives, b) boundary points and c)

running power flow simulations. Note that in this example, even with 200 clusters the improvement in speed is significant, as the Monte Carlo analysis can be done 87 times faster using the reduced set of cluster and hull points.

Table 13: The performance of the clustering algorithm on a 3-dimensional data set.

Number of clusters	Clustering [flops]	Total power flows [flops]	Total over 1000 MC simulations [flops]	Relative improvement
10	2.57E+08	9.36E+06	9.62E+09	264
20	4.46E+08	1.03E+07	1.07E+10	237
50	1.07E+09	1.30E+07	1.40E+10	181
100	1.65E+09	1.75E+07	1.91E+10	133
200	2.91E+09	2.65E+07	2.94E+10	87
28137	-	2.54E+09	2.54E+12	1

The use of a three-dimensional set, as defined in (28), assumes that all loads on the feeder follow the same daily and seasonal pattern. Typically, three categories of loads are considered in distribution system analysis: industrial, commercial and residential - each with distinctively different daily and seasonal load patterns. To be able to model such loads, the dimensionality of the data set may be increased, as follows:

$$X = \{x_i | x_i = (P_i^c, Q_i^c, P_i^i, Q_i^i, P_i^r, Q_i^r, P_{PVi}),\ i = 1, \ldots, N\} \tag{40}$$

where superscripts *c*, *i* and *r* represent commercial, industrial and residential load profiles, respectively. The dimensionality of the set may be increased even further by incorporating more load profiles or profiles of other renewable generators such as, for example wind DG systems.

Although both the clustering and hull algorithms work in general for N-dimensional problems, the computational effort required to cluster very high dimensional sets may not

be justified. However, for a relatively small number of dimensions, the algorithms described previously suffer no such difficulties. The performance of the algorithm on a five-dimensional set is shown in Table 14. The improvement in speed is comparable to the three-dimensional case. For example, the Monte Carlo analysis on a set of 200 cluster points can be done 81 times faster than the equivalent study using all 28137 points.

Table 14: The performance of the clustering algorithm on a 5-dimensional data set.

Number of clusters	Clustering [flops]	Total power flows [flops]	Total over 1000 MC simulations [flops]	Relative improvement
10	2.67E+08	9.36E+06	9.63E+09	264
20	7.07E+08	1.03E+07	1.10E+10	232
50	1.37E+09	1.30E+07	1.43E+10	177
100	2.79E+09	1.75E+07	2.02E+10	125
200	5.08E+09	2.65E+07	3.15E+10	81
28137	-	2.54E+09	2.54E+12	1

4.10 Conclusions

The effects of a random allocation of renewable DG systems in a distribution feeder are investigated in this chapter. The performance assessment of a distribution feeder equipped with renewable distributed generators is a challenging problem at the planning stage, because of the uncertainties involved in predicting the DG output due to stochastic nature of its input, its location on the feeder, and interaction with feeder load, which is also a stochastic process. Simulating stochastic processes that drive the DG output as well as DG placement, combining it with extensive field measurements of load profiles at feeders that are candidates for DG installations, and determining their interaction, results in large data sets. In order to obtain the usual duration curves, a method for reduction of the large input data sets is developed, based on a data clustering technique. In addition, a fast and efficient method of finding the set of extreme points for the analysis of extreme operating

conditions is also presented. Finally, a Monte Carlo analysis (using a reduced data set) is presented, to determine the effects of deploying a large number of renewable DG systems on a distribution feeder.

The developed procedure is used to estimate the effects of varying the sizes of individual PV systems on local voltage conditions and electrical performance of the feeder in general. In addition, the potential for substation-level power factor improvement is demonstrated, if PV inverters are allowed as additional, flexible reactive power resource on the feeder.

The procedure is tested on a 69–segment distribution feeder with randomly placed photovoltaic generators totaling approximately 20% of feeder nominal load. The initial input data set of 28137 data points is reduced to a set of 200 cluster points and 94 boundary points, and the reduced set is successfully used for the Monte Carlo analysis. In this example, the addition of PV decreases the average active and reactive feeder losses between 12.7%–19.7% and 11.7%–18.3% respectively, depending on the PV distribution scheme and inverter configuration. Furthermore, the feeder active power consumption decreases by approximately 8.5%, while the reactive consumption decreases by almost 40%, if the inverters are allowed to inject maximum reactive power allowed by their rating. Consequently, the substation–level power factor in this case is significantly improved – its average value increases to 0.9619 from the value of 0.9280 for the case without PV.

Although the average values do not depend noticeably on the PV distribution scheme (i.e. on the size of each individual PV system), their ranges increase as the size of the individual system increases. For example, for a particular inverter configuration (maximum Q injection), if the size of each individual PV system is fixed at 2 kW, active losses may decrease between 17%–22%, compared to the case without PV. The range increases to 9%–28% if the size of each individual PV system is 40 kW. The average decrease in both cases is 20%.

The proposed algorithms serve as a bridge to incorporate the uncertainties imposed by intermittent, stochastic DG into the conventional tools for analysis of distribution systems.

With smaller data sets, larger number of studies can be performed in comparable time, thus providing more answers to the designer of DG-enhanced networks. Possible applications of the proposed method include studies for DG placement, feeder expansion, Volt/VAR support design, conservation voltage reduction design and reliability studies.

CHAPTER 5

OPTIMIZATION OF RELIABILITY OF RADIAL FEEDERS

5.1 Introduction

The issue of improving customer satisfaction by improving the reliability of service has been a longtime concern of the utilities. The task at hand is to optimally utilize the available technology and limited financial resources to minimize the number, duration and cost of outages.

The primary tool used in this task is a device called the automatic circuit recloser. Since the large majority of faults are of the transient nature, the application of reclosers provides a degree of safety by preventing transient faults from creating permanent outages. A recloser detects a fault and then opens for a preprogrammed time before closing automatically. This automatic close is referred to as an auto-reclose. Multiple open and close operations can be programmed to provide an intelligent procedure in clearing transient faults. If the fault is permanent, the recloser will eventually open and will not attempt to close until instructed to do so by an operator. This state is referred to as a recloser lockout. Reclosers may be either single-phase or three-phase devices; a three-phase recloser opens all three phases in case of a fault.

Other commonly used protection elements include fuses, breakers, sectionalizers and switches. Fuses are single-phase devices, typically placed at feeder laterals that interrupt the flow of fault current after a predetermined time delay. In a fuse burning strategy, a fuse clears a fault before the upstream recloser operates. This approach allows the minimal

number of customers per fault to be disconnected, but may increase the number of faults, as many of the faults are temporary, and could have been avoided if recloser operated first. This strategy is therefore usually implemented only in rural areas. The fuse saving strategy, on the other hand, allows the recloser to operate before the fuse. This strategy disconnects more customers in the case of a permanent fault, but also reduces the number of faults by preventing downstream fuses from blowing in the case of a momentary outage.

Breakers may also be single-phase or three-phase devices, often with reclosing capability. Switches may be normally open or closed, and are used to provide a loop feeder structure that may increase reliability or decrease feeder losses. A normally open switch is often placed on a tie line between two radial feeders. After the fault is cleared, a normally open switch closes to restore service to the customers on a faulted feeder downstream from the fault. Sectionalizers are used to sectionalize the feeder in order to minimize the number of customers affected by the fault, once the flow of the fault current has been interrupted.

The cost of various types of protection devices varies widely, from hundreds of dollars for fuses, up to the tens of thousands of dollars for solid state three phase reclosers. A cost/benefit analysis determines the number and type of the devices that would yield the best reliability characteristics of a given feeder.

In this chapter, the methodologies used to improve the reliability of radial distribution feeders are reviewed. The reliability improvements are demonstrated for three typical distribution feeder layouts. An economic analysis that takes into the account uncertainties in devices' costs is also performed.

5.2 Radial feeder without DG: Design issues

In a conventional radial feeder, reclosers are only expected to detect the unidirectional flow of current. Typically, a recloser upstream from the fault location detects the fault current, trips, and goes into a predefined reclosing sequence in order to restore service, if the fault

is of a temporary nature. If more reclosers are present on the radial feeder, they are time-coordinated, usually using Inverse Definite Minimum Time (IDMT) curves [44]. IDMT allows for the recloser operating time to be inversely proportional to the magnitude of the fault current, forcing the recloser closest to the fault to operate first and clear the fault.

The placement of protection devices in a conventional (radial) feeder is designed to maximize network reliability, and therefore minimize the traditional reliability indices assuming that the energy source is located only at the substation. Typically, utilities use standardized indices such as $SAIFI$ and $SAIDI$, which measure the average accumulated duration and frequency of sustained interruptions per customer [45, 46]. The system average interruption frequency index (SAIFI) and the system average interruption duration index (SAIDI) are defined as follows:

$$SAIFI = \frac{\sum N_i}{N_T} \tag{41}$$

$$SAIDI = \frac{\sum r_i \cdot N_i}{N_T} \tag{42}$$

where N_i is the number of interrupted customers for each interruption event, N_T total number of customers, and r_i is the restoration time for each interruption event. Customer average interruption duration index (CAIDI) is defined as the average time required to restore service to the average customer per sustained interruption:

$$CAIDI = \frac{\sum r_i \cdot N_i}{\sum N_i} = \frac{SAIDI}{SAIFI} \tag{43}$$

The average service availability index (ASAI), represents the fraction of time that a customer has power provided during one year (or other defined reporting period). Assuming one year period (8760 hours), it is calculated via:

$$ASAI = \frac{8760 - SAIDI}{8760} \tag{44}$$

As the importance of temporary faults increases, more utilities are starting to track them using the $MAIFIe$ index, which measures the number of momentary interruptions per customer. The momentary average interruption event frequency index (MAIFIe) is defined

as

$$MAIFIe = \frac{\sum ID_i N_i}{N_T} \tag{45}$$

where ID_i is the number of interrupting device operations.

The recloser placement can be optimized with respect to any of these, or some other, indices. To include the effects of both sustained and momentary interruptions, a composite index may be used, as defined below

$$C = W_1 \frac{SAIFI - SAIFI_T}{SAIFI_T} + W_2 \frac{SAIDI - SAIDI_T}{SAIDI_T} + W_3 \frac{MAIFIe - MAIFIe_T}{MAIFIe_T} \tag{46}$$

where W_1, W_2 and W_3 are weights for indices SAIFI, SAIDI, and MAIFIe, respectively, and the subscript T indicates the target value.

Conventional wisdom suggests placing a recloser at the half-way point of the radial feeder, assuming uniformly distributed load. This would yield a 50% reliability improvement to customers upstream from the recloser. Similarly, locations at 1/3 and 2/3 of feeder length should be considered if two reclosers are to be placed. In real life situations, which include the presence of critical loads and non-uniform load distributions, utilities often resort to engineering judgment to place reclosers according to the reliability guidelines. A typical flowchart showing the steps required for recloser positioning is shown in Figure 60 [47].

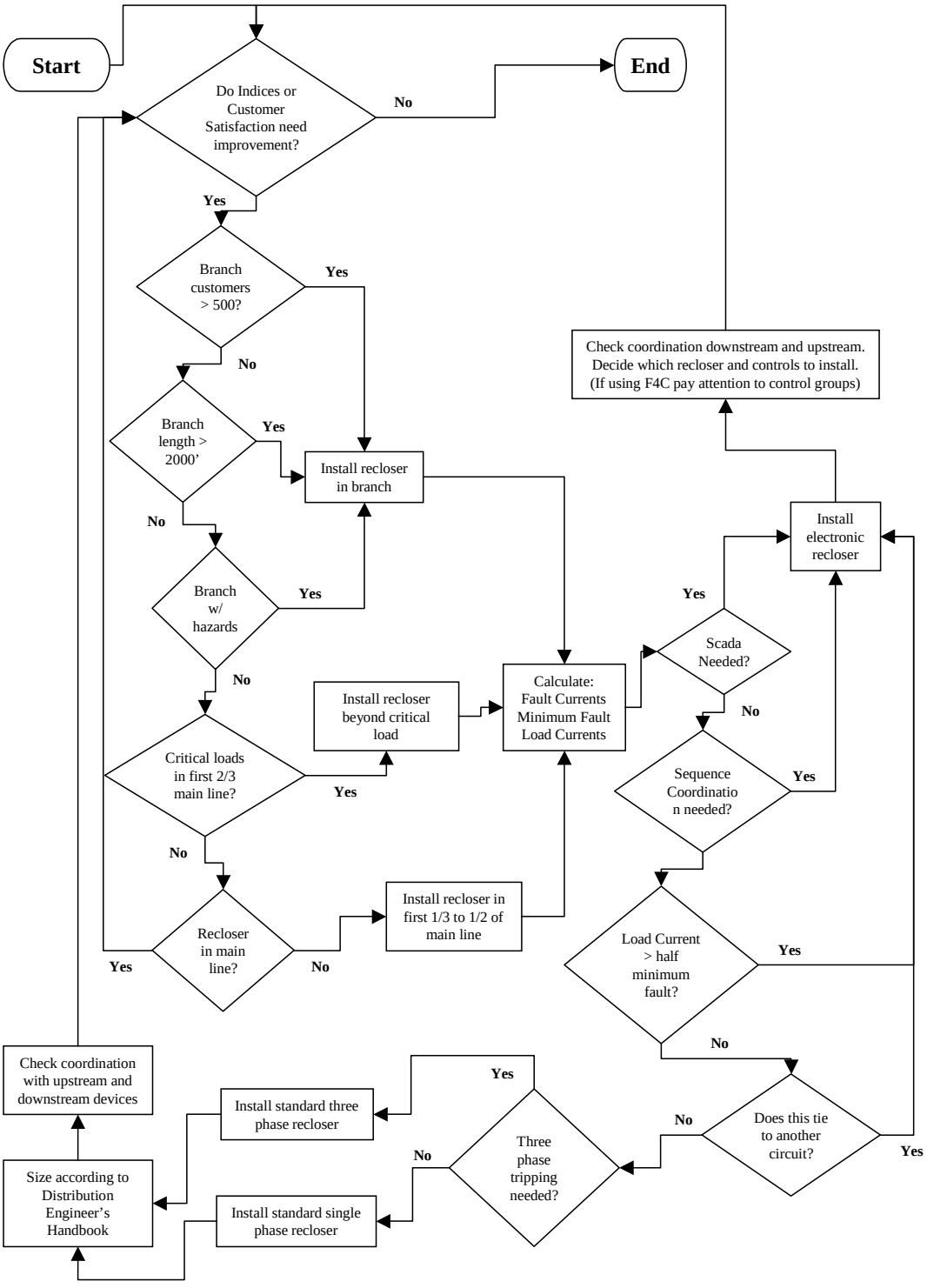

Figure 60: A block diagram indicating various considerations that should be taken into account during the process of designing a feeder protection of acceptable reliability [47].

5.3 Optimal recloser positioning for improved reliability of radial feeders

The impact of various recloser (and fuse) configurations is assessed on three common types of distribution feeders:

- *urban*, characterized by a high customer density and relatively small length,
- *suburban*, having longer length and smaller customer density, and
- *rural*, with a very widespread configuration and a low and uneven customer density.

The topology diagrams of three urban, suburban, and rural feeders used as examples in numerical calculations are shown in Figures 61–64. Figures 61–64 also show the number of customers per bus (and the load power demands) and branch lengths. The additional data necessary to replicate the simulations are given in Appendix B.

For all three feeder layouts, we investigate the following possible recloser placement strategies and compare them to the base case with only a substation breaker installed at the substation:

1. Addition of only one recloser on the main branch.
2. Addition of one recloser on the main branch, and a fuse on each lateral.
3. Addition of two reclosers on the main branch.
4. Addition of two reclosers on the main branch, and a fuse on each lateral.
5. Addition of one recloser on the main branch, and a recloser on each lateral.

The optimal recloser positions are determined with respect to the composite index C, defined in (46), and calculated using the default weights (0.2, 0.4, 0.4) and targets (1, 2.2, 7) for SAIFI, SAIDI and MAIFIe respectively. Note that these target values indicate a satisfactory level of reliability for a conventional feeder, and may be exceeded in a DG-enhanced feeder, yielding negative values for the composite index C. Optimal recloser locations for each scenario are determined using the Distrely Lite reliability analysis program, developed by Cooper Power Systems.

Tables 15-17 summarize the best reliability indices obtained for each of the configurations investigated. The substation breaker with reclosing capability is present in all

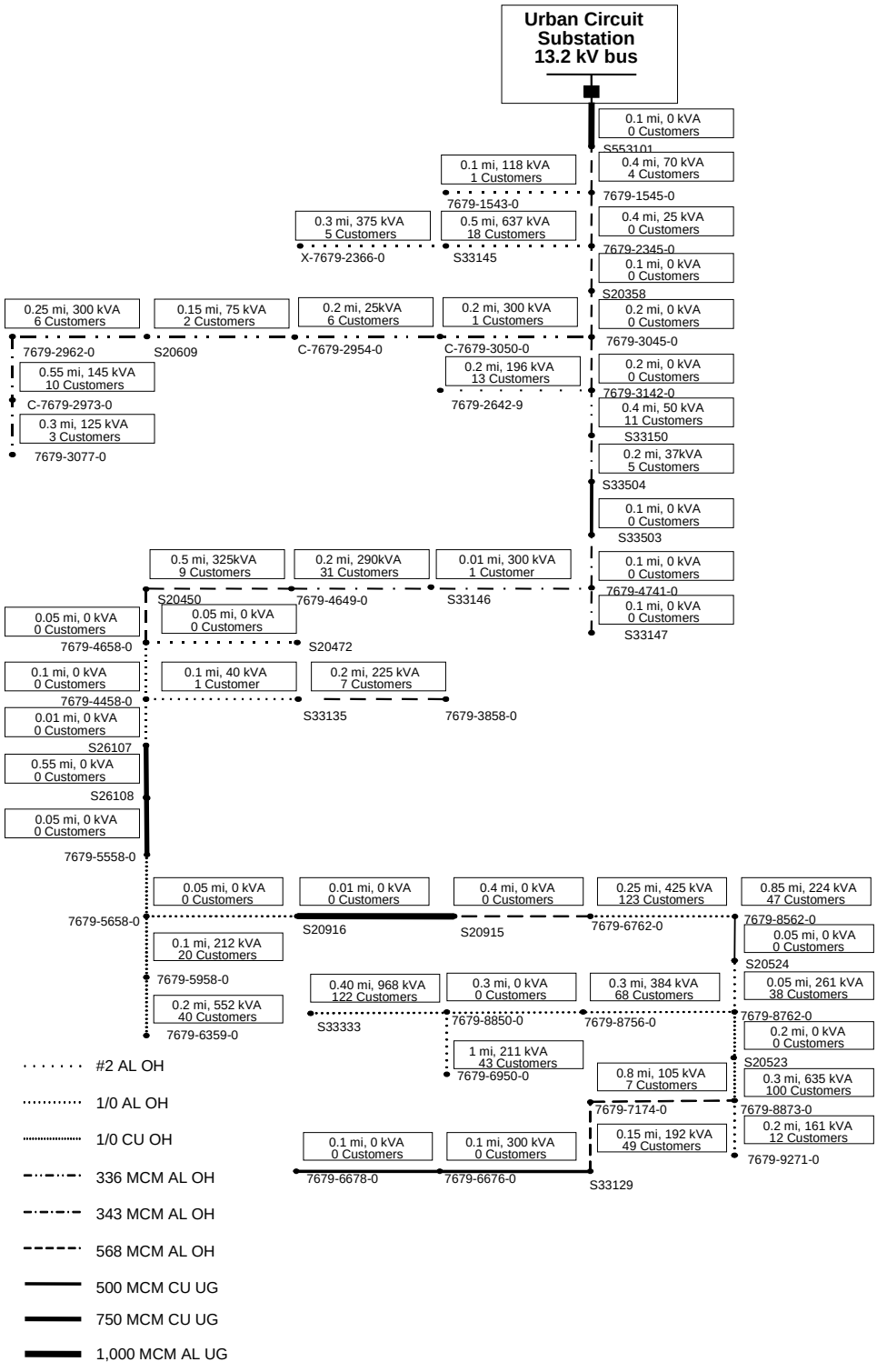

Figure 61: The topology diagram of the urban feeder.

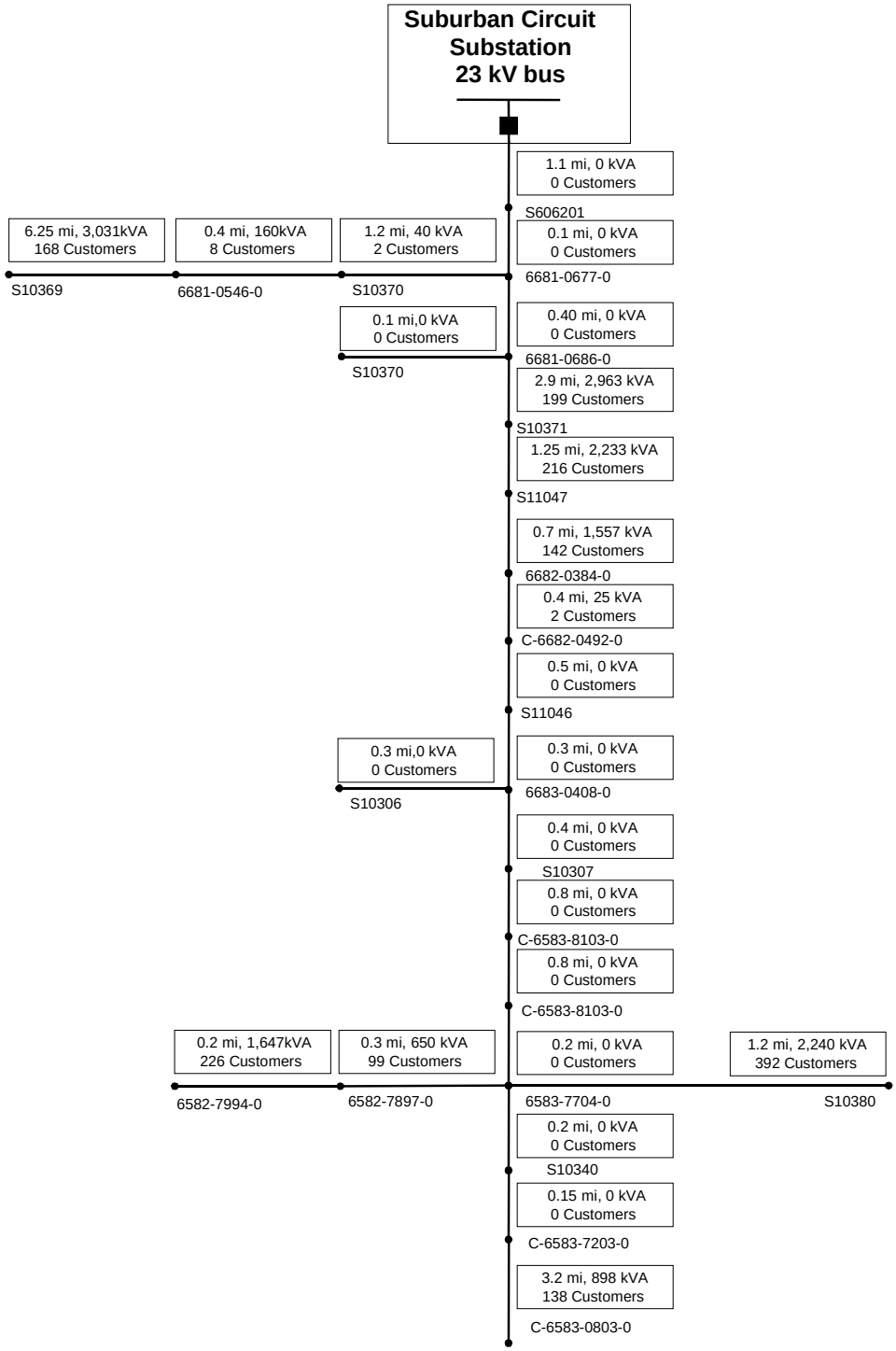

Figure 62: The topology diagram of the suburban feeder.

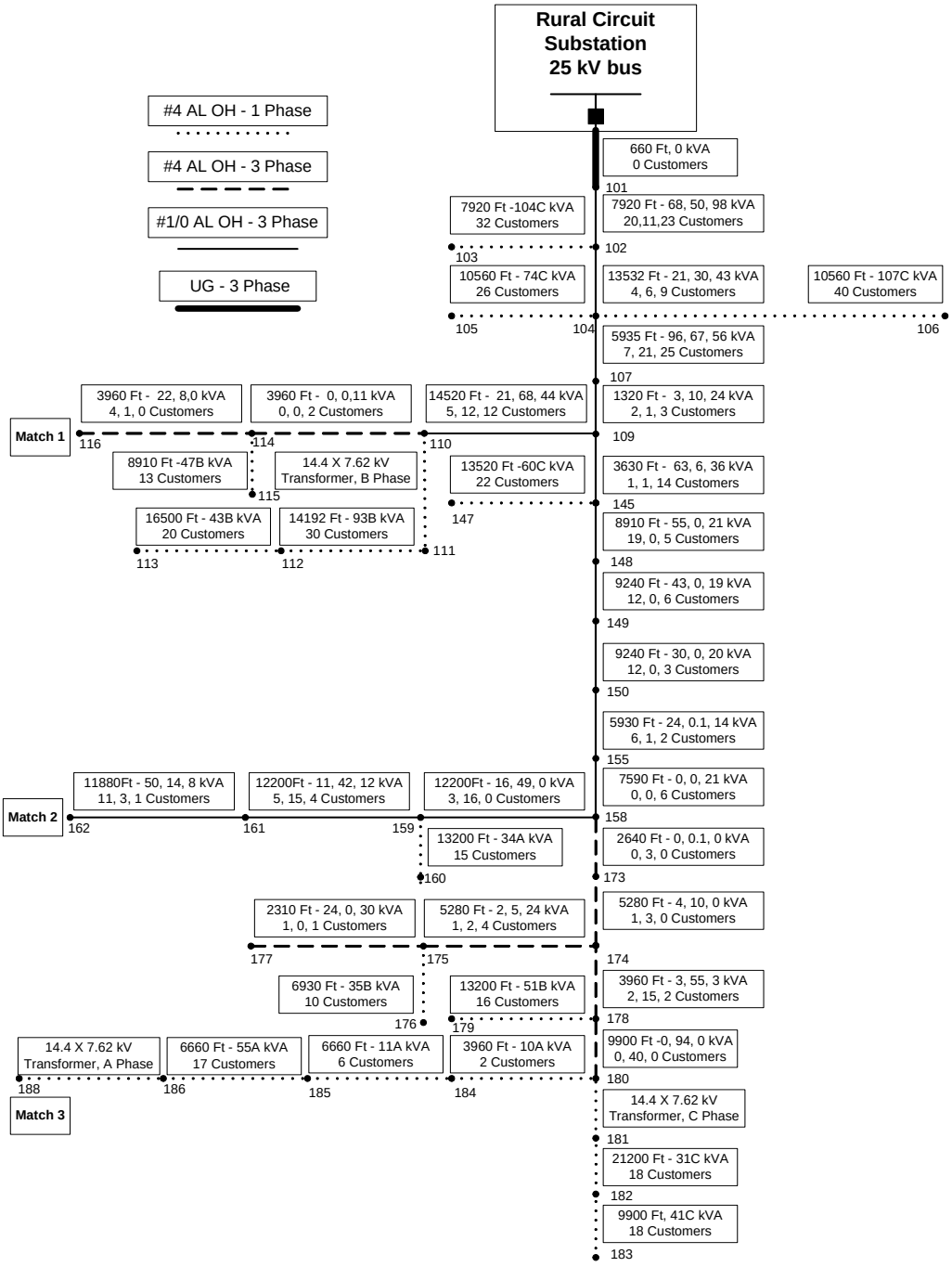

Figure 63: The topology diagram of the rural feeder (continued in Figure 64).

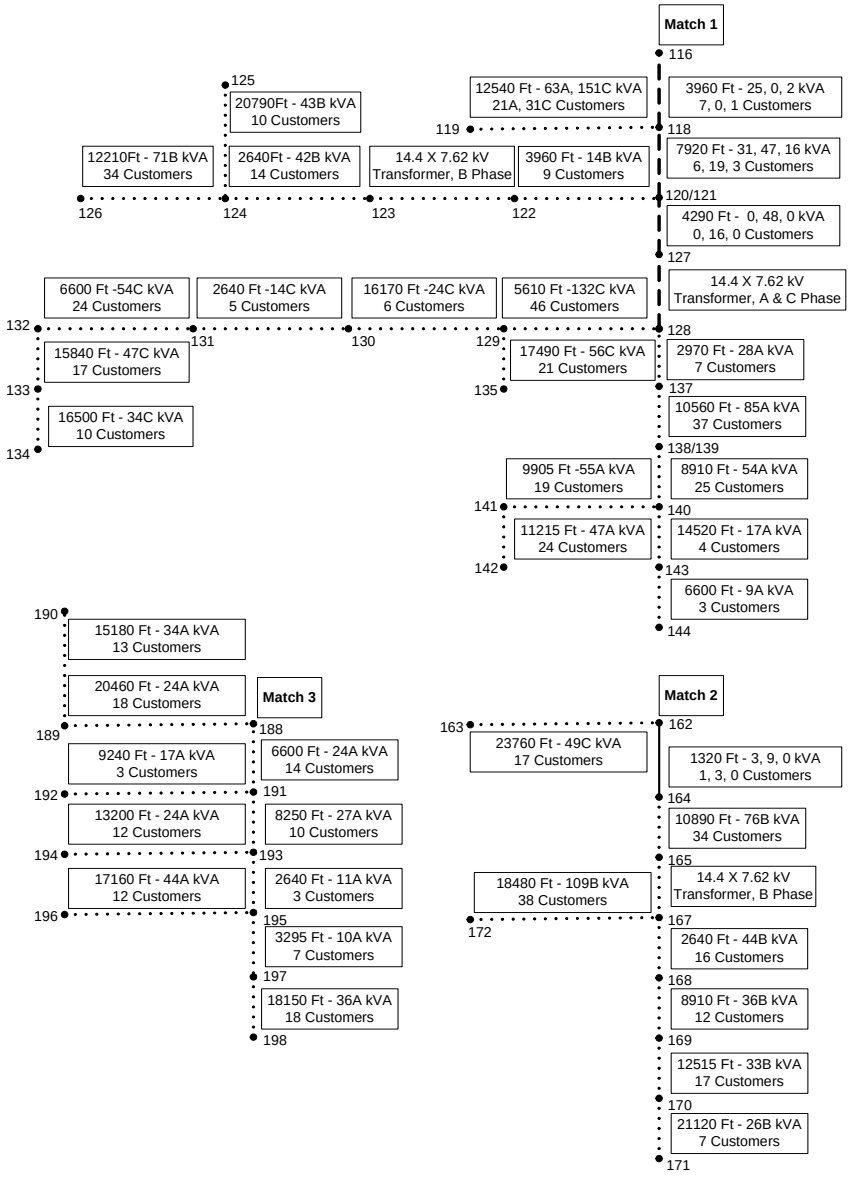

Figure 64: The topology diagram of the rural feeder (continued from Figure 63).

configurations, and a fuse burning scheme is implemented. Note the significant improvement obtained by the use of protection devices. More detailed results for all three feeder types are presented in Appendix B.

Table 15: The best reliability indices obtained for various recloser placement schemes (rural radial feeder).

Protection scheme	Comp	SAIFI	SAIDI	MAIFIe	CAIDI
Base case (only subst. breaker)	8.145	9.389	28.165	37.554	3.000
1 recloser, no lateral elements	5.227	6.393	19.180	25.573	3.000
1 recloser, lateral fuses	2.586	4.510	12.460	7.323	2.762
2 reclosers, no lateral elements	3.388	4.505	13.515	18.020	3.000
2 reclosers, lateral fuses	2.323	4.070	11.359	7.764	2.791
1 recloser, lateral reclosers	1.795	2.870	8.609	11.479	3.000

Table 16: The best reliability indices obtained for various recloser placement schemes (suburban radial feeder).

Protection scheme	Comp	SAIFI	SAIDI	MAIFIe	CAIDI
Base case (only subst. breaker)	3.230	4.343	13.028	17.371	3.000
1 recloser, no lateral elements	1.785	2.860	8.579	11.438	3.000
1 recloser, lateral fuses	0.474	1.617	4.718	5.131	2.917
2 reclosers, no lateral elements	0.876	1.926	5.779	7.705	3.000
2 reclosers, lateral fuses	0.445	1.483	4.450	5.934	3.000
1 recloser, lateral reclosers	0.334	1.473	4.286	4.554	2.909

Table 17: The best reliability indices obtained for various recloser placement schemes (urban radial feeder).

Protection scheme	Comp	SAIFI	SAIDI	MAIFIe	CAIDI
Base case (only subst. breaker)	0.630	1.674	5.021	6.695	3.000
1 recloser, no lateral elements	0.387	1.424	4.271	5.695	3.000
1 recloser, lateral fuses	-0.140	0.934	2.736	3.078	2.930
2 reclosers, no lateral elements	0.182	1.213	3.640	4.854	3.000
2 reclosers, lateral fuses	-0.155	0.868	2.604	3.472	3.000
1 recloser, lateral reclosers	-0.189	0.884	2.586	2.878	2.926

5.4 Sensitivity analysis

The following parameters may significantly influence the reliability of a distribution feeder.

- The *damage restoration time* (DRT) is the average restoration time for permanent faults, in hours. Typical values for DRT are three to six hours. DRT may be given either on a per-feeder or per-branch basis, depending on the accuracy of the study.
- The *manual restoration time* (MRT) is the average restoration time when there is no damage to repair, for example when a temporary fault causes a fuse to blow. MRT is always less than DRT – typical values for MRT are 0.5 to three hours. It can also be given on a per-feeder or per-branch basis.
- The *fault incidence rate* (FIR) is the expected number of faults in each phase per mile per year, including both temporary and sustained outages. It may depend on the type of the conductor, terrain configuration, line maintenance (vegetation control), etc.
- *Fraction of permanent faults* (FPF), expressed as a number between 0 and 1, represents the percentage of permanent interruptions, with typical values around 0.2.
- *Percent protected* (PP) measures the effectiveness of the fuse saving strategy, showing the percentage of times when the reclosers operate first, saving the fuses from burning. Typical values are 75%–80% when the coordination is very good, 30% when the coordination is not as good, and 0% when the fuse burning strategy is used.

A sensitivity analysis may be performed to demonstrate the influence of these feeder parameters on reliability indices. Sensitivity of the reliability index I to the parameter k at a point x is calculated using the following formula (subscript base denotes base case).

$$S_I^k(x) = \frac{\frac{I(x)}{I_{base}} - 1}{\frac{x}{x_{base}} - 1} \tag{47}$$

As seen in Section 5.3, the addition of more protection devices leads to the improved overall feeder reliability. However, those improvements may come at a significant cost.

The utility may be able to reach its reliability goals by influencing some of the parameters defined above (DRT, MRT, FIR, FPF and PP), and the sensitivity analysis may point to the best possible ways to do so. As an example, a suburban feeder with a (reclosing) substation breaker is considered. The recloser is placed at the optimal position along the main feeder, with respect to the composite index. Fuses are present at each of the feeder laterals, and a fuse burning scheme is implemented. The sensitivities of reliability indices with respect to the aforementioned feeder parameters are presented in Tables 18–22. The similar analysis for the rural and urban feeder designs may be found in Appendix B.

Table 18 shows how the change in the damage restoration time (DRT) influences SAIDI and CAIDI but not SAIFI and MAIFIe, as it only changes the time needed for fault repair, not the number of faults. The reduction in DRT by only 15 minutes (from 3 h to 2.75 h) leads to the significant improvement in overall reliability, as composite index C drops from 0.474 to 0.413 (13% improvement). The similar behavior is observed with the changes in the manual restoration time (MRT), naturally with smaller reliability improvement (Table 19). The fault incidence rate (FIR) influences SAIFI and MAIFIe, since it changes both the number of permanent and momentary interruptions (Table 20). Naturally, SAIDI increases since the number of faults increases, but CAIDI remains unchanged as the fault restoration time remains unchanged. As the frequency of permanent faults (FPF) increases, SAIFI increases while MAIFIe decreases (Table 21). Additionally, SAIDI increases as the number of faults increases, and CAIDI also increases as more time is needed to restore additional permanent faults. For example, increasing FPF from 0.15 to 0.20 increases SAIFI from 1.297 to 1.617, but decreases MAIFIe from 5.451 to 5.131, as customers experience increased number of permanent outages. A higher percentage of protected fuses in the fuse saving scheme decreases SAIFI and increases MAIFIe, as fewer permanent and more temporary faults are observed due to better coordination between fuses and reclosers (Table 22). SAIDI decreases as less permanent faults are observed, while CAIDI also slightly increases as more customers are taken offline when a recloser operates instead of a fuse.

Table 18: Sensitivity of reliability indices to the damage restoration time (suburban feeder).

DRT [h]	SAIFI		SAIDI		MAIFIe		CAIDI		ASAI		Composite	
	Value	Sens.	Value	Sens.	Value	Sens.	Value	Sens.	Value	Sens.	Value	Sens.
2.75	1.617	0	4.381	0.86	5.131	0	2.709	0.86	99.950	0.00	0.413	1.54
3.00	1.617		4.718		5.131		2.917		99.946		0.474	
3.25	1.617	0	5.055	0.86	5.131	0	3.126	0.86	99.942	0.00	0.536	1.57

Table 19: Sensitivity of reliability indices to the manual restoration time (suburban feeder).

MRT [h]	SAIFI		SAIDI		MAIFIe		CAIDI		ASAI		Composite	
	Value	Sens.	Value	Sens.	Value	Sens.	Value	Sens.	Value	Sens.	Value	Sens.
2.25	1.617	0	4.651	0.14	5.131	0	2.876	0.14	99.947	0.00	0.462	0.25
2.50	1.617		4.718		5.131		2.917		99.946		0.474	
2.75	1.617	0	4.751	0.07	5.131	0	2.938	0.07	99.946	0.00	0.480	0.13

Table 20: Sensitivity of reliability indices to the fault incidence rate (suburban feeder).

FIR	SAIFI		SAIDI		MAIFIe		CAIDI		ASAI		Composite	
	Value	Sens.	Value	Sens.	Value	Sens.	Value	Sens.	Value	Sens.	Value	Sens.
0.17	1.250	1.00	3.646	1.00	3.965	1.00	2.917	0	99.958	0.00	0.139	3.11
0.22	1.617		4.718		5.131		2.917		99.946		0.474	
0.27	1.985	1.00	5.790	1.00	6.297	1.00	2.917	0	99.934	0.00	0.810	3.12

Table 21: Sensitivity of rel. indices to the fraction of permanent faults (suburban feeder).

FPF	SAIFI		SAIDI		MAIFIe		CAIDI		ASAI		Composite	
	Value	Sens.	Value	Sens.	Value	Sens.	Value	Sens.	Value	Sens.	Value	Sens.
0.15	1.297	0.79	3.748	0.82	5.451	-0.25	2.89	0.04	99.96	0.00	0.252	1.87
0.20	1.617		4.718		5.131		2.917		99.946		0.474	
0.25	1.938	0.79	5.688	0.82	4.81	-0.25	2.935	0.02	99.94	0.00	0.697	1.88

Table 22: Sensitivity of rel. indices to the percentage of fuses protected (suburban feeder).

PP	SAIFI		SAIDI		MAIFIe		CAIDI		ASAI		Composite	
	Value	Sens.	Value	Sens.	Value	Sens.	Value	Sens.	Value	Sens.	Value	Sens.
0%	1.617		4.718		5.131		2.917		99.946		0.474	
15%	1.577	-0.16	4.618	-0.14	12.72	9.86	2.928	0.03	99.95	0.00	0.882	5.74
30%	1.537	-0.16	4.517	-0.14	12.76	4.96	2.939	0.03	99.95	0.00	0.858	2.70

5.5 Economic sensitivity analysis

The analysis in Section 5.3 demonstrated the reliability improvements obtained by using additional feeder protection devices. Section 5.4 showed that other feeder parameters (DRT, MRT, etc.) may also influence feeder reliability. The improvements in reliability indices were demonstrated for all considered feeder designs (urban, suburban and rural). As expected, the overall reliability increases as more protection devices are placed on a feeder. However, protection devices' cost may vary widely, as for example, a three-phase recloser may be two orders of magnitude more expensive than a single-phase fuse. Therefore, an economic analysis is performed in this section to obtain the optimal configuration that yields the optimal cost/benefit ratio.

Typical costs for the protection devices are shown in Table 23.

Table 23: Assumed protection device relative costs.

Breaker	$30,000
Recloser (on main feeder)	$30,000
Recloser (lateral)	$6,000
Fuse	$300

According to these costs, the total cost for each of the considered configuration are calculated, and presented in Table 24. A substation breaker is present in all configurations. Seven lateral devices (fuses or reclosers) are included in the first two examples (urban and suburban feeder), while in the rural feeder there are nine lateral devices present in the appropriate configurations. The exact locations of lateral elements are given in Appendix B.

In order to obtain the configuration that would yield the best reliability improvement per dollar invested, the relative incremental investments needed to obtain the appropriate

Table 24: Total costs of all protection devices on a feeder for various protection schemes.

Protection scheme	Cost [$]		
	Suburban	Urban	Rural
Base case (only subst. breaker)	30,000	30,000	30,000
1 recloser, no lateral elements	60,000	60,000	60,000
1 recloser, lateral fuses	62,100	62,100	62,700
2 reclosers, no lateral elements	90,000	90,000	90,000
2 reclosers, lateral fuses	92,100	92,100	92,700
1 recloser, lateral reclosers	102,000	102,000	114,000

improvement in the reliability indices are calculated. This is done by calculating the sensitivities of the reliability indices to the increased costs incurred by adding more protection devices on the feeder. Note that the smaller values indicate higher sensitivity, and therefore better cost to benefit ratio. The elements in the following tables are obtained using the following formula:

$$S_i^c = \frac{\Delta C}{\Delta I} = \frac{C_k - C_{base}}{I_k - I_{base}} \tag{48}$$

where C_k indicates a cost for the $k-th$ configuration (from Table 24), I_k is the appropriate reliability index, and a subscript *base* indicates a base case with only a substation breaker present on a feeder.

The sensitivities of the four considered reliability indices (SAIFI, SAIDI, MAIFIe and the composite index) are presented in Tables 25–26. The results indicate that for these feeders, a configuration with a single recloser and lateral fuses would generate highest reliability improvement, per dollar invested. For example, this configuration in the case of a suburban feeder yields the sensitivity of SAIFI of $11,775 per interruption and customer (first column of Table 25), which is almost two times lower than the next value ($20229 if only one recloser is added).

These sensitivities are beneficial to utilities since they provide an insight into the amount of incremental investment needed to improve reliability indices. Since some of the utilities are regulated by the absolute number of outages (or outage time) allowed, it is important to also calculate those sensitivities. They can be obtained by dividing the sensitivities in

Tables 25–26 by the total number of customers at the respective feeder, and are shown in Table 27.

Table 25: Sensitivities of indices SAIFI and SAIDI to the costs of protection schemes.

Protection scheme	Δ$ / ΔSAIFI [$ / (int. / customer)]			Δ$ / ΔSAIDI [$ / (h / customer)]		
	Urban	Suburban	Rural	Urban	Suburban	Rural
1 recloser, no lateral elements	20229	120000	10013	6743	40000	3339
1 recloser, lateral fuses	11775	43378	6702	3863	14048	2082
2 reclosers, no lateral elements	24824	130152	12285	8277	43447	4096
2 reclosers, lateral fuses	21713	77047	11788	7239	25693	3731
1 recloser, lateral reclosers	25087	91139	12885	8236	29569	4295

Table 26: Sensitivities of MAIFIe and composite index to the costs of protection schemes.

Protection scheme	Δ$ / ΔMAIFIe [$ / (mom. int. / customer)]			Δ$ / Δ COMPOSITE		
	Urban	Suburban	Rural	Urban	Suburban	Rural
1 recloser, no lateral elements	5056	30000	2504	20761	123457	10281
1 recloser, lateral fuses	2623	8875	1082	11647	41688	5882
2 reclosers, no lateral elements	6207	32591	3072	25489	133929	12613
2 reclosers, lateral fuses	5430	19268	2105	22298	79108	10769
1 recloser, lateral reclosers	5618	18863	3221	24862	87912	13228

Table 27: Sensitivities of the number of sustained interruptions, outage time and momentary interruptions to the costs of protection schemes.

Protection scheme	Δ$ / Δ interruptions			Δ$ / Δh			Δ$ / Δ mom. int.		
	Urban	Suburb.	Rural	Urban	Suburb.	Rural	Urban	Suburb.	Rural
1 recloser, no lateral elements	3.763	49.813	7.314	1.254	16.604	2.439	1.254	16.604	2.439
1 recloser, lateral fuses	2.190	18.007	4.896	0.719	5.832	1.521	0.719	5.832	1.521
2 reclosers, no lateral elements	4.618	54.027	8.974	1.540	18.035	2.992	1.540	18.035	2.992
2 reclosers, lateral fuses	4.039	31.983	8.611	1.347	10.665	2.725	1.347	10.665	2.725
1 recloser, lateral reclosers	4.667	37.833	9.412	1.532	12.274	3.138	1.532	12.274	3.138

5.6 Treatment of uncertainty through Monte Carlo simulations

The costs associated with the protection devices may vary widely, and these variations could be addressed during the design process. By treating all costs as random variables, the statistics for the costs associated with all configurations may be determined. As a motivational example, only the analysis for the configuration with a single recloser and lateral fuses, deemed most promising in the previous section, will be presented.

The essence of the probabilistic procedure is the following:

Step 1. Assume a feeder protection configuration that will be considered. Account for all expenditures as variables (costs of fuses, various types of reclosers, etc.)

Step 2. Assume that the exact prices of the devices are not known, but their probabilistic distributions are. That translates into saying that the price of the fuse is equally probable to be, for example, between $270 and $330 (a 10% uncertainty) instead of claiming the price to be an exact $300.

Step 3. A random number (random cost) generator is used to determine the large sequence of costs (many random numbers) representing costs for every needed device, which complies with the assumed statistics (i.e. uniform distribution of the costs).

Step 4. Since random cost numbers for every device are generated, many combinations of costs may be created by taking one random number (cost) for every device, and summing the costs to obtain the total expenditure. For every such combination of random costs, a separate cost calculation is performed. This procedure is called a Monte Carlo analysis.

Step 5. For every cost calculation, the sensitivity analysis is performed, and the improvement in reliability indices is calculated. The result of the analysis is a sequence of reliability indices equal in length to the sequence of random costs that was generated for every device.

Step 6. The statistics, including the mean, variance and probability density of the sequence of reliability indices is calculated, which yield the impact of price uncertainty on the value of reliability indices.

The final outcome of the analysis is in the form of a statement that a given configuration of feeder protection devices, whose costs are *x* percent uncertain, will provide an improvement in reliability index equal to *y* with probability equal to *z* percent. This assessment of reliability improvement provides additional flexibility in ascertaining the true impact of different system configurations.

As an example to illustrate the proposed procedure, it is assumed that all costs are uniformly distributed, with the distribution boundaries set at ±10% from the values presented in Table 23. The histogram of the obtained configuration costs, over 100,000 Monte Carlo simulations is shown in Figure 65. The assumed probability of the cost is the largest at $62,102, and drops to zero at $56,086 and $68,228 (triangular distribution). Note that the mean value coincides with the value calculated using only mean values for devices' costs, as reported in Table 24.

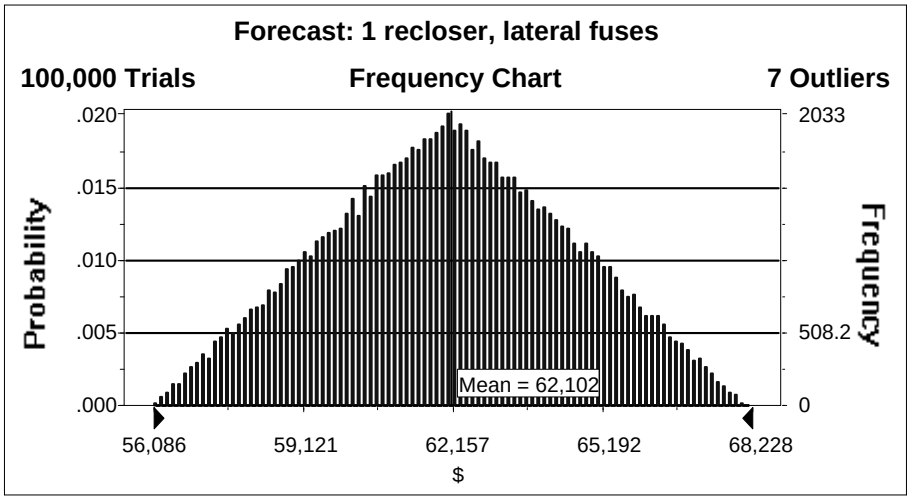

Figure 65: Distribution of the cost for a single-recloser, lateral-fuses scheme (over 100,000 Monte Carlo simulations).

The reliability sensitivities, calculated in Step 5, are now also random variables. Their distributions are also presented below. Note that the mean values match the values obtained using only the mean values for equipment costs. The obtained distributions indicate the magnitude of uncertainty in the calculated reliability sensitivities with respect to the somewhat uncertain cost of the improvements.

Figure 66 shows that under the assumed cost uncertainties, the proposed scheme would require, on average, $11,778 per unit of SAIFI, but the cost will be uniformly probable to be anywhere between $10,654 per unit of SAIFI and $12,908 per unit of SAIFI. The interpretation of Figures 67–69 is analogous to this one.

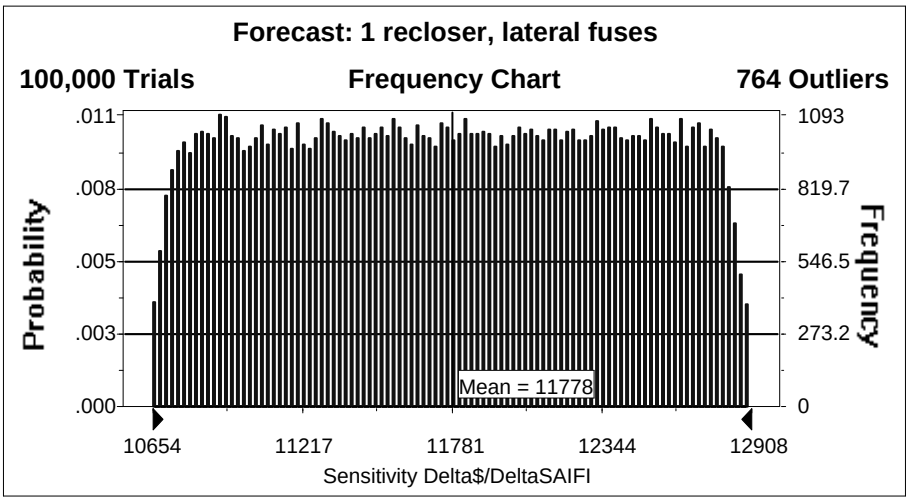

Figure 66: The calculated distribution of the sensitivity $\Delta\$/\Delta SAIFI$.

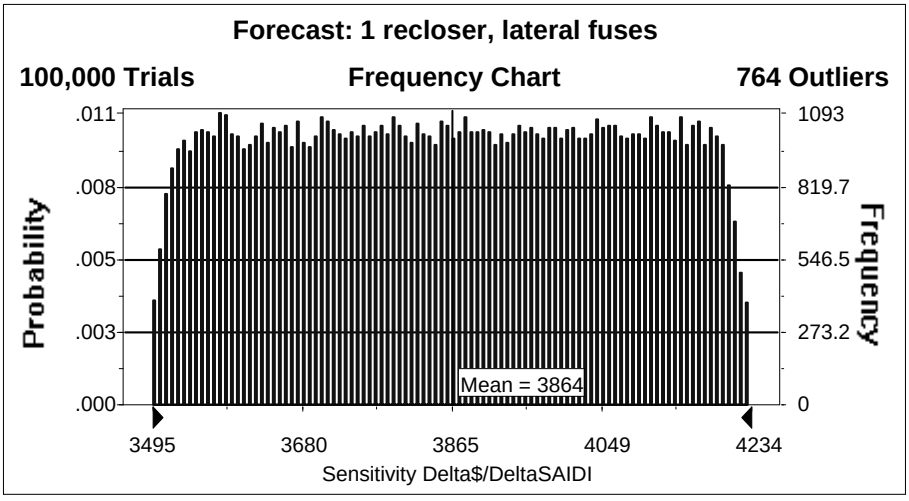

Figure 67: The calculated distribution of the sensitivity $\Delta\$/\Delta SAIDI$.

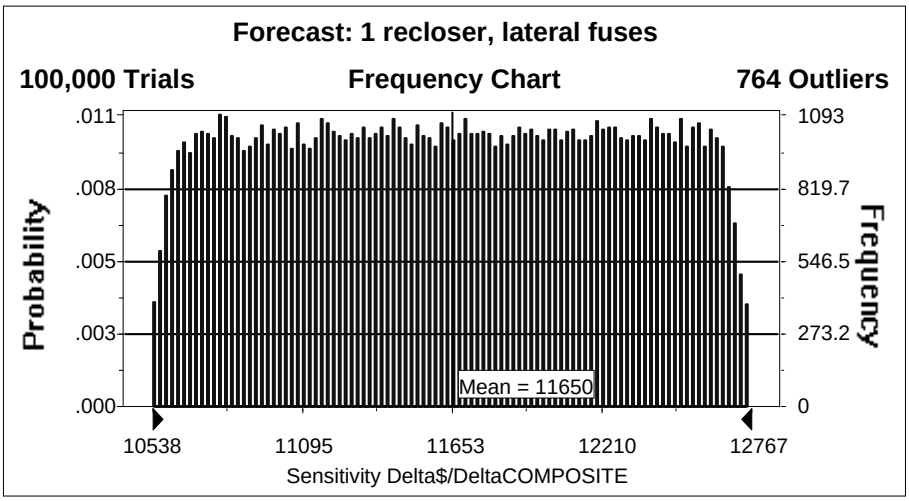

Figure 68: The calculated distribution of the sensitivity $\Delta\$/\Delta COMPOSITE$.

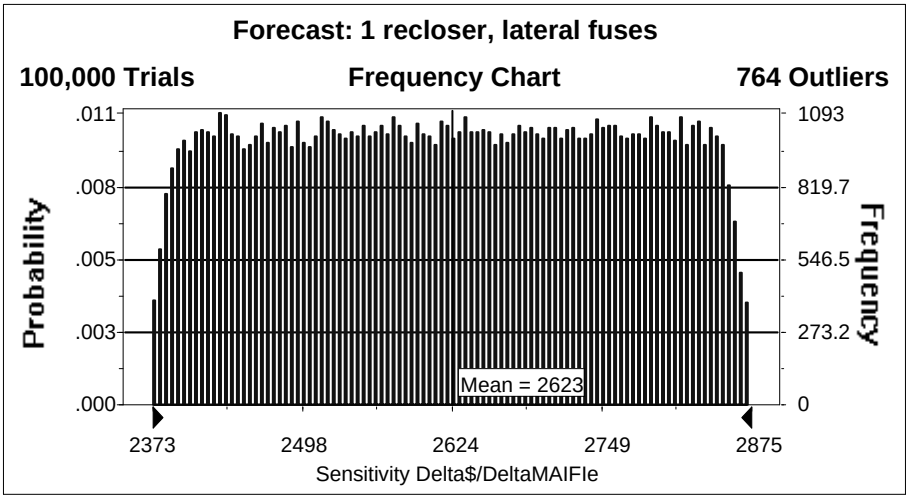

Figure 69: The calculated distribution of the sensitivity $\Delta\$/\Delta MAIFIe$.

5.7 Conclusions

The issue of improving the reliability of electric service for conventional, radial distribution feeders is addressed in this chapter. The ways to improve the reliability through adequate use of protection devices, including reclosers and fuses, is presented.

Incremental improvements can be achieved by adding more protection devices in the feeder, allowing it to be sectionalized into smaller zones in order to affect the smallest number of customers by isolating the fault. This is demonstrated for three feeder designs obtained from the utility (rural, suburban and urban). A sensitivity analysis is performed to determine the impact of damage and manual restoration times, fault incidence rates, fraction of permanent faults and fuse protection strategies on the overall level of reliability.

As the cost of protection devices may vary widely, an economic analysis is also developed to determine the optimal configuration of protection devices that yields the maximum cost to benefit ratio. For all three test feeders, a configuration with a single recloser and lateral fuses yields the highest reliability improvement, per dollar invested. Finally, the modeling uncertainties are incorporated in the forecasted cost of devices, by using a set of custom developed Monte Carlo simulations.

CHAPTER 6

NON-RADIAL, DG-ENHANCED FEEDER DESIGN

6.1 Introduction

The analysis in the previous chapter presented a protection strategy for a radial distribution feeder, without consideration for DG. This chapter addresses the effects caused by the addition of DG constrained in terms of power and/or energy capacity on a non-radial distribution feeder.

As presented in Section 5, overcurrent relays are only expected to detect the unidirectional flow of current in a conventional radial feeder. In a loop (non-radial) DG-enhanced feeder, power flow is not unidirectional, and conventional protection logic must be altered for the fault-detecting devices to successfully perform their function [48]. A faulted branch may be energized from both sides and several protection devices may need to operate in order to completely interrupt the fault current. Various control strategies, using only local or SCADA measurements, may be utilized. Furthermore, distributed generation and storage units may reduce the impact of faults on customers within their protection zones by creating islands of supply, thus increasing the reliability of service. However, these units may be power and/or energy limited and may include renewable generators, whose output is dependent on the meteorological conditions, and may not be able to serve their local loads at all times.

Most reliability assessment tools utilize algorithms designed for radial networks, which may only determine benefits of using DG as a backup source [49]. In this research, the

reliability algorithm designed for non-radial networks is presented and examined. It incorporates the impact of capacity constrained DG units into the calculation of reliability indices. The following related optimization tasks are investigated:

1. Optimize the placement of protection devices for a given DG allocation.
2. Optimize DG placement for a given allocation of protection devices.
3. Optimize both the placement of protection devices and DGs.

A genetic algorithm (GA) is presented here to solve all three problems. First, the results for the recloser placement problem are presented, assuming the DGs are already deployed on the feeder. The problem of optimal GA parameter tuning is then presented, and the algorithm is modified to adaptively change GA parameters, removing the need for the parameter tuning. The performance of both algorithms are then presented for several typical distribution feeders. Finally, the problem of simultaneous allocation of DGs and protection devices is presented.

6.2 Features of the developed reliability model

6.2.1 Network (loop) feeder configuration

The majority of existing distribution feeders are radial, meaning that the flow of power is always from the substation transformer downstream to the individual customers. This approach allows relatively simple coordination between protective devices and significant cost savings. The reliability modeling of such a feeder is therefore relatively easy. For a fault anywhere on the feeder, only one recloser operates – typically the one closest to the fault, to minimize the number of affected customers.

If on the other hand, a single or multiple loops are present on the feeder, the alternate current paths may be possible for a fault in different parts of the feeder. Depending on the location, a fault may be energized from both sides, and operation of more than one protection device is often necessary.

6.2.2 Islanded operation of DG-enhanced feeders

When distributed generators are present on the feeder, the number and duration of outages to some customers may be reduced. After the fault is isolated, generators in parts of the feeder not affected by the fault may be allowed to reconnect, allowing the portions of the feeder to operate as electric "islands". As an example, Figure 70 shows a radial feeder, equipped with a substation breaker and two reclosers. Assuming there is no DG at the end of the feeder, a fault anywhere on the line will lead to the opening of the first recloser upstream from the fault. For example, after a fault between reclosers 1 and 2, recloser 1 operates, leaving all customers downstream from it without service. If DG is present at the end of the feeder, recloser 2 may also operate, allowing the portion of the feeder downstream from recloser 2 to operate as an island as long as the power balance is achievable.

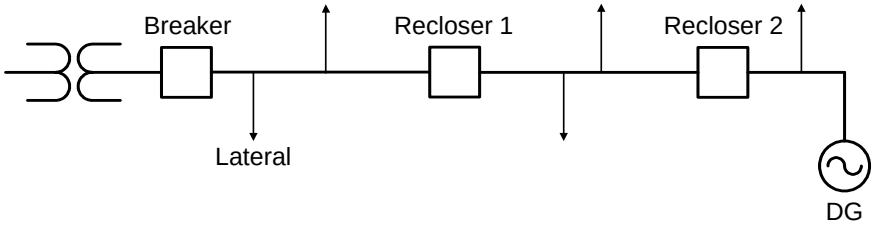

Figure 70: Strategically placed reclosers and DGs on a feeder may reduce the number of customers affected by a fault.

6.2.2.1 Current DG interconnection regulations

The interconnection of distributed resources (both generators and energy storage devices) with electric power systems is regulated by the IEEE 1547 standard [50]. The interconnection of *photovoltaic* DG systems connected through static (solid-state) inverters has been regulated by the IEEE 929 and UL 1741 technical standards [43, 51]. Several US states have adopted interconnection requirements based on these standards.

The IEEE 1547 establishes universally needed criteria and requirements for interconnection of distributed resources (DR) with the aggregate capacity not higher than 10 MVA, interconnected to the electric power systems at typical primary and/or secondary distribution voltages. IEEE 1547 includes requirements applicable to all DG technologies, including synchronous machines, induction machines and systems connected through power inverters.

The following definitions and acronyms, also shown in Figure 71, are used further in the text [50]:

- *Electric power system (EPS).* Facilities that deliver power to the load (including generation).
- *Area EPS.* An EPS that serves local EPSs.
- *Local EPS.* An EPS contained entirely within a single premise or group of premises.
- *Point of common coupling (PCC).* The point where a local EPS is connected to an area EPS.

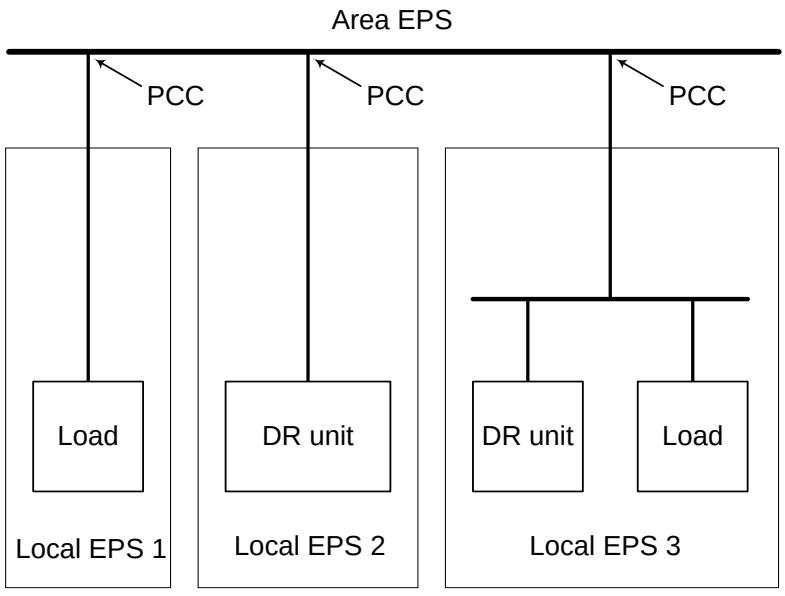

Figure 71: Relationship of interconnection terms [50].

Existing distribution systems were not designed to incorporate generation and storage devices. The complete protection and control strategy is designed under the assumption that the only source of electric power is the substation transformer, as explained in Chapter 5. The interconnection requirements are therefore designed to limit the possible negative effects that DG may have on the operation of existing devices. The following are the most important provisions of IEEE 1547 as they relate to the interoperation of distributed resources (DR) and the existing power system [50]:

- *Voltage regulation.* The distributed resource (DR) shall not actively regulate voltage at the point of common coupling (PCC). The DR shall not cause the area service voltage at other local EPSs to go outside the normal operating range.
- *Integration with area EPS grounding.* The grounding scheme of the DR interconnection shall not cause overvoltages that exceed the rating of the equipment connected to the area EPS and shall not disrupt the coordination of the ground fault protection of the area EPS.
- *Inadvertent energization of the area EPS.* The DR shall not energize the area EPS when the area EPS is de-energized.
- *Area EPS faults.* The DR unit shall cease to energize the area EPS for faults on the area EPS circuit to which it is connected.
- *Area EPS reclosing coordination.* The DR shall cease to energize the area EPS circuit to which it is connected prior to reclosure by the area EPS.
- *Reconnection to area EPS.* After an area EPS disturbance, no DR reconnection shall take place until the area EPS voltage is within acceptable voltage and frequency range. The DR interconnection system shall include an adjustable delay (or a fixed delay of five minutes) that may delay reconnection for up to five minutes after the area EPS steady-state voltage and frequency are restored to the ranges identified above.
- *Islanding.* For an unintentional island in which the DR energizes a portion of the

area EPS through the PCC, the DR interconnection system shall detect the island and cease to energize the area EPS within two seconds of the formation of the island. The topic of intentional islanding is under consideration for future revisions of the standard.

It is clear that the islanded operation of parts of the feeder is currently not allowed by the utilities – after a fault, DG has to disconnect and remain disconnected until the fault is cleared.

6.2.2.2 Intentional islanding

To be able to operate in the island mode, DGs have to be able to serve the island load, and therefore keep both the voltage and frequency within acceptable ranges. Although intentional islanding is very difficult to implement, it may significantly improve the level of reliability to some customers, and thus increase the overall feeder reliability. The subsequent work in this chapter quantifies the reliability benefits achieved by intentional islanding, which may be used to justify the necessary additional investments required to allow such operation.

The sequence of events after the fault, if islanding is not allowed, is:

1. DG is tripped, and fault detected and isolated by one or more protection devices.
2. After the fault is cleared, recloser reconnects the area to the rest of the feeder.
3. DG reconnects after normal operating voltage and frequency are established, with the appropriate time delay.

With this scheme, the DG remains offline throughout the duration of the fault. On the other hand, if DG operation can be synchronized with the operation of the existing feeder protection devices, DG may be able to remain online for the duration of the fault and reduce the number and/or duration of outages to some of the customers. Note however that the islanded operation requires significant coordination of distributed generators with feeder

protection devices, which is outside the scope of this work. The DG system generally relies on the utility to provide its phase reference, and a phase error between the island and utility voltages can develop while the part of the system (equipped with DG) is islanding. If the utility attempts to reclose on the out-of-phase section of the grid, large surge currents could damage the PV system and the local load.

If the islanded operation is allowed, the sequence of events after the fault should be as follows:

1. DG is tripped and the fault is detected and isolated by one or more protection devices.
2. DG reconnects, if it is not within the faulted zone.
3. After the fault is cleared, recloser synchronizes its reclosing operation with DG.

Typically, there will be a momentary interruption to the customers in the island, due to the need for the DG to disconnect after the fault in order not to interfere with the operation of protection devices. If however, reclosers are able to disconnect immediately, there may not be even a momentary interruption, and thus MAIFIe index may also be reduced.

The contribution to the fault current of a DG system connected to the utility using the solid-state inverter is typically negligible. Inverters have no "inertia" in their output and may respond immediately to the changes in the power system's operating conditions. The response time may be a fraction of the utility cycle due to the high frequency ($\geq$1 kHz) switching employed by such inverters. Instead of detecting abnormal conditions by detecting large transient currents, they generally sense a short circuit by detecting the change in voltage (either magnitude or frequency). Grid-connected inverters are in general required to be equipped with standard protective relays, namely over/undervoltage relays (OVR/UVR) and over/underfrequency relays (OFR/UFR), which disconnect from the utility system in the event that either the magnitude or frequency of the system's terminal voltage deviates beyond certain thresholds. These relays will detect islanding conditions in the majority of cases. However, if the load and DG output are sufficiently closely matched, and the load

resonant frequency lies sufficiently close to the nominal utility frequency, the changes in voltage magnitude and frequency when islanding begins will fall within the trip thresholds, and the OFR/UFR/OVR/UVR will not operate [52]. This situation is considered a very low-probability event, but as its consequences may be severe, an additional anti-islanding method is typically required. These methods typically use positive feedback from voltage and frequency to accelerate the drift of voltage or frequency outside of their operating ranges after a fault that causes the loss of utility power [50, 53, 54].

Therefore, the fault currents flowing through a particular recloser may not be large enough to trip it, and alternate methods for fault detection may be necessary. The following study assumes that these methods are available, and that for a fault anywhere on the feeder, the reclosers are coordinated in such a way that only the minimal number of neighboring reclosers operate and isolate the fault.

The positions of protection devices and distributed generators are strongly interdependent. Suboptimal recloser placement may lead to islands with not enough generation, and may not yield significant reliability benefits. On the other hand, by strategically placing reclosers, one may be able to significantly increase the reliability of service to customers in such islands.

The distributed generation and storage systems deployed on the feeder are limited in power and energy capacity, which also limits their reliability contributions.

Capacity constrained generators are able to supply the load up to their rated power as long as the fuel is supplied. If the power output of the generator is sufficient to supply the local island load, the number and duration of faults for those loads will decrease. Both the SAIFI and SAIDI indices will therefore be lower, compared to the base case without DG.

Energy limited generators (and storage systems) are able to sustain the load for a finite period. If a fault is cleared before the energy runs out, both SAIDI and SAIFI will be reduced. However, if the energy runs out before a fault is cleared, only SAIDI will be reduced.

Renewable distributed generators, such as photovoltaic and wind systems, create additional difficulties in quantifying their reliability benefits, due to the probabilistic nature of their input (sunshine, wind) and their power output. If an energy storage system is used in addition to renewable DG, the duration of time and the load that the storage system can support in an island may increase due to renewable DG generation. However, if renewable DGs with random energy input are the only distributed devices in an island, they may not be relied upon to support the local island load.

The developed reliability model is capable of treating all three types of generators and may be used to quantify their impact on standardized reliability indices.

6.2.3 Three phase analysis

The majority of power system studies are performed on a positive-sequence, balanced power system model. While this is adequate for the majority of transmission-level studies, a full three-phase model is generally necessary for the accurate reliability analysis of a distribution system. Unlike the highly balanced three-phase transmission system, a typical US distribution system has many sources of imbalance, such as [55]:

- Single phase loads, connected either line-to-neutral or line-to-line
- Single phase laterals
- Two-phase laterals
- Singe phase protection devices
- Various transformer connections
- Untransposed distribution lines
- Three-phase transformer banks made up of three single–phase transformers of unequal sizes
- Capacitor banks with blown fuses.

For the purpose of reliability studies, the first four sources of imbalance are the most significant. Due to the presence of single phase loads and protection devices, and single and two-phase laterals, the reliability indices must be calculated separately for each phase. The

developed reliability model is capable of modeling all four of the aforementioned scenarios. The necessary inputs for the model are:

- Number of customers per bus per phase
- Real power demand per bus per phase
- Real power generation per bus per phase
- Length of each line
- Type of each line (3-phase, or single-phase and which phase)
- Damage restoration time for each line
- Manual restoration time for each line
- Fault incidence rate for each line
- Fraction of permanent faults for each line

The damage restoration time, manual restoration time, fault incidence rate and the fraction of permanent faults have all been defined in Chapter 5.4. The values used in the subsequent studies are listed in Appendix B.

6.3 Calculating the composite reliability index of a DG-enhanced feeder

This section details the calculations of the composite reliability index (46), which will be later used as a cost function in the optimization algorithm. We assume that only the minimal number of reclosers operate per fault, isolating the smallest possible part of the feeder. The actual recloser control logic is outside the scope of this analysis.

The protection devices placed on the feeder effectively divide the feeder into so-called reliability zones. In a radial feeder, placement of N devices will result in the formation of $(N + 1)$ zones. If the feeder is not radial, the number of zones may decrease. For example, Figure 72 shows the formation of five reliability zones after the allocation of five reclosers on a non-radial distribution feeder.

For a fault anywhere within the zone, all customers within the zone will be disconnected, since there are no protection devices between them. Similarly, for a fault outside

the zone all customers may be either connected (if still connected to the substation, or if the zone operates as an island) or disconnected. Consequently, all customers within the same reliability zone experience the same number of outages and have the same reliability of service.

Note that in general, reliability zones for different phases do not coincide, as some of the protection devices may be single-phase reclosers or fuses not present in other phases. The procedure presented below is therefore repeated for each phase.

The reliability zones for all buses, branches and generators are determined using the algorithm below:

Step 1. Let R be the set of all branches, B set of all buses and G set of all generators in phase A. A generator is defined to be in phase A if it is a three-phase generator or a single-phase generator connected in phase A.

Step 2. Open all protection devices present in phase A, i.e. remove all those branches from set R.

Step 3. Pick an arbitrary bus b_i from set B. Determine all buses and generators connected to bus b_i via branches from set R.

Step 4. Classify all such buses and generators into the same reliability zone.

Step 5. Determine all branches connected to the buses in the current zone and classify them in the same zone.

Step 6. Remove all buses, branches and generators in the current zone from their corresponding sets, B, R and G.

Step 7. Repeat from Step 3, until set B becomes empty.

Step 8. Classify all branches with a protection device to the reliability zone of the bus that is on the other branch end from the protection device. In other words, if the protection

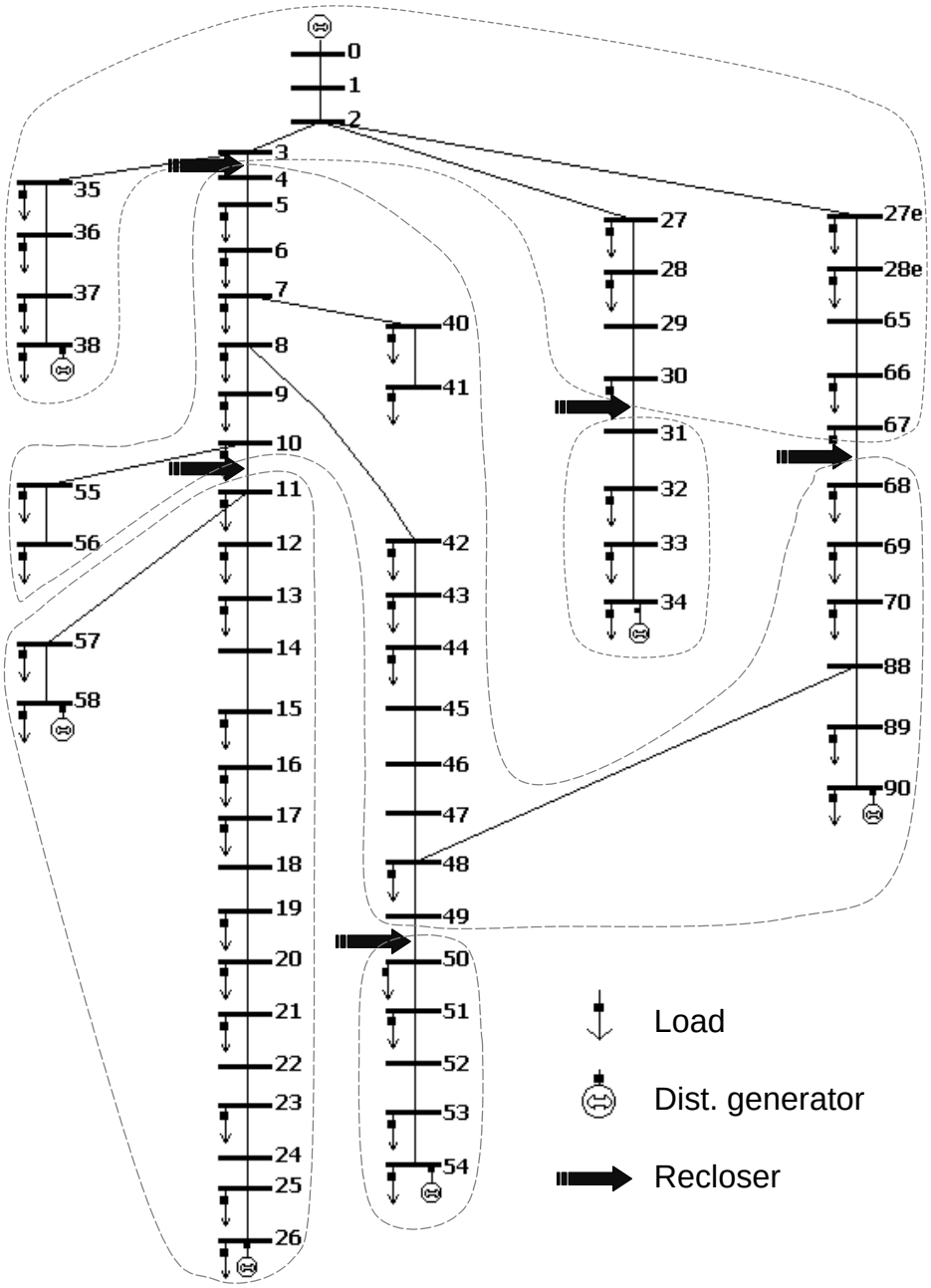

Figure 72: The distribution feeder equipped with six capacity constrained distributed generators and five reclosers, and the corresponding reliability zones defined by dashed lines.

device is connected to the FROM bus of the branch, classify the branch to the zone of the TO bus.

Step 9. Repeat steps 1–8 for phases B and C.

After the algorithm finishes, all feeder buses, branches and generators are classified into appropriate zones. Note that for a given feeder layout, the zones are determined solely by the positions of protection devices. Assuming the appropriate fault incidence rates (FIR) for all feeder branches and the fraction of permanent faults (FPF), the total annual number of permanent and momentary faults per each zone may be calculated.

After a fault in a particular zone, all buses in that zone experience an interruption. For each of the other zones, the maximum output of zone generators is compared with the load duration curve for all zone loads, and the number of permanent faults is reduced by the percentage of time that the zone generation exceeds zone load. Figure 73 shows the load duration curve of a reliability zone, and the maximum active power generation of its distributed generators. In this example, the zone generation (1 MW) is higher than its load for slightly more than 50% of the time, indicating that for more than the half of the failures outside this zone, its customers would not be disconnected.

Let the load active power profile be a discrete function, $P(x)$, where

$$x = \{\Delta t, 2\Delta t, \cdots, N\Delta t\} \tag{49}$$

and Δt is the interval between measurements. The percentage of time that DGs can supply the island is then simply:

$$p_1 = \frac{length(P(x) < \sum P_g)}{N} \tag{50}$$

where $\sum P_g$ is the total island generation.

In the case that all generators in the zone are energy limited, a check is performed to determine if they can maintain the production during the duration of the fault. This is approximated by comparing their energy capacity with the energy curve, calculated as a

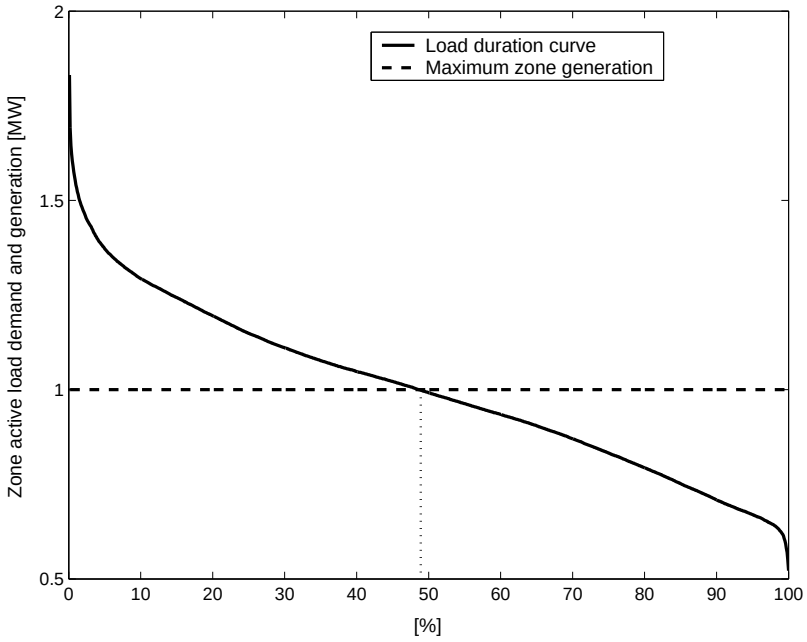

Figure 73: The zone load duration curve and the maximum generation of distributed generators for a particular reliability zone.

running sum of load power (obtained from the load profile data) for the duration of the fault. Again, the number of permanent faults is reduced by the percentage of time that the energy capacity of DGs exceeds the energy curve. Therefore, for a fault with duration T, the energy curve will be a discrete function $E(x)$, defined as:

$$E(x) = \frac{1}{K} \sum_{n=1}^{K} F(x) \tag{51}$$

where K is obtained by:

$$K = round(\frac{T}{\Delta t}) \tag{52}$$

Finally, after the total numbers of interruptions, and their durations for all zones are obtained, the composite reliability index is obtained according to (46).

6.4 Genetic algorithm for the optimal allocation of DGs and protection devices in a non-radial feeder

In a DG-enhanced, non-radial network, the optimal recloser placement problem is not as straightforward as in the case of a conventional feeder, which was treated in Chapter 5. The composite reliability index C depends strongly on the locations of protection devices and distributed generators. A relocation or addition of a single protection device changes the configuration of reliability zones, and the complete procedure explained in the previous section needs to be repeated. The general optimization problem may thus be formulated as follows.

For a given number of protection devices, N, and distributed generators, M, obtain:

- Locations of protection devices: $\mathbf{X} = \{X_1, X_2, \ldots, X_N\}$

- Locations of DGs: $\mathbf{Y} = \{Y_1, Y_2, \ldots, Y_M\}$

such that the composite reliability index C is minimized

subject to normal operating constraints

where

$$N = n_1 + n_2 + n_3 + n_4 \tag{53}$$

$$M = m_1 + m_2 \tag{54}$$

and

- n_1 - number of three-phase reclosers
- n_2 - number of single-phase reclosers
- n_3 - number of three-phase fuses
- n_4 - number of single-phase fuses
- m_1 - number of three-phase generators
- m_2 - number of single-phase generators

The simultaneous optimization of both protection devices and DGs locations may be performed in the planning stage of the feeder design. Typically, either DGs or protection

devices are already present on the feeder, and the optimization problem scales back to finding the optimal locations of the other devices. This can be obtained by making the appropriate vector, X or Y, constant. Incremental studies, where the addition of a new DG or a protection device on a feeder already equipped with DGs and reclosers are considered, may be performed by making the appropriate elements of vectors X and Y constant.

The obvious problem here is the choice of the optimization algorithm, due to the nature of the objective function (composite reliability index). Its inputs may only be discrete values indicating the types and locations of devices to be placed on the feeder. Furthermore, the objective function is neither continuous nor differentiable, with multiple local extreme points.

Clearly, conventional gradient-based algorithms can not be used. Evolutionary algorithms, on the other hand, overcome all of the problems mentioned above, as they base their decision solely on the value of the objective function. In this work, a genetic algorithm is proposed, based on the algorithm presented in [56, 57], and used to solve all three optimization problems presented in Section 6.1.

A genetic algorithm (GA) searches the parameter space by mimicking the natural principles of reproductive evolution [58, 59, 60]. It is a directed search algorithm, in which the search is performed on the set of all possible solutions to a problem. GA is capable of working with discrete data types and does not need any gradient information. Starting from an initial population of solutions, it effectively implements the "survival of the fittest" strategy. Fitter solutions, with higher values of the objective function, are more likely to reproduce and/or survive to the next generation, thus improving the overall population. The population evolves using two genetic operators, mutation and crossover. Various techniques exist for selecting the solutions that will continue on to the next generation, and/or be chosen for mutation and crossover. The GA terminates either after a pre-specified number of generations or after the population converges to a single solution.

However, it should be noted that there is no evidence to support a claim that the goal of

evolution, and thus the goal of a genetic algorithm, is to produce the best possible solution. Therefore, in general, no theoretical proof of global convergence exist for genetic algorithms. This problem is typically tackled by repeating the GA run with different (random) initial conditions.

The main steps of a genetic algorithm are shown in Figure 74, and presented below. More detailed analysis of the algorithm is presented in the following sections.

Step 1. *Initialization.* The algorithm is initialized with a randomly generated starting population X_0. The population is defined as a set of different DG and/or recloser allocations (solutions).

Step 2. *Calculation of the objective function.* For each combination of devices (members of the population), the reliability index C is calculated, using the procedure presented in Section 6.3.

Step 3. *Selection.* The solutions chosen to continue into the new generation are selected using the appropriate selection criteria.

Step 4. *Crossover.* The crossover operator provides random mixture of solutions, allowing the algorithm to search the parameter space.

Step 5. *Mutation.* The mutation operator allows the algorithm to avoid local minima of the objective function, by introducing random changes in the current population.

Step 6. *Convergence check.* Algorithm terminates if the population converges to a single solution, or if the maximal number of generations is reached. Otherwise, the algorithm continues from Step 2.

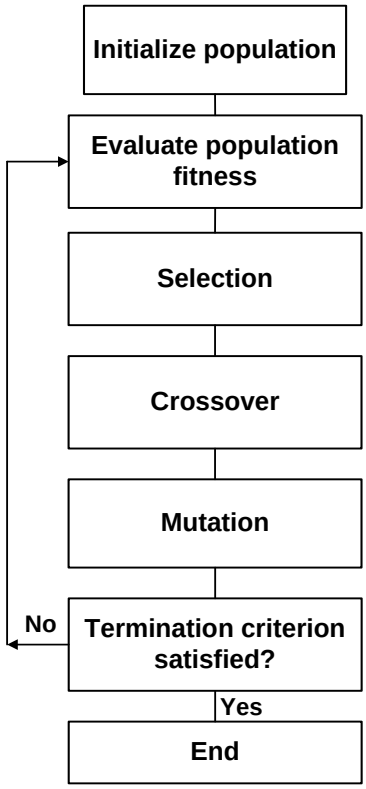

Figure 74: The flowchart of a typical genetic algorithm.

6.4.1 Solution representation

The encoding, or representation of solutions is most commonly done using bit strings, where a single solution is represented just as a sequence of zeros and ones. This representation allows simple and theoretically tractable crossover and mutation operators, but is typically not the most efficient one [61, 62, 63].

In the proposed application, the goal is to obtain the positions of individual devices on the feeder, where these devices may be placed on a limited number of buses or branches. The locations where protection devices may be placed may be coded using discrete numbers between 1 and P, where P is the number of possible branches in the system where protection devices may be placed. Similarly, possible DG locations may be coded using discrete numbers ranging from 1 to R, R being the number of possible buses where DGs may be placed. Although, these values may also be coded using a binary representation, it

is more natural and efficient to use the discrete representation. Thus, let a single solution be defined as a specific allocation of individual DGs and protection devices on the feeder, i.e. the k-th solution in the population is a $(N + M)$-dimensional row vector of discrete numbers:

$$X_k = \{[x\ y] \mid x_i \in \{1, \ldots, P\},\ i = 1, \ldots, N,\ y_j \in \{1, \ldots, R\},\ j = 1, \ldots, M\} \tag{55}$$

where P is the number of possible branches in the system where reclosers may be placed (branches are numbered consequently from 1 to P), R number of possible candidate buses for the allocation of DGs, N number of protection devices to be placed on the feeder and M number of DGs. The population is then defined simply as a group of solutions, i.e.:

$$\mathbf{X} = \{X_k \mid k = 1, \ldots, S\} \tag{56}$$

where S is the population size. For example, for the case with only two protection devices ($N = 2$), two distributed generators ($M = 2$), and with population consisting of 5 solutions ($S = 5$), the population is a 5×4 matrix, and may look like:

$$\mathbf{X} = \begin{pmatrix} 2 & 28 & 31 & 44 \\ 3 & 30 & 40 & 50 \\ 4 & 33 & 44 & 50 \\ 4 & 36 & 42 & 50 \\ 3 & 34 & 43 & 52 \end{pmatrix} \tag{57}$$

where the first solution represents the situation with protection devices at buses 2 and 28, and generators at buses 31 and 44, etc.

As the objective function is the composite reliability index, the vector of solutions, representing the “fitness” of solutions in the population also has S elements:

$$\mathbf{C} = \{C_1, C_2, \ldots, C_S\} \tag{58}$$

The simulation is initialized using a randomly created initial population matrix, X_0. The position of each device is determined by generating a sequence of random numbers, using

a discrete uniform random distribution with probability density function defined as:

$$p(x) = \frac{1}{S},\ x \in \{1, 2, \ldots, S\} \tag{59}$$

6.4.2 Selection process

The selection process determines how many and which solutions from the current population are used to create the new generation, and also which of the current solutions should be erased to make room for new solutions. A variety of selection methods exist; the most commonly used are presented below.

- *Fitness-based Roulette* [63]: In this method, the probability of selecting a solution x_i is proportional to the value of its objective function (fitness) $C(x_i)$, i.e.

$$p(x_i) = \frac{C(x_i)}{\sum_{k=1}^{P} C(x_k)} \tag{60}$$

After a selection is made, the selected solution may be removed from the wheel, or kept on the wheel allowing some solutions to be picked more than once. The roulette method works well, giving fitter solutions a much greater chance of reproducing, if the differences in fitness are relatively large. However, it may have difficulties selecting solutions if their fitness values are relatively similar.

- *Scaled Roulette* [56]: To overcome the problem when the ratio between extreme fitness values in the population is close to unity, the population may be sorted by fitness, and some bias may be introduced toward the front of the list. For example, the minimum fitness may be subtracted from the fitness of each solution, thus making the least fit solution having a fitness of 0, and then performing a roulette selection.

More sophisticated ways to introduce bias toward fitter individuals exist. In a normalized geometric ranking selection procedure [56], the probability of selecting each solution is given by:

$$p(x_i) = \frac{q(1-q)^{r_i - 1}}{1 - (1-q)^S} \tag{61}$$

where q is the probability of selecting the best solution (given in advance), r_i is the rank of the solution after sorting (1 being the best), and S is the population size. By adjusting the parameter q, the amount of introduced bias may be fine-tuned.

As an example, the population with only five members is considered, with fitness levels shown in Table 28. All five population members (solutions) have relatively similar fitness, which are also shown in Table 28. Roulette selection yields almost equal probabilities of selection, shown in Figure 75(a). The highest ranked solution has a 21% probability of being selected, as opposed to 19% probability for a least fittest solution. By using the scaled roulette selection method, normalized geometric ranking selection (NGRS) in particular, the probability of selecting fitter solutions is significantly increased. The amount of bias is controlled using the q parameter, varied from 0.1 to 0.3 in this example, as shown in Figure 75(b)–(d). The introduced bias increases the probability of selecting the most fit solution from 21% to 36%.

- *Tournament* [63]: In a tournament selection, a group of k randomly selected solutions is formed, and only the one with the highest fitness is chosen. A process is repeated n times if n solutions need to be chosen. The most common implementation is when $k = 2$, i.e. two by two solutions are selected and the fitter solution is always selected.

- *Elitist model* [64]: There is no guarantee that the fittest solution in the current population will always be selected using any of the described selection methods. The elitist model assures just that, simply by always selecting the most fit solution to continue to the next generation.

After evaluating all of the mentioned selection methods, a scaled roulette with the normalized geometric ranking selection procedure was implemented as a selection method in the developed algorithm, because of its flexibility. The probability of selecting the best solution, q, was set to 0.08.

Table 28: Population members sorted by their rank and their corresponding fitness functions.

Rank	1	2	3	4	5
Fitness	3.05	3.00	2.95	2.80	2.75

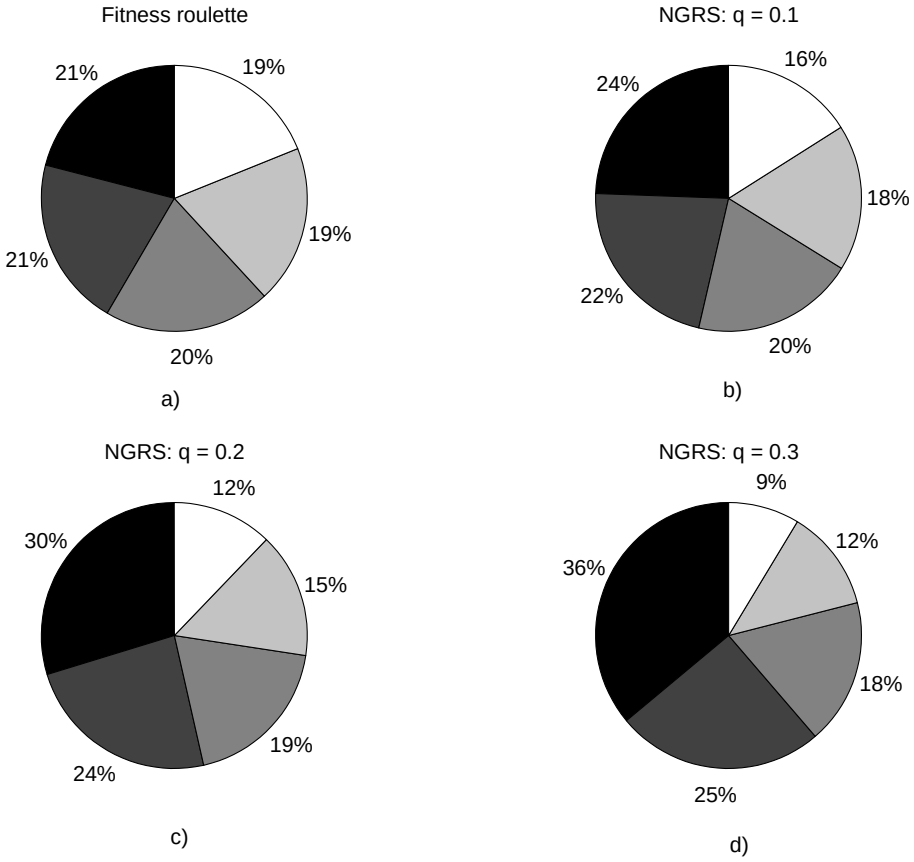

Figure 75: Normalized geometric ranking selection (NGRS) method: The effect of parameter q on the probability of selection of each solution from the current population. Increasing q increases the probability of selecting higher ranked solutions.

6.4.3 Crossover operator

Crossover is a random exchange of genetic information between two selected solutions from the current population (parents) that produces unique new solutions to be included in the next generation. The underlying idea is that "good" solutions may produce "better" ones by interchanging their genetic material. A crossover operator is typically applied only to a percentage of selected solutions determined by the parameter called the *crossover probability*, P_c. Typical values for P_c are in the range of 0.5–1 [58, 64].

We consider three crossover operators:

- *Arithmetic crossover* [63] produces new solutions, c_1 and c_2, from members of the current population, p_1 and p_2, by calculating the linear combination of p_1 and p_2:

$$c_1 = \alpha p_1 + (1 - \alpha) p_2 \tag{62}$$

$$c_2 = (1 - \alpha) p_1 + \alpha p_2 \tag{63}$$

where α is a vector of uniformly distributed random numbers between 0 and 1, whose size is equal to the size of solutions p_1 and p_2. As all solutions are composed of only discrete numbers (positions of recloser and/or DGs), new solutions c_1 and c_2 are rounded to the nearest integer values.

- *Heuristic crossover* [63] incorporates fitness information, resulting in solutions more likely to have higher values of the objective function. It produces new solutions, c_1 and c_2, by linear extrapolation along the line formed by two solutions from the current population, p_1 and p_2, outward in the direction of the solution with higher value of the objective function:

$$c_1 = p_2 + \alpha(p_2 - p_1) \tag{64}$$

$$c_2 = p_2 \tag{65}$$

assuming solution p_2 is fitter than p_1, and α is again a vector of uniformly distributed random numbers between 0 and 1. A new solution c_1 may not be feasible if α is chosen

in such a way that one of its genes (device positions) falls outside of feasible range, i.e. c_1 may indicate that a device is to be placed on a nonexisting branch. To avoid this, a user–selectable parameter r is introduced. If c_1 falls outside of the feasible region, a new value for α is generated and a new candidate for c_1 is obtained. If the feasible solution is not obtained after r tries, c_1 is set to the value of p_1. A value of $r = 3$ has been used in the developed algorithm. Finally, both c_1 and c_2 are rounded to the nearest integer values.

- *One-point crossover operator with creeping* [61, 63] is an extension of the one-point binary operator commonly used in binary genetic algorithms. The idea is to swap parts of two existing solutions, creating two new solutions. Assuming two binary strings representing existing solutions p_1 and p_2, a crossover point is selected at random, and new solutions c_1 and c_2 are created by taking the appropriate parts of p_1 and p_2, as seen in Figure 76.

The same logic is used for the one-point decimal crossover operator, where instead of a zero or one used in the binary representation, each position holds a decimal number indicating the location of a protection device, as defined in (55), and shown in Figure 77. New solutions are obtained by determining the crossover point at random and exchanging the genetic information (device positions) between the existing solutions, just as in a typical one-point binary algorithm. Note, that this operator may only be used when more than one device is placed on the feeder; otherwise arithmetic crossover is performed.

The drawback of the one–point decimal operator is that new solutions c_1 and c_2 are composed only of the decimal numbers contained in previous solutions p_1 and p_2. Remembering that each of the numbers represents the actual device position (recloser or generator), it is clear that the one-point operator never tries to reallocate the device to a new position (not already present in either p_1 or p_2). Thus, a relatively small random number is (with a small, but defined, probability) added to new solutions. Assuming the existing solutions c_1 and c_2 were already one of the fitter solutions, this approach effectively allows a more detailed search of the space that may be close to the optimal point, i.e. the algorithm creeps in the neighborhood of the optimal point.

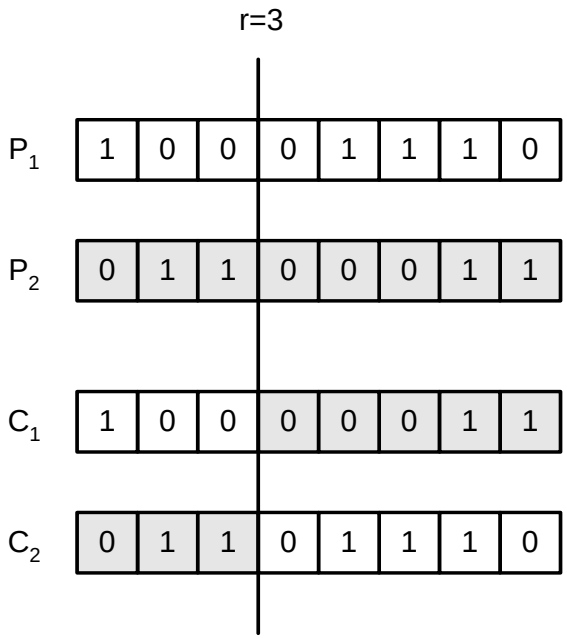

Figure 76: One point binary crossover. Existing solutions p_1 and p_2 are cut at the randomly selected point denoted by the vertical line. New solutions c_1 and c_2 are created by exchanging the genetic material before and after the cut.

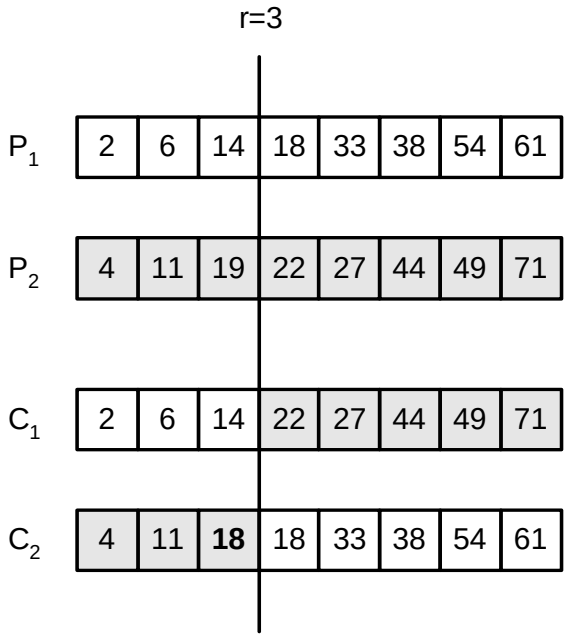

Figure 77: One point decimal crossover with creeping. Existing solutions p_1 and p_2 are cut at the randomly selected point denoted by the vertical line. New solutions c_1 and c_2 are created by exchanging the genetic material before and after the cut. Note the slight change in the location of the third device in new solution c_2.

A number to be added is generated using a normal random distribution with zero mean value and the appropriate (small) variance σ, and then rounded to the nearest integer. The variance σ controls the amount of creeping allowed by the operator. For example, a value of $\sigma = 1$ (value used in the algorithm) assures that 95% of the time, the location of the device will not move by more than two locations up or down the feeder. The creeping operator may also provide unfeasible solutions, although at a very low rate. In that case, the creeping operator is neglected, and the device in question is placed at the location determined by the existing solution, c_1 or c_2.

6.4.4 Mutation operator

Mutation is a random change in the genetic material of a single solution, equivalent to a random search in the neighborhood of the current solution. The rate of its occurrence is determined by the parameter called the *probability of mutation*, P_m, with typical values in the range of 0.005–0.1 for binary algorithms [58, 64].

Uniform mutation [63], implemented in the developed algorithm, changes only one of the parameters of the existing solution (position of one of the protection devices or DGs), by replacing it by a uniformly generated (discrete) number within the allowed parameter space. In other words, one device is relocated randomly on the feeder. For example, one of the five reclosers in Figure 78 is relocated from branch #17 to branch #33.

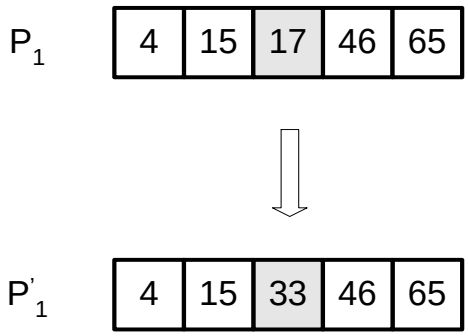

Figure 78: Single-position uniform mutation.

6.5 Parameters of a genetic algorithm

Although the optimal convergence is not guaranteed, typically GAs perform very well for a variety of applications. However, there are several parameters that may significantly affect the convergence properties of the genetic algorithm, and are typically tuned on a per-application basis.

The crossover probability determines the rate at which new solutions are introduced into the population. A large crossover probability yields more new solutions at each generation, but may also lead to the vanishing of fit solutions before their genetic material has been exploited. On the other hand, a small crossover probability may not introduce sufficient changes and the algorithm may settle in a local minimum.

The probability of mutation allows the algorithm to avoid setting in a local minimum by introducing random genetic changes into the current population. A low mutation probability may lead to premature convergence to a local minimum. Too a high mutation rate may negate the benefits of a directed search obtained by the crossover operator, and may transform the algorithm into a general random search algorithm.

The amount of crossover and mutation may be significantly increased, compared to a conventional GA, if the elitist principle is used. In this case the fittest solution is always transferred to the next generation, and applying more disruptions to the current generation does not cause any good solutions to be lost [61].

Population size also significantly influences the overall operation of the genetic algorithm. A small population size may not provide a sufficient sample size over the space of the solutions and may not retain genetic variety as the algorithm progresses from generation to generation. On the other hand, a large population may require a prohibitively large number of function evaluations, slowing down the algorithm. The population size should, therefore, be proportional to the complexity of the problem, i.e. it should depend on the size of the search space spanned by the optimization problem.

The maximum number of generations determines the termination criterion of the algorithm, and should also be carefully chosen. Setting the maximum number of generations to an extremely high value may slow the algorithm considerably. Naturally, setting it to a too low value may not allow the algorithm to search the entire parameter space and could lead to suboptimal results.

DeJong [64] determined the optimal parameter values for a diverse set of optimization problems, called a DeJong test suite. For a binary GA with a single-point crossover and binary mutation operators, the optimal population size was found to be $n = 50$, crossover probability, $P_c = 0.6$ and the probability of mutation $P_m = 0.001$. Although these parameters were tuned for a specific set of optimization problems and for a conventional binary GA, they are still often used as default parameters for various GA implementations.

The optimal parameters for a particular GA may be determined by performing the "hand optimization", i.e. changing one parameter at a time, starting from Dejong's values. This procedure is typically very computationally intensive but may provide parameter values well suited for a specific optimization problem. In addition, a companion genetic algorithm [65] or a brute search method [66] may be used to obtain the optimal parameters. The disadvantage of the latter two methods is the obvious additional computational cost. The drawback of all these methods is that they may yield optimal parameter values good only for a suite of problems that were used to obtain them. In the proposed application, performing the "hand optimization" on a specific set of feeders does not guarantee a satisfactory level of performance for a different set of feeder configurations.

The objective is thus to obtain robust parameter values that perform well on a variety of feeder configurations. A hand optimization is performed on a set of typical feeders and presented later in Section 6.5.2. The influence of both the population size and the maximum number of generations is also presented.

6.5.1 Adaptive genetic algorithm

To avoid the problems associated with obtaining the optimal (or robust) values of P_c and P_m, an adaptive algorithm, based on [67], is also implemented. The idea is to adaptively change the probabilities of crossover and mutation as algorithm progresses from generation to generation. Furthermore, different values of P_c and P_m are applied to different solutions depending on their fitness and the overall fitness of the current population.

The current fitness level of the population is measured by its average fitness $\bar{f}$. The difference between the fitness of the fittest solution f_{max} and average fitness $\bar{f}$ is used for detecting the closeness to the local (or optimal) minimum. As algorithm converges to the minimum, $f_{max} - \bar{f}$ decreases, both P_m and P_c are increased, allowing the algorithm to explore more of the search space and reducing the chances of being stuck at the local minimum of the objective function.

The drawback of this approach is that as the algorithm approaches the optimal extreme point, excessive amount of disruptions may be introduced, preventing the algorithm's convergence. To avoid such behavior, different values of P_c and P_m are introduced to each solution. Fitter solutions have lower P_c and P_m, allowing them to remain in the population, while less fit solutions may be disrupted more often and thus have higher values of P_c and P_m.

The formulas for adaptive changes of P_c and P_m suggested in [67] are:

$$P_c = \begin{cases} \frac{f_{max} - f'}{f_{max} - \bar{f}} & \text{if } f' > \bar{f} \\ 1 & \text{if } f' \leq \bar{f} \end{cases} \tag{66}$$

$$P_m = \begin{cases} \frac{1}{2}\frac{f_{max} - f}{f_{max} - \bar{f}} & \text{if } f > \bar{f} \\ \frac{1}{2} & \text{if } f \leq \bar{f} \end{cases} \tag{67}$$

where f' is the fitness of the fitter of two solutions selected for crossover and f is the fitness of the current solution.

Note that both P_c and P_m are zero for the fittest solution, allowing its direct transfer

to the next generation. Coupled with an aggressive selection criterion (that selects fitter solutions more often), this strategy may lead to the exponential growth of the fittest solution in the population and premature convergence to the local minimum. To avoid this, authors in [67] suggested a default mutation rate for every solution in the population, reducing the chances of premature convergence.

Since the implemented algorithm already incorporates an elitist model that transfers the best solution to the next generation, the adaptation rates for P_c have been adjusted by setting the minimal amount of crossover applied to the fittest solution to a nonzero value P'_c.

$$P_c = \begin{cases} \frac{f_{max} - [(1-P'_c)f' + P'_c \bar{f}]}{f_{max} - f} & \text{if } f' > \bar{f} \\ 1 & \text{if } f' \leq \bar{f} \end{cases} \tag{68}$$

In the implemented algorithm, a value of $P'_c = 0.5$ was used, leading to the following P_c adaptation law:

$$P_c = \begin{cases} \frac{f_{max} - \frac{f' + \bar{f}}{2}}{f_{max} - f} & \text{if } f' > \bar{f} \\ 1 & \text{if } f' \leq \bar{f} \end{cases} \tag{69}$$

A similar approach has been adopted for the mutation operator. By defining the parameter P'_m that sets the minimal amount of mutation, the probability of mutation becomes:

$$P_m = \begin{cases} \frac{1}{2} \frac{f_{max} - [(1-P'_m)f + P'_m \bar{f}]}{f_{max} - f} & \text{if } f > \bar{f} \\ \frac{1}{2} & \text{if } f \leq \bar{f} \end{cases} \tag{70}$$

and using a value of $P'_m = 0.5$, the following adaptation law for P_m is obtained:

$$P_m = \begin{cases} \frac{1}{2} \frac{f_{max} - \frac{f + \bar{f}}{2}}{f_{max} - f} & \text{if } f > \bar{f} \\ \frac{1}{2} & \text{if } f \leq \bar{f} \end{cases} \tag{71}$$

6.5.2 Parametrization of the genetic algorithm

In an effort to determine the optimal crossover operator (arithmetic, heuristic or one-point crossover operator), and the corresponding optimal probabilities of crossover and mutation, P_c and P_m, a hand-optimization is performed for a selected problem of determining the optimal recloser positions on a feeder enhanced with capacity constrained DGs.

The procedure is performed on two different feeder layouts:

- *Test feeder #1*. The 69-segment, 8-lateral three-phase distribution feeder, based on [34]. Total nominal feeder load is 3.8 MW, and the load duration curve is obtained from the utility data provided by Nebraska Public Power District for the city of Scottsbluff, NE. All branches and loads at the feeder are assumed to be three-phase. The feeder is not radial.
- *Test feeder #2.* The 80-segment asymmetric rural radial distribution feeder obtained from Florida Power & Light Company. The feeder has a very widespread configuration and a low and uneven customer density. It consists of a main three-phase branch, with multiple single-phase lines branching from the main feeder. Total nominal feeder load is 4.6 MW, while the load duration curve is obtained from the actual utility data for a rural residential area with large induction irrigation motors.

The parameters of both feeders are given in Appendix C. Table 29 shows the characteristic parameters of the developed genetic algorithm (population size, maximum number of generations, size of the search space) for the two considered feeders.

6.5.2.1 Feeder #1

In the case of a symmetric, three-phase feeder, the goal of the algorithm is to place k devices on n possible locations. The total number of possible combinations S (the size of the search space) is thus:

$$S = \left(\begin{array}{c} n \\ k \end{array} \right) \tag{72}$$

Table 29: Characteristic parameters of the genetic algorithm for the two considered feeders. DG positions correspond to bus numbering in Figure 87 and Figure 88 for Feeders #1 and #2, respectively.

Test systems	Feeder #1	Feeder #2
Size of the search space	1.12E+07	6.76E+05
Population size	100	25
Max.number of generations	100	100
Number of reclosers	5	5 (3 3-phase, 2 1-phase)
DG positions	26, 34, 38, 54, 58, 90	120, 155, 162, 144, 198
DG size	0.3 MW	0.5 MW
Feeder load	3.8 MW	4.6 MW

The considered ranges for the probabilities of crossover and mutation are 50%–90% and 10%–70%, respectively. Initial results showed that high mutation rates may significantly improve the performance of the algorithm, which is why extremely high mutation rates (up to 70%) were considered. For each combination of P_c and P_m, the GA run is repeated 20 times with different initial populations, generated at random as per (59). The percentage of successful runs (in which the optimal solution is found) is recorded, as well as the average number of generations needed to obtain the optimal solution. If a solution is not found in 100 generations, a run is deemed unsuccessful. The procedure is then repeated for three crossover operators defined in Section 6.4.3: arithmetic, heuristic and one-point crossover. Additionally, the same procedure is repeated 20 times using the adaptive algorithm. The results are summarized in Tables 30–35.

The optimal solution (with the composite index equal to $C = 0.0898$) is determined as the smallest value obtained throughout the procedure described above. Furthermore, the adaptive algorithm was run 20 additional times (with all three crossover operators), with increased population size (200) and for 250 generations. The minimal obtained value was again $C = 0.0898$, thus providing additional verification that the obtained value is the

optimal solution.

Tables 30–32 show the results obtained with the arithmetic, heuristic and one-point crossover operator, respectively. The population size is fixed to 100 solutions, and the maximum number of iterations is 100. Note that the primary criterion that describes the operation of the algorithm is its success rate – a P_c and P_m combination that yields a lower success rate, but converges faster (in less generations) is inferior to the combination that produces a higher success rate. The best P_c and P_m combinations are highlighted in bold in Tables 30–32.

The following are the general conclusions that can be drawn from Tables 30–32:

- The performance of the algorithm is generally very good, and the algorithm is typically able to obtain the optimal solution with all three crossover operators. The presented results do not reveal the universally optimal P_c and P_m combination, but may be used to determine the ranges for P_c and P_m that yield satisfactory convergence properties of the algorithm.

- Increase in mutation probability, P_m, increases the success ratio of the algorithm. It also decreases the number of generations needed to reach the solution. The algorithm has over 90% success rate for all three crossover parameters, if the mutation rate is set higher than 10%. Although Tables 30–32 suggest that the algorithm performs best with extremely high mutation rates, these rates may prevent the convergence of the algorithm, which is shown later in this chapter. Therefore, high mutation rates should only be used if the number of generations is set in advance.

- Increase in crossover probability, P_c, also increases the success rate when the arithmetic or heuristic operators are used. The benefits of increasing P_c are not as evident in the case of the one-point crossover operator.

- The success ratio obtained with the adaptive algorithm is also higher than 90%, with

convergence speed comparable to the speed obtained with the best P_c and P_m combination for a given crossover operator. Note however that the success ratio of the adaptive algorithm is typically slightly lower than the success ratio obtained with the best P_c and P_m combination.

Tables 33–35 show the results of the same analysis as described above, if the algorithm has been terminated after 50 generations, indicating the importance of selecting the maximum number of iterations correctly. The success ratio drops significantly, as 50 generations may not be enough for the algorithm to find the optimal solution. However, it should be noted that the increased mutation and crossover rates yield higher percentages of successful algorithm runs. Furthermore, the results obtained with the adaptive algorithm are again comparable with the results obtained with the best combination of P_c and P_m parameters.

Table 30: The performance of the GA: percentage of successful runs and the average number of generations needed to obtain the solution, using the arithmetic crossover operator (feeder #1). Maximum number of generations is 100.

5 reclosers, Arithmetic crossover, Uniform mutation	P_c = 50%		P_c = 70%		P_c = 90%		Adaptive GA	
	Avg # of generations to solution	% successful	Avg # of generations to solution	% successful	Avg # of generations to solution	% successful	Avg # of generations to solution	% successful
P_m = 10%	76.00	40	54.14	70	60.81	80	35.35	100
P_m = 30%	36.40	100	35.56	90	37.94	90		
P_m = 50%	41.20	100	40.70	100	35.70	100		
P_m = 70%	**27.50**	**100**	36.90	100	35.9	100		

Table 31: The performance of the GA: percentage of successful runs and the average number of generations needed to obtain the solution, using the heuristic crossover operator (feeder #1). Maximum number of generations is 100.

5 reclosers, Heuristic crossover, Uniform mutation	P_c = 50%		P_c = 70%		P_c = 90%		Adaptive GA	
	Avg # of generations to solution	% successful	Avg # of generations to solution	% successful	Avg # of generations to solution	% successful	Avg # of generations to solution	% successful
P_m = 10%	75.13	75	55.31	80	58.31	80	36.84	95
P_m = 30%	45.21	95	36.75	100	34.6	100		
P_m = 50%	36.85	100	38.85	100	35.65	100		
P_m = 70%	31.05	100	31.8	100	**29.35**	**100**		

Table 32: The performance of the GA: percentage of successful runs and the average number of generations needed to obtain the solution, using the one-point crossover operator (feeder #1). Maximum number of generations is 100.

5 reclosers, One-point crossover, Uniform mutation	P_c = 50%		P_c = 70%		P_c = 90%		Adaptive GA	
	Avg # of generations to solution	% successful	Avg # of generations to solution	% successful	Avg # of generations to solution	% successful	Avg # of generations to solution	% successful
P_m = 10%	56.46	65	63.00	55	56.30	50	33.22	90
P_m = 30%	44.10	100	41.10	100	34.44	90		
P_m = 50%	37.95	100	**37.10**	**100**	41.42	95		
P_m = 70%	38.65	100	33.67	90	43.89	95		

Table 33: The performance of the GA: percentage of successful runs and the average number of generations needed to obtain the solution, using the arithmetic crossover operator (feeder #1). Maximum number of generations is 50.

5 reclosers, Arithmetic crossover, Uniform mutation	P_c = 50%		P_c = 70%		P_c = 90%		Adaptive GA	
	Avg # of generations to solution	% successful	Avg # of generations to solution	% successful	Avg # of generations to solution	% successful	Avg # of generations to solution	% successful
P_m = 10%	44.50	10	35.17	30	40.33	30	25.31	80
P_m = 30%	24.87	75	28.43	70	25.23	65		
P_m = 50%	30.85	65	33.33	75	26.93	75		
P_m = 70%	**25.16**	**95**	30.38	80	31.39	90		

Table 34: The performance of the GA: percentage of successful runs and the average number of generations needed to obtain the solution, using the heuristic crossover operator (feeder #1). Maximum number of generations is 50.

5 reclosers, Heuristic crossover, Uniform mutation	P_c = 50%		P_c = 70%		P_c = 90%		Adaptive GA	
	Avg # of generations to solution	% successful	Avg # of generations to solution	% successful	Avg # of generations to solution	% successful	Avg # of generations to solution	% successful
P_m = 10%	20	10	37.57	35	32.71	35	30.33	75
P_m = 30%	34.33	60	27.07	75	32.17	90		
P_m = 50%	32.61	90	31.53	85	31.67	90		
P_m = 70%	30	95	29.61	90	**28.21**	**95**		

Table 35: The performance of the GA: percentage of successful runs and the average number of generations needed to obtain the solution, using the one-point crossover operator (feeder #1). Maximum number of generations is 50.

5 reclosers, One-point crossover, Uniform mutation	P_c = 50%		P_c = 70%		P_c = 90%		Adaptive GA	
	Avg # of generations to solution	% successful	Avg # of generations to solution	% successful	Avg # of generations to solution	% successful	Avg # of generations to solution	% successful
P_m = 10%	40.75	40	31.67	15	36.67	30	30.59	85
P_m = 30%	33.23	65	32.60	75	30.69	80		
P_m = 50%	32.50	80	**32.06**	**85**	31.33	60		
P_m = 70%	31.8	80	26	75	34.23	65		

Figures 79–80 show the convergence properties of the algorithm. Figure 79 shows the *best* value of the composite index per generation, averaged over 20 algorithm trials, for several combinations of P_c and P_m. As the mutation probability P_m increases, the algorithm tends to converge faster (for the same crossover probability P_c). Similar behavior is observed when the mutation probability is kept constant, and the crossover probability is varied.

Figure 80 shows the *average* composite index value (average population fitness), per generation, for the same combinations of P_c and P_m. As the algorithm progresses, the average population fitness increases (composite index value decreases), as the crossover operator produces better solutions from generation to generation. On the other hand, the mutation operator introduces new solutions, preserving the diversity of the population and therefore preventing the algorithm from converging to a single (possibly suboptimal) solution. However, an increased mutation rate may keep the algorithm from ever converging to the solution, as indicated in Figure 80. As mentioned before, the genetic algorithm typically terminates either after a prespecified number of generations, or after the difference in population fitness does not change significantly between two successive generations (indicating convergence to a local or global minimum). In the case of a high mutation rate, the latter criterion may not be used, because the mutation operator will introduce a significant amount of new solutions in each generation.

The convergence properties of the adaptive algorithm are also shown in Figures 79–80 (line No. 5 in both figures). The convergence speed of the adaptive algorithm is comparable with the speed obtained with the best combination of P_c and P_m, as shown in Figure 79. The average index value (Figure 80) on the other hand settles at a significantly lower value than that of the value obtained with high mutation rates, which provide comparable convergence properties. Therefore, these results indicate that the adaptive algorithm possesses the good convergence properties obtained by using high mutation rates with the conventional algorithm, while its average fitness value still may be used to detect algorithm convergence.

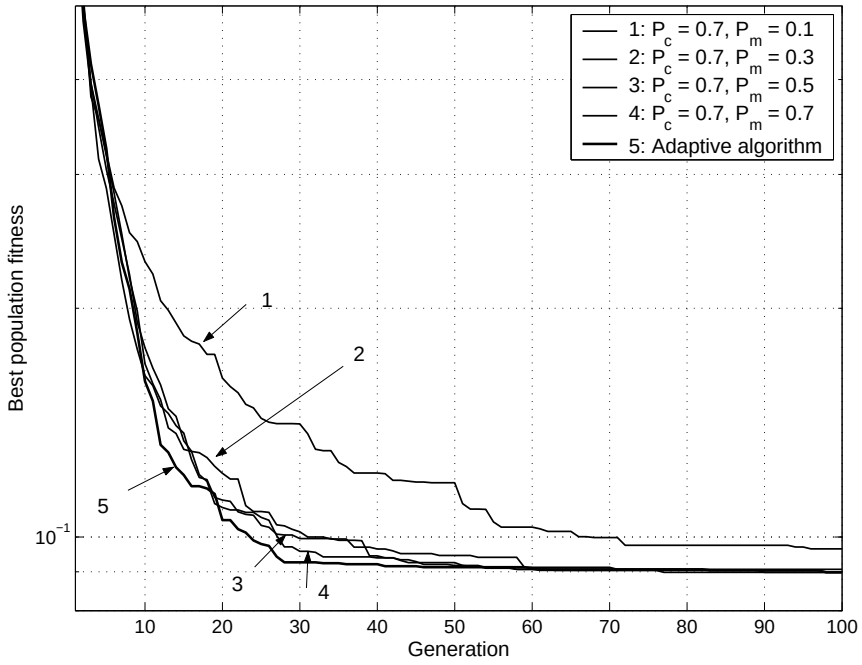

Figure 79: Convergence of the genetic algorithm: the *best* value of the composite index, per generation, for various combinations of crossover and mutation probabilities (using arithmetic crossover).

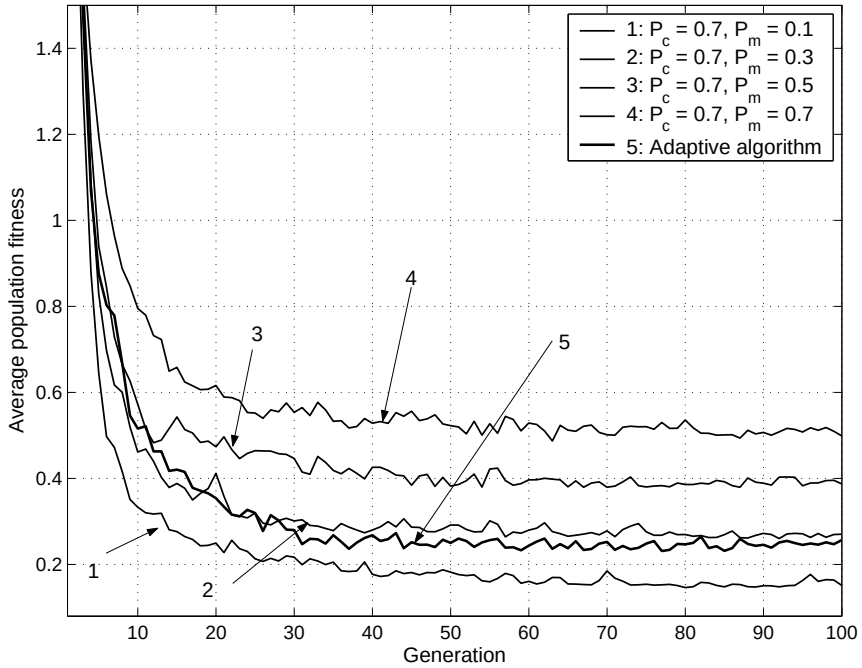

Figure 80: Convergence of the genetic algorithm: the *average* value of the composite index, per generation, for various combinations of crossover and mutation probabilities (using arithmetic crossover).

Note finally that the results shown in Figures 79–80 are obtained using the arithmetic crossover operator, but similar results were observed with the heuristic and one–point crossover operators.

6.5.2.2 Feeder #2

The same hand-optimization study is performed on a second test feeder, and the results are shown in Tables 36–41. In this example, the goal was to place three three-phase and two single-phase reclosers on a feeder with DGs located at buses 120, 155, 162, 144 and 198, as indicated in Table 29. As the single-phase reclosers are typically placed only on single-phase branches [68], the search space of the algorithm is considerably reduced. The number of possible combinations S to place k_1 three-phase reclosers on n_1 three-phase branches and k_2 single-phase reclosers on n_2 single-phase branches is

$$S = \begin{pmatrix} n_1 \\ k_1 \end{pmatrix} \cdot \begin{pmatrix} n_2 \\ k_2 \end{pmatrix} \tag{73}$$

This is typically much smaller than $\begin{pmatrix} n_1 + n_2 \\ k_1 + k_2 \end{pmatrix}$, which would be the size of the search space if all devices and branches were three-phase. The population size is therefore reduced to 25 (instead of 100, which was used for the first test feeder). The maximum number of generations is again 100.

The conclusions drawn for the symmetrical three-phase feeder (feeder No. 1) are further reinforced by the results shown in Tables 36–38. The increased amount of crossover and/or mutation increases the convergence speed and the success ratio of the algorithm, while the performance of the adaptive algorithm is again comparable with the results obtained with the best combination of P_c and P_m. The importance of the termination point of the algorithm (choosing the maximum number of generations) is also illustrated in Tables 39–41, as the success ratio drops significantly if the algorithm is terminated after only 50 generations.

Table 36: The performance of the GA: percentage of successful runs and the average number of generations needed to obtain the solution, using the arithmetic crossover operator (feeder #2). Maximum number of generations is 100.

5 reclosers, Arithmetic crossover, Uniform mutation	P_c = 50%		P_c = 70%		P_c = 90%		Adaptive GA	
	Avg # of generations to solution	% successful	Avg # of generations to solution	% successful	Avg # of generations to solution	% successful	Avg # of generations to solution	% successful
P_m = 10%	51.21	70	63.54	65	57.42	60	**43.41**	**90**
P_m = 30%	44.94	90	51.21	95	**42.11**	**95**		
P_m = 50%	46.72	90	38.78	90	45.05	95		
P_m = 70%	51.06	90	44.18	85	46.87	75		

Table 37: The performance of the GA: percentage of successful runs and the average number of generations needed to obtain the solution, using the heuristic crossover operator (feeder #2). Maximum number of generations is 100.

5 reclosers, Heuristic crossover, Uniform mutation	P_c = 50%		P_c = 70%		P_c = 90%		Adaptive GA	
	Avg # of generations to solution	% successful	Avg # of generations to solution	% successful	Avg # of generations to solution	% successful	Avg # of generations to solution	% successful
P_m = 10%	60.36	55	58.5	50	63.2	75	**42.84**	**95**
P_m = 30%	59.35	85	48.06	85	39.72	90		
P_m = 50%	45.45	90	37.26	95	42.25	100		
P_m = 70%	43.5	90	**40.9**	**100**	36.58	95		

Table 38: The performance of the GA: percentage of successful runs and the average number of generations needed to obtain the solution, using the one-point crossover operator (feeder #2). Maximum number of generations is 100.

5 reclosers, One-point crossover, Uniform mutation	P_c = 50%		P_c = 70%		P_c = 90%		Adaptive GA	
	Avg # of generations to solution	% successful	Avg # of generations to solution	% successful	Avg # of generations to solution	% successful	Avg # of generations to solution	% successful
P_m = 10%	46.27	75	46.00	85	42.29	85	**44.83**	**90**
P_m = 30%	49.78	90	55.72	90	41.76	85		
P_m = 50%	45.44	90	59.06	85	**54.89**	**95**		
P_m = 70%	47.79	70	52.00	35	58.00	65		

Table 39: The performance of the GA: percentage of successful runs and the average number of generations needed to obtain the solution, using the arithmetic crossover operator (feeder #2). Maximum number of generations is 50.

5 reclosers, Arithmetic crossover, Uniform mutation	P_c = 50%		P_c = 70%		P_c = 90%		Adaptive GA	
	Avg # of generations to solution	% successful	Avg # of generations to solution	% successful	Avg # of generations to solution	% successful	Avg # of generations to solution	% successful
P_m = 10%	27.80	25	30.00	15	32.50	30	**33.25**	**60**
P_m = 30%	27.90	50	32.89	45	25.92	45		
P_m = 50%	26.36	55	**28.14**	**70**	30.00	60		
P_m = 70%	38.20	50	34.69	65	34.88	40		

Table 40: The performance of the GA: percentage of successful runs and the average number of generations needed to obtain the solution, using the heuristic crossover operator (feeder #2). Maximum number of generations is 50.

5 reclosers, Heuristic crossover, Uniform mutation	P_c = 50%		P_c = 70%		P_c = 90%		Adaptive GA	
	Avg # of generations to solution	% successful	Avg # of generations to solution	% successful	Avg # of generations to solution	% successful	Avg # of generations to solution	% successful
P_m = 10%	37.5	20	24.67	15	34.2	25	**30.69**	**65**
P_m = 30%	29.17	30	38.08	60	27.15	65		
P_m = 50%	33.08	60	25.38	65	31.47	75		
P_m = 70%	34.79	70	**31.33**	**75**	28.64	70		

Table 41: The performance of the GA: percentage of successful runs and the average number of generations needed to obtain the solution, using the one-point crossover operator (feeder #2). Maximum number of generations is 50.

5 reclosers, One-point crossover, Uniform mutation	P_c = 50%		P_c = 70%		P_c = 90%		Adaptive GA	
	Avg # of generations to solution	% successful	Avg # of generations to solution	% successful	Avg # of generations to solution	% successful	Avg # of generations to solution	% successful
P_m = 10%	34.78	45	37.31	65	**37.07**	**70**	**31.83**	**60**
P_m = 30%	32.30	50	30.17	30	28.83	60		
P_m = 50%	35.46	65	39.38	40	35	40		
P_m = 70%	35.56	45	36.75	20	31	25		

The previous analysis shows the difficulties in determining the optimal parameters that yield a satisfactory combination of convergence properties and provide a reasonable degree of certainty that the obtained solution is the optimal one. As there are no guarantees that the specifically-tuned GA will perform satisfactorily for a large varieties of feeder configurations and sizes, the following conclusions are provided that may be helpful in determining the algorithm parameters for a specific case:

- The nature of the problem indicates that the algorithms perform better for relatively high probabilities of crossover and mutation. The suggested ranges for the probability of crossover and mutation are 70%–90%, and 30%-50%, respectively.
- All three considered crossover operators perform satisfactorily within the reasonable ranges for P_c and P_m. The performed analysis indicates that the arithmetic crossover operator performs marginally better. Furthermore, it is the easiest to implement and always produces feasible solutions, eliminating the need for solution repair. Therefore, it should be given priority over the other two considered operators.
- The performance of the adaptive algorithm is very good, with convergence properties comparable to the results obtained with the best combination of P_c and P_m, although with a slightly lower success rate.
- The algorithm may produce suboptimal solutions if it is terminated prematurely. To avoid premature termination, the algorithm should be either allowed to proceed for a large number of generations, or the relationship between the best and the average fitness in the population should be monitored, and its convergence should be used as a sign that the solution has been reached. A high probability of mutation should not be used if the latter technique is employed.
- As GA may produce suboptimal results, it should be tested multiple times, with different initial conditions. The success ratio and the number of generations needed to reach the solution may be used as the pointers for suitability of applied parameters.

6.6 Application: Optimal DG and recloser placement in distribution networks

As mentioned in Section 6.1, three different optimization problems are investigated:

1. Optimize the placement of protection devices for a given DG allocation.
2. Optimize DG placement for a given protection devices allocation.
3. Optimize both the placement of protection devices and DGs.

Based on the discussion in the previous chapter, the adaptive algorithm with arithmetic crossover was used to calculate optimal positions of protection devices and DGs, for all three cases mentioned above. The results are presented for two test feeders described in Section 6.5.2.

6.6.1 Recloser placement on a feeder equipped with capacity constrained DGs

6.6.1.1 Feeder #1

The first task is to investigate the effect that adding more protection devices has on the reliability of the DG-enhanced feeder. It is assumed, as before, that distributed generators are placed at the end of each lateral, at buses 26, 34, 38, 54, 58 and 90, as shown in Figure 72. Additionally, the effect of the DG sizes on reliability is investigated. Qualitatively, it is expected that larger DGs would be able to support "larger" islands, and therefore would increase overall feeder reliability. The size of each generator is varied (0.3 MW, 0.5 MW and 1 MW per generator), and for each case optimal recloser positions and the corresponding composite reliability index are determined, and the results are compared with the case without DG.

To summarize, the following cases are considered:

- The number of three-phase reclosers is varied from one to five.
- The size of each generator is varied from 0 MW to 1 MW.

The results of the algorithm are presented in Table 42, which shows the best three values for the composite index, and the corresponding branches at which reclosers are placed, when up to five reclosers are strategically placed on the feeder. The branch numbering corresponds with numbering shown in Figure 72.

Table 42: The composite index for various DG sizes and recloser placement strategies (feeder #1). Recloser positions correspond to the branch numbering in Figure 72.

# of reclosers	No DG		P_{max} = 0.3 MW		P_{max} = 0.5 MW		P_{max} = 1 MW	
	Index value	Recloser positions	Index value	Recloser positions	Index value	Recloser positions	Index value	Recloser positions
1	3.2454	8-9	3.1508	8-9	2.7802	8-9	2.7326	8-9
	3.4029	10-11	3.2089	10-11	2.9422	9-10	2.9122	9-10
	3.4160	9-10	3.3038	9-10	3.1026	10-11	3.1023	10-11
2	2.0847	8-9, 30-31	1.9982	8-9, 30-31	1.5624	8-9, 28-29	1.3569	8-9, 48-49
	2.1288	8-9, 27-28	2.0614	8-9, 27-28	1.5904	8-9, 27-28	1.3829	8-9, 49-50
	2.1434	8-9, 28-29	2.0649	8-9, 28-29	1.6258	8-9, 2-27	1.3979	8-9, 27-28
3	1.1937	3-4, 30-31, 47-48	1.1816	3-4, 30-31, 47-48	0.9550	8-9, 28-29, 50-51	0.7745	3-4, 47-48, 27e-28e
	1.1993	4-5, 30-31, 47-48	1.1871	4-5, 30-31, 47-48	0.9733	8-9, 28-29, 51-52	0.7764	4-5, 47-48, 27e-28e
	1.2485	3-4, 2-27, 47-48	1.2345	3-4, 27-28, 47-48	0.9773	8-9, 27-28, 50-51	0.7765	3-4, 47-48, 28e-65
4	0.3981	3-4, 30-31, 47-48, 27e-28e	0.3954	3-4, 30-31, 47-48, 27e-28e	0.3178	4-5, 30-31, 47-48, 67-68	0.2252	8-9, 27-28, 36-37, 49-50
	0.4037	4-5, 30-31, 47-48, 27e-28e	0.4038	3-4, 30-31, 47-48, 28e-65	0.3199	3-4, 30-31, 47-48, 66-67	0.2272	8-9, 28-29, 36-37, 49-50
	0.4068	3-4, 30-31, 47-48, 65-28e	0.4061	3-4, 2-27e, 30-31, 47-48	0.3234	4-5, 30-31, 47-48, 66-67	0.2308	8-9, 27-28, 36-37, 48-49
5	0.1490	3-4, 11-12, 30-31, 47-48, 28e-65	0.0898	3-4, 10-11, 30-31, 47-48, 27e-28e	-0.0305	3-4, 10-11, 30-31, 47-48, 67-68	-0.1484	3-4, 10-11, 30-31, 49-50, 67-68
	0.1546	4-5, 11-12, 30-31, 47-48, 28e-65	0.0982	3-4, 10-11, 30-31, 47-48, 28e-65	-0.0265	4-5, 10-11, 30-31, 47-48, 67-68	-0.1476	3-4, 9-10, 30-31, 49-50, 67-68
	0.1630	4-5, 11-12, 30-31, 47-48, 67-68	0.1041	4-5, 10-11, 30-31, 47-48, 28e-65	-0.0250	3-4, 10-11, 30-31, 47-48, 66-67	-0.1463	4-5, 10-11, 30-31, 49-50, 67-68

In the one-recloser case, recloser placement is dominated by the "conventional" benefits obtained by placing the recloser towards the middle part of the feeder. Additional benefits are realized only from generators located at buses 26 and 58. Generators limited to 0.3 MW may supply the island downstream from branch $8-9$ only for limited portions of time (nominal island load is 0.7 MW), yielding only a marginally better composite index. Generators limited to 0.5 MW provide much better support to the island, resulting in significant composite index improvement. Finally, 1 MW generators are likely to support the island regardless of the instant of the fault, yielding the maximum obtainable improvement.

The similar situation is observed in the case with two reclosers. Generators limited to 0.3 MW and 0.5 MW improve the reliability index, but do not significantly change the optimal recloser positions, compared to the non-DG case. However, in the 1 MW case, the best result is obtained when the second recloser is placed on a $48-49$ branch. Note that this configuration would yield the unsatisfactory composite index value of $C = 2.7179$ if DGs are not present. A similar trend continues for the cases with more than two reclosers. In some cases, the composite index becomes negative, indicating that the target values for reliability indices have been exceeded. This occurs because the target values for reliability indices used in the definition of the composite index in (46) represent a sufficient level of reliability for a conventional distribution network.

Figure 81 shows the optimal placement of *four* reclosers when no DG is available on the feeder, and when six DGs limited to 1 MW are present on the feeder. Note the different optimal recloser positions and lower composite index values in the case of a DG-equipped feeder. Note also the tendency of the algorithm to allocate reclosers as to create islands of supply in the latter case (with DG). For example, without DG a recloser is placed on a branch 47–48 (Figure 81), just upstream from the 48–88 tie line. In a DG-enhanced case, a recloser is placed just downstream from the 48–88 tie line, creating a possible island for all customers downstream from line 49–50. Finally, Figure 82 shows the optimal placement of *five* reclosers, with and without DGs.

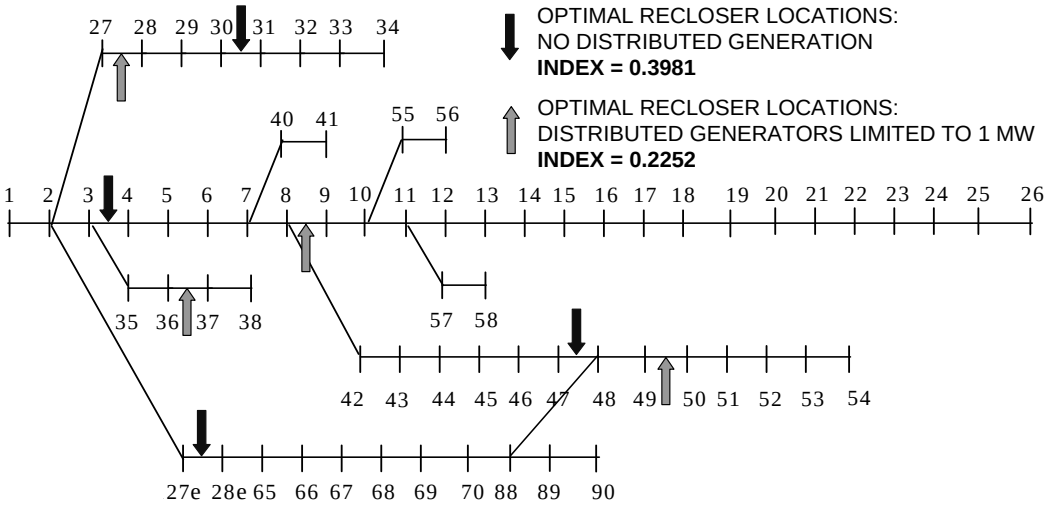

Figure 81: Optimal placement of *four* reclosers on the feeder without DG, and on the feeder equipped with six capacity constrained distributed generators.

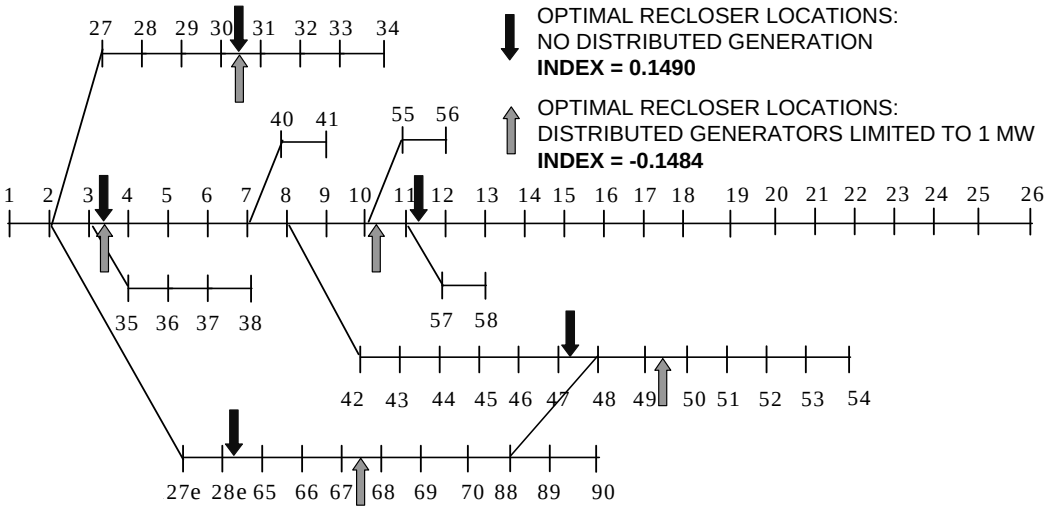

Figure 82: Optimal placement of *five* reclosers on the feeder without DG, and on the feeder equipped with six capacity constrained distributed generators.

Figure 83 shows the improvement in the composite reliability index *C*, as the number of reclosers and the sizes of DGs increase. As expected, *C* is a non-increasing function of both number of reclosers and sizes of individual DGs. Figure 83 also shows the reduced incremental improvements as either of the two parameters (number of reclosers, DG size) increase. Note that the composite index becomes negative for the case with 5 reclosers and 1 MW DGs, indicating that all three target values (for SAIFI, SAIDI and MAIFIe) have been reached.

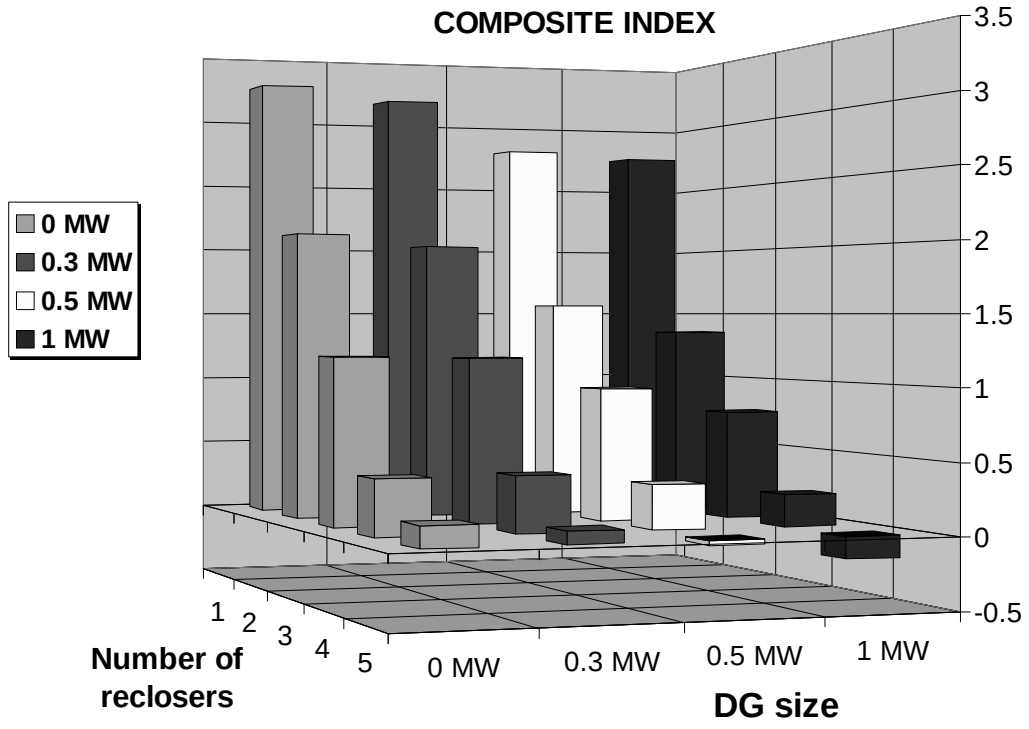

Figure 83: The improvement in composite reliability index as the number of reclosers installed on the feeder and sizes of DGs increase (feeder #1).

6.6.1.2 Feeder #2

The same analysis is repeated for the second test feeder. The distributed generators are placed at buses 120, 155 and 162 (three-phase), and buses 144 and 190 (in phase A). The following cases are considered:

- The number of reclosers is varied from one to five, with up to three three-phase devices and up to two single-phase devices in phase A.
- Size of each generator is varied from 0 MW to 1.0 MW.

For each case, the top three recloser allocations are determined, and presented in Table 43, as well as the corresponding composite indices. Note that single-phase reclosers may only be placed at single-phase branches.

For the case without DG, the addition of more reclosers, increases the overall feeder reliability, as expected and shown in Figure 84. However, the incremental benefits from placing the additional recloser decrease as the total number of reclosers increases. This is especially evident in the last two cases, when the single-phase devices are added.

The addition of DG further improves reliability, and may also change the optimal recloser positions, if the benefits from islanded operation outweigh the "conventional" reliability benefits. For example, in the three-recloser case with DGs limited to 1 MW, the optimal locations of all three reclosers are different than their optimal locations when there are no DGs.

Table 43: The composite index for various DG sizes and recloser placement strategies (feeder #2). Recloser positions correspond to the branch numbering in Figures 63–64.

# of reclosers	No DG		P_{max} = 0.5 MW		P_{max} = 1 MW	
	Index value	Recloser positions	Index value	Recloser positions	Index value	Recloser positions
1 (3-phase)	5.1820	145-148	4.8750	148-149	4.0853	148-149
	5.1842	109-145	4.8882	149-150	4.1069	145-148
	5.2086	148-149	4.9030	145-148	4.1113	149-150
2 (3-phase)	3.4050	109-110, 145-148	3.3129	109-110, 148-149	2.9044	118-120, 149-150
	3.4073	109-110, 109-145	3.3145	109-110, 145-148	2.9242	118-120, 148-149
	3.4316	109-110, 148-149	3.3471	109-110, 149-150	2.9278	110-114, 149-150
3 (3-phase)	2.8986	109-110, 109-145, 158-173	2.7124	109-110, 109-145, 158-159	2.3101	118-120, 148-149, 158-159
	2.9129	109-110, 109-145, 173-174	2.7219	109-110, 145-148, 158-159	2.3196	118-120, 149-150, 158-159
	2.9388	158-173, 109-110, 145-148	2.8235	109-110, 109-145, 158-159	2.3316	109-110, 148-149, 158-159
4 (3 3-phase + 1 1-phase)	2.7108	109-110, 109-145, 158-159, 185-186	2.5045	109-110, 109-145, 158-159, 191-193	2.0507	118-120, 145-148, 158-159, 191-193
	2.7115	109-110, 109-145, 158-159, 180-184	2.5165	109-110, 145-148, 158-159, 191-193	2.0514	118-120, 145-158, 158-159, 186-191
	2.7132	109-110, 109-145, 158-159, 184-185	2.5222	109-110, 145-148, 158-159, 193-195	2.0530	118-120, 148-149, 158-159, 191-193
5 (3 3-phase + 2 1-phase)	2.5990	109-110, 109-145, 158-159, 186-189, 186-191	2.3813	109-110, 109-145, 158-159, 138-140, 191-193	1.8914	109-110, 145-148, 158-159, 138-140, 191-193
	2.6035	109-110, 109-145, 158-159, 138-140, 185-186	2.3933	109-110, 145-148, 158-159, 138-140, 191-193	1.8921	109-110, 145-148, 158-159, 138-140, 186-191
	2.6041	109-110, 109-145, 158-159, 138-140, 180-184	2.3990	109-110, 145-148, 158-159, 138-140, 193-195	1.8999	109-110, 109-145, 158-159, 138-140, 191-193

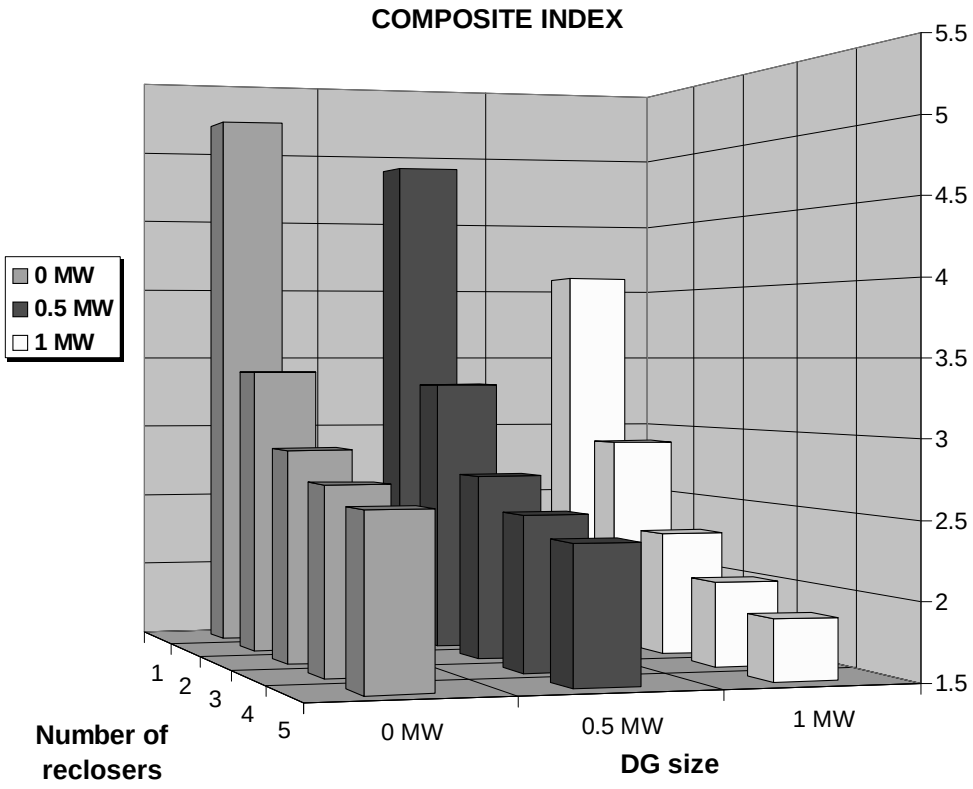

Figure 84: The improvement in composite reliability index as the number of reclosers installed on the feeder and sizes of DGs increase (feeder #2).

6.6.2 DG placement for a given allocation of protection devices

The analogous situation may occur when protection devices are already installed on a feeder, and the task is to determine the best locations for DGs. Although this problem can be solved simply by making the vector of protection devices X in equation (55) constant, the complexity of the problem can be further reduced. Since the existing protection devices divide the feeder into reliability zones (as shown in Figure 72), there is no need to consider different DG locations within the same zone, as they will all lead to the same overall reliability index C. Therefore, instead of coding DG positions as possible buses where DG may be located, it is sufficient to code them using only reliability zones. Furthermore, the calculation of the composite index C is significantly reduced since the reliability zones remain unchanged throughout the optimization procedure, as they only depend on recloser positions.

As mentioned in Section 6.3, placement of N reclosers on the feeder results in up to $(N + 1)$ reliability zones. Thus, there are at most $N' = N + 1$ possible locations for each distributed generator, and possibly less in the case of a non-radial feeder. The number of possible outcomes for placing M distributed generators into N' reliability zones is given by:

$$S = \begin{pmatrix} N' + M - 1 \\ M \end{pmatrix} \tag{74}$$

For example, for test feeder No. 1 with 69 buses and 5 reclosers, the number of possible combinations for placing 4 generators is reduced from 1028790 to no more than 70. Thus, the optimal DG positions may be obtained easily even with the exhaustive search.

6.6.3 Simultaneous allocation of DGs and reclosers

The problem of finding both DG and recloser locations is inherently more complex. The reallocation of only one recloser may change the configuration of reliability zones, and thus may change the reliability index C, even if all DG locations remain unchanged.

The individual solution may be represented as the vector X of DGs and protection devices, as shown before in (55). The elements of the vector X that represent recloser positions correspond to the branch numbers where reclosers may be placed, while the elements that represent DG positions correspond to the appropriate bus numbers. Alternatively, the elements that represent DG positions may again be coded using only the reliability zones, reducing significantly the complexity of the algorithm. In this case, the algorithm is modified slightly, as the number of zones depends on the recloser allocation (N reclosers may create between 1 and $N + 1$ zones).

Tables 44–45 show the results of optimal allocation of reclosers and distributed generators for both test feeders. Table 44 shows the optimal allocation of up to five three-phase reclosers and six generators (limited to 0.5 MW) on a test feeder #1. For comparison, the results obtained without DG and with arbitrary DG allocation considered in Section 6.6.1.1 (DGs at lateral ends) are also presented. Generally, the values for the reliability index C decrease, compared to the case when DGs have been located at lateral ends. The additional improvements are marginal for a small number of reclosers (one or two – not shown in Table 44), as more reclosers are necessary to form significant islands. As the numbers of reclosers increase, the additional benefits due to islanded operation also increase, which is reflected in the significantly reduced reliability index C.

Note that DGs need not be located exactly at the buses shown in Table 44. They may be placed anywhere within the zone that includes the bus shown in Table 44. For example, in the three-recloser case, the reclosers at branches 2-27, 8-9 and 48-49 divide the feeder into four zones. The optimal DG allocation is then, as according to Table 44 – two DGs in the zone that includes bus 26, two DGs in the zone that includes bus 34, and two DGs in

the zone that includes bus 54.

The allocation of reclosers and DGs in the three-recloser case are also shown in Figures 85–86. Figure 85 shows the optimal reclosers allocation when DGs are placed at lateral ends, while Figure 86 shows both the optimal DGs and reclosers positions. Note the creation of three islands downstream from reclosers at branches 2-27, 8-9 and 48-49, and the concentration of DGs within those islands.

Table 45 shows the results of the equivalent study on a test feeder #2.

Table 44: The optimal DGs and reclosers allocation for the test feeder #1. DGs are limited to 0.5 MW.

Number of reclosers	No DG		DG positions fixed			Optimal DG and recloser positions		
	Index value	Recloser positions	Index value	Recloser positions	DG positions	Index value	Recloser positions	DG positions
3	1.1937	3-4	0.9550	8-9	26	0.5480	2-27	26
		30-31		28-29	34		8-9	26
		47-48		50-51	38		48-49	34
					54			34
					58			54
					90			54
4	0.3981	3-4	0.3178	4-5	26	0.2424	7-8	26
		30-31		30-31	34		30-31	26
		47-48		47-48	38		47-48	54
		27e-28e		67-68	54		67-68	54
					58			54
					90			54
5	0.149	3-4	-0.0305	3-4	26	-0.1793	3-4	26
		11-12		10-11	34		10-11	26
		30-31		30-31	38		30-31	26
		47-48		47-48	54		49-50	54
		28e-65		67-68	58		67-68	54
					90			54

Table 45: The optimal DGs and reclosers allocation for the test feeder #2. DGs are limited to 0.5 MW.

Number of reclosers	No DG		DG positions fixed			Optimal DG and recloser positions		
	Index value	Recloser positions	Index value	Recloser positions	DG positions	Index value	Recloser positions	DG positions
3 (3-phase)	2.8986	109-110	2.7124	109-110	120	2.1714	109-110	174
		109-145		109-145	155		109-145	174
		158-173		158-159	162		158-173	174
					144 (A)			198 (A)
					198 (A)			198 (A)
4 (3 3-phase + 1 1-phase)	2.7108	109-110	2.5045	109-110	120	1.9807	109-110	174
		109-145		109-145	155		109-145	174
		158-159		158-159	162		158-173	174
		185-186 (A)		191-193 (A)	144 (A)		191-193 (A)	198 (A)
					198 (A)			198 (A)
5 (3 3-phase + 2 1-phase)	2.599	109-110	2.3813	109-110	120	1.8734	109-110	174
		109-145		109-145	155		109-145	174
		158-159		158-159	162		158-173	174
		186-189 (A)		138-140 (A)	144 (A)		138-140 (A)	198 (A)
		186-191 (A)		191-193 (A)	198 (A)		191-193 (A)	198 (A)

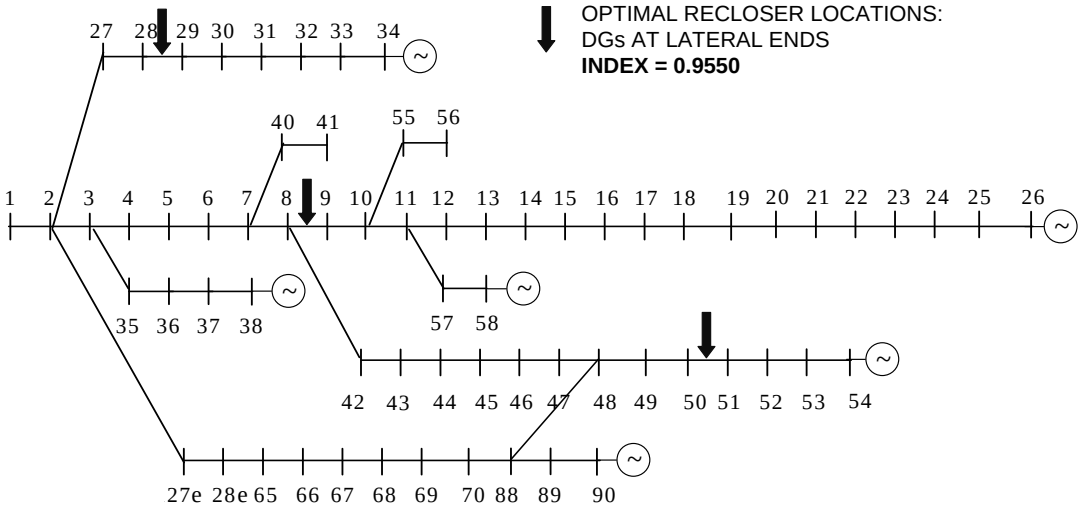

Figure 85: Optimal placement of three reclosers on the test feeder #1 with six DGs placed at lateral ends. DGs are limited to 0.5 MW.

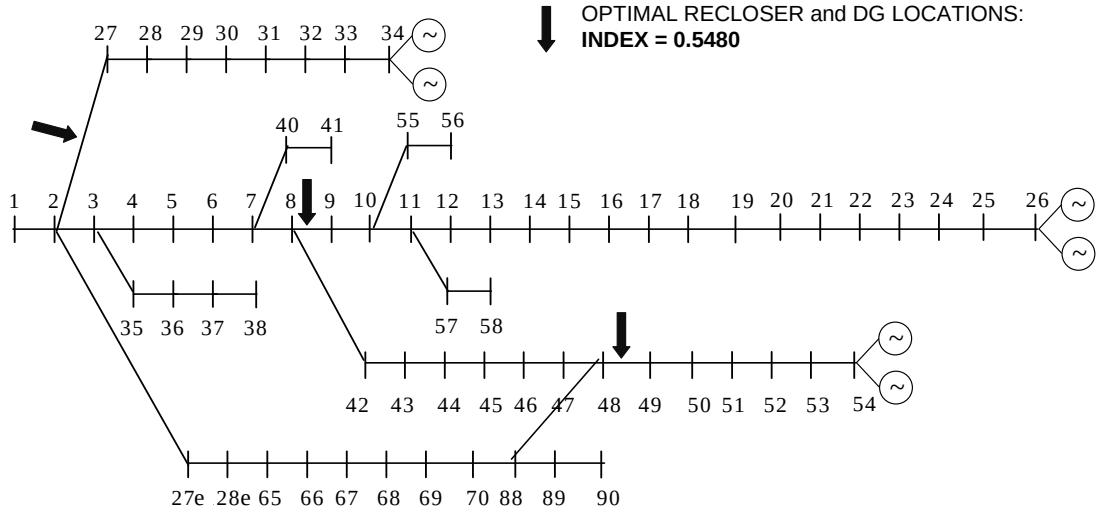

Figure 86: Optimal placement of three reclosers and six DGs on the test feeder #1. DGs are limited to 0.5 MW.

6.7 Conclusions

The issue of improving the reliability of service is presented here, for a complex (non–radial) feeder equipped with DG, by allowing intentional islanding of parts of the feeder. After a fault has been detected and isolated, intentional islanding may be accomplished when parts of the feeder remain online and continue to operate. A reliability model of an asymmetric, three–phase, non–radial distribution feeder equipped with capacity constrained DGs is developed, and used to quantify the improvements due to the islanded operation.

A genetic algorithm (GA) for optimal placement of reclosers on such a feeder is developed and successfully tested on two models of distribution feeders. The influence of several GA parameters (choice of the crossover operator, probabilities of crossover and mutation, etc.) on its convergence properties is investigated and presented in terms of comparative analysis. Furthermore, an adaptive algorithm is presented as a final refinement of the procedure, eliminating the need for determination of optimal probabilities of crossover and mutation.

The incremental reliability improvements, obtained by adding more protection devices and increasing the size of DGs, are also investigated. Finally, the algorithm is used to successfully concurrently optimize both DG and recloser placement, determining the maximum possible reliability improvement for a given number of DGs and reclosers.

The results obtained using two test feeders indicate the possibility for significant reliability improvement. For example, in a test feeder #1, without DG, the composite reliability index decreases from 3.2454 to 0.1490 as the number of reclosers increases from one to five. The addition of six capacity–constrained 0.5 MW distributed generators at lateral ends further reduces the reliability index to 2.7802 and -0.0305, respectively. Note that the optimal recloser positions change, as the benefits due to intentional islanding outweigh the "conventional" reliability benefits. The reliability is further improved if DG locations can also be optimized. For example, in the case with five reclosers, the composite index drops

to -0.1793, if both the DG and reclosers locations are simultaneously determined. Similar results are also obtained with the second test feeder.

The actual reliability improvement for a particular feeder depends on a variety of factors (feeder parameters, frequency of faults, fault restoration times, number of protection devices, sizes of individual DGs, etc.), which all may be treated by the proposed algorithm. The algorithm may be thus used for planning new DG-enhanced feeder designs to maximize the reliability benefits achieved by the addition of distributed generation.

CHAPTER 7

ACCOMPLISHMENTS AND CONTRIBUTIONS

The main contributions of this thesis are:

- A PV system simulation program is developed, which incorporates the most rigorous models for the calculation of insolation, module temperature, and DC and AC power output of a PV system. The ability to model complex system configurations, such as systems with multiple subarrays oriented and/or tilted differently is implemented for the first time. A case study of a multistoried building with PV modules mounted on all four sides showed the annual energy loss of more that 3% due to the operation at the suboptimal power point, which cannot be modeled using existing commercial tools.

  The Monte Carlo procedure for quantifying energy loss due to the random inverter failures is incorporated, as well as the capability of designing the DC/AC conversion stages with multiple parallel inverters. In addition, a novel inverter control strategy is proposed, which further improves the energy yield of systems with multiple parallel inverters. The strategy is designed to selectively shut down one or more inverters during periods of low insolation, enabling the remaining inverters to operate at higher conversion efficiency. Finally, a cost/benefit analysis is presented to determine the optimal system configuration that yields minimal system life–cycle costs.

  The results of a case study for a 342 kW PV system, with inverter failure characteristics obtained from the field data, show the superiority of the parallel inverter configuration. In the considered example, the parallel inverter configuration yields

up to 4% percent more energy over the lifetime of the system, compared to a single–inverter system. The selective inverter shutdown strategy yields additional 2-2.5%, depending on the number of inverters in the system. The optimal inverter configuration in this example, based on the criterion of minimal system life–cycle costs, is a three-inverter system with selective inverter shutdown, yielding a net gain of $53,000 (more than 4% of the total system gain), compared to a single–inverter system.

- A procedure is developed to incorporate the uncertainties imposed by stochastic, renewable DG into the conventional tools for analysis of distribution systems. A clustering algorithm is proposed to reduce large input data sets that result from the interaction of stochastic processes that drive DG output with field measurements of feeder load profiles. The reduced data set is used to obtain conventional duration curves and estimates of feeder operational characteristics (voltage levels, losses, etc.). In addition, a procedure is proposed to determine the boundary points of the original data set, which yield feeder extreme operating conditions. Finally, a Monte Carlo analysis (using a reduced data set) is presented, to determine the effects of deploying a large number of renewable DG systems on a distribution feeder.

  The procedure is demonstrated on a 69–segment distribution feeder with randomly placed photovoltaic generators totaling approximately 20% od feeder nominal load. The effects of sizes of individual systems, their random spatial allocation and different inverter configurations on several feeder characteristics, such as local voltage levels, substation level power factor, and branch loading levels are quantified.

  In the considered example, the addition of PV decreases the average active and reactive feeder losses between 12.7%–19.7% and 11.7%–18.3% respectively, depending on the PV distribution scheme and inverter configuration. Furthermore, the feeder active power consumption decreases by approximately 8.5%, while the reactive consumption decreases by almost 40%, if the inverters are allowed to inject maximum

reactive power allowed by their rating. Consequently, the substation–level power factor in this case is significantly improved – its average value increases to 0.9619 from the value of 0.9280 for the case without PV.

With a reduced data set, larger number of similar studies can be performed in comparable time, thus providing more answers to the designer of DG-enhanced networks. Possible applications of the proposed method include studies for optimal DG placement, feeder expansion, Volt/VAR support design, conservation voltage reduction design and reliability studies.

- The reliability model of an asymmetric, three–phase, non-radial distribution feeder equipped with capacity–constrained DGs is developed. The developed model is used to quantify the potential reliability improvements due to the intentional islanded operation of parts of the feeder.

  To that end, a genetic algorithm (GA) for optimal placement of reclosers and/or DGs on such a feeder is developed, and successfully tested on two models of distribution feeders. The influence of several GA parameters (choice of the crossover operator, probabilities of crossover and mutation, etc.) on its convergence properties is investigated and presented in terms of comparative analysis. Furthermore, an adaptive algorithm is presented as a final refinement of the procedure, eliminating the need for determination of optimal probabilities of crossover and mutation.

  The results obtained using two test feeders indicate the possibility for significant reliability improvement. For example, in a test feeder #1, without DG, the composite reliability index decreases from 3.2454 to 0.1490 when the number of reclosers increases from one to five. The addition of six capacity–constrained 0.5 MW distributed generators at lateral ends further reduces the reliability index to 2.7802 and -0.0305, respectively. Note that the optimal recloser positions change, as the benefits

due to intentional islanding outweigh the “conventional” reliability benefits. The reliability is further improved if DG locations can also be optimized. For example, in the case with five reclosers, the composite index drops to -0.1793 if both the DG and reclosers locations are simultaneously determined. Similar results are obtained with the second test feeder.

The actual reliability improvement for a particular feeder depends on a variety of factors (feeder parameters, frequency of faults, fault restoration times, number of protection devices, sizes of individual DGs, etc.), which all may be treated by the proposed algorithm. The algorithm may be thus used for planning new DG-enhanced feeder designs to maximize the reliability benefits achieved by the addition of distributed generation.

APPENDIX A

CALCULATION OF THE SOLAR ANGLES

The exact position of the sun is determined by calculating the following angles:

- *Declination of the sun*, δ, is the angle between the earth's equatorial plane and the line joining the centers of the sun and the earth.
- *Solar elevation (altitude) angle*, α_s, describes how high the sun appears in the sky. It is measured between the horizontal and the line to the sun. Its complement is the zenith angle, θ_z, the angle between the vertical and the line to the sun.
- *Solar azimuth angle*, γ_s, is the angular displacement (from south) of the projection of the line to the sun on the horizontal plane.

These three angles completely determine the position of the sun. They allow the calculation of the angle of incidence, θ - the angle between the line to the sun and a normal to the array surface. The incidence angle determines the mutual position between the sun and the array and allows the calculation of the plane of array insolation from the standardized insolation measurements. The following is a detailed procedure for determining these solar angles, mostly based on [14], with modifications as noted.

Declination of the sun

Declination of the sun, δ, is the angle between the earth's equatorial plane and the line joining the centers of the sun and the earth.

The plane of the earth's orbit around the sun is called the ecliptic plane. The earth itself rotates around the polar axis, which is 23.45° from the normal to the ecliptic plane

throughout the year. The declination of the sun therefore changes constantly. At winter solstice it is -23.45°, at summer solstice the declination is +23.45°, while at the spring and autumn equinoxes the declination is zero. The declination δ can be calculated using the following formula (d is the day of the year).

$$\delta = 23.45^{\circ} \sin x \tag{75}$$

where

$$x = \frac{360}{365}(d - 81) \tag{76}$$

Solar time and the hour angle

The solar time is based on the apparent angular motion of the sun across the sky, and is not the same as the local (clock) time. All sun-angle relationships used in PV systems modeling are based on the solar time. Therefore, it is necessary to convert local time to solar time. The local time of a particular time zone is based on its standard meridian. The noon (local time) is defined as the time when the sun crosses the standard meridian of that time zone, and is the same for all observers within the time zone. However, solar noon is defined as the time when the sun crosses the local meridian of the observer.

Standard meridians for continental US time zones are Eastern 75°W, Central 90°W, Mountain 105°W and Pacific 120°W, and are located in the middle of their respective time zones. All standard meridians are 15° apart, since it takes 4 minutes for sun to transverse 1° of longitude. Thus, to be able to calculate the solar time, local time needs to be adjusted as follows:

$$T = t + (StandardMeridian - LocalMeridian) \cdot 4' + EoT \tag{77}$$

where T is the solar time, t is the local time, and EoT is a so-called “equation of time”. First correction accounts for the difference between the observer’s local meridian (longitude) and the standard meridian on which the local standard time is based. The correction above should be positive if site is east of the standard meridian. Also, note that the local time should be adjusted for daylight savings time, if necessary.

The equation of time accounts for perturbations in the earth's rate of rotation around the sun, which affects the time the sun crosses the observer's meridian. It can be approximated using the following formula.

$$EoT = 9.87 \sin x - 7.53 \cos x - 1.5 \sin x \tag{78}$$

where, d is the current day of the year, and x is defined as

$$x = \frac{360}{365}(d - 81) \tag{79}$$

Hour angle w is the angle between the line pointing directly to the sun and the line pointing directly to the sun at solar noon. Fifteen degrees represent one hour, since the earth rotates 360 degrees every 24 hours. Hour angle w can thus be calculated using the following formula, assuming that the solar time T is given in hours.

$$w = (T - 12) \cdot 15 \tag{80}$$

Note that the hour angle is just an angular representation of solar time.The hour angle is negative in the morning, zero at solar noon, and positive in the afternoon. Note also that the sun does not necessarily rises/sets when the hour angle is +/- 90°. The hour angle is used to calculate the remaining two solar angles, solar elevation α_s and solar azimuth γ_s. Incorrect calculation of the hour angle may therefore lead to significant errors in POA insolation calculations.

The problem with using historical weather data from the TMY2 database ([10]) is that the insolation is typically given as a total insolation *energy* measured during the *preceding* hour. Since all solar angle calculations require the value of incident instantaneous insolation, it is typically assumed that the insolation was uniform throughout the preceding hour. The insolation value at the middle of the hourly interval (i.e. 30 minutes before the hour) is used for the calculations.

This approach may give erroneous results when calculating insolation early in the morning and late in the afternoon. If, for a particular day, the sun rises after the middle point

of the hourly interval (in the last 30 minutes of the preceding hour), the solar angles calculation may yield incorrect results. This is because the calculations are performed at a time when the sun is still below the horizon. Typically, this leads to incorrect values for solar elevation and altitude, and, in turn, leads to unreasonably high POA insolation values. Similar situation occurs at sunset, when the sun sets in the first 30 minutes of the hour.

To avoid these errors, in the GT simulator the exact times of sunrise w_r and sunset w_s are calculated using the following formulas:

$$w_r = \arccos(-\frac{\sin\Phi \sin\delta}{\cos\Phi \cos\delta}) \tag{81}$$

$$w_s = -\arccos(-\frac{\sin\Phi \sin\delta}{\cos\Phi \cos\delta}) \tag{82}$$

where Φ is the latitude (north positive, south negative) and δ is the declination of the sun. Now, if the hour angle w is more negative than w_r, the hour angle is adjusted as a middle point between w_r and the next hour, i.e. :

$$w = \frac{1}{2}(w + \frac{15^\circ}{2} + w_r) \quad \text{if } w < w_r \tag{83}$$

Similarly, at sunset, the hour angle is adjusted via:

$$w = \frac{1}{2}(w + \frac{15^\circ}{2} + w_s) \quad \text{if } w > w_s \tag{84}$$

This approach assures that the solar angles are always calculated after sunrise in the morning, or before sunset in the evening.

Solar elevation (altitude)

The altitude angle, α_s, describes how high the sun appears in the sky. It is measured between the horizontal and the line to the sun. Its complement is the zenith angle, Θ_z, the angle between the vertical and the line to the sun. The altitude and zenith angle are calculated using the following formula:

$$\sin\alpha_s = \cos\Theta_z = \cos\Phi \cos\delta \cos w + \sin\Phi \sin\delta \tag{85}$$

where Φ is the observers's latitude, δ is the declination of the sun and w is the hour angle.

Solar azimuth

Solar azimuth is the angular displacement from south of the projection of the line to the sun on the horizontal plane. It is calculated as follows.

$$\gamma_s = c_1 c_2 \gamma_s' + c_3(1 - c_1 c_2)\frac{\pi}{2} \tag{86}$$

where

$$\gamma_s' = \arcsin \frac{\sin w \cos \delta}{\sin \Theta_z} \tag{87}$$

$$c_1 = \begin{cases} 1 & \text{if } |w| < w_{ew} \text{ or } \frac{\tan \delta}{\tan \Phi} > 1 \\ -1 & \text{otherwise} \end{cases} \tag{88}$$

$$c_2 = \begin{cases} 1 & \text{if } \Phi(\Phi - \delta) \geq 0 \\ -1 & \text{otherwise} \end{cases} \tag{89}$$

$$c_3 = \begin{cases} 1 & \text{if } w \geq 0 \\ -1 & \text{otherwise} \end{cases} \tag{90}$$

$$w_{ew} = \arccos \frac{\tan \delta}{\tan \Phi} \tag{91}$$

where Θ_z is the zenith angle, Φ is the observer's latitude, w is the hour angle and δ is the declination of the sun.

Angle of incidence

Finally, the angle of incidence Θ is the angle between the beam radiation on a surface and the normal to that surface. The angle of incidence allows the calculation of plane of array insolation components, as described in Chapter 2. It can be calculated using the following equation, where α_s is the altitude angle of the sun, β is the tilt of the array, γ_s is the solar azimuth and γ is the azimuth (orientation) of the array.

$$\Theta = \arccos(\sin \alpha_s \cos \beta + \sin \beta \cos \alpha_s \cos(\gamma_s - \gamma)) \tag{92}$$

APPENDIX B

OPTIMIZATION OF RELIABILITY OF RADIAL FEEDERS

The feeder parameters used for the reliability analysis presented in Chapter 5 are presented in Table 46. All five parameters are defined in Section 5.4.

Table 46: Parameters used for the reliability analysis of three radial feeders.

Parameter	Value
Damage restoration time (DRT)	3 hours
Manual restoration time (MRT)	2.5 hours
Fault incidence rate (FIR)	0.22
Fraction of permanent faults (FPF)	0.2
Percent protected (PP)	0.15

For all three feeder layouts, the following possible recloser placement strategies are investigated and compared to the base case with only a substation breaker installed at the substation:

1. Addition of only one recloser on the main branch.
2. Addition of one recloser on the main branch, and a fuse on each lateral.
3. Addition of two reclosers on the main branch.
4. Addition of two reclosers on the main branch, and a fuse on each lateral.
5. Addition of one recloser on the main branch, and a recloser on each lateral.

The lateral elements (fuses or reclosers) in cases 1), 3) and 5) above are placed on the beginning of each lateral. The locations of lateral elements for all three considered feeders are given in Table 47.

Table 47: The positions of lateral protection devices, for all three considered feeders. The branch numbering corresponds with the branch numbering in Figure 61, Figure 62 and Figures 63–64 for urban, suburban and rural feeders, respectively.

Feeder type	Locations of lateral protection elements
Urban	33135, 33145, 7679-1543, 7679-2642, 7679-3050, 7679-7174, 7679-8762
Suburban	S10306, S10370, S10380, S11253, S25801, 6582-7897-0, 6482-9992-0
Rural	110, 122, 129, 137, 159, 165, 175, 181, 184

The results of the analysis for all three feeders are presented below. For each case, the top five recloser allocations and the corresponding reliability indices are presented. Furthermore, the sensitivity analysis performed for the suburban feeder in Section 5.4 (Tables 18–22) is repeated for rural and urban feeders. The results are presented in Tables 58–62 for the rural feeder and Tables 68–72 for the urban feeder.

Suburban feeder

Table 48: Top five positions for adding a single recloser to the suburban feeder equipped only with a substation breaker.

Case	Recloser Locations	Comp. Index	SAIFI	SAIDI	MAIFIe	CAIDI	ASAI	Dist. from subst. [mi]	% of cust. down-stream
	Base Indices	3.230	4.343	13.028	17.371	3.000	99.851		
1	S10340ABC	1.785	2.860	8.579	11.438	3.000	99.902	9.3	16
2	C-6583-7203-0ABC	1.807	2.882	8.646	11.527	3.000	99.901	9.4	16
3	C-6583-0803-0ABC	1.823	2.899	8.696	11.594	3.000	99.901	12.6	8
4	S10344ABC	2.074	3.156	9.469	12.625	3.000	99.892	12.6	8
5	6483-9902-0ABC	2.080	3.162	9.487	12.650	3.000	99.892	13	4

Table 49: Top five positions for adding a single recloser to the suburban feeder equipped with a substation breaker and lateral fuses.

Case	Recloser Locations	Comp. Index	SAIFI	SAIDI	MAIFIe	CAIDI	ASAI	Dist. from subst. [mi]	% of cust. down-stream
	Base Indices	0.942	2.097	6.157	7.049	2.936	99.930		
1	S10340ABC	0.474	1.617	4.718	5.131	2.917	99.946	9.3	16
2	C-6583-7203-0ABC	0.496	1.640	4.785	5.220	2.918	99.945	9.4	16
3	C-6583-0803-0ABC	0.512	1.656	4.835	5.287	2.919	99.945	12.6	8
4	C-6682-0492-0ABC	0.578	1.723	5.036	5.555	2.922	99.943	6.8	59
5	S11046ABC	0.598	1.744	5.098	5.637	2.923	99.942	7.3	59

Table 50: Top five locations for adding a single recloser to the suburban feeder equipped with a substation breaker and lateral reclosers.

Case	Recloser Locations	Comp. Index	SAIFI	SAIDI	MAIFIe	CAIDI	ASAI	Dist. from subst. [mi]	% of cust. down-stream
	Base Indices	0.912	1.963	5.889	7.852	3	99.933		
1	S10340ABC	0.445	1.483	4.45	5.934	3	99.949	9.3	16
2	C-6583-7203-0ABC	0.467	1.506	4.517	6.023	3	99.948	9.4	16
3	C-6583-0803-0ABC	0.483	1.522	4.567	6.09	3	99.948	12.6	8
4	C-6682-0492-0ABC	0.548	1.589	4.768	6.358	3	99.946	6.8	59
5	S11046ABC	0.568	1.61	4.83	6.44	3	99.945	7.3	59

Table 51: Top five positions for adding two reclosers to the suburban feeder equipped only with a substation breaker.

Case	Recloser Locations	Comp. Index	SAIFI	SAIDI	MAIFIe	CAIDI	Dist. from subst. [mi]		% of cust. down-stream	
							1st	2nd	1st	2nd
	Base Indices	3.230	4.343	13.028	17.371	3.000				
1	S10340A,S10370ABC	0.876	1.926	5.779	7.705	3.000	9.3	2.4	16	90
2	C-6583-7203-0A,S10370ABC	0.898	1.949	5.846	7.794	3.000	9.4	2.4	16	90
3	C-6583-0803-0A,S10370ABC	0.914	1.965	5.896	7.861	3.000	13	2.4	8	90
4	S10340A,6681-0546-0ABC	1.014	2.068	6.204	8.272	3.000	9.3	2.8	16	90
5	C-6583-7203-0A,6681-0546-0ABC	1.036	2.090	6.271	8.361	3.000	9.4	2.8	16	90

Table 52: Top five positions for adding two reclosers to the suburban feeder equipped with a substation breaker and lateral fuses.

Case	Recloser Locations	Comp. Index	SAIFI	SAIDI	MAIFIe	CAIDI	Dist. from subst. [mi]		% of cust. down-stream	
							1st	2nd	1st	2nd
1	Base Indices	0.942	2.097	6.157	7.049	2.936				
2	S10340A,6682-0384-0ABC	0.334	1.473	4.286	4.554	2.909	9.3	6.4	16	59
3	S10340A,C-6682-0492-0ABC	0.337	1.477	4.296	4.568	2.909	9.3	6.8	16	59
4	C-6583-7203-0A,6682-0384-0ABC	0.347	1.487	4.326	4.608	2.910	9.4	6.4	16	59
5	C-6583-7203-0A,C-6682-0492-0ABC	0.349	1.488	4.33	4.613	2.910	9.4	6.8	16	59

Rural feeder

Table 53: Top five positions for adding a single recloser to the rural feeder equipped only with a substation breaker.

Case	Recloser Locations	Comp	SAIFI	SAIDI	MAIFIe	CAIDI	ASAI	Dist. from subst. [mi]	% of cust. down-stream
	Base Indices	8.145	9.389	28.165	37.554	3.000	99.678		
1	148ABC	5.227	6.393	19.180	25.573	3.000	99.781	7.94	43
2	145ABC	5.263	6.430	19.290	25.720	3.000	99.780	6.25	46
3	149ABC	5.264	6.431	19.294	25.725	3.000	99.780	9.69	41
4	150ABC	5.334	6.503	19.509	26.012	3.000	99.777	11.44	40
5	155ABC	5.406	6.577	19.731	26.308	3.000	99.775	12.56	37

Table 54: Top five positions for adding a single recloser to the rural feeder equipped with a substation breaker and lateral fuses.

Case	Recloser Locations	Comp	SAIFI	SAIDI	MAIFIe	CAIDI	ASAI	Dist. from subst. [mi]	% of cust. down-stream
	Base Indices	3.647	5.6	15.728	11.682	2.809	99.82		
1	145ABC	2.586	4.51	12.46	7.323	2.762	99.858	6.25	46
2	148ABC	2.644	4.57	12.638	7.561	2.765	99.856	7.94	43
3	149ABC	2.74	4.669	12.934	7.955	2.77	99.852	9.69	41
4	150ABC	2.854	4.786	13.285	8.424	2.776	99.848	11.44	40
5	155ABC	3.037	4.974	13.849	9.176	2.784	99.842	12.56	37

Table 55: Top five locations for adding a single recloser to the rural feeder equipped with a substation breaker and lateral reclosers.

Case	Recloser Locations	Comp	SAIFI	SAIDI	MAIFIe	CAIDI	ASAI	Dist. from subst. [mi]	% of cust. down-stream
	Base Indices	2.856	3.959	11.878	15.837	3.000	99.864		
1	145ABC	1.795	2.870	8.609	11.479	3.000	99.902	6.25	46
2	148ABC	1.853	2.929	8.788	11.717	3.000	99.900	7.94	43
3	149ABC	1.949	3.028	9.083	12.111	3.000	99.896	9.69	41
4	150ABC	2.063	3.145	9.435	12.580	3.000	99.892	11.44	40
5	155ABC	2.246	3.333	9.998	13.331	3.000	99.886	12.56	37

Table 56: Top five positions for adding two reclosers to the rural feeder equipped only with a substation breaker.

Case	Recloser Locations	Comp	SAIFI	SAIDI	MAIFIe	CAIDI	Dist. from subst. [mi]		% of cust. down-stream	
							1st	2nd	1st	2nd
	Base Indices	8.145	9.389	28.165	37.554	3.000				
1	148A, 110ABC	3.388	4.505	13.515	18.02	3.000	7.94	8.31	43	37
2	145A, 110ABC	3.424	4.542	13.625	18.167	3.000	6.25	8.31	46	37
3	149A, 110ABC	3.425	4.543	13.629	18.172	3.000	9.69	8.31	41	37
4	150A, 110ABC	3.495	4.615	13.844	18.459	3.000	11.4	8.31	40	37
5	155A, 110ABC	3.567	4.689	14.066	18.755	3.000	12.6	8.31	37	37

Table 57: Top five positions for adding two reclosers to the rural feeder equipped with a substation breaker and lateral fuses.

Case	Recloser Locations	Comp	SAIFI	SAIDI	MAIFIe	CAIDI	Dist. from subst. [mi]		% of cust. down-stream	
							1st	2nd	1st	2nd
	Base Indices	3.647	5.6	15.728	11.682	2.809				
1	184A, 145ABC	2.323	4.07	11.359	7.764	2.791	18.9	6.25	11	46
2	185A, 145ABC	2.329	4.082	11.386	7.744	2.790	20.1	6.25	11	46
3	186A, 145ABC	2.338	4.099	11.427	7.705	2.788	21.9	6.25	10	46
4	187A, 145ABC	2.345	4.118	11.469	7.629	2.785	21.9	6.25	9	46
5	188A, 145ABC	2.345	4.118	11.469	7.629	2.785	21.9	6.25	9	46

Table 58: Sensitivity of reliability indices to the damage restoration time (rural feeder).

DRT [h]	SAIFI		SAIDI		MAIFIe		CAIDI		ASAI		Composite	
	Value	Sens.	Value	Sens.	Value	Sens.	Value	Sens.	Value	Sens.	Value	Sens.
2.75	4.510	0	11.868	0.57	7.323	0	2.631	0.57	99.865	0.00	2.478	0.50
3.00	4.510		12.460		7.323		2.762		99.858		2.586	
3.25	4.510	0	13.051	0.57	7.323	0	2.894	0.57	99.851	0.00	2.694	0.50

Table 59: Sensitivity of reliability indices to the manual restoration time (rural feeder).

MRT [h]	SAIFI		SAIDI		MAIFIe		CAIDI		ASAI		Composite	
	Value	Sens.	Value	Sens.	Value	Sens.	Value	Sens.	Value	Sens.	Value	Sens.
2.25	4.510	0	11.924	0.43	7.323	0	2.644	0.43	99.864	0.00	2.488	0.38
2.50	4.510		12.460		7.323		2.762		99.858		2.586	
2.75	4.510	0	12.996	0.43	7.323	0	2.881	0.43	99.852	0.00	2.683	0.38

Table 60: Sensitivity of reliability indices to the fault incidence rate (rural feeder).

FIR	SAIFI		SAIDI		MAIFIe		CAIDI		ASAI		Composite	
	Value	Sens.	Value	Sens.	Value	Sens.	Value	Sens.	Value	Sens.	Value	Sens.
0.17	3.485	1.00	9.628	1.00	5.659	1.00	2.762	0	99.890	0.00	1.771	1.39
0.22	4.510		12.460		7.323		2.762		99.858		2.586	
0.27	5.536	1.00	15.291	1.00	8.988	1.00	2.762	0	99.825	0.00	3.401	1.39

Table 61: Sensitivity of reliability indices to the fraction of permanent faults (rural feeder).

FPF	SAIFI		SAIDI		MAIFIe		CAIDI		ASAI		Composite	
	Value	Sens.	Value	Sens.	Value	Sens.	Value	Sens.	Value	Sens.	Value	Sens.
0.15	4.053	0.41	11.019	0.46	7.781	-0.25	2.719	0.06	99.874	0.00	2.259	0.51
0.20	4.510		12.460		7.323		2.762		99.858		2.586	
0.25	4.968	0.41	13.900	0.46	6.866	-0.25	2.798	0.05	99.841	0.00	2.913	0.51

Table 62: Sensitivity of reliability indices to the percentage of fuses protected (rural feeder).

PP	SAIFI		SAIDI		MAIFIe		CAIDI		ASAI		Composite	
	Value	Sens.	Value	Sens.	Value	Sens.	Value	Sens.	Value	Sens.	Value	Sens.
0%	4.510		12.460		7.323		2.762		99.858		2.586	
15%	4.189	-0.47	11.656	-0.43	27.961	18.79	2.783	0.05	99.867	0.00	3.555	2.50
30%	3.867	-0.48	10.852	-0.43	28.282	9.54	2.806	0.05	99.876	0.00	3.363	1.00

Urban feeder

Table 63: Top five positions for adding a single recloser to the urban feeder equipped only with a substation breaker.

Case	Recloser Locations	Comp. Index	SAIFI	SAIDI	MAIFIe	CAIDI	ASAI	Dist. from subst. [mi]	% of cust. down-stream
	Base Indices	0.630	1.674	5.021	6.695	3.000	99.943		
1	7679-8562ABC	0.387	1.424	4.271	5.695	3.000	99.951	5.3	61.0
2	20524ABC	0.400	1.437	4.312	5.750	3.000	99.951	5.6	55.0
3	7679-8762ABC	0.403	1.440	4.321	5.762	3.000	99.951	5.4	55.0
4	7679-3050ABC	0.426	1.464	4.391	5.854	3.000	99.950	1.4	4 (lat)
5	20523ABC	0.442	1.481	4.442	5.923	3.000	99.949	5.6	21.0

Table 64: Top five positions for adding a single recloser to the urban feeder equipped with a substation breaker and lateral fuses.

Case	Recloser Locations	Comp. Index	SAIFI	SAIDI	MAIFIe	CAIDI	ASAI	Dist. from subst. [mi]	% of cust. down-stream
	Base Indices	-0.056	1.020	2.994	3.421	2.936	99.966		
1	7679-8562ABC	-0.140	0.934	2.736	3.078	2.930	99.969	5.3	61
2	20450ABC	-0.131	0.943	2.764	3.116	2.930	99.968	2.9	85
3	20915ABC	-0.128	0.946	2.774	3.128	2.931	99.968	4.2	76
4	20916ABC	-0.128	0.946	2.773	3.127	2.930	99.968	3.8	78
5	26108ABC	-0.127	0.947	2.775	3.130	2.931	99.968	3.1	83

Table 65: Top five locations for adding a single recloser to the urban feeder equipped with a substation breaker and lateral reclosers.

Case	Recloser Locations	Comp. Index	SAIFI	SAIDI	MAIFIe	CAIDI	ASAI	Dist. from subst. [mi]	% of cust. down-stream
	Base Indices	-0.071	0.954	2.862	3.816	3	99.967		
1	7679-8562ABC	-0.155	0.868	2.604	3.472	3	99.97	5.3	61
2	20450ABC	-0.145	0.878	2.633	3.511	3	99.97	2.9	85
3	20916ABC	-0.143	0.88	2.641	3.521	3	99.97	3.8	78
4	26107ABC	-0.142	0.881	2.643	3.524	3	99.97	3.1	83
5	20915ABC	-0.142	0.881	2.642	3.523	3	99.97	4.2	76

Table 66: Top five positions for adding two reclosers to the urban feeder equipped only with a substation breaker.

Case	Recloser Locations	Comp. Index	SAIFI	SAIDI	MAIFIe	CAIDI	Dist. from subst. [mi]		% of cust. down-stream	
							1st	2nd	1st	2nd
	Base Indices	0.630	1.674	5.021	6.695	3.000				
1	7679-8562A,7679-3050ABC	0.182	1.213	3.640	4.854	3.000	5.3	1.4	61	4
2	20524A,7679-3050ABC	0.195	1.227	3.682	4.909	3.000	5.4	1.4	55	4
3	7679-8762A,7679-3050ABC	0.198	1.230	3.691	4.921	3.000	5.4	1.4	61	4
4	7679-8562A,7679-2954ABC	0.206	1.239	3.716	4.955	3.000	5.3	1.6	61	4
5	20524A,7679-2954ABC	0.220	1.252	3.757	5.010	3.000	5.4	1.6	61	4

Table 67: Top five positions for adding two reclosers to the urban feeder equipped with a substation breaker and lateral fuses.

Case	Recloser Locations	Comp. Index	SAIFI	SAIDI	MAIFIe	CAIDI	Dist. from subst. [mi]		% of cust. down-stream	
							1st	2nd	1st	2nd
	Base Indices	-0.056	1.020	2.994	3.421	2.936				
1	20523A, 20450ABC	-0.189	0.884	2.586	2.878	2.926	5.6	2.9	21	85
2	20523A, 26107ABC	-0.184	0.889	2.601	2.898	2.926	5.6	3.1	21	83
3	20523A, 7679-4658ABC	-0.183	0.889	2.602	2.900	2.926	5.6	3	21	84
4	7679-8562A, 20450ABC	-0.183	0.889	2.602	2.899	2.926	5.3	2.9	61	85
5	20523A, 26108ABC	-0.183	0.889	2.602	2.899	2.926	5.6	3.6	21	83

Table 68: Sensitivity of reliability indices to the damage restoration time (urban feeder).

DRT [h]	SAIFI		SAIDI		MAIFIe		CAIDI		ASAI		Composite	
	Value	Sens.	Value	Sens.	Value	Sens.	Value	Sens.	Value	Sens.	Value	Sens.
2.75	0.934	0	2.535	0.88	3.078	0	2.715	0.88	99.971	0.00	-0.176	-3.09
3.00	0.934		2.736		3.078		2.930		99.969		-0.140	
3.25	0.934	0	2.936	0.88	3.078	0	3.144	0.88	99.966	0.00	-0.104	-3.09

Table 69: Sensitivity of reliability indices to the manual restoration time (urban feeder).

MRT [h]	SAIFI		SAIDI		MAIFIe		CAIDI		ASAI		Composite	
	Value	Sens.	Value	Sens.	Value	Sens.	Value	Sens.	Value	Sens.	Value	Sens.
2.25	0.934	0	2.703	0.12	3.078	0	2.894	0.12	99.969	0.00	-0.146	-0.43
2.50	0.934		2.736		3.078		2.930		99.969		-0.140	
2.75	0.934	0	2.768	0.12	3.078	0	2.965	0.12	99.968	0.00	-0.134	-0.43

Table 70: Sensitivity of reliability indices to the fault incidence rate (urban feeder).

FIR	SAIFI		SAIDI		MAIFIe		CAIDI		ASAI		Composite	
	Value	Sens.	Value	Sens.	Value	Sens.	Value	Sens.	Value	Sens.	Value	Sens.
0.17	0.722	1.00	2.114	1.00	2.378	1.00	2.930	0	99.976	0.00	-0.335	-6.13
0.22	0.934		2.736		3.078		2.930		99.969		-0.140	
0.27	1.146	1.00	3.357	1.00	3.777	1.00	2.930	0	99.962	0.00	0.055	-6.13

Table 71: Sensitivity of reliability indices to the fraction of permanent faults (urban feeder).

FPF	SAIFI		SAIDI		MAIFIe		CAIDI		ASAI		Composite	
	Value	Sens.	Value	Sens.	Value	Sens.	Value	Sens.	Value	Sens.	Value	Sens.
0.15	0.741	0.83	2.154	0.85	3.27	-0.25	2.906	0.03	99.98	0.00	-0.273	-3.80
0.20	0.934		2.736		3.078		2.930		99.969		-0.140	
0.25	1.126	0.82	3.317	0.85	2.885	-0.25	2.945	0.02	99.96	0.00	-0.007	-3.80

Table 72: Sensitivity of rel. indices to the percentage of fuses protected (urban feeder).

PP	SAIFI		SAIDI		MAIFIe		CAIDI		ASAI		Composite	
	Value	Sens.	Value	Sens.	Value	Sens.	Value	Sens.	Value	Sens.	Value	Sens.
0%	0.934		2.736		3.078		2.930		99.969		-0.140	
15%	0.914	-0.14	2.686	-0.12	6.204	6.77	2.939	0.02	99.97	0.00	0.026	-7.90
30%	0.894	-0.14	2.637	-0.12	6.224	3.41	2.949	0.02	99.97	0.00	0.014	-3.67

APPENDIX C

TEST SYSTEMS

Test feeder #1

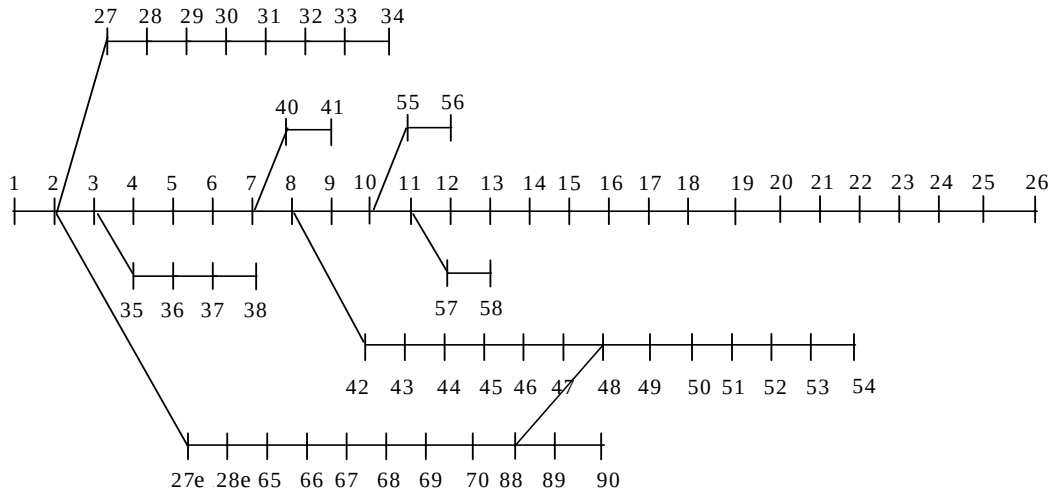

Figure 87: The layout of test feeder #1.

Table 73: Parameters of test feeder #1.

Sending node	Receiving node	r [p.u.]	x [p.u.]	Length [mi]	Rv. Nd. P[kW]	Rv. Nd. Q[kVAr]	Rv. Nd. customers
1	2	0.00031	0.00075	0.010	0	0	0
0	1	0.00031	0.00075	0.010	0	0	0
2	3	0.00094	0.00225	0.010	0	0	0
2	27	0.00275	0.00674	0.030	26	11.16	5
2	27e	0.00275	0.00674	0.030	26	11.13	5
3	4	0.01566	0.01834	0.160	0	0	0
3	35	0.00212	0.00524	0.020	414.67	177.6	55
4	5	0.22836	0.11630	2.280	2.6	1.32	1
5	6	0.23778	0.12110	2.380	40.4	18	8
6	7	0.05753	0.02932	0.580	75	32.4	3
7	8	0.03076	0.01566	0.310	30	13.2	2
7	40	0.05790	0.02951	0.580	40.5	16.98	8
8	9	0.51099	0.16890	5.110	28	11.4	5
8	42	0.10856	0.05528	1.090	4.35	2.1	1
9	10	0.11680	0.03862	1.170	145	62.4	26
10	11	0.44386	0.14668	4.440	145	62.4	16
10	55	0.12553	0.03812	1.260	18	7.8	1
11	12	0.64264	0.21213	6.430	8	3.3	1
11	57	0.46133	0.15249	4.610	28	12	1
12	13	0.65138	0.21525	6.510	8	3.3	1
13	14	0.66011	0.21812	6.600	0	0	0
14	15	0.12266	0.04056	1.230	45.5	18	1
15	16	0.23360	0.07724	2.340	60	21	5
16	17	0.00293	0.00100	0.030	60	21	1
17	18	0.20440	0.06757	2.040	0	0	0
18	19	0.13140	0.04343	1.310	1	0.36	0
19	20	0.21313	0.07044	2.130	114	48.6	3
20	21	0.00873	0.00287	0.090	5.3	2.1	0
21	22	0.09927	0.03282	0.990	0	0	0
22	23	0.21607	0.07144	2.160	28	12	5
23	24	0.46720	0.15442	4.670	0	0	0
24	25	0.19273	0.06370	1.930	14	6	0
25	26	0.10806	0.03569	1.080	14	6	1
27	28	0.03993	0.09764	0.400	26	11.16	1

Table 74: Parameters of the test feeder #1 (continued from Table 73).

Sending node	Receiving node	r [p.u.]	x [p.u.]	Length [mi]	Rv. Nd. P[kW]	Rv. Nd. Q[kVAr]	Rv. Nd. customers
28	29	0.24820	0.08205	2.480	0	0	0
29	30	0.04380	0.01448	0.440	414.67	177.6	78
30	31	0.21900	0.07238	2.190	0	0	0
31	32	0.52347	0.17570	5.230	14	6	3
32	33	1.06566	0.35227	10.660	19.5	8.4	0
33	34	0.91967	0.30404	9.200	6	2.4	1
35	36	0.05310	0.12996	0.530	79	33.84	8
36	37	0.18081	0.44243	1.810	384.7	164.7	18
37	38	0.05129	0.12547	0.510	384.7	164.7	78
40	41	0.20708	0.06951	2.070	3.6	1.62	1
42	43	0.12666	0.06451	1.270	26.4	11.4	4
43	44	0.17732	0.09028	1.770	24	10.32	1
44	45	0.17551	0.08941	1.760	0	0	0
45	46	0.99204	0.33299	9.920	0	0	0
46	47	0.48897	0.16409	4.890	0	0	0
47	48	0.18980	0.06277	1.900	100	43.2	8
48	49	0.24090	0.07312	2.410	0	0	0
49	50	0.31664	0.16128	3.170	414.67	177.6	107
50	51	0.06077	0.03095	0.610	32	13.8	2
51	52	0.09047	0.04605	0.900	0	0	0
52	53	0.44330	0.22580	4.430	227	97.2	62
53	54	0.64951	0.33081	6.500	59	25.2	4
55	56	0.00293	0.00087	0.030	18	7.8	0
57	58	0.00293	0.00100	0.030	28	12	5
65	66	0.01897	0.02215	0.190	24	10.2	6
28e	65	0.06570	0.07674	0.660	0	0	0
66	67	0.00112	0.00131	0.010	24	10.2	1
67	68	0.45440	0.53090	4.540	1.2	0.6	0
68	69	0.19342	0.22605	1.930	0	0	0
69	70	0.02558	0.02982	0.260	6	2.58	1
70	88	0.00574	0.00724	0.060	0	0	0
88	89	0.06795	0.08566	0.680	39.22	15.78	4
89	90	0.00056	0.00075	0.010	39.22	15.78	4
27e	28e	0.03993	0.09764	0.400	26	11.13	1
48	88	0.04492	0.10985	0.450	0	0	0

Test feeder #2

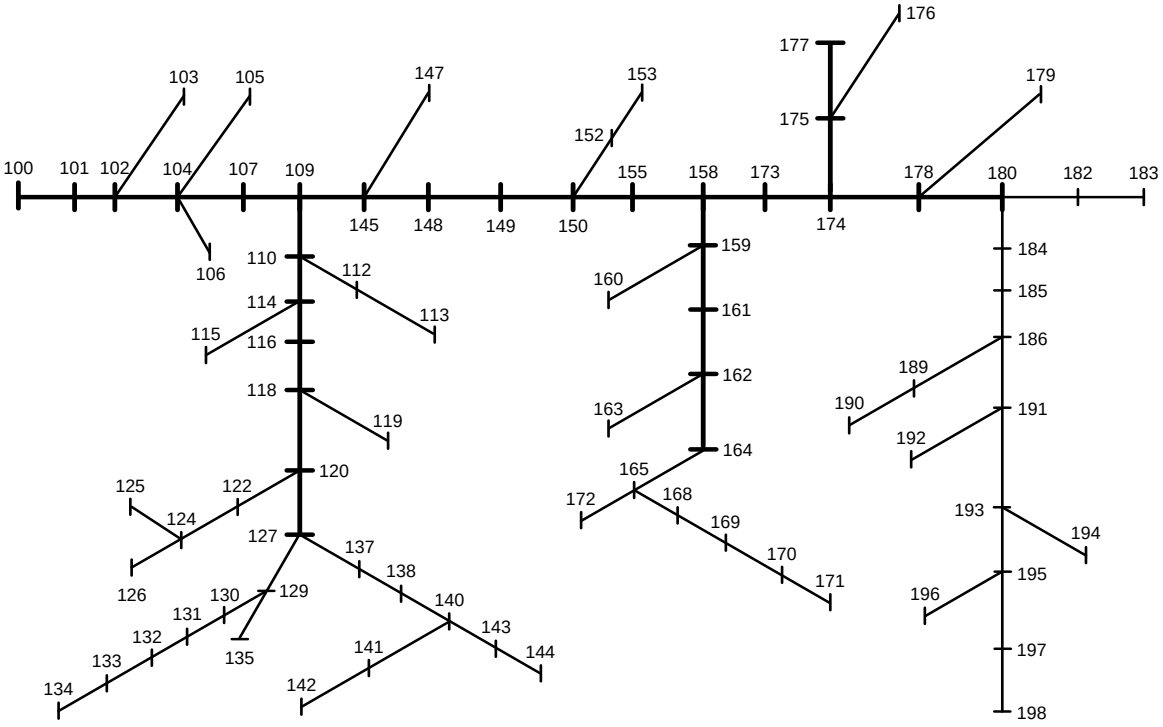

Figure 88: The layout of test feeder #2. Bold lines indicate three-phase lines; thin lines indicate single-phase lines.

Table 75: Parameters of test feeder #2.

Sending node	Receiving node	Phase	Length [mi]	Rv. Nd. P[kW] (A)	Rv. Nd. P[kW] (B)	Rv. Nd. P[kW] (C)	Rv. Nd. customers (A)	Rv. Nd. customers (B)	Rv. Nd. customers (C)
100	101	0	0.125	0	0	0	0	0	0
101	102	0	1.500	200	110	230	20	11	23
102	104	0	2.563	40	60	90	4	6	9
104	107	0	1.124	70	210	250	7	21	25
107	109	0	0.250	20	10	30	2	1	3
109	145	0	0.688	10	10	140	1	1	14
145	148	0	1.688	190	0	50	19	0	5
148	149	0	1.750	120	0	60	12	0	6
149	150	0	1.750	120	0	30	12	0	3
150	155	0	1.124	60	10	20	6	1	2
155	158	0	1.438	0	0	60	0	0	6
158	173	0	0.500	0	30	0	0	3	0
173	174	0	1.000	10	30	0	1	3	0
174	178	0	0.750	20	150	20	2	15	2
178	180	0	1.875	0	400	0	0	40	0
180	182	3	4.000	0	0	180	0	0	18
182	183	3	1.875	0	0	180	0	0	18
180	184	1	0.750	20	0	0	2	0	0
184	185	1	1.250	60	0	0	6	0	0
185	186	1	1.750	170	0	0	17	0	0
186	191	1	1.250	140	0	0	14	0	0
191	193	1	1.563	100	0	0	10	0	0
193	195	1	0.500	30	0	0	3	0	0
195	197	1	0.624	70	0	0	7	0	0
197	198	1	3.438	180	0	0	18	0	0
195	196	1	3.250	120	0	0	12	0	0
193	194	1	2.500	120	0	0	12	0	0
191	192	1	1.750	30	0	0	3	0	0
186	189	1	3.875	180	0	0	18	0	0
189	190	1	2.875	130	0	0	13	0	0
178	179	2	2.500	0	160	0	0	16	0
174	175	0	1.000	10	20	40	1	2	4
175	177	0	0.438	10	0	10	1	0	1
175	176	2	1.312	0	100	0	0	10	0
158	159	0	2.312	30	160	0	3	16	0
159	161	0	2.500	50	150	40	5	15	4
161	162	0	2.250	110	30	10	11	3	1
162	164	0	0.250	10	30	0	1	3	0
164	165	2	2.063	0	340	0	0	34	0
165	172	2	3.500	0	380	0	0	38	0

Table 76: Parameters of test feeder #2 (continued from Table 75).

Sending node	Receiving node	Phase	Length [mi]	Rv. Nd. P[kW] (A)	Rv. Nd. P[kW] (B)	Rv. Nd. P[kW] (C)	Rv. Nd. customers (A)	Rv. Nd. customers (B)	Rv. Nd. customers (C)
165	168	2	0.500	0	160	0	0	16	0
168	169	2	1.687	0	120	0	0	12	0
169	170	2	2.376	0	170	0	0	17	0
170	171	2	4.000	0	70	0	0	7	0
162	163	3	4.500	0	0	170	0	0	17
159	160	1	1.250	150	0	0	15	0	0
150	152	3	2.000	0	0	160	0	0	16
152	153	3	1.124	0	0	140	0	0	14
145	147	3	2.562	0	0	220	0	0	22
109	110	0	2.750	50	120	120	5	12	12
110	112	2	2.688	0	300	0	0	30	0
112	113	2	3.125	0	200	0	0	20	0
110	114	0	0.750	0	0	20	0	0	2
114	116	0	0.438	40	10	0	4	1	0
116	118	0	0.750	70	0	10	7	0	1
118	120	0	1.500	60	190	30	6	19	3
120	127	0	0.812	0	160	0	0	16	0
127	129	3	1.063	0	0	460	0	0	46
129	135	3	3.313	0	0	210	0	0	21
129	130	3	3.063	0	0	60	0	0	6
130	131	3	0.500	0	0	50	0	0	5
131	132	3	1.250	0	0	240	0	0	24
132	133	3	3.000	0	0	170	0	0	17
133	134	3	3.124	0	0	100	0	0	10
127	137	1	0.563	70	0	0	7	0	0
137	138	1	2.000	370	0	0	37	0	0
138	140	1	1.687	250	0	0	25	0	0
140	143	1	2.750	40	0	0	4	0	0
143	144	1	1.250	30	0	0	3	0	0
140	141	1	1.876	190	0	0	19	0	0
141	142	1	2.124	240	0	0	24	0	0
120	122	2	0.750	0	0	0	0	0	0
122	124	2	0.500	0	140	0	0	14	0
124	126	2	2.312	0	340	0	0	34	0
124	125	2	3.938	0	100	0	0	10	0
118	119	1	2.375	520	0	0	52	0	0
114	115	2	1.688	0	130	0	0	13	0
104	106	3	1.312	0	0	400	0	0	40
104	105	3	1.000	0	0	260	0	0	26
102	103	3	1.500	0	0	320	0	0	32

REFERENCES

[1] B , C. E., "Less is more: Why gas turbines will transform electric utilities," *Public Utilities Forthnightly*, December 2001.

[2] "California distributed resource guide." Available electronically at `http://www.energy.ca.gov/distgen`, September 2002.

[3] D , P. A. and M , J., "Understanding the potential benefits of distributed generation on power delivery systems," in *Proceedings of the 2001 Rural Electric Power Conference*, pp. A2/1–A2/13, 2001.

[4] "Wind power outlook 2003." Available electronically at `http://www.awea.org/pubs`, American Wind Energy Association, 2003.

[5] M , P., "PV market update," *Renewable Energy World*, July–August 2003.

[6] M , P. *PV news*, vol. 22, no. 3, 2003.

[7] F., M. D. and F , J. P., "User's manual for PVFORM: Photovoltaic system simulation program for stand–alone and grid–interactive applications." Sandia National Laboratories publication SAND85-0376, October 1989.

[8] W , H. J., "PVGRID 7.1 - a photovoltaic system simulation program." Pacific Energy Group, June 2002.

[9] P , M., "PV–DesignPro photovoltaic simulation program." Available electronically at `http://www.mauisolarsoftware.com`, Maui Solar Energy Software Corporation, 2002.

[10] M , W. and U , K., "User's manual for TMY2s," June 1995.

[11] M , D. and F , J., "Verification of photovoltaic system modeling codes based on system experimental data," in *Proceedings of the* 17^{th} *IEEE Photovoltaic Specialists Conference (PVSC)*, (Kissimmee, FL), 1984.

[12] L , B. Y. H. and J , R. C., "The interrelationship and characteristic distribution of direct, diffuse and total solar radiation," *Solar Energy*, vol. 4, pp. 1–19, July 1960.

[13] P , R., S , R., I , P., S , R., and M , D., "A new simplified version of the perez diffuse irradiance model for tilted surfaces," *Solar Energy*, vol. 39, no. 3, pp. 221–231, 1987.

[14] D , J. A., *Solar Engineering of Thermal Processes*. New York: Wiley, 2 ed., 1991.

[15] K , D. L., K , J. A., B , W. E., and B , W. I., "Field experience with a new performance characterization procedure for photovoltaic arrays," in *Proceedings of the* 2*nd World Conference and Exhibition on Photovoltaic Solar Energy Conversion*, (Vienna, Austria), pp. 1947–1952, 6–10 July 1998.

[16] F , M. K., "A simplified thermal model for flat-plate photovoltaic arrays." Sandia National Laboratories publication SAND85-0330, May 1987.

[17] T , T. U., "A method for estimating the long-term performance of direct-coupled photovoltaic systems," Master's thesis, University of Wisconsin - Madison, 1989.

[18] R , M. E., B , M., and R , A., "Determination of the curvature derating factor for the Georgia Tech Aquatic Center photovoltaic array," in *Proceedings of the* 26*th IEEE Photovoltaics Specialists Conference (PVSC)*, pp. 1297–1300, September–October 1997.

[19] F , T. A., M , B., and S , M., "Approximate analytical solution of generalized diode equation," *IEEE Transactions on Electron Devices*, vol. 38, no. 8, pp. 1976–1977, 1991.

[20] R , M. E., B , M., R , R., and L , R., "Design considerations for large roof-integrated photovoltaic arrays," *Progress in Photovoltaics: Research and Applications*, vol. 5, pp. 55–67, January–February 1997.

[21] B , M., R , M. E., R , A., and L , R., "Performance evaluation of the Georgia Tech aquatic center photovoltaic array," in *Proceedings of the* 14*th European Photovoltaic Solar Energy Conference (EPVSEC)*, (Barcelona, Spain), pp. 374–379, 1997.

[22] B , M., R , M., R , A., D , S., and R , A., "Monitoring and data acquisition for a large roof-mounted photovoltaic array," in *Proceedings of the IEEE Region 3 Conference (SECON '97)*, (Blacksburg, VA), pp. 297–300, April 1997.

[23] B , M., P , A., and R , A., "Four-year performance assessment of the 342 kW PV system at Georgia Tech," in *Proceedings of the* 28*th IEEE Photovoltaics Specialists Conference (PVSC)*, (Anchorage, AK), pp. 1575–1578, September 2000.

[24] "Building integrated photovoltaics: Power Tower project." British Columbia Institute of Technology, Available electronically at `http://www.tc.bcit.ca/pv/projects/pwer.shtml`.

[25] B , W., "Inverters - critical photovoltaic balance-of-system components: status, issues, and new-millennium opportunities," *Progress in Photovoltaics: Research and Applications*, vol. 8, pp. 113–126, January–February 2000.

[26] M , B., A , C., H , S., G , D., O , D., and C , D., "Photovoltaic system reliability," in *Proceedings of the* 26th *IEEE Photovoltaics Specialists Conference (PVSC)*, (Anaheim, CA), pp. 1049–1054, 29 September–03 October 1997.

[27] G , B., P , I., U , I., and C , S., *Statistical reliability engineering*. John Wiley & Sons, Ltd., 1999.

[28] H , T. and S , D. S., "The value of grid-support photovoltaics in reducing distribution system losses," *IEEE Transactions on Energy Conversion*, vol. 10, pp. 569–576, September 1995.

[29] F , B. C., "Trends in public perceptions and preferences on energy and environmental policy." National Renewable Energy Laboratory (NREL), NREL/TP-461-4587, February 1993.

[30] F , B. C., "Willingness to pay for electricity from renewable resources: A review of utility market research." National Renewable Energy Laboratory (NREL), NREL/TP-550-26148, July 1999.

[31] F , B. C. and C , T. C., "Colorado homeowner preferences on energy and environmental policy." National Renewable Energy Laboratory (NREL), NREL/TP-550-25285, June 1999.

[32] T , J. and M , D. L., "Regional capability building – utility restructuring survey," tech. rep., Social and Economic Sciences Research Center, Washington State University, Data report 98-40, 1998.

[33] F , E. G., "Renewable resources and conservation: What consumers want." Boneville Power Administration, Portland, OR, 1999.

[34] B , M. E. and W , F. F., "Optimal capacitor placement on radial distribution systems," *IEEE Transactions on Power Delivery*, vol. 4, pp. 725–732, January 1989.

[35] Z , R. D. and G , D., "MATPOWER, a MATLAB^{TM} power system simulation package." Available electronically at `http://www.pserc.cornell.edu/matpower/matpower.html`, December 1997.

[36] T , S. and K , K., *Pattern Recognition*. Academic Press, 1 ed., 1999.

[37] L , S. P., "Least squared quantization in PCM," *IEEE Transactions on Information Theory*, vol. 28, no. 4, pp. 129–137, 1982.

[38] E , W. H., "A new vector quantization clustering algorithm," *IEEE Transactions on Acoustics, Speech, and Signal Processing*, vol. 37, pp. 1568–1575, 1989.

[39] C , B., "An optimal convex hull algorithm and new results on cuttings," in *Proceedings of the* 32th *Annual Symposium on Foundations of Computer Science*, pp. 29–38, 1991.

[40] O , T., S , S., and S , S., "Enumerating extreme points in higher dimensions," in *Proceedings of the* 12th *Annual Symposium on Theoretical Aspects of Computer Science (STACS)*, pp. 562–570, 1995.

[41] B , C. B., D , D. P., and H , H. T., "The quickhull algorithm for convex hulls," *ACM Transactions on Mathematical Software*, vol. 22, pp. 469–483, December 1996.

[42] B , M., P , A., R , A., and H , C., "Green power: Status and perspectives," *Proceedings of the IEEE*, vol. 89, pp. 1734–1743, December 2001.

[43] "Recommended practice for utility interface of photovoltaic (PV) systems." IEEE 929–2000 Standard, 2000.

[44] B , A. R., *Power system analysis*. Prentice-Hall, 1 ed., 1986.

[45] "IEEE trial-use guide for electric power distribution reliability indices." IEEE 1366–1998 Standard, 1998.

[46] W , C. A., A , R., and W , G., "A survey of distribution reliability measurement practices in the U.S.," *IEEE Transactions on Power Delivery*, vol. 14, pp. 250–257, January 1999.

[47] K , J. Georgia Power, personal communication.

[48] K , L. A. and W , R. D., "Integration of distributed generation in a typical USA distribution system," in *Proceedings of the* 16th *International Conference and Exhibition on Electricity Distribution,(CIRED)*, vol. 4, (Amsterdam, The Netherlands), p. 5, June 2002.

[49] B , R. E. and F , L. A., "Analyzing the reliability impact of distributed generation," in *Proceedings of the 2001 Power Engineering Society Summer Meeting*, vol. 2, (Vancouver, B. C.), pp. 1013–1018, 2001.

[50] "IEEE standard for interconnecting distributed resources with electric power systems." IEEE 1547–2003 Standard, June 2003.

[51] "UL 1741 standard for inverters, converters, and controllers for use in independent power systems." Underwriters Laboratories Inc., 1999.

[52] B , M., R , M., R , A., and P , A., "Determining the sufficiency of standard protective relaying for islanding prevention in grid-connected PV systems," in *Proceedings of the* 2nd *World Conference on Photovoltaic Solar Energy Conversion*, (Vienna, Austria), pp. 2519–2524, 1999.

[53] R , M., B , M., R , A., K , G. A., B , R., and G , S., "Determining the relative effectiveness of islanding detection methods using phase criteria and nondetection zones," *IEEE Transactions on Energy Conversion*, vol. 15, pp. 290–296, September 2000.

[54] R , M., B , M., and R , A., "Analysis and performance assessment of the active frequency drift method of islanding prevention," *IEEE Transactions on Energy Conversion*, vol. 14, pp. 810–816, September 1999.

[55] D , R. C., "On the necessity of three-phase feeder modeling for DG planning purposes," in *Proceedings of the 2002 Power Engineering Society Summer Meeting*, vol. 1, pp. 438–441, 2002.

[56] H , C. R. and J , J. A., "A genetic algorithm for function optimization: A MATLAB implementation," tech. rep., NCSU-IE, 1995.

[57] P , A., B , M., R , A., and N , D., "On optimization of reliability of distributed generation-enhanced feeders," in *Proceedings of the* 36^{th} *Hawaii International Conference on System Sciences (HICSS)*, January 2003.

[58] G , D. E., *Genetic Algorithms in Search, Optimization, and Machine Learning*. Addison-Wesley, 1989.

[59] C , L. D., *Practical Handbook of Genetic Algorithms: Complex Coding Systems*, vol. 3. CRC Press, 1999.

[60] Q , D., P , J., P , C., and W , G., *Genetic Algorithms and Evolution Strategies in Engineering and Computer Science*. John Wiley & Sons, 1998.

[61] D , L., *Handbook of genetic algorithms*. Van Nostrand Reinhold, 1991.

[62] G , D. E., "Real-coded genetic algorithms, virtual alphabets, and blocking," tech. rep., University of Illinois at Urbana-Champaign, 1990.

[63] M , Z., *Genetic Algorithms + Data Structures = Evolution Programs*. Springer, 3 ed., 1999.

[64] D J , K. A., *An analysis of the behavior of a class of genetic adaptive systems*. PhD thesis, University of Michigan, 1975.

[65] G , J. J., "Optimization of control parameters for genetic algorithms," *IEEE Transactions on Systems, Man and Cybernetics*, vol. 16, no. 1, pp. 122–128, 1986.

[66] S , E., C , R. A., E , L. J., and D , R., "A study of control parameters affecting online performance of genetic algorithms for function optimization," in *Proceedings of the Third International Conference on Genetic Algorithms*, pp. 51–60, 1989.

[67] S , M. and P , L. M., “Adaptive probabilities of crossover and mutation in genetic algorithms,” *IEEE Transactions on Systems, Man and Cybernetics*, vol. 24, pp. 656–667, April 1994.

[68] L , F. NEETRAC, personal communication.

VITA

Aleksandar Pregelj was born in Belgrade, Serbia on November 11, 1970. He received the B.S. degree in Electrical Engineering from Belgrade University in 1997, and the M.S. degree in Electrical Engineering from Georgia Institute of Technology in 1998. Since 1997 he has been a graduate research assistant at the University Center of Excellence for Photovoltaic Research and Education at the Georgia Institute of Technology. He is currently pursuing the Doctorate of Philosophy from the Georgia Institute of Technology in School of Electrical and Computer Engineering, under the supervision of Dr. Miroslav Begović and Dr. Ajeet Rohatgi. He is a student member of IEEE and a member of Sigma Xi. His interests include modeling and design of renewable DG systems, and analysis of DG-enhanced distribution networks. This work has resulted in 11 publications in professional journals and conference proceedings.